

**SYNTHESIS OF pH RESPONSIVE CARRIERS FOR PULMONARY DRUG DELIVERY OF
ANTI-TUBERCULOSIS THERAPEUTICS: MESOPOROUS SILICA NANOPARTICLES AND
GELATIN NANOPARTICLES**

MPHO PHEHELLO NGOEPE

A thesis submitted to the Faculty of Science, Rhodes University, in
fulfilment of the requirements for the degree of
Doctor of Philosophy



Supervisor:

Professor Rui M.W. Krause

Department of Chemistry, Faculty of Science, Rhodes University, Grahamstown, South Africa

Grahamstown

2018

DECLARATION

I, Mpho Phehello Ngoepe, declare that this thesis is my own work. It has been submitted for the degree of Doctor of Philosophy in the Faculty of Science at the Rhodes University, Grahamstown, South Africa. It has not been submitted before for any degree or examination at this or any other University.

A handwritten signature in black ink, consisting of several overlapping loops and a trailing horizontal line.

Signed this 31 day of January 2018

PUBLICATIONS

Mpho P Ngoepe, Rui W.M Krause. Recent technological developments in pulmonary drug delivery systems: improving aerosol properties. [To be submitted]

Mpho P Ngoepe, Rui W.M Krause. Design of chemometric tool for simultaneous analysis of ascorbic acid, rifampicin and isoniazid drug combination. [To be submitted]

Mpho P Ngoepe, Rui W.M Krause. Evaluation of rifampicin loaded mesoporous silica nanoparticle synthetic parameters using box-benhken design: pH responsive system. [To be submitted]

Mpho P Ngoepe, Rui W.M Krause. Synthesis of pH responsive gelatin nanoparticle using non-ionic surfactant. [To be submitted]

Mpho P Ngoepe, Rui WM Krause. Control of mesoporous silica nanoparticles physicochemical properties through control of synthetic parameter using Box-Behnken design. International Meeting on Advanced Nanomaterials and Nanotechnology. November 07-08, 2017 Singapore. Nano Res Appl 2017, 3:4 DOI: 10.21767/2471-9838-C1-006. (Abstract)

Mpho P Ngoepe. Rui WM Krause. Control of mesoporous silica nanoparticles physicochemical properties through control of synthetic parameter using Box-Behnken design. 22nd International Conference and Expo on NANOSCIENCE AND MOLECULAR NANOTECHNOLOGY. November 06-08, 2017, Frankfurt, Germany. J Nanomed Nanotechnol 2017, 8:6(Suppl) DOI: 10.4172/2157-7439-C1-058 (Abstract)

Appendix 11.1

RESEARCH PRESENTATIONS

Mpho P Ngoepe. Rui W Krause. Synthesis of Mesoporous Silica Nanoparticles Core for Design of Responsive Aerosol Drug Delivery Carrier. The 17th South African Chemical Institute Inorganic Chemistry Conference. 28 June - 2 July 2015, Rhodes University, South Africa (Poster)

Mpho P Ngoepe. Rui WM Krause. pH responsive drug delivery system for pulmonary delivery of anti-TB drugs the interdisciplinary postgraduate conference. 29-30 September 2017, Rhodes University, South Africa (Podium)

Mpho P Ngoepe. Rui WM Krause. Control of mesoporous silica nanoparticles physicochemical properties through control of synthetic parameter using Box-Behnken design. 22nd International Conference and Expo on Nanoscience and Molecular Nanotechnology. November 06-08, 2017, Frankfurt, Germany (Podium)

Mpho P Ngoepe. Rui WM Krause. Inhalable nanomedicine – Pulmonary delivery of anti-TB drugs using pH responsive carriers. Swiss-SA Nanomedicine (TB and HIV/AIDS Symposium). 05-06 December 2017, CSIR, Pretoria, South Africa. (Podium).

ACKNOWLEDGEMENTS

I would like to acknowledge my parents Victor and Lucy Nengovhela, for the love and support they have always given me through my years of studying. Thank you for the patience and sacrifices made for me to pursue to fulfil my academic plans. Without you, I wouldn't be here without you.

To my siblings Kgaugelo, Lebogang, Baleseng and Tshegofatso for the loving support and encouragement.

To my supervisor Professor Rui Krause, thank you for giving me the opportunity to learn more. Thank you for the support and the sharing of your limitless knowledge. Without you I wouldn't have learnt so much as I have if it wasn't for your guidance, patience and trust.

To my colleagues and friends: Felix Mashingaidze, Dr Steven Mufamadi, Ogunyemi Oderinlo, Khethobole Sekgota, Kubheka Gugu, Marwarwa Sinobomi, Thanduxolo Mtshare, Mziyanda Mbaba, Gwiba Makalima, Matshitse Refilwe, Melody Manyeruke, Nkanga Isalomboto Christian, Jean Pierre Kayembe, Nozuko Makayonke, Waleguele Christine Claire, Mafukidze Donovan, Tarryn Potts, Dr Rich Mbi, Lukhanyiso Nqeno, Shwempe Noluvuyo, Fostino Bokosi, Okafor Nnamdi, Klementine Kaluizi, Gervase Makoni, Dr Xavier Siwe Noundou, Lekokotla Lungelo, Bertha Chithambo, Msane Gugu, Tshenkeng Keamogetse, Kalinski Jarmo.

Special thanks to Dr Setshaba D Khanye, Dr Kevin A. Lobb, Professor Perry T. Kaye, Mr M Mafani, Ms. B. Tarr, Ms. B.L. Ah Yui, Mr F Chindeka, Mr A Adriaan, Mr H L R Douglas, Mr V Dondashe, Ms. N. Mbebe, Mr S Sukula.

I would like to also thank National Research Foundation (NRF) and Rhodes University for financial assistance. This research would not have been possible without their support.

ABSTRACT

Pulmonary drug delivery has historically been used as a route for delivery of therapeutics for respiratory disease management. However, while there are many advantages, there are also some serious limitations, arising mostly from the physical aspects of the inhaler devices. This is more profound when the devices are the driving force for controlling particle size generation, which results in non-uniform particles that end up being swallowed/wasted/expelled.

One promising solution to overcome this limitation is to pre-formulate nano/microscale particles with a high degree of manufacturing control. Nanomedicine has advanced such that there are already several nanoparticle formulations commercially available.

In the case of tuberculosis treatment, there is an opportunity not only to examine the use of nanoparticles for inhalation therapy, but to take advantage of the fact that the physicochemical environment of diseased tissue is significantly different to health lung tissue (lower pH and increased enzyme concentrations). We formulated two series of nanoparticles, whose design included moieties that could respond to pH and enzymes.

To address variability, a Box-Behnken statistical approach was followed to construct mesoporous silica nanoparticles. These “hard nanoparticles” can entrap both lipophilic and hydrophilic drugs and were coated with a pH-sensitive hydrazone linker.

It was observed that pH, calcination temperature and ratio of water to silica source played the greatest role, not only in controlling the physicochemical properties of the nanoparticles but also the drug release rate.

A second series of nanoparticles were synthesized based on gelatin. This was done partly to add support the comparison of hard (inorganic silica) versus soft, organic particles, but also to enable enzymatic degradation and drug release. Again, diseased lung tissue expresses increased concentrations of gelatinase enzymes that could be used to stimulate drug release at the site of the disease. In addition, it was observed that the non-ionic surfactant C₁₂E₁₀ could interact with the protein via hydrophobic interactions thus affecting the gelatin folding. The folding states affected crosslinking with the pH responsive linker, which in turn affected the rate of drug release. To support the synthetic work, we sought to develop a unique 3D lung model directly from MRI data of tuberculosis infected lungs. This would not only permit the evaluation of our nanoparticles but could be used as a proxy for *in-vivo* studies in future to predict lung deposition in diseased lung.

Thus, this study shows that it is possible to synthesize pH and enzyme sensitive nanoparticles for pulmonary drug delivery in the treatment and management of pulmonary tuberculosis. These particles could be loaded with either hydrophobic or hydrophilic drugs and their distribution in the airway modelled using an *in-silico* 3D model based on real data. Further development and verification of these results should improve treatment for pulmonary diseases and conditions such as tuberculosis. This is especially urgent in the face of multi-drug resistance and poor side effects profiles for current treatment.

DEDICATION

This thesis is dedicated to my parents Victor and Lucy Nengovhela for the loving support and sacrifices throughout my studies

*God grant me the serenity
to accept the things, I cannot change;
courage to change the things I can;
and wisdom to know the difference.*

*Living one day at a time;
enjoying one moment at a time;
accepting hardships as the pathway to peace;
taking, as He did, this sinful world
as it is, not as I would have it;
trusting that He will make all things right
if I surrender to His Will;
that I may be reasonably happy in this life
and supremely happy with Him
forever in the next.*

Amen.

- Reinhold Niebuhr (1892-1971)

TABLE OF CONTENTS

	Page
DECLARATION.....	i
PUBLICATIONS.....	ii
RESEARCH PRESENTATIONS.....	iii
ACKNOWLEDGEMENTS.....	iv
ABSTRACT.....	v
DEDICATION.....	vii
LIST OF ABBREVIATIONS.....	xiv
LIST OF EQUATIONS.....	xvii
LIST OF FIGURES.....	xviii
LIST OF TABLES.....	xviii

LIST OF CHAPTERS

CHAPTER 1 : INTRODUCTION AND BACKGROUND TO STUDY	1
1.1. BACKGROUND TO THE STUDY	1
1.2. RATIONALE AND MOTIVATION OF THE STUDY	5
1.3. MECHANISM OF ACTION OF PH RESPONSIVE AEROSOL CARRIERS	6
1.4. NOVELTY OF THE STUDY	8
1.5. POSSIBLE THERAPEUTIC APPLICATIONS OF THE STUDY	8
1.6. AIM AND OBJECTIVES OF THE STUDY	9
1.7. OVERVIEW OF THE THESIS	10
1.8. REFERENCES	12
CHAPTER 2 : LITERATURE REVIEW ON PULMONARY DRUG DELIVERY	1
2.1. CHRONOLOGICAL OVERVIEW	1
2.2. LUNG ANATOMICAL FEATURES	2
2.2.1. <i>Nasal and oral cavity</i>	2
2.2.2. <i>Upper and lower respiratory tract</i>	3
2.2.3. <i>Variations in anatomical features</i>	4
2.3. LUNG BARRIERS (DEPOSITION, DISSOLUTION, ABSORPTION AND CLEARANCE)	5
2.3.1. <i>Targeting or overcoming mucus clearance</i>	5
2.3.2. <i>Macrophage defence and surfactant</i>	6
2.3.3. <i>Particle transport and absorption</i>	6
2.4. MOLECULAR BIOLOGY FOR RESPONSIVE AND TARGET DELIVERY	7
2.4.1. <i>Immune cell targeting</i>	7
2.5. ENGINEERING CARRIERS FOR PULMONARY DELIVERY	9
2.5.1. <i>Inertial impaction</i>	10
2.5.2. <i>Sedimentation</i>	11
2.5.3. <i>Interception</i>	13
2.5.4. <i>Diffusion</i>	14
2.5.5. <i>Electrostatic</i>	14
2.6. INHALER DEVICE SELECTION	15
2.6.1. <i>Nebulizers</i>	16
2.6.2. <i>Metered dose Inhaler</i>	17
2.6.3. <i>Dry powder inhalers</i>	18
2.7. DISEASE STATES AND THERAPEUTIC INNOVATIONS	19
2.7.1. <i>Tuberculosis</i>	20
2.7.2. <i>Asthma and chronic obstructive pulmonary disease</i>	21
2.7.3. <i>Cystic Fibrosis</i>	22
2.7.4. <i>Cancer</i>	23
2.8. SYSTEMIC DELIVERY, GENE DELIVERY AND VACCINATION	25
2.9. CHARACTERIZATION OF EFFECTIVENESS THE PULMONARY DRUG DELIVERY SYSTEM	26
2.10. CONCLUDING REMARKS	27
2.11. REFERENCE	28

CHAPTER 3 : SIMULTANEOUS ANALYSIS OF ANTI-TUBERCULOSIS DRUGS THROUGH UV-VIS SPECTROMETRY USING CHEMOMETRIC TECHNIQUE..... 41

3.1.	INTRODUCTION.....	41
3.2.	MATERIALS AND METHODS.....	43
3.2.1.	<i>Materials.....</i>	43
3.2.2.	<i>Standard solutions.....</i>	44
3.2.3.	<i>Central composite design.....</i>	44
3.2.4.	<i>Spectral design.....</i>	45
3.2.5.	<i>Partial least square analysis.....</i>	45
3.2.6.	<i>Prediction accuracy.....</i>	46
3.2.7.	<i>High performance liquid chromatography method.....</i>	47
3.3.	RESULTS AND DISCUSSION.....	48
3.3.1.	<i>Derivative spectra.....</i>	48
3.3.2.	<i>High-performance liquid chromatography evaluation.....</i>	50
3.3.3.	<i>Method accuracy using cross-validation method.....</i>	50
3.3.4.	<i>Method application using commercial tablet mixture.....</i>	51
3.4.	CONCLUDING REMARKS.....	52
3.5.	REFERENCE.....	53

CHAPTER 4 : SYNTHESIS AND CHARACTERIZATION OF HYDRAZONES FROM DIALDEHYDE FOR PH RESPONSIVE DRUG DELIVERY SYSTEM 56

4.1.	INTRODUCTION.....	56
4.2.	MATERIALS AND METHODS.....	57
4.2.1.	<i>General procedures and materials.....</i>	57
4.2.2.	<i>Synthesis of Hydrazine Derivatives.....</i>	59
4.2.3.	<i>Synthesis of Aliphatic Aldehyde Derivatives.....</i>	59
4.2.4.	<i>Hydrazine Hydrazones (compound 1-4).....</i>	60
4.2.5.	<i>Formohydrazide Hydrazone (compound 5).....</i>	60
4.2.6.	<i>Thiosemicarbazide Hydrazones (compound 10-12).....</i>	60
4.2.7.	<i>Aminoglycine Hydrazones (compound 6-9).....</i>	60
4.2.8.	<i>Hydrolysis Kinetics at acidic and neutral pH.....</i>	60
4.3.	RESULTS AND DISCUSSION.....	61
4.3.1.	<i>Structural chemistry analysis using infrared spectrometry.....</i>	62
4.3.2.	<i>Ultraviolet analysis of $\pi \rightarrow \pi^*$ transitions.....</i>	63
4.3.3.	<i>Characterization of hydrazone molecular structure.....</i>	64
4.3.4.	<i>Hydrazine monohydrate based hydrazones.....</i>	65
4.3.5.	<i>Formylhydrazine.....</i>	66
4.3.6.	<i>Aminoglycine.....</i>	67
4.3.7.	<i>Thiosemicarbazide hydrazones.....</i>	68
4.3.8.	<i>Hydrolysis kinetics.....</i>	69
4.4.	CONCLUDING REMARKS.....	71
4.5.	REFERENCE.....	71

CHAPTER 5 : SYNTHESIS AND CHARACTERIZATION OF GLUCOSE BASED POLYMER FOR POSSIBLE USE AS HYGROSCOPIC LAYER AND MACROPHAGE RECRUITING SURFACE COAT . 73

5.1.	INTRODUCTION.....	73
5.2.	MATERIALS AND METHODS.....	74
5.2.1.	<i>Materials.....</i>	74
5.2.2.	<i>Synthesis of dibromopropane.....</i>	75

5.2.3.	<i>Synthesis of dibromobutane</i>	75
5.2.4.	<i>Synthesis of coat</i>	75
5.3.	RESULTS AND DISCUSSION.....	77
5.3.1.	<i>Pure glucose</i>	77
5.3.2.	<i>Acetal protected glucose</i>	78
5.3.3.	<i>Chain length extension</i>	79
5.4.	CONCLUDING REMARKS	85
5.5.	REFERENCE	86
CHAPTER 6 : EVALUATION OF SYNTHETIC PARAMETERS OF MESOPOROUS SILICA NANOPARTICLE THROUGH BOX-BEHNKEN DESIGN		88
6.1.	INTRODUCTION	88
6.2.	MATERIALS AND METHODS	89
6.2.1.	<i>Materials</i>	89
6.2.2.	<i>Experimental design</i>	89
6.2.3.	<i>Preparation of mesoporous silica nanoparticles</i>	90
6.2.4.	<i>Determination of the grafting potential using ninhydrin test</i>	90
6.2.5.	<i>Functionalization of mesoporous silica nanoparticles with epoxy group</i>	91
6.2.6.	<i>Preparation of chitosan-capped mesoporous silica nanoparticles (CS-MSNs)</i>	91
6.2.7.	<i>Drug loading and in vitro drug release</i>	92
6.2.8.	<i>Enzyme degradation drug release</i>	92
6.2.9.	<i>Morphological evaluation of mesoporous silica nanoparticles</i>	92
6.2.10.	<i>Surface chemistry of mesoporous silica nanoparticles</i>	93
6.2.11.	<i>Evaluation particle surface area and pore size</i>	93
6.2.12.	<i>Evaluation of particle size diameter and size distribution</i>	93
6.2.13.	<i>Solid state analysis (²⁹Si NMR)</i>	93
6.2.14.	<i>Dissolution profiling</i>	93
6.3.	RESULTS AND DISCUSSION.....	94
6.3.1.	<i>Particle size and distribution evaluation</i>	94
6.3.2.	<i>Morphological analysis</i>	95
6.3.3.	<i>Evaluation of nanoparticle surface chemistry</i>	98
6.3.4.	<i>In vitro drug release profiles of rifampicin</i>	100
6.3.5.	<i>Effect of synthetic parameters (Box-Behnken design)</i>	105
6.4.	CONCLUDING REMARKS	106
6.5.	REFERENCE	106
7. : EVALUATION OF SYNTHETIC PARAMETERS OF GELATIN SPHERES THROUGH BOX-BEHNKEN DESIGN		109
7.1.	INTRODUCTION	109
7.2.	MATERIAL AND METHODS	110
7.2.1.	<i>Materials</i>	110
7.2.2.	<i>Experimental design</i>	110
7.2.3.	<i>Critical micelle and critical association concentration</i>	111
7.2.4.	<i>Dynamic light scattering study of gelatin-surfactant interaction</i>	111
7.2.5.	<i>Gelatin conformational changes through circular dichroism</i>	113
7.2.6.	<i>Synthesis of pH responsive hydrazone linker</i>	114
7.2.7.	<i>Synthesis of gelatin nanoparticles</i>	115
7.2.8.	<i>X-ray powder diffraction (XRD)</i>	116
7.2.9.	<i>Swelling studies</i>	116

7.2.10.	<i>Structural molecular analysis using infrared</i>	117
7.2.11.	<i>Drug loading and drug content (rifampicin)</i>	117
7.2.12.	<i>In vitro drug release</i>	117
7.3.	RESULTS AND DISCUSSIONS	119
7.3.1.	<i>Determination of critical micelle concentration</i>	119
7.3.2.	<i>Dynamic light scattering for critical micelle concentration</i>	121
7.3.3.	<i>Fourier-transform spectroscopy analysis</i>	123
7.3.4.	<i>Conformational changes of gelatin in different surfactant concentrations</i>	124
7.3.5.	<i>Degree of crystallinity analysis</i>	126
7.3.6.	<i>Morphological analysis of gelatin nanoparticles</i>	127
7.3.7.	<i>Particle size, distribution characterization and entrapment efficacy</i>	129
7.3.8.	<i>Swelling studies</i>	130
7.3.9.	<i>Drug release profile</i>	131
7.3.10.	<i>Analysis of response surface design</i>	134
7.4.	CONCLUDING REMARKS	136
7.5.	REFERENCE	137
8.	: OPTIMIZED MESOPOROUS SILICA NANOPARTICLES: USE OF NATURAL POLYMERS GATE-KEEPERS: CYCLODEXTRIN AND GELATIN CONJUGATED TO SYNTHESIZED HYDRAZONE LINKER	140
8.1.	INTRODUCTION	140
8.2.	MATERIALS AND METHODS	141
8.2.1.	<i>Materials</i>	141
8.2.2.	<i>Preparation of carboxymethyl-α-CD (CM-β-CD)</i>	141
8.2.3.	<i>Synthesis of pentane-2,4-diylidenebis(hydrazine)</i>	142
8.2.4.	<i>Synthesis of epoxy functionalized mesoporous silica nanoparticle</i>	142
8.2.5.	<i>Natural polymer gate keeping</i>	142
8.2.6.	<i>Analysis of molecular binding using NMR</i>	144
8.2.7.	<i>Analysis of molecular structural groups using infrared</i>	144
8.2.8.	<i>Morphological analysis using transmission microscopy</i>	144
8.2.9.	<i>X-ray diffraction patterns analysis</i>	144
8.2.10.	<i>Thermostability studies</i>	145
8.2.11.	<i>Mean size, particle distribution and stability</i>	145
8.2.12.	<i>Direct drug content analysis</i>	145
8.2.13.	<i>In vitro drug release models</i>	146
8.3.	RESULTS AND DISCUSSION	148
8.3.1.	<i>Microscopic analysis of coated mesoporous silica nanoparticles</i>	148
8.3.2.	<i>Dynamic light scattering analysis</i>	149
8.3.3.	<i>Analysis of functional groups</i>	151
8.3.4.	<i>Crystallinity of modified mesoporous silica nanoparticle</i>	152
8.3.5.	<i>Analysis of particles thermostability and degradation temperature</i>	153
8.3.6.	<i>Evaluation of drug content</i>	154
8.3.7.	<i>Drug release profiles</i>	155
8.4.	CONCLUDING REMARKS	160
8.5.	REFERENCES	160
9.	: DEVELOPMENT OF COMPUTATIONAL FLUID DYNAMICS MODEL OF TUBERCULOSIS INFECTED LUNGS	164
9.1.	INTRODUCTION	164

9.2.	METHODS.....	167
9.2.1.	<i>Design of the airway geometry</i>	167
9.2.2.	<i>Drug deposition prediction using OpenFoam</i>	168
9.3.	RESULTS AND DISCUSSION.....	169
9.4.	CONCLUDING REMARKS	170
9.5.	REFERENCE	170
10.	: CONCLUDING REMARKS, RECOMMENDATIONS AND OUTLOOK.....	172
10.1.	CONCLUDING REMARKS	172
10.2.	RECOMMENDATIONS	173
10.3.	OUTLOOK.....	174
10.4.	REFERENCE	174
11.	APPENDIX	176
10.1.	11.1 RESEARCH PRESENTATIONS.....	176

LIST OF ABBREVIATIONS

AAV	- Adeno-associated virus
AFM	- Atomic Force Microscope
AIDS	- Acquired Immune Deficiency Syndrome
ALI	- Air-Liquid Interface
API	- Active pharmaceutical ingredient
APTES	- 3-Aminopropyl) triethoxysilane
ASL	- Airway surface liquid
BC	- Before Christ
CF	- Cystic fibrosis
CFC	- Chlorofluorocarbons
CFD	- Computational fluid dynamics
CFTR	- CF transmembrane conductance regulator
COPD	- Chronic obstructive pulmonary disease
CPP	- Cell-penetrating peptides
CTAB	- Cetyltrimethyl ammonium bromide
dA	- Aerodynamic diameter
DC	- Dendritic cells
DOE	- Design of experiments
DPI	- Dry Powder Inhaler
DRH	- Deliquescence relative humidity
DSC	- Differential Scanning Calorimetry
EEG	- Enhanced excipient growth
ERH	- Efflorescence relative humidity
FDA	- Food and Drug Administration
FDP	- Fine particle deposition
FEV1	- Forced expiratory volume
FOM	- Figures of Merit
FPF	- Fine particle fraction
FTIR	- Fourier Transform Infrared Spectroscopy
GPTMS	- 3-glycidoxypropyltrimethoxysilane
HFA	- Hydrofluoroalkane

HGI	- Hygroscopic growth inhibitors
HIV	- Human immunodeficiency virus
HPLC	- High Performance Liquid Chromatography
KPLS	- Kernel Partial Least Squares
MAP	- Mucoadhesive particles
MC	- Mast cells
MCC	- Mucociliary clearance
MDI	- Metered Dose Inhaler
MDR	- Multi-drug resistance
MDSC	- Myeloid-derived suppressor cells
MMAD	- Median mass aerodynamic diameter
MPP	- Mucus-penetrating particles
MT	- Mouth-Throat
NAC	- N-acetyl-L-cysteine
NIPALS	- Non-linear Iterative Partial Least Squares
O/W	- Oil in water
OSC	- Orthogonal Signal Correction
PCA	- Principal Component Analysis
PCL	- Periciliary liquid
PEG	- Polyethylene glycol
PET	- Positron Emission Tomography
PLGA	- Poly (lactic-co-glycolic acid)
pMDI	- pressured Metered Dose Inhaler
RH	- Relative humidity
RNS	- Reactive nitrogen species
ROS	- Reactive oxygen species
SP	- Surfactant protein
SPECT	- Single Photon Emission Computed Tomography
TB	- Tuberculosis
TEOS	- Tetraethoxysilane
TGA	- Thermogravimetric Analysis
UPLC	- Ultra-Performance Liquid Chromatography
VHC	- Valve holding chamber
W/O	- Water in oil

XRD - X-ray Powder Diffraction

LIST OF EQUATIONS

$SECSEP = i = 1NCiAdded - CiFound2n - 1$ (3.1)	46
$PRESS = iNCiAdded - CiFound2$ (3.2)	47
$RMSECV = PRESSn$ (3.3)	47
$R2 = 1 - SSRSSY$ (3.4)	47
$fi = nleftnrightrcnsi + n$ (3.5)	48
$Y = Y01 - e - kt$ (4.1)	61
$t12 = 0.693k$ (4.2)	61
$ALmmolg = MVWs$ (6.1)	91
$W1 = mW2 \times ASiO2AGPTMS$ (6.2)	91
$MtM\infty = ktn$ (6.3)	94
$MDT = J = tj\Delta Qjj = ln\Delta Qj$ (6.4)	94
$DE = t1t2y.dty100 \times t2 - t1 \times 100$ (6.5)	94
$GI\tau = ItIt + \tau$ (7.1)	112
$gI\tau = GI\tau It2$ (7.2)	112
$gI\tau = 1 + BgE\tau2$ (7.3)	112
$gE\tau = exp - \gamma\tau$ (7.4)	112
$F = fvolmass = 6\pi Dvol6\pi Dmass = DvolDmass = DHDmass$ (7.5)	112
$\%Helix = \theta obs \times 100\theta helix \times 1 - 2.57l$ (7.6)	113
$Swelling \% = W1 - W2W2 \times 100$ (7.7)	116
$Mmeasured = MUV measuredVsupernatant volume$ (7.8)	117
$EE\% = MmeasuredMinitial load \times 100$ (7.9)	117
$WtW\infty = ktn$ (7.10)	117
$WtW\infty = 4Dt\pi L20.5$ (7.11)	118
$MDT = 0W\infty t.dWt0W\infty dWt$ (7.12)	118
$MDT = ABCatmax$ (7.13)	118
$DE = 0ty.dty100.t \times 100$ (7.14)	118
$Mmeasured = MUV measuredVsupernatant volume$ (8.1)	145
$EE\% = MmeasuredMinitial load \times 100$ (8.2)	145
$Qt = Q0 + K0t$ (8.3)	146
$logC = logC0 - Kt2.303$ (8.4)	147
$Qt = KHt0.5$ (8.5)	147
$3Q0 - 3Qt = KH Ct$ (8.6)	147
$MtM\infty = Ktn$ (8.7)	147

LIST OF TABLES

TABLE 1.1: VARIOUS THERAPEUTICS DELIVERED VIA PULMONARY DRUG DELIVERY ROUTE [6-9].	1
TABLE 1.2: COMMON ANTITUBERCULOTIC DRUG MECHANISMS OF ACTION AND SIDE EFFECT PROFILES (ADAPTED FROM [24, 26-28])	6
TABLE 2.1: LUNG IMMUNE CELLS (ADAPTED FROM [50])	9
TABLE 2.2: LIST NOVEL APPROVED DRY POWDER INHALERS	19
TABLE 3.1: CALIBRATION AND VALIDATION FORMULATIONS USING CENTRAL COMPOSITE DESIGN	44
TABLE 3.2: COMPARISON BETWEEN THE PLS AND KPLS ALGORITHMS (ADAPTED FROM [23])	46
TABLE 3.3: ANALYSIS OF RIF, INH AND ASC USING HPLC METHOD	47
TABLE 3.4: ANALYTICAL DATA FROM THE CALIBRATION FOR THE DETERMINATION OF ISONIAZID, RIFAMPICIN AND ASCORBIC ACID SPECTROSCOPY	51
TABLE 3.5: RESULTS OF DETERMINATION OF ANTI-TUBERCULOSIS COMMERCIAL TABLETS MIXTURE USING PLS ANALYSIS METHOD.	52
TABLE 4.1: ILLUSTRATION OF ALIPHATIC ALDEHYDES DERIVATIVES AND HYDRAZINE DERIVATIVES USED	58
TABLE 4.2: ANALYTICAL DATA AND PHYSICAL PROPERTIES OF SYNTHESIZED COMPOUNDS	62
TABLE 4.3: PREDICTED DECAY RATE OF THE EVALUATED HYDRAZONES IN RESPECTIVE PH	71
TABLE 5.1: STRATEGIES TO ENHANCE OR AVOID PARTICLE UPTAKE BY ALVEOLAR MACROPHAGES (ADAPTED FROM [7]).	74
TABLE 6.1: EXPERIMENTAL PARAMETERS FOR SYNTHESIS OF MESOPOROUS NANOPARTICLES	90
TABLE 6.2: EVALUATION PHYSICOCHEMICAL FEATURES THAT CAN PLAY A ROLE IN DRUG DELIVERY SYSTEMS	95
TABLE 6.3: MEAN DISSOLUTION TIME (MDT), DISSOLUTION EFFICIENCY (DE) AND RELEASE EXPONENT (N)	104
TABLE 7.1: TABLE ILLUSTRATING THE PROPERTIES OF THE SURFACTANTS USED FOR PROTEIN-SURFACTANT INTERACTION.	110
TABLE 7.2: FORMULATIONS FOR CRITICAL MICELLES CONCENTRATION DETERMINATION	111
TABLE 7.3: FORMULATION STRATEGIES FOR THE IMPACT OF NON-IONIC SURFACTANT (BOX-BEHNKEN DESIGN)	115
TABLE 7.4: EVALUATION OF C ₁₂ E ₁₀ AND BRIJ 52	122
TABLE 7.5: DEPICTION OF SURFACTANT CONCENTRATION IN FIGURE 7.7	125
TABLE 7.6: EVALUATION OF GELATIN SPHERES SIZE, DISPERSITY, AND STABILITY	130
TABLE 7.7: EVALUATION OF THE MODE OF DRUG RELEASE, MEAN DISSOLUTION TIME AND DISSOLUTION EFFICIENCY.	134
TABLE 8.1: INTERPRETATION OF DIFFUSIONAL RELEASE MECHANISMS	148
TABLE 8.2: SUMMARY OF OBSERVED DLS DATA	151
TABLE 8.3: DRUG ENTRAPMENT EFFICIENCY	155
TABLE 8.4: DRUG RELEASE KINETIC MODELS	157
TABLE 9.1: PROPOSED OPENFOAM PARAMETERS (ADAPTED FROM [14])	168

LIST OF FIGURES

FIGURE 1.1: DRUG DEPOSITION FRACTION USING METERED DOSE INHALER (MDI) (ADAPTED FROM [10]).....	2
FIGURE 1.2: IMAGE DEPICTING PARTICLE DEPOSITION IN THE RESPIRATORY TRACT BASED ON PARTICLE SIZE (ADAPTED FROM [16]).	3
FIGURE 1.3: SCHEMATIC DEPICTING THE SIZE OF THE OF THE AIRWAYS AND CELL TYPE (ADAPTED FROM [19]).	5
FIGURE 1.4: MECHANISM FOR DELIVERY OF NANOPARTICLES TO THE DEEP LUNG AND UPTAKE BY MACROPHAGES LEADING TO INTRACELLULAR DRUG RELEASE.	7
FIGURE 1.5: OVERVIEW OF THE EXPERIMENTAL PLAN FOR SYNTHESIS OF PH RESPONSIVE DRUG DELIVERY CARRIER SYSTEMS.....	10
FIGURE 1.6: FLOW DIAGRAM DEPICTING THESIS OVERVIEW.....	11
FIGURE 2.1: CHRONOLOGICAL VIEW OF PULMONARY DRUG DELIVERY (ADAPTED FROM [1]).	1
FIGURE 2.2: DIAGRAM DEPICTING THE ROUTE OF ENTRY FOR PULMONARY DRUG DELIVERY.....	3
FIGURE 2.3: DIAGRAM REPRESENTING THE RESPIRATORY TRACT WALL STRUCTURE (ADAPTED FROM [17]).	4
FIGURE 2.4: BARRIERS AGAINST DRUGS AND CARRIERS (ADAPTED FROM [34]).	7
FIGURE 2.5: DEPOSITION MECHANISM (ADAPTED FROM [32]).	10
FIGURE 2.6: HYGROSCOPIC GROWTH BASED ON FUNCTIONAL GROUPS (ADAPTED FROM [68]).....	12
FIGURE 2.7: MODES OF ASSESSING AND OPTIMIZING CARRIERS FOR PULMONARY DRUG DELIVERY.	27
FIGURE 3.1: IMAGES OF RIFAMPICIN, ISONIAZID AND ASCORBIC ACID AND CHARACTERISTICS BASED ON DRUG BANK DATABASE.	42
FIGURE 3.2: UV SPECTRA OF ASC, INH, RIF AND DRUG COMBINATION.	43
FIGURE 3.3: FIRST (A) AND SECOND DERIVATIVE (B) OF ASC, INH AND RIF DRUG INDIVIDUAL AND DRUG MIXTURE.....	49
FIGURE 3.4: HPLC CHROMATOGRAM OF RIF, INH AND ASC.	50
FIGURE 4.1: OVERVIEW OF INTRACELLULAR PH VARIATIONS IN VARIOUS COMPARTMENTS.	56
FIGURE 4.2: STRUCTURE OF PH-LABILE HYDRAZONE AND HYDROLYSIS PRODUCTS.	57
FIGURE 4.3: FTIR SPECTRA OF SYNTHESIZED HYDRAZONES.....	63
FIGURE 4.4: UV-VIS ANALYSIS OF THE HYDRAZONES C1-C12 DEPICTS COMPOUND 1-12, RESPECTIVELY.....	64
FIGURE 4.5: HYDRAZONES SYNTHESIZED FROM HYDRAZINE MONOHYDRATE.....	66
FIGURE 4.6: FORMYLHYDRAZINE HYDRAZONE.	67
FIGURE 4.7: AMINOGLYCINE HYDRAZONES.	68
FIGURE 4.8: PROTON NMR SPECTRA OF SYNTHESIZED THIOSEMICARBAZIDE HYDRAZONES.	69
FIGURE 4.9: HYDROLYSIS KINETICS AT NEUTRAL PH 7.4 AND ACID PH 4.5.	70
FIGURE 5.1: PROTECTING OF GLUCOSE HYDROXYL GROUPS USING ACETAL GROUP.	76
FIGURE 5.2: CHAIN LENGTH EXTENSION VIA DIBROMO ALKYLs.	76
FIGURE 5.3: HYDROXYL GROUP DEPROTECTION IN ACIDIC CONDITIONS.....	77
FIGURE 5.4: NMR SPECTRA OF PURE GLUCOSE BEFORE PROTECTION AND CHAIN EXTENSION.	78
FIGURE 5.5: PROTECTION OF HYDROXYL GROUPS INTO ACETAL FUNCTIONAL GROUPS.....	79
FIGURE 5.6: DIBROMOMETHANE CONJUGATION.	80
FIGURE 5.7: NMR SPECTRA OF DIBROMO-ETHANE MODIFIED GLUCOSE.....	81
FIGURE 5.8: NMR SPECTRA OF DIBROMO-PROPANE MODIFIED GLUCOSE.....	82
FIGURE 5.9: NMR SPECTRA OF DIBROMO-BUTANE MODIFIED GLUCOSE.....	83
FIGURE 5.10: NMR SPECTRA OF DIBROMO-PENTANE MODIFIED GLUCOSE.	84
FIGURE 5.11: NMR SPECTRA OF DIBROMO-HEXANE MODIFIED GLUCOSE.	85
FIGURE 6.1: TEM IMAGES OF F01-F15 MSNs.	97
FIGURE 6.2: FTIR SPECTRA OF MSNs FORMULATIONS AFTER CALCINATION.	99
FIGURE 6.3: SOLID STATE NMR OF MSNs FORMULATIONS EVALUATING THE DIFFERENT SILANOL GROUPS.....	100

FIGURE 6.4: CUMULATIVE DRUG RELEASE AT ACID PH 4.5 (ACETIC ACID-SODIUM ACETATE).	101
FIGURE 6.5: CUMULATIVE DRUG RELEASE UNDER ENZYMATIC DEGRADATION BY LYSOZYME (PH 6.8).	102
FIGURE 6.6: CUMULATIVE DRUG RELEASE AS NEAR NEUTRAL PH 7.4 (PBS).	103
FIGURE 6.7: SURFACE PLOTS SHOWING THE RESPONSE OF EACH PARAMETER ROLE ON CRITICAL PHYSIOCHEMICAL PROPERTIES OF THE MSNS.	105
FIGURE 7.1: STANDARD CD SPECTRA OF THE THREE BASIC SECONDARY STRUCTURES OF A POLYPEPTIDE CHAIN (A-HELIX, B-SHEET AND RANDOM COIL (ADAPTED FROM [12]).	114
FIGURE 7.2: SCHEMATIC FOR THE SYNTHESIS OF HYDRAZONE.	114
FIGURE 7.3: SYNTHESIS OF PH SENSITIVE GELATIN SPHERES VIA HYDRAZONE LINKAGE.	116
FIGURE 7.4: DETERMINATION OF CMC OF BRIJ 52 IN WATER (3.2×10^{-4} MM).	120
FIGURE 7.5: DETERMINATION OF $C_{12}E_{10}$ CMC IN WATER (1.58×10^{-6} MM).	121
FIGURE 7.6: FTIR SPECTRA OF CROSSLINKED GELATIN SPHERES.	124
FIGURE 7.7: CIRCULAR DICHROISM DATA ILLUSTRATING THE FOLDING OF GELATIN WITH VARIOUS SURFACTANT CONCENTRATIONS (A)-BRIJ 52 AND (B)- $C_{12}E_{10}$.	126
FIGURE 7.8: X-RAY DIFFRACTION OF CROSSLINKED AND UN-CROSSLINKED GELATIN NANOPARTICLES.	127
FIGURE 7.9: SEM IMAGES OF GELATIN NANOPARTICLES.	129
FIGURE 7.10: SWELLING RATIO OF GELATIN NANOPARTICLES IN WATER AT ROOM TEMPERATURE.	131
FIGURE 7.11: CUMULATIVE DRUG RELEASE PROFILE OF RIFAMPICIN AT PH 7.4.	132
FIGURE 7.12: CUMULATIVE DRUG RELEASE PROFILE RIFAMPICIN AT PH 4.5.	133
FIGURE 7.13: EVALUATION OF PARTICLE SIZE IN RELATION TO SURFACTANT CONCENTRATION AND SONICATION TIME.	135
FIGURE 7.14: EVALUATION OF DRUG RELEASE MECHANISM IN RELATION TO CROSSLINKING TIME AND SONICATION TIME.	136
FIGURE 8.1: SYNTHESIS OF PENTANE-2, 4-DIYLIDENE BIS (HYDRAZINE).	142
FIGURE 8.2: CONJUGATION OF HYDRAZONES TO MSNS AND CD.	143
FIGURE 8.3: CONJUGATION OF GELATIN PH RESPONSIVE GATE.	144
FIGURE 8.4: TEM IMAGES OF MESOPOROUS SILICA NANOPARTICLES A) MSNS B) EPOXY-MSNS C) GELATIN-MSNS D) CD-MSNS.	149
FIGURE 8.5: ZETA POTENTIAL DRIFTS OF MESOPOROUS SILICA NANOPARTICLES.	150
FIGURE 8.6: SIZE DRIFTS OF MESOPOROUS SILICA NANOPARTICLES.	150
FIGURE 8.7: FTIR SPECTRA OVERLAY OF MSN COATED WITH GELATIN AND CYCLODEXTRIN GATES.	152
FIGURE 8.8: XRD DIFFRACTION PATTERNS OF MSN BEFORE AND AFTER COATING.	153
FIGURE 8.9: TGA GRAPHS OF MSN BEFORE AND AFTER COATING.	154
FIGURE 8.10: CUMULATIVE DRUG RELEASE OF RIF FROM CYCLODEXTRIN COATED NANOPARTICLES.	156
FIGURE 8.11: CUMULATIVE DRUG RELEASE OF INH FROM CYCLODEXTRIN COATED NANOPARTICLES.	157
FIGURE 8.12: DRUG RELEASE KINETICS OF RIFAMPICIN RELEASE FROM GELATIN COATED MSNS.	159
FIGURE 9.1: DIAGRAM DEPICTING VARIOUS AIRWAY GENERATIONS USED IN CFD MODELLING (ADAPTED FROM [11]).	166
FIGURE 9.2: MRI SCANS OF TUBERCULOSIS INFECTED LUNG (A) AXIAL VIEW) AND (B) CORONAL VIEW.	167
FIGURE 9.3: IMAGES OF THE SEGMENTED LUNGS.	168
FIGURE 9.4: GENERATED MESH OF THE WHOLE LUNG MODEL.	169

CHAPTER 1 : INTRODUCTION AND BACKGROUND TO STUDY

1.1. Background to the study

The respiratory tract is stated to constitute of a large surface area (70-140m²), which has been utilized for delivery of both non-peptide and peptidomimetic drugs (Table 1.1) [1]. However, the lung constitutes of barriers that allow filtration of large particles from reaching the deep lung. Administration to the lungs can be via the nasal or oral inhalation. The nasal route however is limited by the narrow airway lumen (5µm particles inhalation, 80% lost), thus warranting inhalation via oral route (5µm particles inhalation, 20% lost). Due to particle size, the mode of pulmonary deposition is governed by inertial impaction, sedimentation, diffusion, interception, and electrostatic effects [2]. The inertial impaction occurs in regions where there is high air velocity and turbulent airflow. For particles, within a range of 0.5-5µm, sedimentation by gravitational force occurs in smaller airways (low velocity-smaller bronchi and bronchioles) and can be facilitated further by breath-holding and hygroscopic growth of the particles as they pass through the warm, humid airway passages. From a range below 0.5µm, particles are deposited by diffusion which is based on the Brownian motion [3]. Interception is more pronounced with fibres where particle physical shape or size plays a factor when particle encounter the airway wall [4]. For electrostatic effect, the charges that particles accumulate during dispersion leads to interaction with the airways by inducing an opposite charge to the airways [5]

Table 1.1: Various therapeutics delivered via pulmonary drug delivery route [6-9].

Class	Drugs	Topical treatment of pulmonary diseases	
			Localized diseases
Antimicrobial	Tobramycin, (Arikace™), Aztreonam, Colistin (polypeptide), (Lipoquin® and Levofloxacin	Amikacin Ciprofloxacin Pulmaquin),	Cystic fibrosis, Pneumonia
Antiviral	Zanamivir (Relenza®, GlaxoSmithKline, Middlesex, UK), Laninamivir (Inavir®, Daiichi Sankyo Company Ltd, Tokyo, Japan and Biota Pharmaceuticals, Alpharetta, USA)		Influenza
Antifungal	Amphotericin B, Itraconazole and Voriconazole		Broad spectrum antifungal
Vaccines	Flumist (MedImmune, Gaithersburg, MD, USA)		Influenza

Immunosuppressive Peptides/Nucleic acids	Tacrolimus, corticosteroids mRNA, siRNA	Asthma, Lung Transplant Cystic Fibrosis
Systemic diseases		
Peptides	Insulin, Heparin, Calcitonin	Ergotamine, Miscellaneous
Other	Zaleplon, Levodopa, Dihydroergotamine	Morphine/fentanyl, Loxapine, Miscellaneous

The most commonly used inhalation device is the metered dose inhaler (MDI). As illustrated in figure 1.1, this depiction of the MDI inhaler indicates that most of the inhaled drug is lost in through swallowing. Depending on the physicochemical properties of the drug, most the swallowed drug can be recovered in the gastrointestinal (GI) tract, whilst most of the dose can be subjected to hepatic first-pass metabolism (e.g. corticosteroid budesonide). The use of spacers can also lead to reduction in the administered dose reaching the deep lungs. Thus, the current aerosolizing technique of using the device mechanics to control particle size is not ideal for treatment of respiratory tract infections like Tuberculosis (TB). Thus warrants the need for nanotechnology to generate predefined particle physicochemical properties.

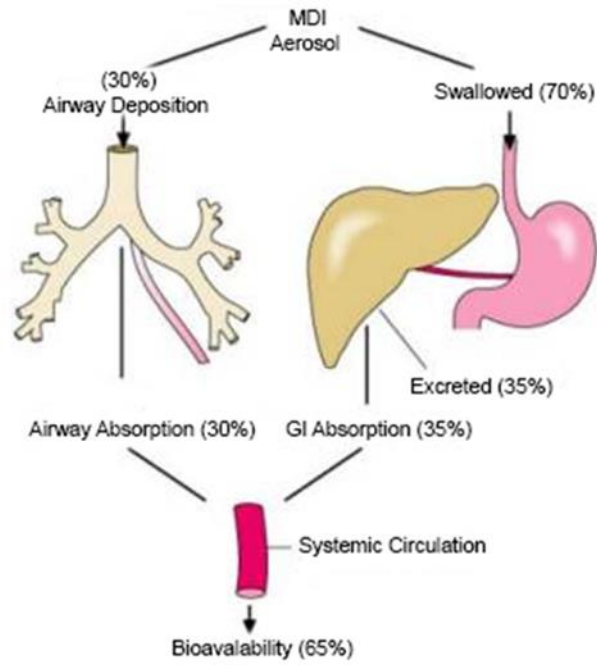


Figure 1.1: Drug deposition fraction using metered dose inhaler (MDI) (Adapted from [10]).

The application of nanotechnology in medical application led to the field of nanomedicine. As briefly discussed, it's clear that particle size plays a major role in deposition and drug diffusion across the epithelial barrier (Figure 1.2). Phagocytosis is sensitive to particle size, whereby macrophages are able to engulf particles of 0.5-3 μm in diameter, whilst particles of less than 0.26 μm can escape from phagocytosis process [11]. Although large particles are known to be taken up by macrophages, recent studies have shown that particles less than 0.5 μm can be rapidly internalized by pulmonary epithelial cells, 10 times more than 1 μm particles and 100 times more than 2 or 3 μm particles[12]. For nanoparticles, the decrease in particle size can lead to an increase in surface area which enhances dissolution rate, whilst also creating relatively uniform distributed drug dose in the alveoli regions [13]. Nanoparticles can provide the advantage of sustained-release in the lung tissue, resulting in reduced dosing frequency and improved patient compliance. Once the inhaled particles are inside the peripheral lung, particles are supposed to dissolve and allow drug to diffuse through the epithelial barrier and into the blood stream [14]. However, large particles dissolve slowly which makes them to be subjected to phagocytosis by alveolar macrophages. The use of penetration enhancers can be incorporated into pulmonary formulations to enhance systemic bioavailability [15].

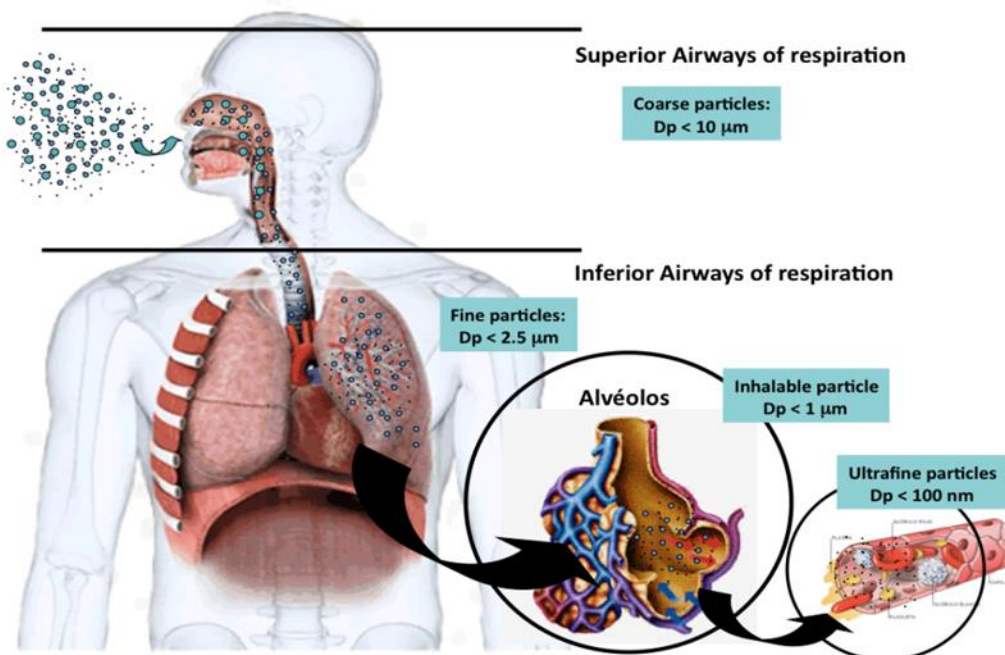


Figure 1.2: Image depicting particle deposition in the respiratory tract based on particle size (Adapted from [16]).

Based on the characteristics of particle required to reach the deep lung and improve drug bioavailability, it indicates that particle size engineering is crucial. The particle size (Mass median aerodynamic diameter (MMAD)) and morphology has been shown to have a pronounced effect on all aspects of drug delivery to the lungs which include deposition, dissolution and clearance mechanism [17]. For smaller particles ($\leq 0.5\mu\text{m}$), slow deep breathing and breath holding can aid in particle deposition instead of particles being exhaled. Unlike microparticles, nanoparticles have been shown to be deposited in a greater concentration throughout the lung. Their small size also enhances the delay in phagocytic uptake, thus they have increased interaction/binding with certain proteins and enhanced translocation from the epithelium into circulation [18]. Thus particles that deposit within the human bronchi region will be exposed to the mucociliary escalator that removes microparticles deposited in the mucus blanket; whilst the alveoli and terminal bronchioles are ideal regions for pulmonary drug delivery deposition due to small diffusion barriers (Figure 1.3). This indicates that the nanoparticles can offer a more immediate release as they become in contact with the surfactant layer, the underlying epithelial lining fluid (ELF) and proteins (enzymes) more rapidly than microparticles. Due to nanoparticles having a good polydispersity, these make them ideal for targeting deposition of particles within a specific airway region. Furthermore, in patients with constricted airways, the nanoparticles can evade regions of high turbulence and laminar flow and deposit through Brownian diffusion across the airways. Thus, nanoparticles are ideal for both normal and diseased lungs in overcoming complex aerodynamics caused by lung anatomical changes.

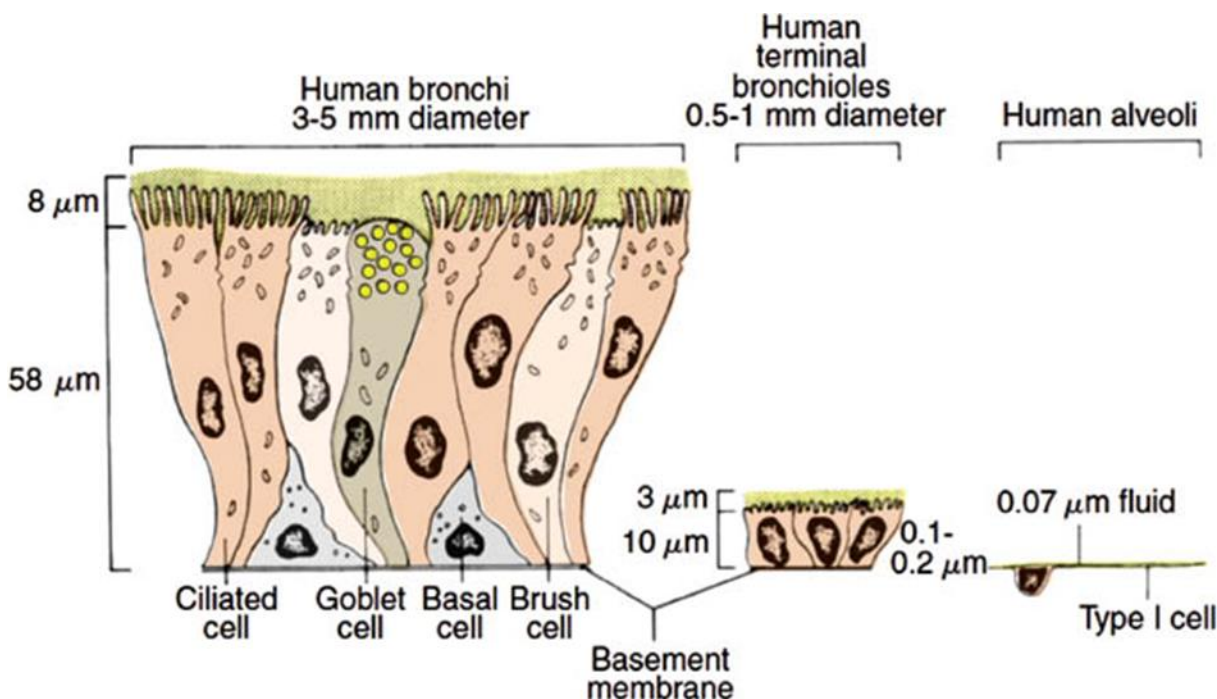


Figure 1.3: Schematic depicting the size of the of the airways and cell type (Adapted from [19]).

1.2. Rationale and motivation of the study

Tuberculosis (TB) is stated to be second leading cause of death after HIV/AIDS [20]. Based on the WHO report, in 2017, 9.0-11.1 million people fell ill with TB, whereby 1.2-1.4 million patients who died from the disease were HIV-negative (266 000-335 000) [21]. Over 95% of TB deaths occur in low- and middle-income countries. India, Indonesia, China, Nigeria, Pakistan, and South Africa accounted to the 64% new TB cases [22]. Tuberculosis is spread by airborne droplet nuclei, which are particles of 1-5 μ m in diameter that contain *Mycobacterium tuberculosis* [23]. Upon inhalation of the bacilli, *M tuberculosis* is then taken up by alveolar macrophages, initiating a cascade of events that result in either successful containment of the infection or progression to active disease (primary progressive tuberculosis). The goals of treatment are to ensure cure without relapse, to prevent death, to stop transmission, and to prevent the emergence of drug resistance. It is stated that treatment of active tuberculosis should never be attempted to be treated with a single, and a single drug should never be added to a failing regimen [24]. However due to side effects profile of TB drugs, this can lead to poor adherence. Nanoparticle-based antitubercular drug delivery systems can be utilized to delivery various TB drug listed in table 1.2. Literature has shown that application of nanoparticles for antituberculous treatment has various advantages such as: high constancy/longer time, high capacity by being able to encapsulate multiple drugs in the matrix, produce side effects compared to conventional drug delivery

administration, improve bioavailability through slow, sustained, and/or controlled drug release, offer various routes of administration such as oral and pulmonary delivery and improved compliance [25].

Table 1.2: Common antituberculous drug mechanisms of action and side effect profiles (Adapted from [24, 26-28])

Drug	Mechanism of action	Side Effects
Isoniazid (0.02-0.20µg/mL)	Inhibits the formation of mycolic acids of the bacterial cell wall, causing DNA damage and, subsequently, the death of the bacillus.	Peripheral neuritis, Hepatitis, convulsions, muscle twitching, toxic encephalopathy, fever, rash.
Rifampicin (0.05-0.50µg/mL)	Inhibits the gene transcription of mycobacteria by blocking the DNA-dependent RNA polymerase.	Orange urine, flu-like syndrome, hepatitis, renal failure, haemolysis and thrombocytopenia.
Pyrazinamide (6.25-50.0µg/mL)	Impairment of mycolic acid biosynthesis.	acute gout, hepatotoxicity, nausea, anorexia, causing difficulty in diabetes management.
Ethambutol (1-5µg/mL)	Interferes with the biosynthesis of arabinogalactan, the principal polysaccharide on the mycobacterial cell wall.	Optic neuritis and skin rash.

1.3. Mechanism of action of pH responsive aerosol carriers

The study focuses on the development of two forms of particles for pulmonary drug delivery. The mesoporous silica nanoparticles are of tuneable physicochemical properties (Chapter 6), whereby drug loading content and surface chemistry play a major role in release profile. The study also considers the synthesis of hydrazones responsive to acidic pH (Chapter 4). This is incorporated into the particles to facilitate in responsive drug delivery. The second particles are made of gelatin, whereby the synthetic path considers protein conformational changes for directed particle physicochemical properties attenuation via use of non-ionic surfactant (Chapter 7). The purpose of the study is for the delivery of anti-tuberculosis drug to the lungs via pulmonary route. Due to the lung constituting of various deposition sections based on the particle size, care is taken into the directing of the particle size during synthesis. The upper respiratory tract is known to trap particle larger than 5µm, whereas particles smaller than 1µm are susceptible to be exhaled whilst they also could cross cellular membranes by non-phagocytic mechanisms [29]. Breath-holding technique or hygroscopic growth can assist in ensuring deposition of nanoparticles in the deep

lungs. As illustrated in figure 1.4, upon deposition (Figure 1.4 (A)), these will then be taken up by macrophages (Figure 1.4 (B)) or diffuse into the blood stream (Figure 1.4 (A)-insert).

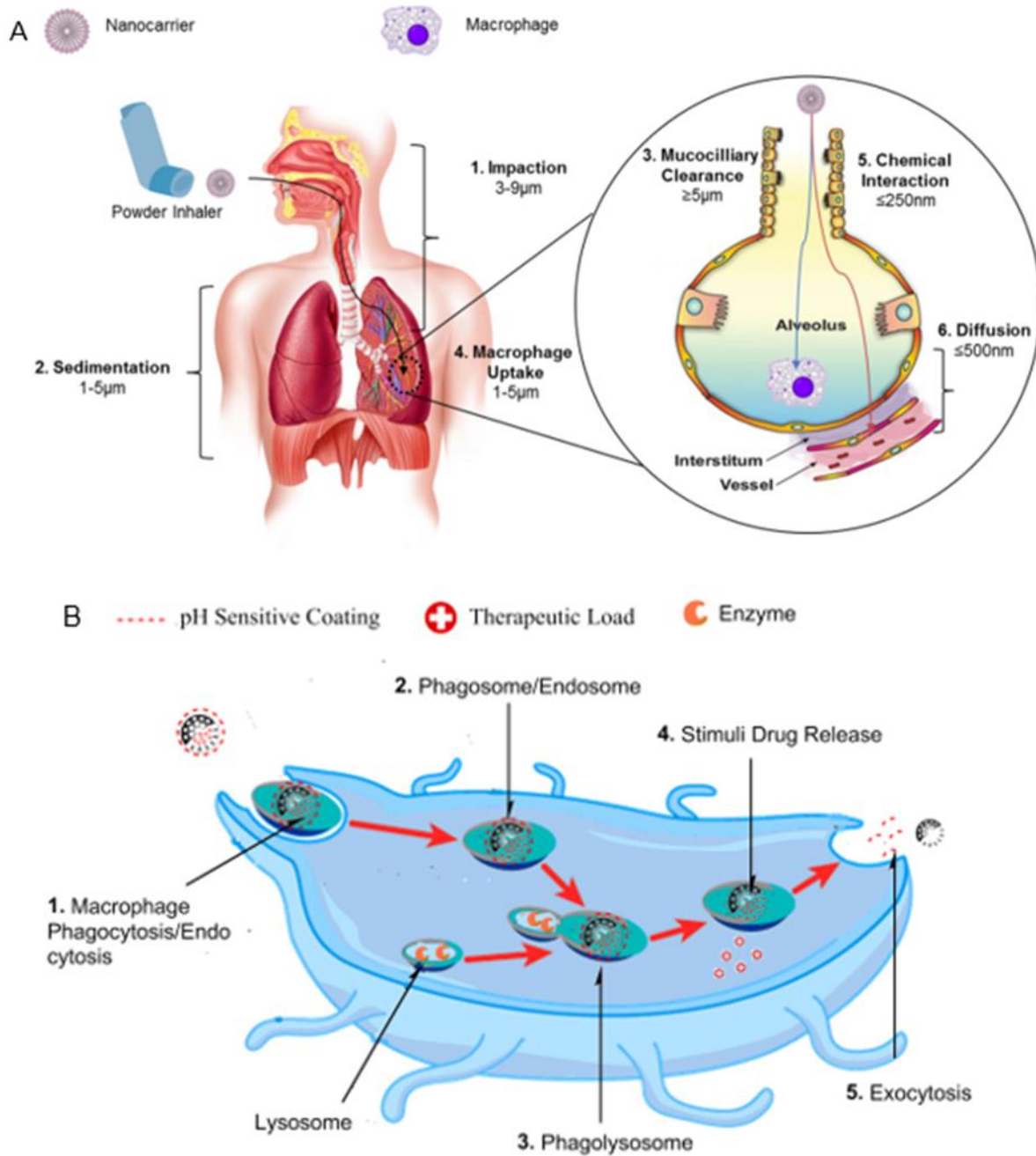


Figure 1.4: Mechanism for delivery of nanoparticles to the deep lung and uptake by macrophages leading to intracellular drug release.

1.4. Novelty of the study

Pulmonary drug delivery is a well-established field. Various stimuli responsive and targeted delivery systems have been well researched. In our study, these well-established features are used to direct the design of novel pH responsive linkers. These linkers have tuneable hydrolysis rate based on the synthetic routes used. The use of mesoporous silica nanoparticles is well studied. However, our study considers novel synthetic procedure that aid in improving the physicochemical properties of the nanoparticle. These tuneable properties allow improvements in drug loading. By focusing on both targeting the macrophages based on the particle size and surface chemistry, the nanoparticles can be ideal for tuberculosis targeting and systemic drug delivery via pulmonary route. Furthermore, the use of biocompatible gelatin indicates that the particles can also be enzyme responsive in inflamed regions which produce collagen degradation enzymes (Matrix metalloproteinase). Thus, the nanoparticles can be dual responsive to changes in pH and enzyme concentration.

1.5. Possible therapeutic applications of the study

Pulmonary disease continues to be a burden whereby the airflow is altered which can lead to exertion and death. Although many inhalation devices (nebulizers, metered dose inhaler and dry powder inhalers) have been designed, each have their own limitation in generated particle size and manoeuvres used. The designed nanoparticles would allow a predetermined particle size which can be used in any inhalation device with less manoeuvres.

Inhalation of peptides, peptidomimetics and nucleotides drugs can be an alternative mode of administration of sensitive drugs. Due to low degradation physicochemical features in the lung, the pulmonary delivery of this therapeutics can improve bioavailability and patient compliance (alternative to intravenous delivery). Furthermore, pulmonary administration of these therapeutics can also lead to rapid response.

Targeted and responsive drug delivery indicates that irritation associated with inhaled therapeutics can be reduced as the nanoparticles would only release therapeutics at targeted site. Thus, reducing side effects profile.

Nanoparticles are also able to translocate into the circulation system upon inhalation, which can make the system an alternative to intravenous delivery due to the lung large surface area and high capillary system.

The pH responsive hydrazine linkers can be utilized in various conditions that affect changes in physiological pH such as: inflamed lung regions, intracellular compartments and tumour regions. The use of gelatin allows a highly biocompatible and biodegradable system.

1.6. Aim and objectives of the study

The aim of this study is to design two types of particles which are applicable for pulmonary drug delivery (Figure 1.5). The mesoporous silica nanoparticles are designed with controlled physicochemical properties that would allow high drug loading content. The gelatin spheres are designed in a manner that does not lead to damage of the protein structure during synthesis. All the particles are then linked to a pH responsive linker to release therapeutics at an acidic pH.

For pragmatic fulfilment of the aim, the following objectives will be undertaken:

- Synthesis of mesoporous silica nanoparticles by taking pH, polar and nonpolar solvent ratio and calcination temperature as parameter for changing the physicochemical properties of the particles. The Box-Behnken design will be used for formulation studies.
- Preliminary screening using chitosan as a pH responsive linker for assessing drug release profile.
- Synthesis of hydrazone linker from di-aldehydes. Incorporation of latent acids on the di-aldehydes for tuning the hydrolytic rate of the hydrazine linkers.
- Linkers of various functional groups will be synthesized for future possible coupling with various polymers/surfaces.
- Assessment of the rate of hydrolysis of the hydrazones using kinetics study on the 600Hz NMR.
- Synthesis of gelatin based particles with the incorporation of a selected non-ionic surfactant identified from the critical micelle concentration studies (UV), protein NMR and circular dichroism studies (protein conformational changes).
- Selection of the non-ionic surfactant and assessment of the synthetic parameters such as surfactant concentration, sonication time and crosslinking time using the Box-Behnken Design.
- Optimization of the mesoporous silica nanoparticles and incorporation of the synthesized hydrazone linker. Characterization and drug release profile studies.
- Assessment and optimization of the gelatin nanoparticles.
- Synthesis of glucose moiety for possible hygroscopic growth layer and macrophages uptake stimulation
- Design on the lung model using MRI scans of TB infected lungs
- *In silico* simulation of the particles deposition inside the lung models

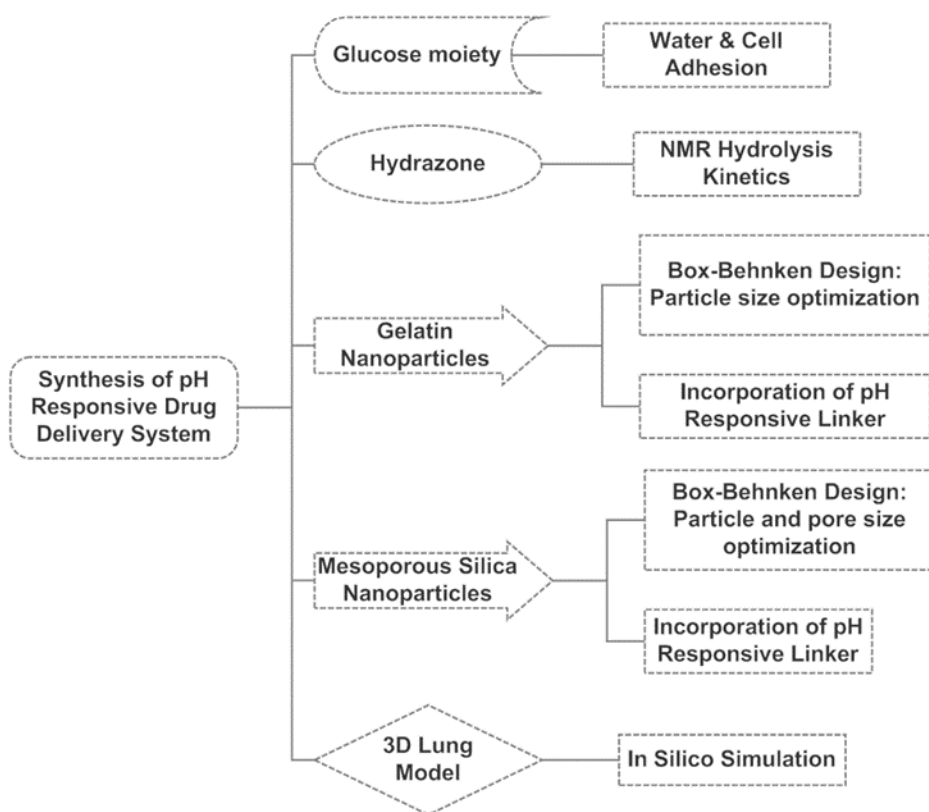


Figure 1.5: Overview of the experimental plan for synthesis of pH responsive drug delivery carrier systems.

1.7. Overview of the thesis

A brief overview of the thesis layout is illustrated in flow diagram (Figure 1.6). Briefly, rationale of the study and background of pulmonary drug delivery are covered in the Chapter 1 & 2. This is then followed by design of the components that would make up responsive drug delivery nanoparticles (Chapter 4 – hydrazones and Chapter 5 – hygroscopic layer). Two types of nanoparticles were designed in this study. Inorganic particles were made from silica (Chapter 6) and their formulation was optimized (Chapter 8), whilst organic particles were made from gelatin (Chapter 7). Both were evaluated for their possible applications in delivery of anti-TB drugs directly to the lungs. Lastly, a 3D model for lung deposition was also designed for prediction of aerosol deposition in TB infected lungs (Chapter 9). Due to the use of many formulation, a rapid chemometric UV analysis model was designed for rapid drug multiple analysis (Chapter 3). Chapter 10 focuses on the conclusion and recommendations as various limitations were identified from the novel study.

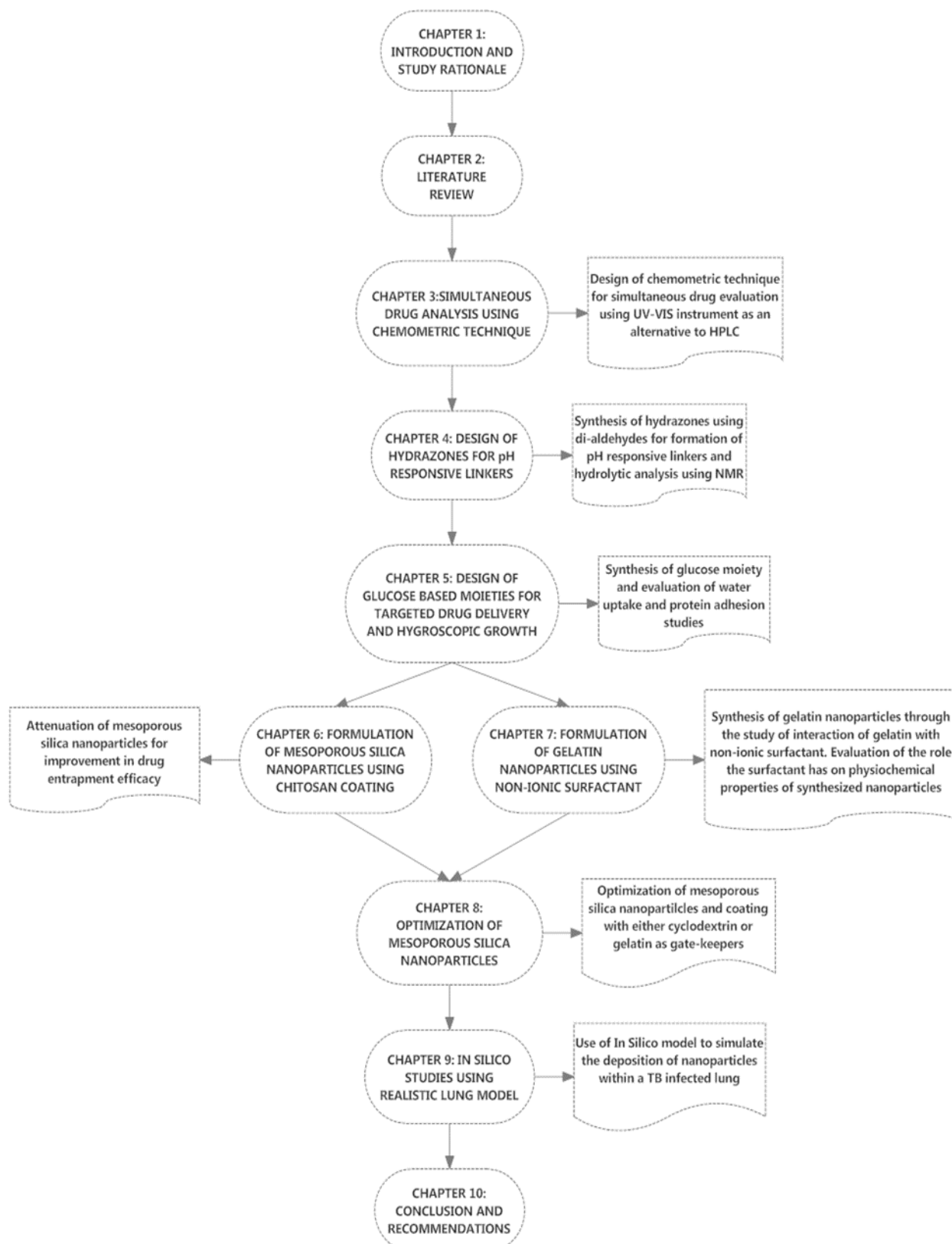


Figure 1.6: Flow diagram depicting thesis overview.

1.8. References

- [1] D.A. Groneberg, C. Witt, U. Wagner, K.F. Chung, A. Fischer, Fundamentals of pulmonary drug delivery, *Respiratory Medicine*, 97 (2003) 382-387.
- [2] Y.S. Cheng, Mechanisms of Pharmaceutical Aerosol Deposition in the Respiratory Tract, *AAPS PharmSciTech*, 15 (2014) 630-640.
- [3] N.R. Labiris, M.B. Dolovich, Pulmonary drug delivery. Part I: Physiological factors affecting therapeutic effectiveness of aerosolized medications, *British Journal of Clinical Pharmacology*, 56 (2003) 588-599.
- [4] M. Smola, T. Vandamme, A. Sokolowski, Nanocarriers as pulmonary drug delivery systems to treat and to diagnose respiratory and non respiratory diseases, *International Journal of Nanomedicine*, 3 (2008) 1-19.
- [5] J. Wong, H.-K. Chan, P.C.L. Kwok, Electrostatics in pharmaceutical aerosols for inhalation, *Therapeutic delivery*, 4 (2013) 981-1002.
- [6] M. Moreno-Sastre, M. Pastor, C.J. Salomon, A. Esquisabel, J.L. Pedraz, Pulmonary drug delivery: a review on nanocarriers for antibacterial chemotherapy, *Journal of Antimicrobial Chemotherapy*, 70 (2015) 2945-2955.
- [7] Q. Zhou, S.S.Y. Leung, P. Tang, T. Parumasivam, Z.H. Loh, H.-K. Chan, Inhaled formulations and pulmonary drug delivery systems for respiratory infections, *Advanced Drug Delivery Reviews*, 85 (2015) 83-99.
- [8] A. Kuzmov, T. Minko, Nanotechnology approaches for inhalation treatment of lung diseases, *Journal of Controlled Release*, 219 (2015) 500-518.
- [9] D. Cipolla, Will pulmonary drug delivery for systemic application ever fulfill its rich promise?, *Expert Opinion on Drug Delivery*, 13 (2016) 1337-1340.
- [10] L. Thorsson, Influence of inhaler systems on systemic availability, with focus on inhaled corticosteroids, *Journal of aerosol medicine : the official journal of the International Society for Aerosols in Medicine*, 8 Suppl 3 (1995) S29-36; discussion S37.
- [11] H.M. Mansour, Y.-S. Rhee, X. Wu, Nanomedicine in pulmonary delivery, *International Journal of Nanomedicine*, 4 (2009) 299-319.
- [12] K.A. Foster, M. Yazdanian, K.L. Audus, Microparticulate uptake mechanisms of in-vitro cell culture models of the respiratory epithelium, *Journal of Pharmacy and Pharmacology*, 53 (2001) 57-66.
- [13] R.H. Müller, C. Jacobs, O. Kayser, Nanosuspensions as particulate drug formulations in therapy: Rationale for development and what we can expect for the future, *Advanced Drug Delivery Reviews*, 47 (2001) 3-19.

- [14] M.M. Bailey, C.J. Berkland, Nanoparticle formulations in pulmonary drug delivery, *Medicinal Research Reviews*, 29 (2009) 196-212.
- [15] A. Hussain, J.J. Arnold, M.A. Khan, F. Ahsan, Absorption enhancers in pulmonary protein delivery, *Journal of Controlled Release*, 94 (2004) 15-24.
- [16] S.H. van Rijt, T. Bein, S. Meiners, Medical nanoparticles for next generation drug delivery to the lungs, *European Respiratory Journal*, 44 (2014) 765-774.
- [17] A.H. Chow, H.H. Tong, P. Chattopadhyay, B.Y. Shekunov, Particle engineering for pulmonary drug delivery, *Pharmaceutical research*, 24 (2007) 411-437.
- [18] W.G. Kreyling, M. Semmler-Behnke, W. Moller, Ultrafine particle-lung interactions: does size matter?, *Journal of aerosol medicine : the official journal of the International Society for Aerosols in Medicine*, 19 (2006) 74-83.
- [19] X. Murgia, C. de Souza Carvalho, C.-M. Lehr, Overcoming the pulmonary barrier: new insights to improve the efficiency of inhaled therapeutics, *European Journal of Nanomedicine*, 6 (2014) 157-169.
- [20] T.R. Frieden, T.R. Sterling, S.S. Munsiff, C.J. Watt, C. Dye, Tuberculosis, *The Lancet*, 362 (2003) 887-899.
- [21] W.H. Organization, Global tuberculosis report 2018, 2018.
- [22] World Health Organization, Tuberculosis, 2018.
- [23] S. Ahmad, Pathogenesis, Immunology, and Diagnosis of Latent Mycobacterium tuberculosis Infection, *Clinical and Developmental Immunology*, 2011 (2011) 814943.
- [24] L.C. Du Toit, V. Pillay, M.P. Danckwerts, Tuberculosis chemotherapy: current drug delivery approaches, *Respiratory research*, 7 (2006) 118.
- [25] M. Nasiruddin, M.K. Neyaz, S. Das, Nanotechnology-Based Approach in Tuberculosis Treatment, *Tuberculosis Research and Treatment*, 2017 (2017) 4920209.
- [26] M.A. Arbex, M.d.C.L. Varella, H.R.d. Siqueira, F.A.F.d. Mello, Drogas antituberculose: interações medicamentosas, efeitos adversos e utilização em situações especiais - parte 1: fármacos de primeira linha, *Jornal Brasileiro de Pneumologia*, 36 (2010) 626-640.
- [27] Y.L. Janin, Antituberculosis drugs: Ten years of research, *Bioorganic & Medicinal Chemistry*, 15 (2007) 2479-2513.
- [28] W.W. Addington, The Side Effects and Interactions of Antituberculosis Drugs, *CHEST*, 76 782-784.
- [29] M. Geiser, B. Rothen-Rutishauser, N. Kapp, S. Schürch, W. Kreyling, H. Schulz, M. Semmler, V.I. Hof, J. Heyder, P. Gehr, Ultrafine Particles Cross Cellular Membranes by Nonphagocytic

Mechanisms in Lungs and in Cultured Cells, *Environmental Health Perspectives*, 113 (2005) 1555-1560.

CHAPTER 2 : LITERATURE REVIEW ON PULMONARY DRUG DELIVERY

2.1. Chronological overview

The development of aerosol devices for pulmonary drug delivery dates back as far as 1554 BC Egypt, whereby fumes from the burned black henbane (contain anticholinergic alkaloid atropine) were smoked (Figure 2.1). Smoking has been considered a form of pulmonary drug delivery whereby opium was recorded to have been used in China since 1100BC [1]. It is of note that smoking cigarettes (e.g. asthma cigarettes) for therapeutic delivery were also used dating back to 600BC till the 20th century. This can be supported by delivery of nicotine via smoking, despite cause of cancer due inhalation of carcinogens. The oldest known illustration of the therapeutic inhaler was developed by Christopher Bennet in 1654 [2]. As fumes are known to carry lung irritants that can cause respiratory irritation, thus inhalation of medicated vapour becomes a favourable option. John Mudge invented the Mudge inhaler (1778) whereby opium is mixed with water which was then heated for aerosolization [3]. This was the first introduction to nebulizer technology. By 1899, Helbing and Pertch developed a propellant based liquid aerosol generator to atomize drug liquid suspension [4]. This is considered the precursor of the pressured metered dose inhaler. This led to the developed of the first successful dry powder inhaler (DPI) Aerohaler by Mack Fields of Abbott Laboratories [5]. Since 1956, the introduction of the metered-dose inhaler (MDI) aided in management of asthma [6].

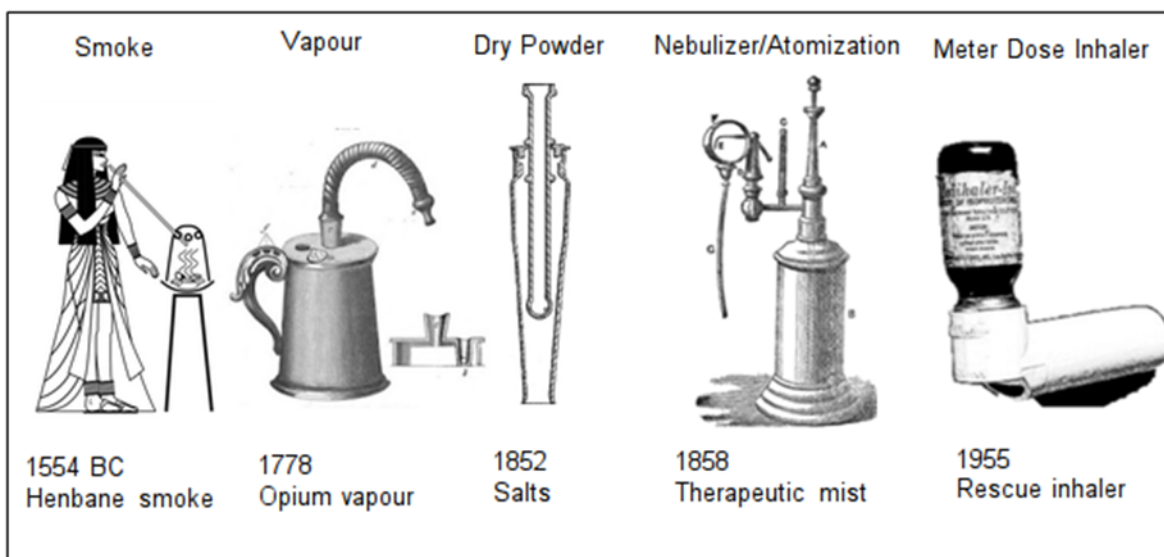


Figure 2.1: Chronological view of pulmonary drug delivery (adapted from [1]).

However, it is known historically that MDI used propellants that were classified environmentally unfriendly. Even though the development of the breath actuated Autohaler which offered better delivery, the use of CFC (chlorofluorocarbons) was “outlawed” and replaced with HFA (hydrofluoroalkane) due to the Montreal Protocol [7]. This transition however, promoted the development and favour of DPI as alternative devices (Spinhaler, Rotahaler). The introduction of the DPI originates from Ira Warren's invention in 1852 of glass inhaler [1]. From the nebulizer and pressure metered dose inhaler, the droplet size and flow rate from the device were seen as a problem that caused low deposition fraction (low therapeutic benefit). In terms of DPI, the problem is a combination of powder cohesive forces and particle size. From these problems, it occurs that particle physicochemical properties formulation is vital in ensuring good therapeutic response. As discussed, pulmonary drug delivery has historically been used for treatment of known respiratory diseases. The pulmonary drug delivery application can extend to systemic therapeutic delivery via pulmonary route. Furthermore, with improvements in computational power, the fate of particles in the respiratory tract can now be studied *in silico* using various lung models through computational fluid dynamics. The particle size and various surface chemical properties (charge and hydrophilicity) can be used to predict the deposition characteristics of the particles [8]. This is constituted by understanding of the lung anatomical features which are known to play a role in deposition. Therefore, understanding of the anatomical features of the respiratory tract is vital in targeted and improving drug delivery.

2.2. Lung anatomical features

2.2.1. Nasal and oral cavity

Starting from the nasal route of administration, the nose is used as the primary mode of respiration whereby inspired air is cleaned and conditioned before reaching the deep lung. From the nostrils, which are guarded with vibrissae (hairs), the large particles are filtered off whilst the temperature and humidity of the inhaled air is adjusted. Within the nasal cavity lies a bony projection (turbinate) whereby air currents pass during inhalation (Fig 2.2, Insert A). The nasal cavity is covered by mucosa with a surface area of 160cm², whereby the olfactory region only covers 5cm² [9]. The olfactory region offers a deposition site for central nervous system targeting [10]. Inspired air passes through the turbinate region which is covered by respiratory 2mm thick pseudostratified and ciliated mucosa (0.1mm), whereby air resistance and turbulence occur [11]. Thus, the geometry of the nasal cavity can affect nasal drug delivery. The mucosa has a major role in cleaning (particle entrapment), warming (37°C) and humidification (up to 90% relative humidity) of inspired air. The entrapped particles are then moved towards the pharynx region by means of

cilia beat at an average rate of 8mm/min taking 15-20 minutes [12]. Various cells are located within the nasal cavity: basal cells, columnar cells: ciliated and non-ciliated, goblet cells (Figure 2.2, Insert B) and inflammatory cells [13]. The airstream then bends toward the pharynx and continues into the larynx and trachea. Contrary to the nasal cavity, the oral cavity provides maximum entry of airborne particles. During elevated respiratory rates or during nasal congestion, the oral route aids as an alternative respiratory route. After nasal and oral cavity mix at the pharynx region, the larynx region follows, whereby the epiglottis prevents food from entering the respiratory tract (Figure 2.2 Insert C). The glottis is used to prevent penetration of the foreign particles into the airways and for rapid repulsion (coughing) of foreign matter [14]. Once particles pass the epiglottis they reach the trachea region.

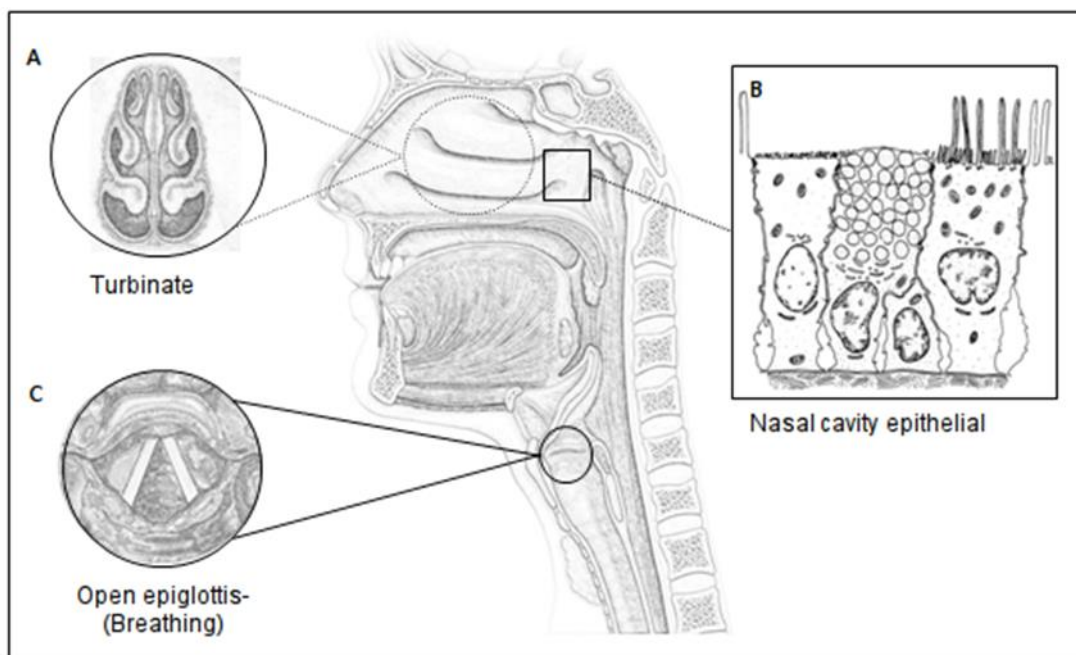


Figure 2.2: *Diagram depicting the route of entry for pulmonary drug delivery.*

2.2.2. Upper and lower respiratory tract

The trachea contains a ciliated surface (0.25 μ m diameter, 5-50 μ m length) coated with a thick mucus layer (Figure 2.3). The trachea then divides into the two bronchi. As the diameter of the airways decreases towards 1mm in diameter, the bronchioles region begins. In this region, the goblet cells, mousers' glands and cartilage disappear. Clara cells become the dominant mucus producing cells (found to give rise to surfactant producing cells). Ciliated cells are found in large branches whilst small branches have no ciliated cells. At the terminal end of the bronchioles lies the alveoli region whereby gas exchange takes place. The air-blood barrier in the alveoli region

is only 0.2 μ m thick [15]. The region surface is populated with as much as 2.3 $\times 10^{11}$ cells. This consist of 93% alveolar type I epithelial cells and 7% surfactant producing type II cells, even though the surfactant cells are more abundant in number. Macrophages are also located in the lung as much as 2 $\times 10^7$ cells making 7% of the lung parenchyma [16]. The amount of macrophages varies depending on the lung disease state and smoking habit (macrophages stimuli). The connective tissue surrounding the lungs is also of vital importance for retention of particles. The fate of the inhaled particles depends on the immune strength of the host and the physiochemical properties of the particle. These particles can either enter the interstitial space or be engulfed by the surface macrophages. Permanent “detainment” of particles is discussed in the disease section of the literature review. Some of the particles enter the lymph node system as seen with tuberculosis. Variations in anatomical features due to disease state or genetics can cause changes to deposition pattern and particle clearance.

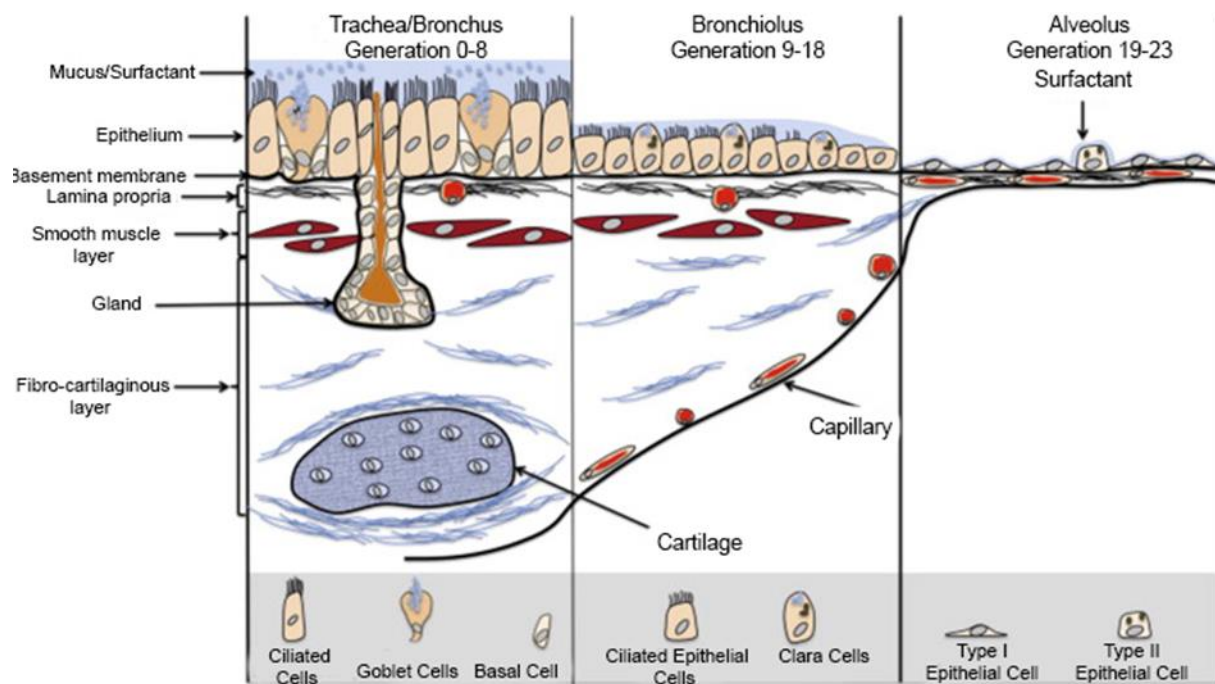


Figure 2.3: Diagram representing the respiratory tract wall structure (adapted from [17]).

2.2.3. Variations in anatomical features

There are number of variation in the respiratory tract based on the gender of the patient. Males have larger lungs than females. These variations are also evident in various ethnic groups based on dimensional sizes respective to body size. Age also plays an important factor in the morphometric characteristics of the airways. As the lung lose its elasticity with age, the clearance

mechanism is also affected [18]. Thus, understanding of variations caused by these factors can aid in patient specific drug delivery system and for improving delivery/efficiency to each specific patient group. Apart from physical factors that are inherited to change, other factors such as disease and life style habits can affect the remodelling of the lung features. The major determining way of evaluating of changes is the lung function test. It is known that the extrathoracic region is characterized with high airflow resistance [19]. This airflow resistance plays a major role in the deposition of inhaled foreign particles. Understanding of the anatomical features (cell types, airway dimensions and clearance mechanism) and relation to airflow dynamics can aid prediction studies for the fate of inhaled therapeutic aerosols. This can be used to correlate with the computational fluid dynamics mathematical models in assessing the delivery of inhaled therapeutics for treatment of various respiratory diseases due to obstruction/restriction and breathing patterns. These variations affect inspiratory and expiratory flow phases and wall shear stresses, thus impairing deposition [20]. Apart from lung anatomical features, drug absorption is determined by the physiological features of the lung surface (clearance versus absorption).

2.3. Lung barriers (deposition, dissolution, absorption and clearance)

2.3.1. Targeting or overcoming mucus clearance

For aerosolized drug to reach target cells within the airways or for systemic delivery, the therapeutic should bypass various barriers (lung surfactant, surface lining fluid, epithelium, interstitial and basement membrane and the endothelium). As illustrated with the various cells types that make up the airway, the first contact point is with the secreted mucus/surfactant. The mucus is stated to be a viscoelastic gel that consisting of 95% water (humidifier), 2% mucin, 1% salts, 1% albumin, immunoglobins and enzymes and <1% lipids [21]. The complex gel-aqueous layer lines the entire conducting air-ways and becomes progressively thinner from the trachea (up to 100 μ m) to the bronchi (around 8 μ m), and then to terminal bronchioles (about 3 μ m) [22]. The insoluble particles are trapped by the gel and they are moved toward the pharyngolaryngeal region by the movements of the ciliated epithelium, where it is either coughed up or swallowed. The soluble particles are eliminated by absorptive mechanisms. The lipophilic molecules can cross the respiratory epithelium by passive transport; whilst the hydrophilic molecules can cross the epithelial barrier either through the intercellular spaces or by active transport (by mechanisms of endocytosis and exocytosis) [23]. Once in the submucosal region, the particles can enter the systemic circulation, bronchial circulation or lymphatic system [24]. Mucoadhesive particles (MAP) have been made to deliver drugs, but are removed rapidly by the mucociliary escalator and expiratory clearance. For overcoming the mucus layer, mucus-penetrating particles (MPP)

engineered to diffuse through mucus can avoid rapid mucociliary clearance (MCC) *in vivo* and persist in the lung longer [25]. Mucus clearance provides the mechanical clearance that removes bacteria from the airways in less than 6h under normal conditions antimicrobial activities, provided by lactoferrin and lysozyme, to suppress bacterial growth over these time frames [26].

2.3.2. Macrophage defence and surfactant

In the alveolar region, the gel-aqueous layer is replaced by a thin liquid layer ($<0.1\mu\text{m}$), which is composed of a pulmonary surfactant film and an aqueous subphase. The surfactant consists of 80% phospholipids, 5-10% neutral lipids and 8-10% proteins, playing a role in avoiding the alveolar collapse by reducing surface tension within the alveoli [27]. The proteins making up the surfactant are surfactant protein (SP) A-D, which belongs to a collectins family. SP-A and SP-D have been linked to adsorbing to the surface of the foreign particulate to facilitate clearance by alveolar macrophages. These are involved in innate immune response. The alveolar macrophages are known to make up 90% of the lung immune cells. The dendritic cells play a role in innate and adaptive response, whilst the mast cells are linked to allergy response, inflammation, fibrotic site [28]. The insoluble particles that are deposited ($1-5\mu\text{m}$) in the alveoli can be devoured and eliminated by the alveolar macrophages; whilst soluble particles can be absorbed into the systemic circulation. To overcome these barriers, surface chemistry has been applied to carriers to aid in evading or targeting the clearance mechanism system. The particles that can evade macrophage clearance can immediately be displaced to the hypophase and put in close contact with the alveolar epithelium or might be internalized by type II pneumocytes via receptor mediated recycling of pulmonary surfactant components [29]. The particulates internalized by epithelial cells by means of endocytic routes might penetrate the capillaries and be suitable for therapeutic systemic delivery. This shows measures are required to avoid protein adsorption (surfactant proteins) to nanoparticles to allow increased residence time in the deep lung (evading macrophages) or promote adsorption to facilitate immediate engulfment (targeting macrophages).

2.3.3. Particle transport and absorption

As depicted in figure 2.4, there are several mechanisms that facilitate absorption from the lung into the blood, lymph or cells. Passive diffusion is an important one. It has been reported that hydrophilic compounds tend to be absorbed (over an hour) via paracellular diffusion and intercellular junction pores while the absorption of hydrophobic compounds occurs through transcellular diffusion (within minutes) [30]. If the aerosol particles are not immediately dissolved in the pulmonary lining fluid, they might be able to transport across the airway and alveolar

epithelial cells as intact particles. Additionally, the high viscosity of mucus can trap the particles and subject them to mucociliary clearance. Insoluble particles deposited in the airways having a geometric size larger than $< 6\mu\text{m}$ are preferably cleared by MCC within 24 hours [31]. Whereas, smaller/disintegrating particles deposited in the upper airway tend to penetrate the mucus layer, and are taken up by epithelial cells; thereby escaping from MCC. MCC can be impaired by various diseases that affect the ciliated cells and mucus viscosity. In the alveolar region, the thin layer of lining fluid and alveolar type I cells provides very little resistance to particle transport; hence particle transport across the epithelial layer is mostly enhanced in this region [32]. The mechanism of particle transport across the epithelial cells is transcytosis, which can be mediated by protein-binding or receptor-mediated caveolae [33]. Lung diseases that reduce the surface area and mucus hypersecretion impair the amount of drug adsorption. Targeted and responsive delivery can aid in disease lungs. Molecular biology knowledge is important in design of tuneable, targeted and/or responsive carriers.

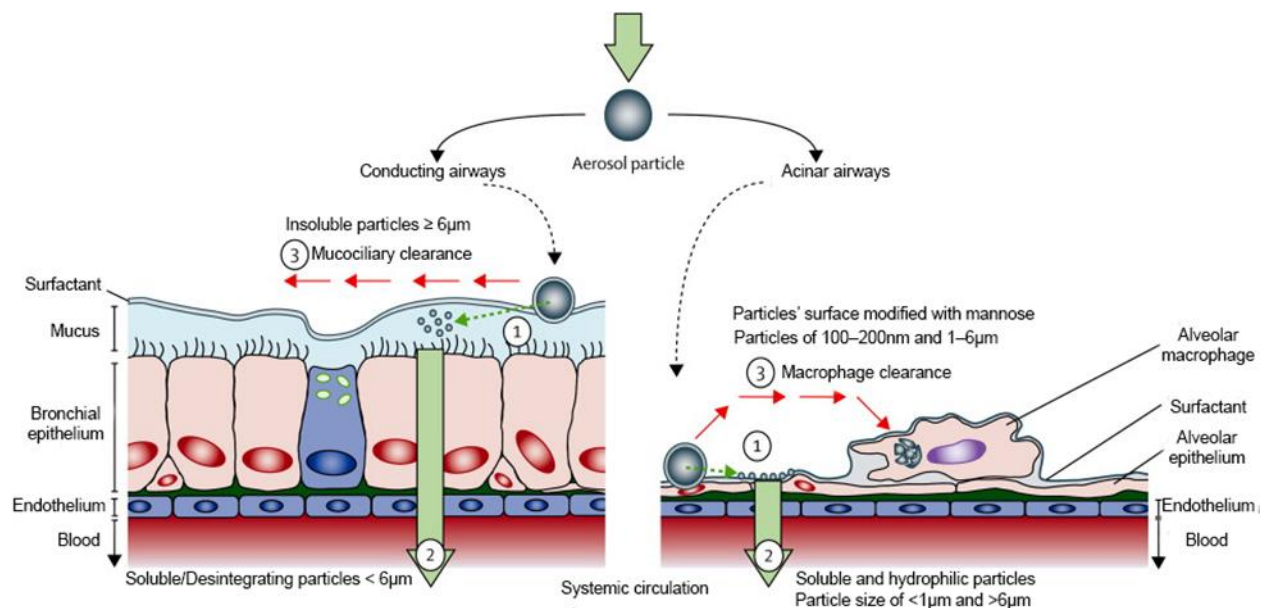


Figure 2.4: Barriers against drugs and carriers (adapted from [34]).

2.4. Molecular biology for responsive and target delivery

2.4.1. Immune cell targeting

The two main approaches for the targeted drug delivery are active and passive strategies. Passive targeting can occur due to extravasation of the nanoparticles at the diseased site where the microvasculature has leakage (tumour and inflamed regions) [35]. These regions also overexpress receptors which can be targeted via ligands. Within these region, various immune

cells, enzymes, reactive oxygen species, reactive nitrogen species, lipid mediators pH changes and cytokines are present which can be used for targeted/stimuli-responsive drug delivery (Table 2.1). The targeting of macrophages (pro-inflammatory (M1-phagocytotic), and ii) anti-inflammatory (M2-wound healing, tissue repair, and turn-off immune system activation) can have benefits as they are found in high numbers in rheumatoid arthritis, Acquired Immune Deficiency Syndrome (AIDS), leishmaniasis, tuberculosis, gaucher disease and cancer [36]. By using carbohydrate based surface chemistry, macrophages uptake can be done with low inflammatory induction by the carriers [37, 38]. Mast cells (MCs) have also been shown to be good target candidates for inflammatory diseases (central role in allergies, defence against some pathogens, resistance to venoms, and development or exacerbation of certain autoimmune diseases). Rheumatoid arthritis and Multiple sclerosis are some of the autoimmune diseases linked with MCs activity. Like macrophages, they MCs can be classified into two: MC_T , which express high levels of the MC-specific protease tryptase but not of chymase, and MC_{TC} , which express both tryptase and chymase can be targeted [39].

Neutrophil and eosinophil recruitment to the site of injury is the first line of host defence, but excessive neutrophil infiltration and activation at the airway walls is also the primary cause of inflammation and tissue damage [40]. Recently, the use of antibody conjugated PEGylated PLGA nanoparticle have been shown to be able to target neutrophils that are present in both acute and chronic inflammatory response phases of CF and COPD [41]. Various stimuli responsive polymers are reported in various research and review papers that go beyond the scope of this paper [42, 43]. Briefly, current enzyme responsive pulmonary delivery has been focusing on overexpressed matrix metalloproteinase which are found in various disease (lung cancer, tuberculosis and COPD) [44]. In terms of ROS, Saravanakumar (2016) reviewed various ROS drug delivery systems advantages and challenges [45]. For pH responsive, the endosomal pH is known to be acidic, thus allowing responsive stimuli in cancer tumours and macrophages [46, 47]. For ROS responsive system, Yue and colleagues (2016) evaluated targeting mitochondria for lung cancer chemo- and photodynamic synergistic therapy [48]. This shows that the mitochondria can be a target for both ROS and RNS responsive drug delivery system [49]. Once targeted regions/response stimuli have identified, particles engineering can be conducted to features of interest.

Table 2.1: Lung immune cells (adapted from [50])

Product	Macrophages[51]	Mast Cells [52]	Neutrophil [53]	Eosinophil [54]
Protein (Enzyme)	Neutral proteases, Lipases, Glucosaminidase, Lysosomal acid hydrolases & Deaminase:	Lysosomal Enzymes, Proteases, Caspase, Cyclooxygenases, Kinogenases & Heparanase	Proteases, Oxidase, Peroxidase & Elastase,	Oxidase, Protease & Phosphatase
Receptors	Fibronectin, Gelatin-binding protein of 95 kD, Thrombospondin, & Proteoglycans,	Proteoglycans & IgG	IgG, Proteoglycans & C3	Costimulatory molecules & Integrin
ROS	$H_2O_2, O_2^{\cdot-}, OH^{\cdot-}$, HOX	HOX,	O_2, H_2O_2, HOX	O_2, H_2O_2, HOX, OH
RNS	$NO^{\cdot}, ONOO^{\cdot-}$	NO^{\cdot}	NO^{\cdot}	$ONOO^{\cdot-}$

2.5. Engineering carriers for pulmonary delivery

The use of carrier based delivery allows protection of sensitive therapeutics from enzymatic degradation, sustained/controlled drug release (slow adsorption and reduced localized irritation), prolonged residence time (evade clearance and reducing dosing frequency) and targeted drug delivery (reduce side effects whilst increasing bioavailability to site of action) [55]. Carrier properties such as size and shape play an important role in the aerosolization, whilst surface chemistry plays a role in the interaction of the particulate with the biological system. Various developments have been conducted to improve various aspects of delivery and targeting. In terms of aerodynamic diameter (optimal 1-5 μ m), the well-known advancement is Pulmospheres™ (MMAD $\geq 5\mu$ m, density ≤ 0.1 g/L) and Technospheres™ (MMAD 2-3 μ m) where large porous are used offering improved flow and dispersion for various device application [56, 57]. These particles show that by reducing the density of particles, large particles (decreased tendency to aggregate and improved evasion of clearance by alveolar macrophages offering long residence time for drug release) can still reach the deep lung [58]. Furthermore, the carriers allow control of the ionization state of the drug, thus controlling dissolution and residence time [59].

It has also been reported that aerosol particles with aerodynamic diameter less than 1 μ m can be exhaled up to 80% without deposition due to their low inertia [36]. This indicates that decreasing the size does not guarantee increase in deposition in the deep lungs. However, breath-holding technique can improve deposition of such small particles. Therefore, other properties should be

added to these particles such as induced surface charge and hygroscopic behaviour. The reduction in density has also been shown to improve deposition; whilst particle size is large enough to promote inertial impaction and/or gravitational sedimentation. The use of hygroscopic growth can aid in ensuring their sedimentation as they gain mass during humidification [60]. In terms of shape, asbestos lung deposition mechanism and uptake by macrophages indicates that various shaped particulates can also offer an alternative deposition mechanism. Furthermore, it has been shown that macrophages have reduced phagocytosis activity on irregular shaped particles, thus enabling them to have increased residence time for sustained drug release [61]. For engineered particles, various deposition mechanism can be favoured as illustrated in figure 2.5. In airways, there are five possible deposition mechanisms: inertial impaction, sedimentation, diffusion, interception and electrostatic. Each is discussed based on the innovative technology to overcome or support the deposition mechanism.

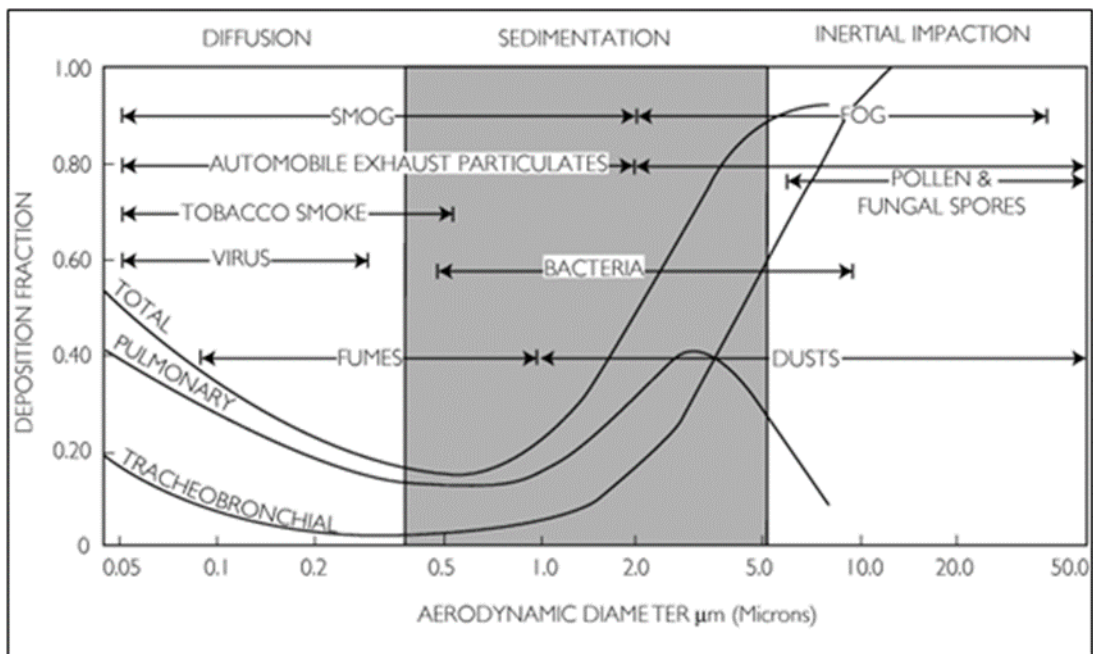


Figure 2.5: Deposition mechanism (adapted from [32]).

2.5.1. Inertial impaction

Inertial impaction occurs when particles of large size are unable to follow the fluid flow path due to diameter and mass ($\geq 5\mu\text{m}$). When the airflow changes direction due to bifurcation, particles will encounter the surrounding wall and be deposited. This occurs within the first ten generations (region of high air velocities). Factors that lead to increase in impaction deposition is the increase

in the aerodynamic size of the particles (hygroscopic, aggregation), increase in airflow rate and reduced airway dimensions due to disease state. Hyper-mucus secretion and reduction of diameter due to inflammation change the airway to favour inertial impaction [38]. This is seen with patients suffering from obstructed airways such as asthma and COPD whereby particles locally deposit with the central region of the airway. This leads to low deposition fraction in the deep lung, which will affect targeted delivery.

Drug–drug cohesive force and drug-exciipient adhesive forces (van der Waals forces and surface energy) are features that are linked to reduction of dispensability of the powders [62]. Large particles do not to exhibit these forces. However large particles particle size and inertia lead to deposition in the upper respiratory tract. To overcome this, porous particles can be synthesized to have the same particle size but low density. Pulmospheres™ technology is one of the examples of overcoming inertial impaction limitation of large particles. Currently the TOBI® Podhaler™ (Novartis; Basel, Switzerland) uses the Pulmospheres™ technology for the treatment of chronic *Pseudomonas aeruginosa* infections in cystic fibrosis (CF) patients [56]. Various methods can be utilized for the synthesis of porous particles such as gas formed particles using CO₂ and NH₃ from salts, inorganic salts like sodium chloride, hydrocarbon waxes, linear polymers, carbohydrates, gelatin, ice, sugar and synthesis procedure such as spray drying [63-65].

2.5.2. Sedimentation

Sedimentation describes particle deposition due to the influence of gravity (1-8µm). The important forces in sedimentation are gravitational force, drag force and buoyancy (density). When the air velocity is reduced such as in the small airways and alveoli cavities, sedimentation is favoured. Similar factor as impaction can promote sedimentation, with the exception that air velocity is reduced, and residence time is increase. The promotion of gravitational sedimentation is supported by the inhalation device manoeuvres of breath holding. However, if the manoeuvre is not done properly due to psychological/physical factors during the use of rescue inhaler can lead to reduced deposition. As the particles that deposit via sedimentation have a fixed particle size, the use of enhanced excipient growth (EEG) can aid in increasing the impact of gravitation sedimentation. Evaluation of sedimentation at altered gravity indicated that even of 5µm diameter would have lower depiction in lower airways [66]. The condensation of water due to hygroscopic carrier properties can aid in increasing the density of the particle. The rate of growth is a function of the initial diameter of the particle, with the potential for the diameter of fine particles <1µm to increase five-fold compared with two-to-three-fold for particles >2µm. *In vivo* studies have

confirmed that particles 0.02-5 μm can have increase deposition due to hygroscopic growth [67]. The rate of growth is also deepened on the kind of functional groups that play a role on the degree of hygroscopic growth as seen with organic aerosols in the environment (Figure 2.6).

The lung has a relative humidity of approximately 99.5%. The addition and removal of water can significantly affect the particle size of a hygroscopic aerosol and thus deposition the particles of aerosolized drugs can be hygroscopic to a greater or lesser extent. The phase transition of dry particle material into a saturated aqueous solution is called deliquescence and occurs when a substance-specific RH threshold value (deliquescence relative humidity, DRH) is exceeded. The reverse transition and its RH threshold value are called efflorescence and efflorescence relative humidity (ERH), respectively [45]. In general, it is considered that hygroscopic growth does not have much of an effect in particles with MMAD less than 0.1 μm ; whereas it is very intense in particles with MMAD larger than 0.5 μm . It is of note that hygroscopic properties can have a negative impact on storage of carriers. Exposure to moisture as seen with DPI can lead to increase in size and particle interaction, thus leading to inertial impaction in the upper respiratory tract.

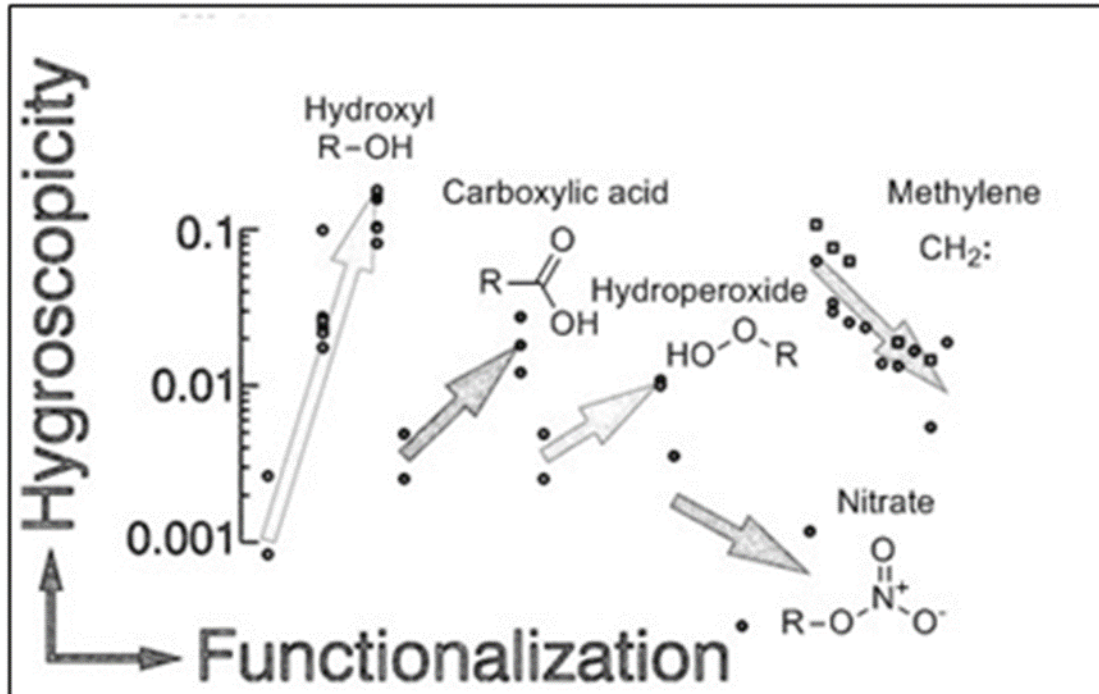


Figure 2.6: Hygroscopic growth based on functional groups (adapted from [68]).

In this regard, hygroscopic growth inhibitors (HGI, e.g. leucine) can be used for DPI as they are known to be sensitive to hygroscopic growth whilst in storage. Thus, particles increase in size/ agglomerate before being aerosolized for delivery. This will therefore promote impaction. Fine particle deposition (FDP) of budesonide was shown to be decreased for Turbuhaler, Spiromax and Easyhaler by 18%, 10% and 68% respectively, at 40 °C/75% RH [45]. Hygroscopic growth is shown not to be favourable for protein aerosol also. HGIs with their low moisture absorptivity properties will reduce the rate at which the formulation absorbs moisture and so reduce the structural changes that normally occur in their absence. Hygroscopic is only vital during deposition as indicated by reduction of mouth-throat (MT) deposition to 2.6% with HandiHaler DPI [69]. The utilization of excipient enhanced growth (EEG e.g. sodium chloride, citric acid and mannitol) has been shown to be able to reduce MT deposition $\leq 1\%$ in comparison to the conventional deposition of Respimat inhaler loss of 34.6-55.1% in the MT and inhaler mouth piece or 69.8% of Diskus DP[70]. Studies have shown that hygroscopic growth can also aid in evading macrophages due to large size [71]. Therefore, despite sensitivity of DPI to hygroscopic growth during storage, growth enhancement can contrarily improve deposition. For respirable particles, the incorporation of EEG allows enhanced deposition in the deep lung through increase of particle mass, which increases the sedimentation velocity [72]. Evaluation of Flovent HFA MDI, Diskus DPI and 5- μm Respimat aerosol by Tian and colleagues (2013), it indicated that EEG aerosol are highly effective for alveolar delivery with an increase in deposition by 90% [34].

2.5.3. Interception

For particles with irregular shape such as those consisting of fibres, interception occurs whereby shape and size prevent particles from going deeper into the narrowing airway generations. The narrowed region could be due to inflammation or due to mucus hyper-secretion. The shape factor can play a significant role in transport mechanism as the non-spherical shape particles will experience different drag force to spherical ones. This feature is the cause of computational difficulties in predicting the deposition mechanism of non-spherical particles. In relation to asbestos and pollen, the shape factor can affect targeting of macrophages. The orientation of the particle during uptake will affect internalization. As indicated in barriers that carriers have to overcome, internalization of particles by macrophages can impair drug delivery to required tissues if macrophages are not the intended targets [73]. Therefore, the non-spherical (depend on flexibility and stiffness) geometrical symmetry of the carriers can be used to aid in evading phagocytosis in combination to deposition mechanism.

Carbon nanotubes represent one of the known non-spherical well used drug delivery carriers. Their use in pulmonary drug delivery has generated concern over toxicological features similar asbestos been observed [69]. Long fibres deposit in the lungs can cause oxidative stress and inflammation. These can also be retained in the pleural tissues where more oxidative stress and inflammation can occur as seen with silicosis and asbestos [74]. The solubility of the carrier plays an important role in overcoming induction of inflammatory and oxidative stress. The ideal fibres must be non-biopersistent. After deposition, they must not release toxic ions or other components while undergoing dissolution and they break leading to shortening in length. These features will then allow effective phagocytosis and macrophage clearance [69]. As depicted in the lung immune cells enzyme products, biodegradation of these tubes can be applied to aid clearance. Peroxidase-driven biodegradation has been shown possible [75]. However, this still requires evaluation *in vivo* as this follows oxidative degradation. *In vitro* indicates that neutrophil myeloperoxidase can degrade carbon nanotubes with less pulmonary inflammation [76].

2.5.4. Diffusion

Random bombardment occurs on the particles of diameter less than 1 μ m, where airflow velocity is low leads to diffusion deposition. As particles decrease in size, Brownian motion is favoured. Particles below 1 μ m are known to be exhaled during pulmonary delivery. For nanoparticles, a combination of electrostatic surface charge is required for deep lung delivery, whilst sedimentation by means of hygroscopic growth occurs to be an alternative route to ensure particles get enough inertia for deposition. However, nanoparticles are known to have rapid absorption in the epithelium cells and can avoid the mucociliary clearance [77]. Thus nanoparticles are ideal for both localized and systemic drug delivery.

2.5.5. Electrostatic

Electrically charged particles close to airways surfaces induce image force charges on the surface or force charge effect [78]. Charged particles are then electrostatically attracted to the airway walls, and as a consequence this leads to increased deposition of charged particles in comparison to neutral particles [79]. In the absence of applied field, both liquid droplets (nebulizer and MDI) and solid particles (DPI) can get charged. The charge in liquid droplets occurs when a liquid surface is disrupted (atomization) or when liquid flows against a solid surface (valve). With solids this is due to contact charging (frictional force due to rubbing, sliding, rolling or impaction) [80]. However, these charges are known to cause deposition in the upper respiratory tract, thus requiring spacers to aid in removing charged particles [81]. In terms of DPI, the charges lead to

agglomeration and adhesion of particles causing inertial impaction to be favoured [82]. This can further cause inconsistent dosing, jamming of devices, uneven mixing and impaired aerodynamic behaviour. Despite these known devices based limitations in relation to charged particles, Experimental work carried out showing that charged aerosols deposited better than uncharged particles [83, 84].

Triboelectrification (contact charge) is stated as complex event that can be affected by many factors such as relative humidity, temperature, surface impurities, surface roughness, contact area, and other physicochemical factors, thus making it difficult to control [85]. The airways are neutral due to the humidity which has been also linked to reduction of charge on the surface of particles. The impact of electrostatic charge is more favoured in the lower respiratory tract due to small airway diameter. This is due to Coulomb's law stating that electrostatic force is inversely proportional to the square of the distance between two charges [85]. Based on Balachandran et al. (1997) it was found that image force is more predominant in the lower airways, whilst space force is favoured in the upper airways space [86]. This applied to particles with a diameter of $\leq 2.5\mu\text{m}$. A high surface charge leads to deposition in the upper respiratory tract, which is why spacers are used to reduce the number of charged particles. This allows particles with a negligible degree of charge to be delivered into the lower respiratory tract. The electrostatic deposition can be beneficial in targeting upper respiratory tract drug delivery when charged particles are used. This is supported by a study that shows that even particle that do not deposit via impaction (small particles) get deposited in the upper region [87]. As discussed that charge is induced during aerosolizing process, the selection of the inhalation device is also crucial in successful pulmonary drug delivery.

2.6. Inhaler device selection

The selection of the inhaler plays a significant role in therapeutic management as the device ease of use affects patient compliance and disease management. The choice depends of the capability of the patient to conduct the necessary manoeuvres to deliver optimum dose to reach the deep lungs. Each category of device has advantages and limitations. The nebulizers are limited by size but ensure high deposition, whilst MDI and DPI require manoeuvres for efficient delivery. Based on Laube et al. (2011), healthcare providers are required ensure that their patients can and will use these devices correctly. This requires that the clinician be aware of the devices that are currently available to deliver the prescribed drugs. Be able to educate the patient of the various

techniques that are appropriate for each device for proper use [88]. Here within, is discussed briefly various innovation that aid in improving delivery and ease of use for various patients.

2.6.1. Nebulizers

The nebulizers offer various advantages such as that they do not require specific inhalation technique or co-ordination, can deliver a variety of drug solutions at various doses and they are suitable for infants and immobile people. Disadvantages include that some of them are time consuming to use, bulky and non-portable, and the contents can be easily contaminated [89]. There are two different categories of nebulisers based on the mode of aerosol dispersion mechanism. The jet nebulizer that uses a compression mechanism has various advantages and disadvantages. These can be used by patients of different ages, does not require complex techniques to use and can deliver large doses in various diseases (complex medications) despite the severity. The setback like all nebulizers is the sensitivity to contamination thus requires disinfection and proper cleaning. In terms of jet nebulizer, their bulk size means they require power supply and cannot be carried around.

The other category is the ultrasonic nebulizer which offers added benefits such as faster aerosol output and portability. However, due to its hardware features, its more expensive than the jet nebulizer and the sonic waves generate heat can damage heat sensitive therapeutics [90]. The mesh nebulizer was designed to overcome this problem, as the mesh vibrates on top of the liquid suspension to generate small droplets (Aeroneb® and Aerogen®). This improved treatment time and less wastage of the drug. Respimat® Soft Mist™ inhaler represent innovative handheld nebulizer with a 40% whole lung deposition [91]. This uses mechanical energy from spring to produce fine-particle fraction ($\leq 5.8\mu\text{m}$). The Aradigm's AERx® system utilizes a single-use laser-micromachined polymer nozzle that is integrated with the single-use dosage form. This leads to 53.3% deposition [92]. Breath actuated AeroEclipse® and SideStream has deposition of 38.7% and 15.8%, respectively [93]. The I-neb AAD System which is used for treating CF patients has a 63-73% lung deposition [94]. Other innovative nebulizers of note are AeroEclipse® II BAN, AKITA2 APIXNEB, CompAIR™ NE-C801, Micro Air® NE-U22, PARI LC® Plus and PARI eFlow® rapid [95]. These represent vibrating mesh nebulizer with metering chambers and adaptive aerosol. The designs indicate that the mechanism of controlling particle size plays a major role in deposition fractions.

2.6.2. Metered dose Inhaler

The current MDI retain the same features such as metering valve, canister, and actuator mouthpiece as the predeceasing inhaler (MediHaler). The introduction of the MDI allowed portability with rapid delivery time. In terms of improving deposition, several hardware modifications or add-ons have been used. For more depth information of MDI technology readers are encouraged to read Stein *et al* review [96]. The change from chlorofluorocarbon (CFC) to hydrofluoroalkane (HFA) lead to improvement in deposition dose from 10-20% in CFC devices to 40-60% with HFA [93]. Metered dose inhalers require good coordination between actuation and inhalation. This leads to only a small fraction of aerosols reaching the deep lung due to high particle velocity on exit from the device. The metered valve design plays a role ensuring that there is a consistent amount of therapeutic formulation being released from the canister each time the patient actuates the device. As the valve design relates to the performance of the pMDI, each design will have advantages and disadvantages. QVAR® and Modulite® are examples of incorporation of valve design with formulation strategies. The canister design is also important as the size must relate to the size of valve to be used. In canister design, the inner coat is important to ensure formulations do not interact with the canister surface. Thus, avoid formation of charged particles.

The actuator plays a role in the atomization of the liquid suspension, thus pay a role in the aerosol characteristics of the therapeutic solution. Conventional mode of actuation mechanism plays independently on the patient's inhalation, thus leading to most of the therapeutic being deposited on the throat. The introduction of the breath-actuated MDI (synchronized inhalation and dosing), was to aid in overcoming coordination problems, thus making them useful to children (over 5 years). However, compression still requires some manoeuvre, thus led to development of the valve holding chamber (VHC) [97]. SmartMist® System is one of the add-on that offer breach-actuation control and dosing feedback during use. However, high deposition in the upper respiratory tract persists due to impaction and sedimentation. Various other add-on devices have been used to try to overcome the high deposition in the upper respiratory tract which causes side effects/irritation. This is one of the contributing factors to poor compliance. The add-ons allow people of various ages to be able to use the inhalers. They however still require some techniques to use and technical requirement after use (cleaning and replacement) and the spacers can reduce the drug output that reaches the lung. This also indicates that formulation strategies are required to improve pulmonary drug delivery. The incorporation of PulmoSpheres™ technology has led to improvement of suspension stability and dose uniformity [98]. Drug-drug interaction is

known to cause hetero-flocculation and increase aerosol particle size thus affecting the aerosolization efficiency. The use of carrier particles occurs as the viable option for improving delivery.

2.6.3. Dry powder inhalers

The DPI consist of an active pharmaceutical ingredient (API) with aerodynamic size (1-5 μ m) favourable to allow high deposition fraction [99]. The limitation of aerosolization of API is the interaction of particles due to cohesive/adhesive forces. This leads to reduced flowability and aerosolization is impaired as most of the drug remains retained in the device. The other major concerns are that most of the API are highly potent, the use of patient own inspiratory force has been used to encourage aerosolization. Various formulation strategies such as micronization (milling), spray drying, spray freeze drying and supercritical fluid technology are used for powder development [100]. Therefore, there should be a balance between formulation and choice of device. This can lead to variation in dosing and deposition fraction depending on the inspiratory force used during inhalation. To improve the performance of DPI, the use of carriers can aid in improving the aerosolization of the particles by improving deagglomeration of the particles (improved flowability and dispersion). Furthermore, these can aid in controlling the dose. Dispersion of powder from a DPI device is stated to require energy, which can come from pneumatic, vibrational or mechanical means. The forces that are responsible for dispersion of the powder in DPI include aerodynamic forces (drag and lift), inertial forces [101] (vibrational, rotational, centrifugal and collision), and shear and frictional forces [102].

As stated, patient inspiratory effort is required to overcome device resistance force ($\text{kPa}^{0.5} \text{ min/L}$) to generate turbulence that promotes dispersion. The device with lowest intrinsic resistance (e.g. Breezhaler® Neohaler™) is stated to be able to generate the highest inspiratory flow rate during patients' inspiratory effort. Contrary, the high intrinsic resistance (e.g. TwinCaps®) would generate low inspiratory flow rate [103, 104]. Thus, the amount of work (product of pressure drop, flow rate, and inhalation time) exerted by patients during maximal inhalation efforts decreases with increasing inhaler resistance [105]. Some technological advancements have been made to allow device generated force (Inhance™, Aspirair™) and motor driven dispersion (Spiros® - development stopped) [106]. The sensitivity to humidity is also seen as a drawback to use of DPI, as this change the size of the aerosols thus favouring deposition in the upper respiratory tract. Listed in table 2.2 are marketed DPI inhalers that offer various technological advancements to overcome limitations and improve deposition.

Table 2.2: List novel approved dry powder inhalers

Dry Powder Inhalers	Features	Deposition Fraction
3M Taper™	Utilizes a reverse cyclone 120 doses on a microstructured carrier tape	N/A
Staccato®	Loxapine (Adasuve®) Drug vaporized upon breath actuation 0.025 kPa ^{0.5} min/L	N/A [107]
Genuair® (Almirall Sofotec GmbH, Bad Homburg v.d. Höhe, Germany)	Aclidinium bromide Visual and acoustic feedback 0.031 kPa ^{0.5} min/L	30%[107]
NEXThaler® (Chiesi Farmaceutici, Parma, Italy)	Formoterol fumarate and beclomethasone dipropionate Humidity protection, breath actuated and dose counter 0.036 kPa ^{0.5} min/L	42% [108]
Ellipta (GSK, Middlesex, UK)	fluticasone furoate and vilanterol once-daily (asthma and COPD) 0.027 kPa ^{0.5} min/L	52% [109]
Breezhaler ® Neohaler™	Indacaterol and glycopyrronium bromide Audible feedback 0.02 kPa ^{0.5} min/L	31% [110]
Dreamboat inhaler	Insulin (Technospheres™) No user feedback 0.093 kPa ^{0.5} min/L	60%[101, 107]
TwinCaps® (Hovione, Loures, Portugal)	Laninamivir (Inavir®) Humidity protection, 0.057 kPa ^{0.5} min/L	N/A [107]
TOBI® Podhaler (Novartis, Basel, Switzer- land)	Tobramycin PulmoSphere™ 0.025 kPa ^{0.5} min/L	34% [111]

*N/A- data not available

2.7. Disease states and therapeutic innovations

Although there have been a number of improvements in inhaler devices for lung deposition, it is clear that the disease state can still hamper the performance of the inhaler. This is due to disease state affecting the aerodynamics flow and behaviour of the patient. As discussed briefly in [Chapter 1](#) and section [2.2. Lung anatomical features](#), besides aerodynamic diameter, the site of aerosol deposition in the respiratory tract are also affected by the anatomy of the airway, breathing

pattern, flow rate and tidal volume of the patients. Pavia and colleagues have shown a correlation between changed FEV₁ and depth of aerosol deposition. It was shown that patients with COPD had a significantly lower aerosol penetration than healthy volunteers [112]. Various animal models have been used to illustrate various disease states which can play a role in affecting the deposition of aerosol therapeutics [17]. Deposition patterns can be changed due to alteration of the lung anatomy. The reduction of the airways due to obstruction, inflammation and infection can lead to localized deposition in the tracheobronchial region in cystic fibrosis [113]. The work was supported by computational fluid and particle dynamics model whereby surface abnormalities and tubular constrictions have been shown to significantly alter the airstreams and the related local aerosol deposition distributions [114]. This indicates that anatomical changes must also be considered in particle engineering and prediction studies. Among various diseases breathing pattern is not linked to changes in the deposition fractions. In studies of aerosol deposition in COPD patients, correlation between deposition fraction and lung function parameter was shown [115]. Various diseases are known to lead to impaired lung function which will have impact on effective pulmonary drug delivery.

2.7.1. Tuberculosis

Tuberculosis (TB) is an infectious disease caused by the bacillus *Mycobacterium tuberculosis* (*M. tuberculosis*). It typically affects the lungs (pulmonary TB), but can affect other sites as well (extrapulmonary TB-15% of the patients) [116]. The TB bacilli is inhaled and then engulfed by the macrophages to be destroyed in the lysosome. The bacterium that evades degradation is then entrapped in a granuloma (macrophages and T lymphocytes aggregation). The currently recommended treatment for patients with pulmonary TB is a six-month regimen of four first-line drugs: namely isoniazid, rifampicin, ethambutol and pyrazinamide. The treatment success rate is at least 85% (67% in South Africa due to HIV co-infection) [117]. Treatment failure is mostly related to lack of patient adherence to the drug regimen (multiple drugs, side effects and up to 36 months' treatment plan (kidneys and liver drug metabolism overload)) and HIV-AIDS co-infection [118]. The introduction of fixed dose regiment was to improve compliance due to the number of drugs used. However, interaction between drugs has been shown to affect bioavailability and degree of absorption. HIV is also known to cause some changes in the level of bioavailability of these drugs when taken orally [119]. Due to lung lesion being poorly vascularized and fortified with thick fibrous tissue, oral and parental delivery have been shown to have sub-therapeutic levels of one or more antibiotics. Thus, leading to MDR-TB occurrence. This combination of pharmacokinetic variability and non-adherence can lead to resistance [120].

Pulmonary drug delivery avoids bioavailability filters (first pass metabolism and adsorption barriers) by directly delivering the therapeutics to site of action. Therefore, local delivery may lead to high drug concentration localized in the lung. Thereby reducing the duration of treatment and preventing multi-drug resistance (MDR). Nebulization of aminoglycosides solution has been to remove bacteria from the alveoli and prevent transmission [121]. However, this did not affect the bacteria within the macrophages. Due to instability of liquid formulation, various DPI formulations have been made from liposomes (non-immunogenic, can be phagocytosed by immune cells, high encapsulation efficacy, controlled drug release over a prolonged period); niosome; microparticles (MMAD of 1-5 μ m reach deep lung); nanoparticles (high drug loading, mucosal cell adherence, improved alveolar macrophages uptake, limitation from being exhaled [122]. Capreomycin inhalation via Cyclohaler is still under trials [123, 124]. In respect to microparticles, large porous particles have also been utilized which improved FPF percentage to the whole lung. For further reading on TB carrier design readers can read review [125, 126]. To target macrophages, the particles have been developed for this task should dissolve more slowly, making them susceptible to internalization by phagocytosis [124]. Surface features such as mannitol has been shown to increase stimulation of phagocytosis. However, severe cases of TB in the lungs exhibit large numbers of granulomas and tubercles, the latter exhibiting caseation and necrosis at their centre. Thus, drugs need to penetrate these barriers to access the pathogen in the intracellular or extracellular environment. It was proposed by Ekins (2014) that the use of antibody conjugation can help in entering the granuloma as seen with cancer research. However, no feasible evidence is available for this hypothesis [127].

2.7.2. Asthma and chronic obstructive pulmonary disease

Asthma and chronic obstructive pulmonary disease (COPD) are complex chronic lung inflammations that are characterized by airway obstruction which leads to many clinical complications like coughing, wheezing, and/or uneasiness in breathing. A brief pathogenesis of asthma involves the recruitment of eosinophils and neutrophils due to inflammatory response [128]. Apart from allergens, pathogens such as viruses can also induce asthmatic responsive in asthma patients. The pathogenesis of COPD has similar features to asthma due to abnormal inflammatory response in the lungs to the inhalation of toxic particles and gases, derived from tobacco smoke, air pollution, or occupational exposures [129]. This displays similar features to asthma. Hyper mucus secretion is associated with shortness of breath due to reduction of airways, in association with inflamed airways. There is currently no cure for asthma, but

management of the disease severity. Anti-inflammatory corticosteroids have been used since the 1980s to aid in suppression of the lung inflammatory response. Inflammation is present throughout the airways, including peripheral ones or small airways <2mm in diameter [130]. However, the repeated long-term use of corticosteroids has recently been shown to lead to drug resistance to the chronic and low responsiveness in COPD patients due to increase oxidative stress [131]. Thus, require new modes of inflammation management. As alveolar macrophages play a critical role in orchestrating the chronic inflammation in COPD to attract neutrophils into the airways [132].

Asthma is considered a chronic disease whereby respiratory tract cellular component (mast cells, eosinophils, T lymphocytes, macrophages, neutrophils, and epithelial cells) play a role [133]. These cells play a role in inflammatory response which leads to reversible airway obstruction. The obstruction can lead to tissue remodelling. These changes are discussed are they are linked to the effect on deposition mechanism of the therapeutic intervention. The changes in the mucosa and sub-mucosa due to epithelial hyperplasia and metaplasia of the goblet cells lead to increased mucus secretion. In the sub-mucosa, smooth muscle hypertrophy, collagen deposition, and larger mucous production occur [134]. The combination of these features leads to narrowing of the airways during asthma attacks. The modification of the airway diameter can alter the aerodynamics and airflow behaviour. This leads to patients not obtaining the required therapeutic effect during episodes. This impairs patient compliance to asthma inhalers. The use of spacers has been shown to bring some improvement in the delivery of aerosol in asthma and COPD patients. However, the size of the droplets will still be affected by the narrowing of the airways impairing the device optimized delivery condition. Thus, the changes in the airways brought by the asthma/COPD episodes affect the predetermined aerosol delivery to the lower airways. Thus, this warrants the need for alternative control of particle size during aerosolization step. Furthermore, localized delivery can be efficient in treatment of asthma as receptors are localized in various regions of the airways.

2.7.3. Cystic Fibrosis

Cystic fibrosis (CF) is a disease distinguished by electrolyte and water content imbalances. This develops because of mutations in the CF transmembrane conductance regulator (CFTR) gene. This encodes a membrane-bound cAMP-regulated chloride channel, whereby diminished chloride and water secretion leads to viscous secretions in the affected airways. In the airways, the mucus becomes thick with altered electrolyte composition and dehydration. The thick mucus due to

depletion of the periciliary liquid (PCL) impairs mucociliary clearance (cilia cannot extend normally) which leads facilitation chronic bacterial infections. It is hypothesized that the mucus interacts with the cell surface glycocalyx that effectively " glue" the mucus layer to airway surfaces [135]. The adhesive interactions between these two layers may be further strengthened by the low pH that appears to characterise CF airway epithelial airway surface liquid (ASL) [136]. These variations are caused by defective ion transport mechanism which has been shown to also lead to changes in bio-electrical properties. The epithelial is stated to behave like a ohmic resistor, whereby the potential difference reflects the relation between the magnitude of the ion current and the passive ion conductance [137]. In healthy individuals, the epithelial was found to conduct 19-21mV whilst in patients with cystic fibrosis the potential ranged from 38-41mV [138]. There is a correlation with the potential difference and the rate of sodium absorption. Various inhaled antibiotics, mucolytic/mucous mobilizers, anti-inflammatory and bronchodilators are used for management of cystic fibrosis [90].

Designing aerosol therapies for CF is particularly challenging, since the disease affects a wide age range, from new-borns to adults, and the spectrum of disease severity from normal lung function to severe airway obstruction [139]. Alternative approach to CF management is through gene therapy. However, clinical trials of gene therapy for cystic fibrosis suggest that current levels of gene transfer efficiency are probably too low to result in clinical benefit, largely because of the barriers faced by gene transfer vectors within the airways [140]. Adeno-associated virus (AAV) and cationic lipids have been used for gene transfer. The mucus negatively charged components are hypothesized to bind to lipoplexes thus changing surface properties promoting mucus transport and cellular uptake [141]. In term of AAV use, the immune system is designed to remove viruses. This also impairs the efficiency of AAV use as carriers. Once inside the cells, the genetic part is susceptible to degradation thus requiring system of evading lysozyme degradation. pH-sensitive liposomes and polyethylenimine as gene transfer agents can be used due to high buffering capacity and the flexibility to swell when protonated. This will cause large increase in the ionic concentration inside the endosome, thus changing the osmotic gradient exchange cause the endosome to rupture [140]. There are various FDA approved and clinical trials for CF pulmonary drug delivery [142].

2.7.4. Cancer

Cancer is one of the leading cause of death that has various forms from lung, breast, colorectal and stomach cancers that account to 40% of cancers diagnosed [143]. Various treatment

measures are used such as surgery; chemotherapy and radiation are used depending on the stage of malignancy. Chemotherapy (paclitaxel, docetaxel, cisplatin, gemcitabine, and vinorelbine) is one of the used methods of cancer treatment whereby toxic compounds are used to inhibit cells proliferation. Chemotherapy is known to have various adverse side effects such as bone marrow suppression, pain, nerve damage, skin allergic reactions, gastrointestinal problems (nausea, vomiting, diarrhoea), and alopecia [144]. These drugs are unable to differentiate between killing tumour cells and normal cells. Pulmonary drug delivery does not only benefit localised management of lung cancer (improved bioavailability), but can also be used as alternative route for systemic delivery. The main feature of cancer is the presence of tumours, whereby various cells such as myeloid-derived suppressor cells (MDSC), macrophages, and dendritic cells (DC) act as regulatory cells in the tumour microenvironment [145]. These cells express various molecules (enzymes) and surface receptors and ROS which can be targeted and responsive drug delivery.

There are currently various stimuli (endogenous or exogenous) responsive polymers that are being explored for carrying anti-cancer drugs. This system offers reduction in side effects profile and improved efficacy for cancer treatment. Both endogenous stimuli- including redox-/pH-/enzyme-responsive polymers and exogenous stimuli- including thermo-/photo- and ultrasound-responsive polymers for delivery of anti-cancer drugs are reviewed by Cheng et al. (2014) [146]. Due the lung barriers against pulmonary drug delivery, Garbuzenko et al (2014) studied the impact of carrier composition, size and shape on their lung accumulation and retention. It was found that lipid-based nanoparticles had considerably higher accumulation and longer retention time in the lungs when compared with non-lipid-based carriers after the inhalation delivery [147]. In combination with polyethylene glycol (PEG), lipid based carriers can have enhance the sustained-release properties and provide a “stealth” shield to bypass macrophage clearance [148]. The overexpression of epidermal growth factor and folic acid on cancer cells also offer an opportunity for targeted delivery. Macrophages also offer the opportunity to carry drug into the lymphatic system. Various clinical trials have been reported [149]. This shows that pulmonary drug delivery offers an advantage to enhance the efficacy of treatment of lung diseases and limit adverse side effects on healthy tissues. By designing particles that evade macrophage uptake, systemic delivery can become possible.

2.8. Systemic delivery, gene delivery and vaccination

Various therapeutics such as antiprotease, opioids, dihydroergotamine, parathyroid hormone, growth hormone releasing factor, interferon β , leuprolide acetate immunoglobulin G, peptide YY (an endogenous anorectic gut-secreted peptide), salmon calcitonin, albumin and insulin have been utilized for pulmonary drug delivery clinical trials [150-152]. Molecules such as insulin are formulated either as liquids or in highly water-soluble aerosol particles that dissolve rapidly in the lungs and thereby largely avoid macrophage degradation. Protein therapeutics that are taken up by macrophages can be rapidly destroyed in the lysosomal 'guts' of the phagocytic cells. The effect of pulmonary function was seen with Exubera® inhaled insulin, whereby insulin binding antibodies were found in combination with reduction in lung function parameters [153]. In combination to costs and size of the inhaler, the product was discontinued. AFREZZA® pocket sized insulin using Technospheres® (MannKind Corporation, CA, USA) has been FDA approved in 2014 (USA), whilst Adagio™ (Dance Biopharm, Brisbane, CA, USA) a liquid formulation insulin is still undergoing trials [154]. The technology allows rapid solubility, thus allowing systemic delivery. Many pathogens are known to be able to evade the immune response such as evasion of phagosome once taken up by the macrophages. This can also be applied in protein macrophage delivery. Proteins are known to have weak physical interactions such as electrostatic interactions, hydrogen bonding, van der Waals forces and hydrophobic interactions. Due to these weak interactions, proteins can easily undergo conformational changes, which can lead to a reduction of their biological activity during formulation. The use of formulation strategies such as Technospheres™, Pulmospheres® would allow improved bioavailability and tolerance during peptide delivery [155].

In relation to gene delivery, cystic fibrosis is one of the diseases that has multiple clinical trials for gene delivery utilizing various delivery carriers. This comes with challenges as CF is known to have hyper mucus secretion which acts as a barrier for carriers to pass through. This is followed navigation of the carrier in the cytoplasm to deliver the gene to the nucleus for expression. By using viral vectors improvement of genetic integrations has been shown to be possible. Alternatively, the use of cell-penetrating peptides (CPPs - cationic peptides (HIV-1 Tat or oligoarginine) and amphiphilic peptides (penetratin)) has shown successful delivery of insulin [156]. With the combination of mucus penetrating agents (Pulmozyme®, a recombinant human DNase (rhDNase) or Mucinex® (N-acetyl-L-cysteine; NAC)) or surface chemistry (hydrophilic) that allows hydrogen bonding with the mucus (hydroxyl (PEG) or carboxyl or amine groups), Suk et al. (2011) indicated that a combination of NAC + rhDNase could increase average effective

diffusivities 13-fold whilst utilizing DNA nanoparticles [157, 158]. Vaccination by inhalation has many benefits such as localized vaccination for various respiratory diseases such as influenza. The PuffHaler® and Solovent® are some of the inhalers that are being developed for delivering measles vaccines in children and infants in developing countries [159]. The use of DPI allows mass immunisation without concern of disease transmission and contamination/disposal as seen with intravenous vaccination. This also offers product stability when therapeutic is in a dry state. There are various techniques that can be utilized for stability characterization and effectiveness of the designed pulmonary drug delivery systems.

2.9. Characterization of effectiveness the pulmonary drug delivery system

For assessment of pulmonary deposition, various equipment can be used for characterization of factors that can contribute to mode of deposition. Size characterization is vital in correlating the size of the aerosol to the deposition mechanism discussed. The surface properties are also of importance in assessing interaction between particles that can affect deposition such as cohesion in DPI and charges in droplets. Various analytical steps are illustrated in figure 2.7 which can be used in the optimization of the aerosol deposition in various stages of the study. Fröhlich and Sharareh Salar-Behzadi (2014) reviewed various *in vivo*, *ex vivo* and *in silico* techniques that can be used for assessment of inhaled nanoparticles toxicology [160]. The techniques used can aid in assessing the toxic effect of the inhaled aerosol in relation to lung clearance mechanism. Cell, tissue and animal models test can correlate to simulated computational models (reviewed CFD models by Longest and Holbrook (2012) [161]) in predicting the deposition of the aerosolized particles. However, each technique used has its own limitation, thus requiring various methods to support the required information to conclude.

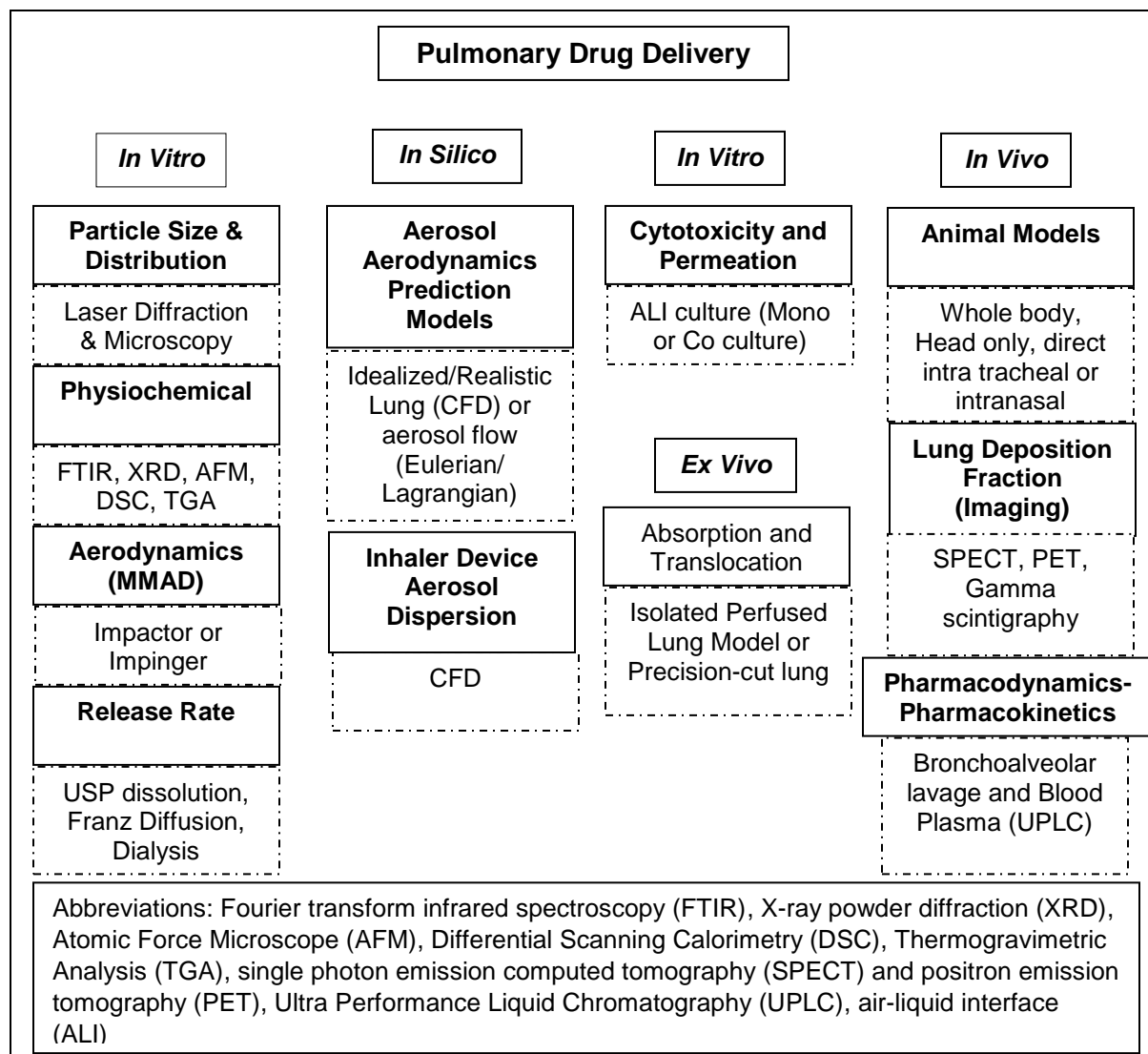


Figure 2.7: Modes of assessing and optimizing carriers for pulmonary drug delivery.

2.10. Concluding remarks

The use of nanoparticle based drug delivery is shown to be vital in improving lung deposition in combination to various inhalation devices. The particles enable predetermined aerodynamic properties that can be tailored by understanding pulmonary factors such as humidity, airflow patterns and defensive barriers. Other features such as surface chemistry and morphology play a vital role in improving the region of deposition. The success of TOBI® Podhaler™ using Pulmospheres™ technology has improved lung deposition whereby particle size and density play a major role. These nanoparticles can be used for various drugs as drug delivery can encapsulate both hydrophilic and hydrophobic drugs. In relation to devices, each device has its own limitations and benefits. However, DPI indicates to be the currently favoured inhalation devices that

overcome various stability features such as storage. As long-term effects of some nanoparticles are unknown, more work is required in avoiding causing changes to lung function whilst administering drug via pulmonary route. Furthermore, improving costs of production for chronic systemic therapeutic in relation to affordability. The failure of Exebura indicates the need for balance between formulation strategies and patient use. The choice of the inhaler (resistance) in relation to disease severity (lung function) can aid in improving deposition. Pulmonary drug delivery particle engineering indicates to be the alternative option of ensuring improved deposition for various drugs. This also has benefits for sustained release for once-daily use, thus improving patient compliance.

2.11. Reference

- [1] S.W. Stein, C.G. Thiel, The History of Therapeutic Aerosols: A Chronological Review, *Journal of Aerosol Medicine and Pulmonary Drug Delivery*, (2016).
- [2] M. Sanders, Pulmonary drug delivery: an historical overview, *Controlled pulmonary drug delivery*, Springer 2011, pp. 51-73.
- [3] K. Gourd, John Mudge, *The Lancet Respiratory Medicine*, 4 (2016) 16-17.
- [4] A.R. Clark, Medical Aerosol Inhalers: Past, Present, and Future, *Aerosol Science and Technology*, 22 (1995) 374-391.
- [5] J.L. Rau, The Inhalation of Drugs: Advantages and Problems, *Respiratory Care*, 50 (2005) 367-382.
- [6] G. Crompton, A brief history of inhaled asthma therapy over the last fifty years, *Primary Care Respiratory Journal*, 15 (2006) 326-331.
- [7] M.R. Partridge, Metered-dose inhalers and CFCs: what respiratory physicians need to know, *Respiratory Medicine*, 88 645-647.
- [8] J. Heyder, Deposition of Inhaled Particles in the Human Respiratory Tract and Consequences for Regional Targeting in Respiratory Drug Delivery, *Proceedings of the American Thoracic Society*, 1 (2004) 315-320.
- [9] M.G. Ménache, upper respiratory tract surface areas and volumes of laboratory animals and humans: considerations for dosimetry models, *Journal of Toxicology and Environmental Health*, 50 (1997) 475-506.
- [10] G.J. Garcia, J.D. Schroeter, J.S. Kimbell, Olfactory deposition of inhaled nanoparticles in humans, *Inhalation toxicology*, 27 (2015) 394-403.
- [11] H. Kublik, M.T. Vidgren, Nasal delivery systems and their effect on deposition and absorption, *Advanced Drug Delivery Reviews*, 29 (1998) 157-177.

- [12] E. Marttin, N.G.M. Schipper, J.C. Verhoef, F.W.H.M. Merkus, Nasal mucociliary clearance as a factor in nasal drug delivery, *Advanced Drug Delivery Reviews*, 29 (1998) 13-38.
- [13] N. Mygind, R. Dahl, Anatomy, physiology and function of the nasal cavities in health and disease, *Advanced Drug Delivery Reviews*, 29 (1998) 3-12.
- [14] G.P. Bridger, D.F. Proctor, Laryngeal Mucociliary Clearance, *Annals of Otology, Rhinology & Laryngology*, 80 (1971) 445-449.
- [15] J.G. Jones, Clearance of inhaled particles from the alveoli, *Aerosols and the lung: clinical and experimental aspects*, (1984) 290.
- [16] P. Gehr, Annexe A. Anatomy and morphology of the respiratory tract, *Annals of the ICRP*, 24 (1994) 121-166.
- [17] M. Hittinger, J. Juntke, S. Kletting, N. Schneider-Daum, C. de Souza Carvalho, C.-M. Lehr, Preclinical safety and efficacy models for pulmonary drug delivery of antimicrobials with focus on in vitro models, *Advanced Drug Delivery Reviews*, 85 (2015) 44-56.
- [18] G. Sharma, J. Goodwin, Effect of aging on respiratory system physiology and immunology, *Clinical Interventions in Aging*, 1 (2006) 253-260.
- [19] K.P. Strohl, J.P. Butler, A. Malhotra, Mechanical Properties of the Upper Airway, *Comprehensive Physiology*, 2 (2012) 1853-1872.
- [20] B. Sul, A. Wallqvist, M.J. Morris, J. Reifman, V. Rakesh, A computational study of the respiratory airflow characteristics in normal and obstructed human airways, *Computers in Biology and Medicine*, 52 (2014) 130-143.
- [21] C.A. Fernandes, R. Vanbever, Preclinical models for pulmonary drug delivery, *Expert Opin Drug Deliv*, 6 (2009) 1231-1245.
- [22] J.S. Patton, Mechanisms of macromolecule absorption by the lungs, *Advanced Drug Delivery Reviews*, 19 (1996) 3-36.
- [23] B. Forbes, C. Ehrhardt, Human respiratory epithelial cell culture for drug delivery applications, *European Journal of Pharmaceutics and Biopharmaceutics*, 60 (2005) 193-205.
- [24] A. Fernandez Tena, P. Casan Clara, Deposition of inhaled particles in the lungs, *Arch Bronconeumol*, 48 (2012) 240-246.
- [25] A. Popov, L. Schopf, J. Bourassa, H. Chen, Enhanced pulmonary delivery of fluticasone propionate in rodents by mucus-penetrating nanoparticles, *International Journal of Pharmaceutics*, 502 (2016) 188-197.
- [26] M.R. Knowles, R.C. Boucher, Mucus clearance as a primary innate defense mechanism for mammalian airways, *The Journal of clinical investigation*, 109 (2002) 571-577.

- [27] J. Goerke, Pulmonary surfactant: functions and molecular composition, *Biochimica et Biophysica Acta (BBA) - Molecular Basis of Disease*, 1408 (1998) 79-89.
- [28] C. de Souza Carvalho, N. Daum, C.-M. Lehr, Carrier interactions with the biological barriers of the lung: Advanced in vitro models and challenges for pulmonary drug delivery, *Advanced Drug Delivery Reviews*, 75 (2014) 129-140.
- [29] X. Murgia, C. de Souza Carvalho, C.-M. Lehr, Overcoming the pulmonary barrier: new insights to improve the efficiency of inhaled therapeutics, *European Journal of Nanomedicine*, 6 (2014) 157-169.
- [30] S.M. Majumdar, A.K., Chemical modification and formulation approaches to elevated drug transport across cell membranes, *Expert Opinion on Drug Delivery*, 3 (2006) 511-527.
- [31] W. Möller, K. Häußinger, R. Winkler-Heil, W. Stahlhofen, T. Meyer, W. Hofmann, J. Heyder, Mucociliary and long-term particle clearance in the airways of healthy nonsmoker subjects, *Journal of Applied Physiology*, 97 (2004) 2200-2206.
- [32] N.R. Labiris, M.B. Dolovich, Pulmonary drug delivery. Part I: Physiological factors affecting therapeutic effectiveness of aerosolized medications, *British Journal of Clinical Pharmacology*, 56 (2003) 588-599.
- [33] S. Xu, B.Z. Olenyuk, C.T. Okamoto, S.F. Hamm-Alvarez, Targeting receptor-mediated endocytotic pathways with nanoparticles: rationale and advances, *Advanced drug delivery reviews*, 65 (2013) 121-138.
- [34] C.A. Ruge, J. Kirch, C.-M. Lehr, Pulmonary drug delivery: from generating aerosols to overcoming biological barriers—therapeutic possibilities and technological challenges, *The Lancet Respiratory Medicine*, 1 (2013) 402-413.
- [35] R.T. Sadikot, Chapter sixteen - Peptide Nanomedicines for Treatment of Acute Lung Injury, in: N. Düzgüneş (Ed.) *Methods in Enzymology*, Academic Press 2012, pp. 315-324.
- [36] A.K. Azad, M.V.S. Rajaram, L.S. Schlesinger, Exploitation of the Macrophage Mannose Receptor (CD206) in Infectious Disease Diagnostics and Therapeutics, *Journal of cytology & molecular biology*, 1 (2014) 1000003.
- [37] N.K. Jain, V. Mishra, N.K. Mehra, Targeted drug delivery to macrophages, *Expert Opinion on Drug Delivery*, 10 (2013) 353-367.
- [38] Y. Pei, Y. Yeo, Drug delivery to macrophages: Challenges and opportunities, *Journal of Controlled Release*, 240 (2016) 202-211.
- [39] L.L. Reber, N. Frossard, Targeting mast cells in inflammatory diseases, *Pharmacology & therapeutics*, 142 (2014) 416-435.

- [40] J.K. Quint, J.A. Wedzicha, The neutrophil in chronic obstructive pulmonary disease, *Journal of Allergy and Clinical Immunology*, 119 (2007) 1065-1071.
- [41] N. Vij, T. Min, M. Bodas, A. Gorde, I. Roy, Neutrophil targeted nano-drug delivery system for chronic obstructive lung diseases, *Nanomedicine: Nanotechnology, Biology and Medicine*, 12 (2016) 2415-2427.
- [42] S. Mura, J. Nicolas, P. Couvreur, Stimuli-responsive nanocarriers for drug delivery, *Nat Mater*, 12 (2013) 991-1003.
- [43] D. Bennet, S. Kim, Polymer Nanoparticles for Smart Drug Delivery, Application of Nanotechnology in Drug Delivery, InTech, Rijeka, 2014, pp. Ch. 0.
- [44] E. Secret, K.E. Crannell, S.J. Kelly, M. Villancio-Wolter, J.S. Andrew, Matrix metalloproteinase-sensitive hydrogel microparticles for pulmonary drug delivery of small molecule drugs or proteins, *Journal of Materials Chemistry B*, 3 (2015) 5629-5634.
- [45] G. Saravanakumar, J. Kim, W.J. Kim, Reactive-Oxygen-Species-Responsive Drug Delivery Systems: Promises and Challenges, *Advanced Science*, (2016) 1600124-n/a.
- [46] A. Bhardwaj, A. Grobler, G. Rath, A.K. Goyal, A.K. Jain, A. Mehta, Pulmonary Delivery of Anti-Tubercular Drugs Using Ligand Anchored pH Sensitive Liposomes for the Treatment of Pulmonary Tuberculosis, *Current drug delivery*, 13 (2016) 909-922.
- [47] Y. Lv, L. Hao, W. Hu, Y. Ran, Y. Bai, L. Zhang, Novel multifunctional pH-sensitive nanoparticles loaded into microbubbles as drug delivery vehicles for enhanced tumor targeting, *Scientific Reports*, 6 (2016) 29321.
- [48] C. Yue, Y. Yang, C. Zhang, G. Alfranca, S. Cheng, L. Ma, Y. Liu, X. Zhi, J. Ni, W. Jiang, J. Song, J.M. de la Fuente, D. Cui, ROS-Responsive Mitochondria-Targeting Blended Nanoparticles: Chemo- and Photodynamic Synergistic Therapy for Lung Cancer with On-Demand Drug Release upon Irradiation with a Single Light Source, *Theranostics*, 6 (2016) 2352-2366.
- [49] J.P. Bolanos, M.A. Moro, I. Lizasoain, A. Almeida, Mitochondria and reactive oxygen and nitrogen species in neurological disorders and stroke: Therapeutic implications, *Adv Drug Deliv Rev*, 61 (2009) 1299-1315.
- [50] J.M. Stark, G.A. Mueller, 7 - Lung Defenses: Intrinsic, Innate, and Adaptive A2 - Wilmott, Robert W, in: T.F. Boat, A. Bush, V. Chernick, R.R. Deterding, F. Ratjen (Eds.) *Kendig & Chernick's Disorders of the Respiratory Tract in Children (Eighth Edition)*, W.B. Saunders, Philadelphia, 2012, pp. 89-109.
- [51] C.F. Nathan, Secretory products of macrophages, *Journal of Clinical Investigation*, 79 (1987) 319.

- [52] E.Z.M. da Silva, M.C. Jamur, C. Oliver, Mast Cell Function: A New Vision of an Old Cell, *Journal of Histochemistry and Cytochemistry*, 62 (2014) 698-738.
- [53] T.N. Mayadas, X. Cullere, C.A. Lowell, The Multifaceted Functions of Neutrophils, *Annual review of pathology*, 9 (2014) 181-218.
- [54] M.E. Rothenberg, S.P. Hogan, The eosinophil, *Annu. Rev. Immunol.*, 24 (2006) 147-174.
- [55] I.M. El-Sherbiny, N.M. El-Baz, M.H. Yacoub, Inhaled nano- and microparticles for drug delivery, *Global Cardiology Science and Practice*, 2015 (2015) 2.
- [56] J. Weers, T. Tarara, The PulmoSphere platform for pulmonary drug delivery, *Ther Deliv*, 5 (2014) 277-295.
- [57] A. Pfutzner, T. Forst, Pulmonary insulin delivery by means of the Technosphere drug carrier mechanism, *Expert Opin Drug Deliv*, 2 (2005) 1097-1106.
- [58] D.A. Edwards, A. Ben-Jebria, R. Langer, Recent advances in pulmonary drug delivery using large, porous inhaled particles, *Journal of applied physiology (Bethesda, Md. : 1985)*, 85 (1998) 379-385.
- [59] J.G. Weers, Enhanced design of inhaled therapeutics: what does the future hold?, *Ther Deliv*, 7 (2016) 145-148.
- [60] J. Löndahl, A. Massling, J. Pagels, E. Swietlicki, E. Vaclavik, S. Loft, Size-Resolved Respiratory-Tract Deposition of Fine and Ultrafine Hydrophobic and Hygroscopic Aerosol Particles During Rest and Exercise, *Inhalation Toxicology*, 19 (2007) 109-116.
- [61] M. Jansch, A.B. Jindal, B.M. Sharmila, A. Samad, P.V. Devarajan, R.H. Muller, Influence of particle shape on plasma protein adsorption and macrophage uptake, *Die Pharmazie*, 68 (2013) 27-33.
- [62] M.Y. Yang, J.G.Y. Chan, H.-K. Chan, Pulmonary drug delivery by powder aerosols, *Journal of Controlled Release*, 193 (2014) 228-240.
- [63] F. Ungaro, C. Giovino, C. Coletta, R. Sorrentino, A. Miro, F. Quaglia, Engineering gas-foamed large porous particles for efficient local delivery of macromolecules to the lung, *European Journal of Pharmaceutical Sciences*, 41 (2010) 60-70.
- [64] Y. Cai, Y. Chen, X. Hong, Z. Liu, W. Yuan, Porous microsphere and its applications, *International Journal of Nanomedicine*, 8 (2013) 1111-1120.
- [65] D.E. Geller, J. Weers, S. Heuerding, Development of an Inhaled Dry-Powder Formulation of Tobramycin Using PulmoSphere™ Technology, *Journal of Aerosol Medicine and Pulmonary Drug Delivery*, 24 (2011) 175-182.
- [66] C. Darquenne, Aerosol deposition in the human lung in reduced gravity, *J Aerosol Med Pulm Drug Deliv*, 27 (2014) 170-177.

- [67] G.A. Ferron, S. Upadhyay, R. Zimmermann, E. Karg, Model of the deposition of aerosol particles in the respiratory tract of the rat. II. Hygroscopic particle deposition, *J Aerosol Med Pulm Drug Deliv*, 26 (2013) 101-119.
- [68] S.R. Suda, M.D. Petters, G.K. Yeh, C. Strollo, A. Matsunaga, A. Faulhaber, P.J. Ziemann, A.J. Prenni, C.M. Carrico, R.C. Sullivan, S.M. Kreidenweis, Influence of Functional Groups on Organic Aerosol Cloud Condensation Nucleus Activity, *Environmental Science & Technology*, 48 (2014) 10182-10190.
- [69] K. Donaldson, C.A. Poland, F.A. Murphy, M. MacFarlane, T. Chernova, A. Schinwald, Pulmonary toxicity of carbon nanotubes and asbestos — Similarities and differences, *Advanced Drug Delivery Reviews*, 65 (2013) 2078-2086.
- [70] G. Tian, P.W. Longest, X. Li, M. Hindle, Targeting aerosol deposition to and within the lung airways using excipient enhanced growth, *J Aerosol Med Pulm Drug Deliv*, 26 (2013) 248-265.
- [71] P. Selvam, I.M. El-Sherbiny, H.D. Smyth, Swellable hydrogel particles for controlled release pulmonary administration using propellant-driven metered dose inhalers, *J Aerosol Med Pulm Drug Deliv*, 24 (2011) 25-34.
- [72] A.H.H. de Boer, P.; Hoppentocht, M.; Buttini, F.; Grasmeyer, F.; Frijlink, H. W., Dry powder inhalation: past, present and future, *Expert Opinion on Drug Delivery*, 14 (2017) 499-512.
- [73] J.A. Champion, Y.K. Katare, S. Mitragotri, Particle shape: a new design parameter for micro- and nanoscale drug delivery carriers, *Journal of controlled release : official journal of the Controlled Release Society*, 121 (2007) 3-9.
- [74] J. Muller, F. Huaux, D. Lison, Respiratory toxicity of carbon nanotubes: How worried should we be?, *Carbon*, 44 (2006) 1048-1056.
- [75] G.P. Kotchey, Y. Zhao, V.E. Kagan, A. Star, Peroxidase-mediated biodegradation of carbon nanotubes in vitro and in vivo, *Advanced Drug Delivery Reviews*, 65 (2013) 1921-1932.
- [76] V.E. Kagan, N.V. Konduru, W. Feng, B.L. Allen, J. Conroy, Y. Volkov, I.I. Vlasova, N.A. Belikova, N. Yanamala, A. Kapralov, Y.Y. Tyurina, J. Shi, E.R. Kisin, A.R. Murray, J. Franks, D. Stolz, P. Gou, J. Klein-Seetharaman, B. Fadeel, A. Star, A.A. Shvedova, Carbon nanotubes degraded by neutrophil myeloperoxidase induce less pulmonary inflammation, *Nat Nano*, 5 (2010) 354-359.
- [77] N. Islam, M.J. Cleary, Developing an efficient and reliable dry powder inhaler for pulmonary drug delivery – A review for multidisciplinary researchers, *Medical Engineering & Physics*, 34 (2012) 409-427.

- [78] H. Majid, P. Madl, W. Hofmann, K. Alam, Implementation of charged particles deposition in stochastic lung model and calculation of enhanced deposition, *Aerosol Science and Technology*, 46 (2012) 547-554.
- [79] C. Darquenne, Aerosol deposition in health and disease, *J Aerosol Med Pulm Drug Deliv*, 25 (2012) 140-147.
- [80] J. Wong, H.K. Chan, P.C. Kwok, Electrostatics in pharmaceutical aerosols for inhalation, *Ther Deliv*, 4 (2013) 981-1002.
- [81] P.C.L. Kwok, R. Collins, H.-K. Chan, Effect of spacers on the electrostatic charge properties of metered dose inhaler aerosols, *Journal of aerosol science*, 37 (2006) 1671-1682.
- [82] M.P. Timsina, G.P. Martin, C. Marriott, D. Ganderton, M. Yianneskis, Drug delivery to the respiratory tract using dry powder inhalers, *International Journal of Pharmaceutics*, 101 (1994) 1-13.
- [83] G. Scheuch, J. Gebhart, C. Roth, Uptake of electrical charges in the human respiratory tract during exposure to air loaded with negative ions, *Journal of Aerosol Science*, 21 (1990) S439-S442.
- [84] A.G. Bailey, A.H. Hashish, T.J. Williams, Drug delivery by inhalation of charged particles, *Journal of Electrostatics*, 44 (1998) 3-10.
- [85] P.C. Lip Kwok, Pharmaceutical aerosol electrostatics: a field with much potential for development, *Therapeutic Delivery*, 6 (2015) 105-107.
- [86] W. Balachandran, W. Machowski, E. Gaura, C. Hudson, Control of drug aerosol in human airways using electrostatic forces, *Journal of Electrostatics*, 40 (1997) 579-584.
- [87] M. Azhdarzadeh, J.S. Olfert, R. Vehring, W.H. Finlay, Effect of electrostatic charge on oral-extrathoracic deposition for uniformly charged monodisperse aerosols, *Journal of Aerosol Science*, 68 (2014) 38-45.
- [88] B.L. Laube, H.M. Janssens, F.H.C. de Jongh, S.G. Devadason, R. Dhand, P. Diot, M.L. Everard, I. Horvath, P. Navalesi, T. Voshaar, H. Chrystyn, What the pulmonary specialist should know about the new inhalation therapies, *European Respiratory Journal*, 37 (2011) 1308-1417.
- [89] L. Lannefors, Inhalation therapy: practical considerations for nebulisation therapy, *Physical Therapy Reviews*, 11 (2006) 21-27.
- [90] H. Heijerman, E. Westerman, S. Conway, D. Touw, Inhaled medication and inhalation devices for lung disease in patients with cystic fibrosis: A European consensus, *Journal of Cystic Fibrosis*, 8 (2009) 295-315.
- [91] P. Anderson, Use of Respimat® Soft Mist™ Inhaler in COPD patients, *International Journal of Chronic Obstructive Pulmonary Disease*, 1 (2006) 251-259.

- [92] S.J. Farr, S.J. Warren, P. Lloyd, J.K. Okikawa, J.A. Schuster, A.M. Rowe, R.M. Rubsamen, G. Taylor, Comparison of in vitro and in vivo efficiencies of a novel unit-dose liquid aerosol generator and a pressurized metered dose inhaler, *International Journal of Pharmaceutics*, 198 (2000) 63-70.
- [93] J.L. Rau, A. Ari, R.D. Restrepo, Performance comparison of nebulizer designs: constant-output, breath-enhanced, and dosimetric, *Respir Care*, 49 (2004) 174-179.
- [94] R. Dhand, Intelligent Nebulizers in the Age of the Internet: The I-neb Adaptive Aerosol Delivery (AAD) System, *Journal of Aerosol Medicine and Pulmonary Drug Delivery*, 23 (2010) iii-v.
- [95] M. Ibrahim, R. Verma, L. Garcia-Contreras, Inhalation drug delivery devices: technology update, *Medical Devices (Auckland, N.Z.)*, 8 (2015) 131-139.
- [96] S.W. Stein, P. Sheth, P.D. Hodson, P.B. Myrdal, Advances in Metered Dose Inhaler Technology: Hardware Development, *AAPS PharmSciTech*, 15 (2014) 326-338.
- [97] A. Lexmond, B. Forbes, *Drug Delivery Devices for Inhaled Medicines*, Springer Berlin Heidelberg, Berlin, Heidelberg, pp. 1-16.
- [98] J.G.Y. Chan, J. Wong, Q.T. Zhou, S.S.Y. Leung, H.-K. Chan, Advances in Device and Formulation Technologies for Pulmonary Drug Delivery, *AAPS PharmSciTech*, 15 (2014) 882-897.
- [99] C. Kumaresan, THE INHALATION OF ACTIVE PHARMACEUTICAL INGREDIENTS AND ITS PHARMACEUTICAL STUDIES, *Journal of Global Pharma Technology*, 8 (2016) 15-18.
- [100] E. Cordts, H. Steckel, Formulation considerations for dry powder inhalers, *Ther Deliv*, 5 (2014) 675-689.
- [101] D. Brashier, A. Khadka, T. Anantharamu, A. Sharma, A. Gupta, S. Sharma, N. Dahiya, Inhaled insulin: A puff; than a shot; before meals, *Journal of Pharmacology and Pharmacotherapeutics*, 6 (2015) 126-129.
- [102] P. Muralidharan, D. Hayes, Jr., H.M. Mansour, Dry powder inhalers in COPD, lung inflammation and pulmonary infections, *Expert Opin Drug Deliv*, 12 (2015) 947-962.
- [103] R.W. Dal Negro, Dry powder inhalers and the right things to remember: a concept review, *Multidisciplinary Respiratory Medicine*, 10 (2015) 13.
- [104] D. Price, H. Chrystyn, Concept review of dry powder inhalers: correct interpretation of published data, *Multidisciplinary Respiratory Medicine*, 10 (2015) 36.
- [105] C.C. Smutney, M. Grant, P.S. Kinsey, Device factors affecting pulmonary delivery of dry powders, *Ther Deliv*, 4 (2013) 939-949.
- [106] H.W. Frijlink, A.H. De Boer, Dry powder inhalers for pulmonary drug delivery, *Expert Opin Drug Deliv*, 1 (2004) 67-86.

- [107] K. Berkenfeld, A. Lamprecht, J.T. McConville, Devices for Dry Powder Drug Delivery to the Lung, *AAPS PharmSciTech*, 16 (2015) 479-490.
- [108] M. Corradi, H. Chrystyn, B.G. Cosio, M. Pirozynski, S. Loukides, R. Louis, M. Spinola, O.S. Usmani, NEXThaler, an innovative dry powder inhaler delivering an extrafine fixed combination of beclometasone and formoterol to treat large and small airways in asthma, *Expert Opin Drug Deliv*, 11 (2014) 1497-1506.
- [109] O.D. Wolthers, Extra-fine particle inhaled corticosteroids, pharmacokinetics and systemic activity in children with asthma, *Pediatric Allergy and Immunology*, 27 (2016) 13-21.
- [110] P. Haidl, S. Heindl, K. Siemon, M. Bernacka, R.M. Cloes, Inhalation device requirements for patients' inhalation maneuvers, *Respiratory Medicine*, 118 (2016) 65-75.
- [111] K. McKeage, Tobramycin Inhalation Powder: A Review of Its Use in the Treatment of Chronic Pseudomonas aeruginosa Infection in Patients with Cystic Fibrosis, *Drugs*, 73 (2013) 1815-1827.
- [112] D. Pavia, M.L. Thomson, S.W. Clarke, H.S. Shannon, Effect of lung function and mode of inhalation on penetration of aerosol into the human lung, *Thorax*, 32 (1977) 194-197.
- [113] T. Martonen, I. Katz, W. Cress, Aerosol Deposition as a Function of Airway Disease: Cystic Fibrosis, *Pharmaceutical Research*, 12 (1995) 96-102.
- [114] Á. Farkas, I. Balásházy, Simulation of the effect of local obstructions and blockage on airflow and aerosol deposition in central human airways, *Journal of Aerosol Science*, 38 (2007) 865-884.
- [115] J.S. Brown, K.L. Zeman, W.D. Bennett, Ultrafine Particle Deposition and Clearance in the Healthy and Obstructed Lung, *American Journal of Respiratory and Critical Care Medicine*, 166 (2002) 1240-1247.
- [116] D. Hillemann, S. Rüscher-Gerdes, C. Boehme, E. Richter, Rapid molecular detection of extrapulmonary tuberculosis by the automated GeneXpert MTB/RIF system, *Journal of clinical microbiology*, 49 (2011) 1202-1205.
- [117] N.R. Gandhi, A. Moll, A.W. Sturm, R. Pawinski, T. Govender, U. Lalloo, K. Zeller, J. Andrews, G. Friedland, Extensively drug-resistant tuberculosis as a cause of death in patients co-infected with tuberculosis and HIV in a rural area of South Africa, *The Lancet*, 368 (2006) 1575-1580.
- [118] J. Jin, G.E. Sklar, V. Min Sen Oh, S. Chuen Li, Factors affecting therapeutic compliance: A review from the patient's perspective, *Therapeutics and Clinical Risk Management*, 4 (2008) 269-286.
- [119] A. Sosnik, Á.M. Carcaboso, R.J. Glisoni, M.A. Moreton, D.A. Chiappetta, New old challenges in tuberculosis: Potentially effective nanotechnologies in drug delivery, *Advanced Drug Delivery Reviews*, 62 (2010) 547-559.

- [120] S. Srivastava, J.G. Pasipanodya, C. Meek, R. Leff, T. Gumbo, Multidrug-Resistant Tuberculosis Not Due to Noncompliance but to Between-Patient Pharmacokinetic Variability, *The Journal of Infectious Diseases*, 204 (2011) 1951-1959.
- [121] L.V. Sacks, S. Pendle, D. Orlovic, M. Andre, M. Popara, G. Moore, L. Thonell, S. Hurwitz, Adjunctive salvage therapy with inhaled aminoglycosides for patients with persistent smear-positive pulmonary tuberculosis, *Clinical infectious diseases*, 32 (2001) 44-49.
- [122] D.D. Pham, E. Fattal, N. Tsapis, Pulmonary drug delivery systems for tuberculosis treatment, *Int J Pharm*, 478 (2015) 517-529.
- [123] A.S. Dharmadhikari, M. Kabadi, B. Gerety, A.J. Hickey, P.B. Fourie, E. Nardell, Phase I, Single-Dose, Dose-Escalating Study of Inhaled Dry Powder Capreomycin: a New Approach to Therapy of Drug-Resistant Tuberculosis, *Antimicrobial Agents and Chemotherapy*, 57 (2013) 2613-2619.
- [124] A.J. Hickey, P.G. Durham, A. Dharmadhikari, E.A. Nardell, Inhaled drug treatment for tuberculosis: Past progress and future prospects, *Journal of controlled release : official journal of the Controlled Release Society*, 240 (2016) 127-134.
- [125] A. Costa, M. Pinheiro, J. Magalhães, R. Ribeiro, V. Seabra, S. Reis, B. Sarmento, The formulation of nanomedicines for treating tuberculosis, *Advanced Drug Delivery Reviews*, 102 (2016) 102-115.
- [126] D. Dube, G.P. Agrawal, S.P. Vyas, Tuberculosis: from molecular pathogenesis to effective drug carrier design, *Drug discovery today*, 17 (2012) 760-773.
- [127] S. Ekins, Hacking into the granuloma: could antibody antibiotic conjugates be developed for TB?, *Tuberculosis (Edinburgh, Scotland)*, 94 (2014) 715-716.
- [128] V. Frangova, O. Sacco, M. Silvestri, S. Oddera, A. Balbo, E. Crimi, G.A. Rossi, BAL neutrophilia in asthmatic patients. A by-product of eosinophil recruitment?, *Chest*, 110 (1996) 1236-1242.
- [129] W. Macnee, J. Vestbo, A. Agusti, 43 - COPD: Pathogenesis and Natural History A2 - Broaddus, V. Courtney, in: R.J. Mason, J.D. Ernst, T.E. King, S.C. Lazarus, J.F. Murray, J.A. Nadel, A.S. Slutsky, M.B. Gotway (Eds.) *Murray and Nadel's Textbook of Respiratory Medicine (Sixth Edition)*, W.B. Saunders, Philadelphia, 2016, pp. 751-766.e757.
- [130] S.L. Loo, P.A. Wark, Recent advances in understanding and managing asthma, *F1000Research*, 5 (2016).
- [131] Z. Jiang, L. Zhu, Update on molecular mechanisms of corticosteroid resistance in chronic obstructive pulmonary disease, *Pulmonary pharmacology & therapeutics*, 37 (2016) 1-8.

- [132] P.J. Barnes, K. Ito, I.M. Adcock, Corticosteroid resistance in chronic obstructive pulmonary disease: inactivation of histone deacetylase, *The Lancet*, 363 (2004) 731-733.
- [133] B.L. Bradley, M. Azzawi, M. Jacobson, B. Assoufi, J.V. Collins, A.M. Irani, L.B. Schwartz, S.R. Durham, P.K. Jeffery, A.B. Kay, Eosinophils, T-lymphocytes, mast cells, neutrophils, and macrophages in bronchial biopsy specimens from atopic subjects with asthma: comparison with biopsy specimens from atopic subjects without asthma and normal control subjects and relationship to bronchial hyperresponsiveness, *The Journal of allergy and clinical immunology*, 88 (1991) 661-674.
- [134] J.W. Mims, Asthma: definitions and pathophysiology, *International forum of allergy & rhinology*, 5 Suppl 1 (2015) S2-6.
- [135] P.H. Gilligan, Microbiology of airway disease in patients with cystic fibrosis, *Clinical microbiology reviews*, 4 (1991) 35-51.
- [136] R.C. Boucher, New concepts of the pathogenesis of cystic fibrosis lung disease, *The European respiratory journal*, 23 (2004) 146-158.
- [137] R.C. Boucher, M.R. Knowles, M.J. Stutts, J.T. Gatzky, Epithelial dysfunction in cystic fibrosis lung disease, *Lung*, 161 (1983) 1-17.
- [138] M. Knowles, J. Gatzky, R. Boucher, Increased bioelectric potential difference across respiratory epithelia in cystic fibrosis, *The New England journal of medicine*, 305 (1981) 1489-1495.
- [139] K.C. Kesser, D.E. Geller, New aerosol delivery devices for cystic fibrosis, *Respir Care*, 54 (2009) 754-767; discussion 767-758.
- [140] S. Ferrari, D.M. Geddes, E.W.F.W. Alton, Barriers to and new approaches for gene therapy and gene delivery in cystic fibrosis, *Advanced Drug Delivery Reviews*, 54 (2002) 1373-1393.
- [141] T. Montier, P. Delépine, C. Pichon, C. Férec, D.J. Porteous, P. Midoux, Non-viral vectors in cystic fibrosis gene therapy: progress and challenges, *Trends in Biotechnology*, 22 (2004) 586-592.
- [142] I. d'Angelo, C. Conte, M.I. La Rotonda, A. Miro, F. Quaglia, F. Ungaro, Improving the efficacy of inhaled drugs in cystic fibrosis: Challenges and emerging drug delivery strategies, *Advanced Drug Delivery Reviews*, 75 (2014) 92-111.
- [143] W.-H. Lee, C.-Y. Loo, D. Traini, P.M. Young, Inhalation of nanoparticle-based drug for lung cancer treatment: Advantages and challenges, *Asian Journal of Pharmaceutical Sciences*, 10 (2015) 481-489.
- [144] V. MacDonald, Chemotherapy: Managing side effects and safe handling, *The Canadian Veterinary Journal*, 50 (2009) 665-668.

- [145] H. Lemjabbar-Alaoui, O. Hassan, Y.-W. Yang, P. Buchanan, Lung cancer: biology and treatment options, *Biochimica et biophysica acta*, 1856 (2015) 189-210.
- [146] W. Cheng, L. Gu, W. Ren, Y. Liu, Stimuli-responsive polymers for anti-cancer drug delivery, *Materials Science and Engineering: C*, 45 (2014) 600-608.
- [147] O.B. Garbuzenko, G. Mainelis, O. Taratula, T. Minko, Inhalation treatment of lung cancer: the influence of composition, size and shape of nanocarriers on their lung accumulation and retention, *Cancer biology & medicine*, 11 (2014) 44-55.
- [148] P. Zarogoulidis, E. Chatzaki, K. Porpodis, K. Domvri, W. Hohenforst-Schmidt, E.P. Goldberg, N. Karamanos, K. Zarogoulidis, Inhaled chemotherapy in lung cancer: future concept of nanomedicine, *International Journal of Nanomedicine*, 7 (2012) 1551-1572.
- [149] A. Kuzmov, T. Minko, Nanotechnology approaches for inhalation treatment of lung diseases, *Journal of Controlled Release*, 219 (2015) 500-518.
- [150] M. Takano, M. Kawami, A. Aoki, R. Yumoto, Receptor-mediated endocytosis of macromolecules and strategy to enhance their transport in alveolar epithelial cells, *Expert Opinion on Drug Delivery*, 12 (2015) 813-825.
- [151] B.L. Laube, The expanding role of aerosols in systemic drug delivery, gene therapy and vaccination: an update, *Translational Respiratory Medicine*, 2 (2014) 3.
- [152] R. Uchenna Agu, M. Ikechukwu Ugwoke, M. Armand, R. Kinget, N. Verbeke, The lung as a route for systemic delivery of therapeutic proteins and peptides, *Respiratory Research*, 2 (2001) 198.
- [153] L. Heinemann, The Failure of Exubera: Are We Beating a Dead Horse?, *Journal of diabetes science and technology (Online)*, 2 (2008) 518-529.
- [154] B.K. Rubin, R.W. Williams, Emerging aerosol drug delivery strategies: From bench to clinic, *Advanced Drug Delivery Reviews*, 75 (2014) 141-148.
- [155] R. Angelo, K. Rousseau, M. Grant, A. Leone-Bay, P. Richardson, Technosphere(®) Insulin: Defining the Role of Technosphere Particles at the Cellular Level, *Journal of diabetes science and technology (Online)*, 3 (2009) 545-554.
- [156] N. Kamei, E.J. Nielsen, S. Khafagy el, M. Takeda-Morishita, Noninvasive insulin delivery: the great potential of cell-penetrating peptides, *Ther Deliv*, 4 (2013) 315-326.
- [157] J.S. Suk, N.J. Boylan, K. Trehan, B.C. Tang, C.S. Schneider, J.-M.G. Lin, M.P. Boyle, P.L. Zeitlin, S.K. Lai, M.J. Cooper, J. Hanes, N-acetylcysteine Enhances Cystic Fibrosis Sputum Penetration and Airway Gene Transfer by Highly Compacted DNA Nanoparticles, *Molecular Therapy*, 19 (2011) 1981-1989.

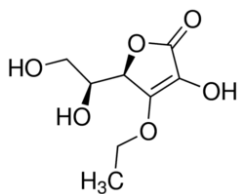
- [158] S.K. Lai, Y.-Y. Wang, J. Hanes, Mucus-penetrating nanoparticles for drug and gene delivery to mucosal tissues, *Advanced drug delivery reviews*, 61 (2009) 158-171.
- [159] S.P. Cape, L. Rebits, Needle-Free Inhalable Dry Powder Aerosol Measles Vaccine Developed for Pulmonary Delivery with a PuffHaler DPI, *C36. Asthma therapy ii*, pp. A4284-A4284.
- [160] E. Fröhlich, S. Salar-Behzadi, Toxicological Assessment of Inhaled Nanoparticles: Role of *in Vivo*, *ex Vivo*, *in Vitro*, and *in Silico* Studies, *International Journal of Molecular Sciences*, 15 (2014) 4795-4822.
- [161] P.W. Longest, L.T. Holbrook, *In Silico* Models of Aerosol Delivery to the Respiratory Tract – Development and Applications, *Advanced Drug Delivery Reviews*, 64 (2012) 296-311.

CHAPTER 3 : SIMULTANEOUS ANALYSIS OF ANTI-TUBERCULOSIS DRUGS THROUGH UV-VIS SPECTROMETRY USING CHEMOMETRIC TECHNIQUE

3.1. Introduction

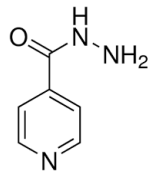
In pharmaceutical formulation, fixed-dose combination (FDC) are known to be vital in treatment and management of HIV/AIDS (Truvada® and Atripla®) [1], malaria (Eurartesim®) and tuberculosis (Rimactazid® , Rimcure Paed 3FDC®, Rifafour® and Rimstar 4FDC®) [2]. Multiple diseases can also be treated using FDC formulations e.g. Juvisync™ for the treatment of type 2 diabetes and high cholesterol [3]. In FDC, two or more drugs are formulated together and dosed as a single tablet to target a single disease [4]. In tuberculosis FDC, there are several challenges which have been shown to affect the treatment efficiency of TB. It has been shown that there is a loss of bioavailability of rifampicin upon administration and occurrence of instability of drugs within the formulation environment. This was ascribed to the decomposition of rifampicin in the presence of isoniazid to isonicotinyl hydrazone (HYD) in the stomach [5]. In the pH range of 1.2-2.1 (fasted stated), rifampicin has been shown to degrade in the presence of isoniazid to HYD. Thus, the bioavailability of rifampicin is reduced due to the formation of the insoluble HYD product [6]. It has been shown that even in pH 7.4 it is oxidized to rifampicin quinone in phosphate buffer, whilst at pH 8.2, it forms 25-desacetyl rifampicin, which is insoluble in the alkaline medium [7].

In South Africa, TB management becomes more complicated. This is due to TB-HIV coinfection. Rifampicin is known as a very potent enzyme inducer which can lead to subtherapeutic antiretroviral drug concentrations [8]. The other issue associated with anti-TB drug is hepatotoxicity [9]. To prevent hepatotoxicity, monotherapy of either isoniazid or rifampicin is a preferable means of treatment of latent TB in patients who have a higher risk of hepatotoxicity [10]. A recent study has shown that vitamin C (ascorbic Acid) was able to offer hepatotoxicity protection against hepatotoxicity induced by drugs, heavy metals, organophosphate insecticides and some chemical agents [11]. Figure 3.1 shows the characteristics of rifampicin, isoniazid and ascorbic acid which can be beneficial in TB treatment and its antituberculous hepatotoxicity side effects. This drug combination is novel for tuberculosis treatment and would require novel quantification method. Due to use of a large number of formulations in drug delivery design, a rapid method is more favourable.



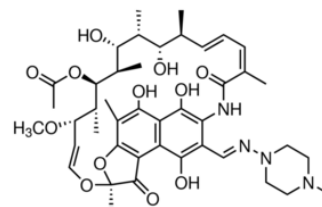
Ascorbic Acid

Action: helps with increase in ferrous ion concentration leading to ROS production
Water Solubility: E+005mg/L (at 40 °C)
Protein Binding: 25%
Half-Life: 16 days or 3.4 hours (if in excess)
Toxicity: N/A



Isoniazid

Action: inhibits the synthesis of mycolic acids (cell wall synthesis)
Water Solubility: 1.4E+005mg/L (at 25 °C)
Protein Binding: 0-10%
Half-Life: Fast acetylators: 0.5 to 1.6 hours. Slow acetylators: 2 to 5 hours
Toxicity: LD₅₀ 100mg/kg



Rifampicin

Action: inhibits DNA-dependent RNA polymerase (cell replication)
Water Solubility: 1400mg/L (at 25 °C)
Protein Binding: 89%
Half-Life: 3.35 (+/- 0.66) hours
Toxicity: 0.19 +/- 0.06L/hr/kg [300mg IV]

Figure 3.1: Images of Rifampicin, Isoniazid and Ascorbic acid and characteristics based on Drug Bank database.

There are various formulation designs and processes development for FDC oral products [12]. Analytical technique for FDC usually required high/ultra-performance liquid chromatography (HPLC/UPLC) systems. The preparation procedures are laborious and good analysis requires gradient elution techniques which take long periods of time. Furthermore, HPLC grade solvents are expensive. The use of spectroscopy can reduce the costs. Since World Health Organization (WHO) and International Union against Tuberculosis and Lung Disease (IUATLD) have recommended the use of FDCs of anti-TB drugs for TB treatment since 1994, the most frequently used FDC is rifampicin and isoniazid (4-6 month continuation phase) [13]. Recent work has shown that it is possible to quantify RIF and INH in combination in pharmaceutical preparations without the necessity of sample pre-treatment using derivative spectrophotometry. Derivative spectrophotometry is used as a useful technique for the suppression of additive interference, and it has been used extensively for the simultaneous determination of substances in mixtures [14]. Ultra-violet spectrometry is an analytical technique that can be utilized in pharmaceutical analysis. It is stated that "Spectrophotometry is the quantitative measurement of the reflection or transmission properties of a material as a function of wavelength" [15]. The advantage of the use of ultra-violet (UV) spectrometry is reduced analytical time and less laborious work (preparation and analysis). The precision and accuracy are also excellent, conditioned that the sample concentration lies with the linear range for Beer's law.

As it has been discussed that rifampicin interacts with isoniazid. Apart from indicated hepatotoxicity protection, it has been shown that addition of ascorbic acid (ASC) to the dissolution medium and plasma sample as anti-oxidant can protect degradation of RIF in the presence of INH [16]. Furthermore, it has been shown that ASC sterilizes cultures of drug-susceptible and drug-resistant *Mycobacterium tuberculosis* due to pro-oxidant activity [17]. In our work, it was observed that ASC peak of maximum absorbance occurs within the same region as INH (Figure 3.2). Due to issues of samples spectra overlapping, partial least squares (PLS) was utilized. PLS is beneficial as it builds a linear relationship between x and y that is then used for prediction of y for new data x [18]. It is stated that “designing a calibration set is the most crucial first step in developing a multivariate spectroscopic calibration method for quantitative analysis” [19]. Due to the success of model development depending on the suitability of the calibration data, a 3-factor central composite design was used for this study. Each component concentration lies within the linear range (Beer’s Law). Each design was conducted in triplicate.

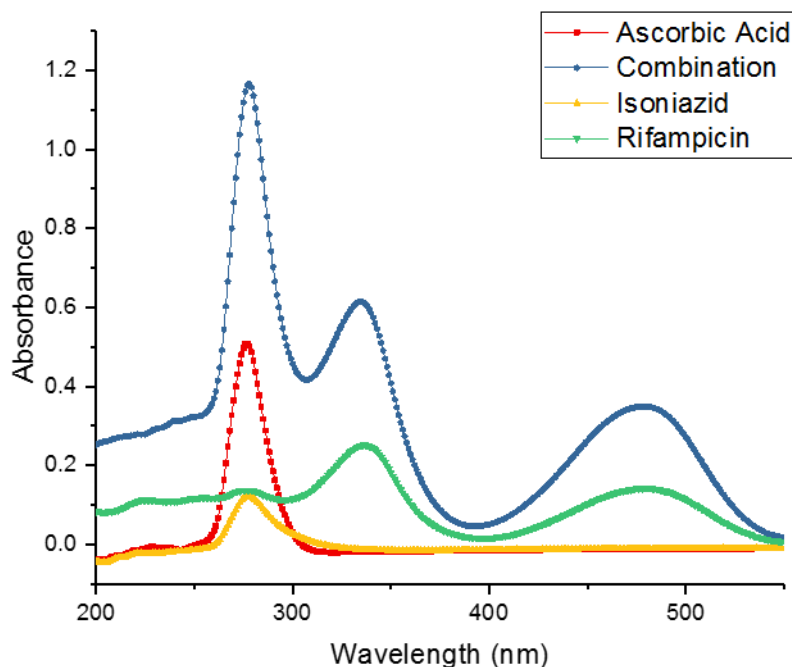


Figure 3.2: UV spectra of ASC, INH, RIF and Drug combination.

3.2. Materials and methods

3.2.1. Materials

Rifampicin, isoniazid and ascorbic acid were purchased from Sigma-Aldrich. Methanol (analytical grade) was purchased from Fluka. The chemicals were used without further purification.

3.2.2. Standard solutions

Stock solutions of RIF, INH and ASC of concentrations of 1.82, 7.29 and 56.78mM were prepared, respectively. The solutions were prepared by dissolving appropriate amount of drug in methanol. Working solutions for UV spectra absorbance analysis of RIF, INH and ASC of concentration 0.182, 0.729 and 5.678mM were prepared, respectively from the stock solution.

3.2.3. Central composite design

Central composite design was selected for design of calibration set. The selected upper and lower limits were selected based on the range of linearity (Beer's law) for each respective drug. Concentrations of three drugs for the calibration set are presented in table 3.1, laying within known linear absorbance–concentration range of each drug. The concentration ranges of 0.0567-0.8517mM (ASC), 0.00182-0.0273mM (RIF) and 0.00725-0.1088mM (INH). Standard solutions of calibration and validation sets were prepared in 10mL volumetric flasks by addition of appropriate amounts of each stock solution and diluted by methanol to the mark.

Table 3.1: Calibration and validation formulations using central composite design

Formulation	Ascorbic Acid (mM)	Isoniazid (mM)	Rifampicin (mM)
Calibration Set			
C1	0.4542	0.0581	0.0146
C2	0.4542	0.0000	0.0146
C3	0.8517	0.0073	0.0018
C4	1.1227	0.0581	0.0146
C5	0.4542	0.0581	0.0360
C6	0.4542	0.0581	0.0146
C7	0.0567	0.0073	0.0273
C8	0.0567	0.1088	0.0018
C9	0.4542	0.0581	0.0146
C10	0.0000	0.0581	0.0146
C11	0.8517	0.0073	0.0273
C12	0.4542	0.0581	0.0146
C13	0.8517	0.1088	0.0273
C14	0.4542	0.0581	0.0146
C15	0.4542	0.0581	0.0000
C16	0.0567	0.0073	0.0018
C17	0.4542	0.05805	0.0146
C18	0.0567	0.1088	0.0273
C19	0.8517	0.1088	0.0018
C20	0.4542	0.1434	0.0146

	Test Validation Set		
V1	0.3372	0.0827	0.0160
V2	0.1148	0.0147	0.0212
V3	0.4345	0.0230	0.0034
V4	0.8072	0.0748	0.0132
V5	0.5741	0.0518	0.0183
V6	0.7298	0.0330	0.0083
V7	0.6579	0.0624	0.0258
V8	0.2634	0.0446	0.0112
V9	0.1789	0.0932	0.0058
V10	0.4907	0.1025	0.0232

3.2.4. Spectral design

Electronic absorption measurements were carried out on UV on PerkinElmer Lambda 25, utilizing PerkinElmer UV Winlab software (Version 6) (Waltham, Massachusetts, USA). The scanning rate utilized was 120 scans/min at a 1nm data interval. 1.00cm quartz cuvettes were used. The experiment was conducted in duplicate. All spectra were saved in *.sp* file format, imported into Unscrambler® X (CAMO Software AS, Norway).

3.2.5. Partial least square analysis

A calibration and validation set of 16 and 10 samples, respectively were prepared. The concentration range for each component was lying within the linear absorbance-concentration range. The imported data was analysed using the Unscrambler® X software for selecting the optimum spectral region for each component. The calibration spectra were then converted into second derivative. The PLS model was adjusted by recalculation after adjustments of outliers or variables caused near the UV-C (200-280 nm range). Instead of the Non-linear Iterative Partial Least Squares (NIPALS) validation method, Kernel Partial Least Squares (KPLS) was used. Due to PLS regression model being based on linear transformation, this can lead to an over fitted model that is too sensitive to the noise in the modelling data [20, 21]. Therefore, KPLS does not require any nonlinear optimizations (table 3.2). Through the adaptation of the Orthogonal signal correction (OSC) algorithm, the sequence starts by (1) centering and scaling the data to give the raw matrices X and Y, (2) calculation of the first principal component (PC1) from a PCA of X and letting t_{\perp} be the PC1, (3) Orthogonalizing t_{\perp} to Y : $t_{new} = (1 - Y(Y^T Y)^{-1} Y^T) t_{\perp}$, (4) calculation of the PLS weight vector, w, that satisfies $X_w = t_{new}$, (5) calculation of the new score vector t_{\perp} from X and w: $t_{\perp} = X_w$, (6) repetition of steps 3, 4, and 5 until t_{\perp} has converged, (7) Computation of the loading vector , and finally (8) subtracting the 'correction' from X to obtain the residuals [22].

The difference between conventional PLS method and KPLS are illustrated in table 3.2. Cross validation method was also used.

Table 3.2: Comparison between the PLS and KPLS algorithms (adapted from [23])

PLS	Kernel PLS
1. Randomly initialize u	Randomly initialize u
2. $w = X^T u$	$t = \Phi \Phi^T u = Ku$ $t \leftarrow t / \ t\ $
3. $t = Xw$ $t \leftarrow t / \ t\ $	
4. $c = Y^T t$	$c = Y^T t$
5. $u = Yc$ $u \leftarrow u / \ u\ $	$u = Yc$ $u \leftarrow u / \ u\ $
6. Repeats steps 2,3,4, and 5, until convergence	Repeats steps 2,3,4, and 5, until convergence
7. Deflate X, Y matrices: $X \leftarrow X - tt^T X$ $Y \leftarrow Y - tt^T Y$	$Y \leftarrow Y - tt^T Y$

3.2.6. Prediction accuracy

The determination of figures of merit (FOM) is stated as an important requisite for the validation of chemometric acceptability [24]. FOM, such as accuracy, linearity and bias were estimated in this study. Rimactane® 150 (150mg rifampicin) and Winthrop Isoniazid 100 (100mg isoniazid) were sonicated for 1 hour in 100mL methanol. A 100mL solution of 1000mg of ascorbic acid was also made from 100mL methanol. The samples were then diluted into acceptable linear range concentration of 0.561, 0.0725 and 0.0182mM for ASC, INH and RIF, respectively. The samples were scanned on UV instrument using the same setup parameters as the calibration and validation. Spectra were imported into Unscrambler® X software without modification. To help define the ability of a calibration, the estimations of the standard variation of the chemometric calibrations in the case of the investigated mixtures were calculated. The standard error of calibration (SEC) and prediction (SEP) are given by the following expression.

$$SEC(SEP) = \sqrt{\sum_{i=1}^N (C_i^{Added} - C_i^{Found})^2 / n - 1} \quad (3.1)$$

Where, $C_{i_{Added}}$ represents the added concentration, $C_{i_{Found}}$ denotes the determined concentration, and n is the total number of samples.

The prediction for the residual error sum-of-squares (PRESS) of the calibration step was also calculated as using the equation:

$$PRESS = \sum_i^N (C_i^{Added} - C_i^{Found})^2 \quad (3.2)$$

The root mean squares error of cross validation (RMSECV) was also calculated:

$$RMSECV = \sqrt{PRESS/n} \quad (3.3)$$

Where n=number of predicted samples.

For measuring of the model fit to the training data, the R^2 defined as

$$R^2 = 1 - SSR/SSY \quad (3.4)$$

Whereby SSR is the sum of squares of the residual, and SSY is the sum of squares of the response variable corrected for the mean. It is stated that a value of $R^2 = 1$ denotes that the model fits the data perfectly, a value of $R^2 = 0.5$ shows that only half of the total sum of squares in the training set is explained by the model, and that the other half is in the residuals. And a model with an R^2 value of 0.7 can be considered a useful representation of the calibration data and a model $R^2 > 0.9$ is considered the best fit [22].

3.2.7. High performance liquid chromatography method

Analysis of ASC, INH and RIF mixture was evaluated using HPLC method. The working solution were mixed together to design a HPLC method for analysis of the three-drug mixture. The setup parameters are illustrated in table 3.3.

Table 3.3: Analysis of RIF, INH and ASC using HPLC method

Parameter	HPLC parameters
	Condition
Column	C18
Particle size	5µm
Mobile Phase	Buffer: 0.1M NaH_2PO_4 & 0.1M Na_2HPO_4 (pH 6.8) Solution A: 96% Buffer: 4% Acetonitrile

Flow rate	Solution B: 45% Buffer: 55% Acetonitrile	
Detection wavelength	1.5mL/min	
Column temperature	238nm	
Injection volume	25°C	
	20µl	
	Gradient Program	
Time (min)	Solution A (%)	Solution B (%)
0.00	100	0
5.00	100	0
6.00	15	85
15.00	15	85
15.01	100	0

3.3. Results and discussion

3.3.1. Derivative spectra

The use of derivative spectrophotometry is stated to have greatly improve the value in eliminating the interference from excipients and co-formulated drugs [25]. An overlap of ASC and INH on the UV spectra was observed. Prior to PSL analysis, first derivative spectra were calculated from the raw spectra (Figure 3.2). The Savitzky-Golay method was used. At the beginning and the end of the UV spectra, the analysis can be interrupted by the recorded noise within these regions. By means of smoothing the spectra using the Savitzky-Golay smoothing method, this can enable the reduction of the level of noise whilst keeping spectrum details. In a spectrum that is supposedly have equally spaced values,

$$f_i = \sum_{n_{left}}^{n_{right}} c_n s_{i+n} \quad (3.5)$$

Whereby n_{left} and n_{right} represent the number of points to the left and right of a current point, respectively. And c_n represents the weight coefficients. By using the polynomial order, Least-squares fitting is then utilized to fit the polynomial to the data inside the moving window. The analysis indicates that isoniazid overlaps with ascorbic acid (Figure 3.3). To improve detection sensitivity, the second derivative was finally used. Recent literatures indicate the use of ascorbic acid as an anti-oxidant in isoniazid-rifampicin mixtures. However, in our studies, the ascorbic acid indicated to additive behaviour to the drug at regions of maximum absorbance. Therefore, the analysis of rifampicin and isoniazid mixture in combination with ascorbic acid should be evaluated with caution of UV analysis.

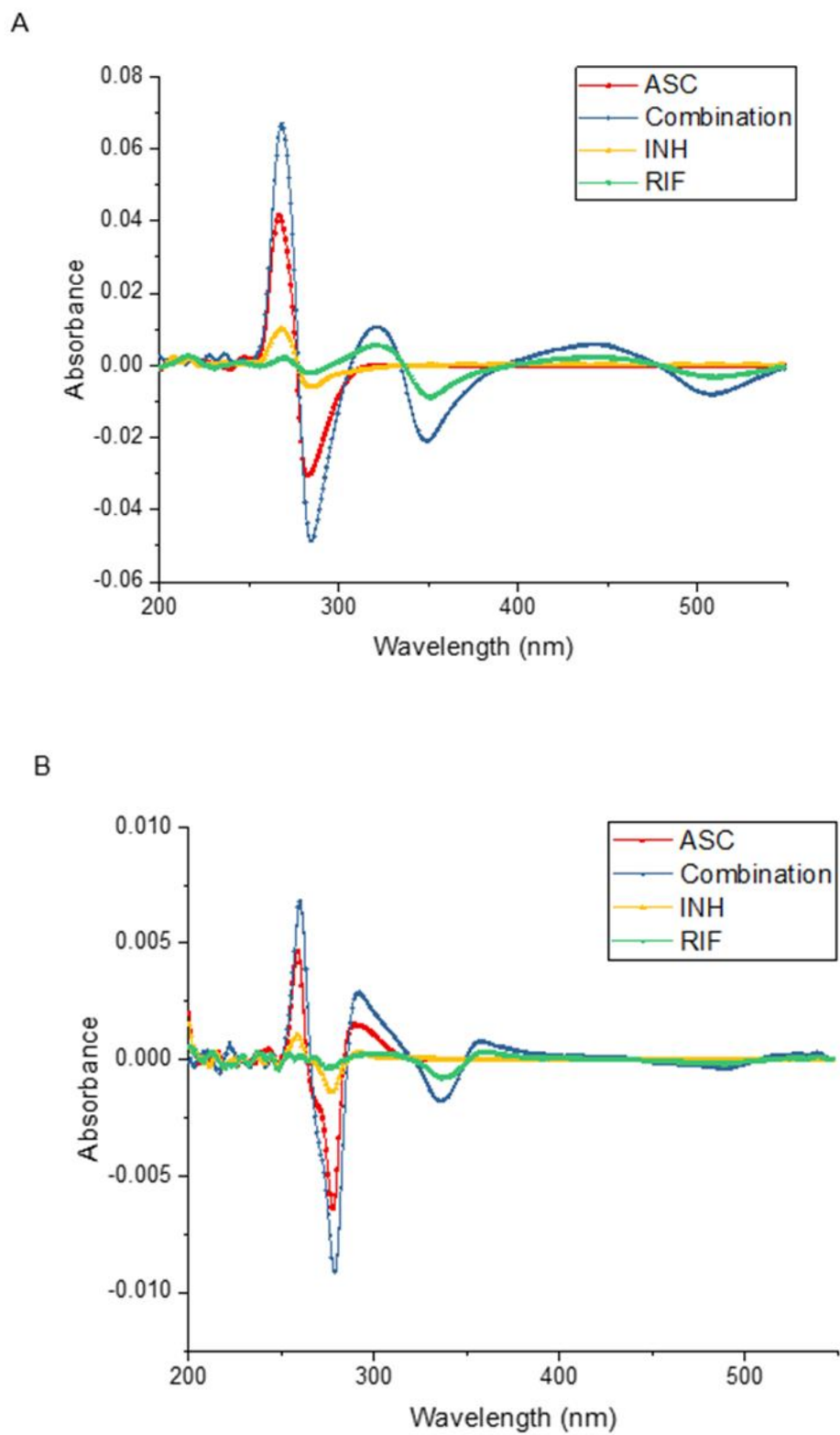


Figure 3.3: First (A) and second derivative (B) of ASC, INH and RIF drug individual and drug mixture.

3.3.2. High-performance liquid chromatography evaluation

HPLC method was designed to show successful separation of the drug combination. Figure 3.4 illustrate the HPLC chromatogram of combined working solution of ASC, INH and RIF indicating respective retention times, 1.603, 8.097 and 10.115 min. There are currently no formulations on the market that uses a combination of ASC, INH and RIF. The developed method indicates that the drug combination can be successfully separated within 12 min followed by allowing cleaning time of 8 minutes. In comparison to UV analysis, the HPLC method has an advantage of clear isolation of the distinct peaks of each respective drug. However, the preparations for the analysis in HPLC are laborious and require the use of expensive HPLC grade solvents for analysis. On the contrary, the UV method could be run under 2 min 45 sec. This method is inexpensive. After method development, one can analyse all the samples simultaneously within the selected software put importing the UV spectra.

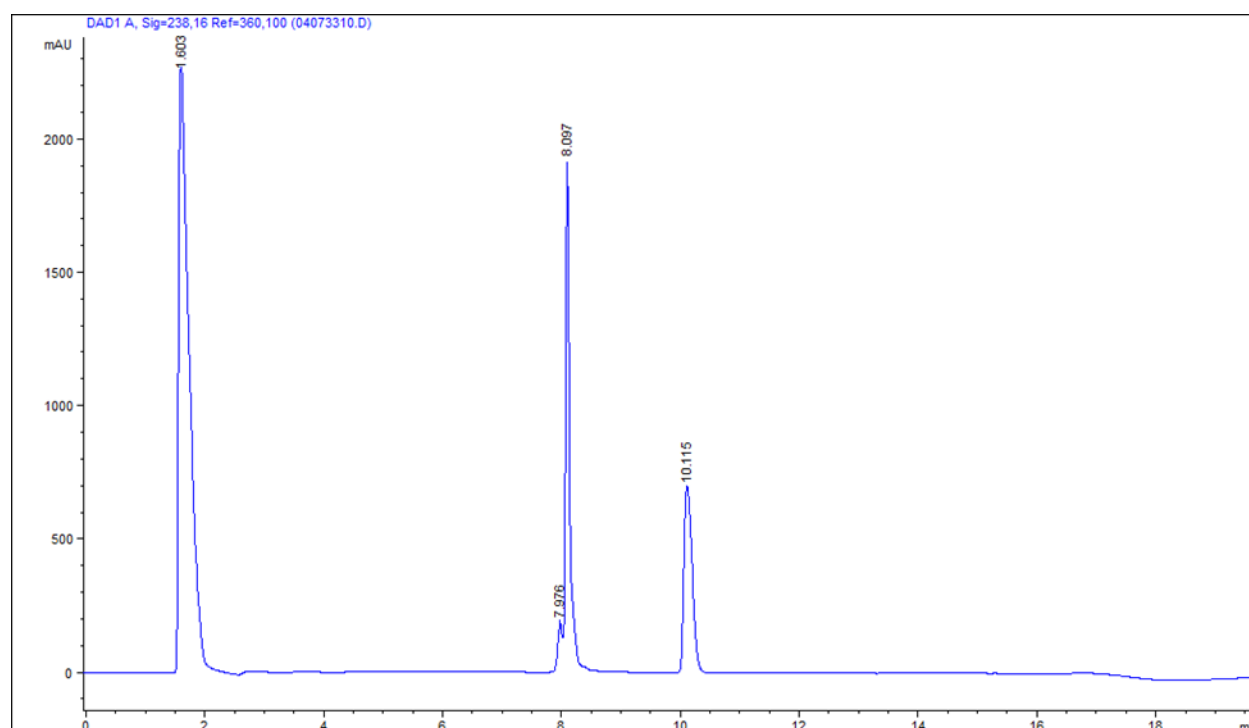


Figure 3.4: HPLC chromatogram of RIF, INH and ASC.

3.3.3. Method accuracy using cross-validation method

The chemometric PLS method was developed with the calibration dataset and validated set. The degree of accuracy and sensitivity were evaluated to assess the limitations of the method (Table 3.4). The method shows high degree accuracy for the 3-drug combination. The figures of merit

indicate high degree of accuracy for rifampicin, followed by isoniazid and then ascorbic acid. This is due to rifampicin having multiple distinctive peaks (λ_1 max 272nm, λ_2 max 337nm and λ_3 max 479nm) for identification, whereas INH (λ_1 max 274nm) and ASC (λ_1 max 273nm) overlap within the same region.

Table 3.4: Analytical data from the calibration for the determination of isoniazid, rifampicin and ascorbic acid spectroscopy

Parameters	Ascorbic Acid	Isoniazid	Rifampicin
Slope	0.978	0.940	0.988
Offset	0.0101	0.00306	1.924e ⁻⁴
Correlation	0.998	0.989	0.997
R ² (Pearson)	0.996	0.978	0.995
R ²	0.996	0.980	0.995
RMSECV	0.0101	0.00404	0.000617
SECV	0.0105	0.00418	0.000634
Bias	-0.0015	-0.00068	1.919e ⁻⁵

It is worth noting that recent studies on stability of RIF in various solvents (DMF, DMSO, and methanol) have shown that RIF is highly unstable. The use of methanol for RIF preparation resulted was shown to result in 22.3% RIF degradation compared with that using DMF and DMSO as the solvents [26]. It is recommended that RIF stock solution when stored at either 4°C or -20°C. This was observed with HPLC analysis and the impact is expected to affect the PLS analysis as some of the total percentage may be reduced. Thus, analysis of the samples containing the drug combination should not be stored for a long period of time. For the detection of RIF, the model indicated it was necessary to remove the interference of the overlap in ASC and INH absorbance region. In the analysis of INH, it was necessary to remove outliers using a component system. The UV-C region indicated to be problematic for both ASC and INH as the noise affected the accuracy of the prediction. This also required the removal of the variables with the region 200-250nm. The solvent choice is vital in improving the noise within this region as buffers salts are known to also generate high interference within this region. Prior to use of the tool in drug delivery system drug quantification, the tool was tested on known drug brands to observe if the accuracy lies within the accepted Pharmacopeia range.

3.3.4. Method application using commercial tablet mixture

The designed method was then evaluated using known drug brands mixture. Rimactane® and Winthrop Isoniazid were mixed together. As there is no current brand combination of ASC, INH and RIF, ASC was added to the level required for daily dosing of 1000mg. This would allow

determination of the accuracy of the tool in quantification drug release from synthesized nanoparticles. Table 3.5 shows the results of ASC, INH and RIF predicted values.

Table 3.5: Results of determination of anti-tuberculosis commercial tablets mixture using PLS analysis method.

	Components		
	Ascorbic Acid	Isoniazid	Rifampicin
Sample 1 (mg) ^a	900.33	96.13	148.13
Sample 2 (mg) ^a	931.15	100.52	153.07
Sample 3 (mg) ^a	926.92	99.014	152.24
Average of samples (mg)	919.46	98.56	151.15
Manufactures depicted amount (mg)	1000	100	150
% of the predicted content	91 (RSD 1.46%)	98 (RSD 1.47%)	100 (RSD 0.08%)
% range accepted by Pharmacopeia ¹	90-110	90-110	90-130

^aAmount estimated by the PLS method,

¹Reference

3.4. Concluding remarks

Based on the UV spectra, it shows that the addition of the ascorbic acid as a stabilizer can have additive effects on the maximum absorbance peak of isoniazid. Thus, the analysis of the isoniazid and rifampicin mixture stabilized by ascorbic acid can generate inaccurate UV readings for isoniazid. The model generated in this study, shows applicability in quantification of isoniazid and rifampicin despite the ascorbic acid interference. Although there is currently no commercial tablet that constitutes these drug combinations, the method can be used for detection of all the drugs simultaneously. The multivariate method is cheaper and less laborious in comparison to the developed HPLC method. Due increasing work demonstrating the use of ascorbic acid for stabilization of rifampicin and its use as a supplement for TB treatment, this work illustrates an alternative rapid analytic method [27, 28]. To obtain accurate data in chromatography separation, proper method development is vital which may be time consuming. The incorporation of chemometric as an analytic tool in this study has shown that multivariate analysis is vital in analysis of ascorbic acid stabilized rifampicin and isoniazid drug combination. The data showed that ascorbic acid had additive effects mainly on the peak maxima of isoniazid. The tool allowed better noise reduction, handling of the interference and control of the experimental outliers [29]. For rapid in-vitro drug release testing, chemometric tool is the key for rapid formulation strategy [30]. This tool was utilized in characterization of drug release and drug content (Chapter 6-8) in the preceding chapters.

3.5. Reference

- [1] A. Mitra, Y. Wu, Challenges and Opportunities in Achieving Bioequivalence for Fixed-Dose Combination Products, *The AAPS Journal*, 14 (2012) 646-655.
- [2] F. Farrer, Making sense of antibiotics: therapeutic, *Professional Nursing Today*, 15 (2011) 29-36.
- [3] W.H. Ramadan, W.K. Kabbara, Sitagliptin/Simvastatin: a first combination tablet to treat type 2 diabetes and hypercholesterolemia – a review of its characteristics, *Vascular Health and Risk Management*, 11 (2015) 125-132.
- [4] J. Hao, R. Rodriguez-Monguio, E. Seoane-Vazquez, Fixed-Dose Combination Drug Approvals, Patents and Market Exclusivities Compared to Single Active Ingredient Pharmaceuticals, *PLoS ONE*, 10 (2015) e0140708.
- [5] H. Bhutani, S. Singh, K.C. Jindal, A.K. Chakraborti, Mechanistic explanation to the catalysis by pyrazinamide and ethambutol of reaction between rifampicin and isoniazid in anti-TB FDCs, *Journal of Pharmaceutical and Biomedical Analysis*, 39 (2005) 892-899.
- [6] C.J. Shishoo, S.A. Shah, I.S. Rathod, S.S. Savale, M.J. Vora, Impaired bioavailability of rifampicin in presence of isoniazid from fixed dose combination (FDC) formulation, *International Journal of Pharmaceutics*, 228 (2001) 53-67.
- [7] M.C. Gohel, K.G. Sarvaiya, A novel solid dosage form of rifampicin and isoniazid with improved functionality, *AAPS PharmSciTech*, 8 (2007) E133-E139.
- [8] H.H. Semvua, G.S. Kibiki, E.R. Kisanga, M.J. Boeree, D.M. Burger, R. Aarnoutse, Pharmacological Interactions Between Rifampicin and Antiretroviral Drugs: Challenges and Research Priorities for Resource-Limited Settings, *Therapeutic Drug Monitoring*, 37 (2015) 22-32.
- [9] V. Ramappa, G.P. Aithal, Hepatotoxicity Related to Anti-tuberculosis Drugs: Mechanisms and Management, *Journal of Clinical and Experimental Hepatology*, 3 37-49.
- [10] World Health Organization, Guidelines for treatment of tuberculosis, 2009.
- [11] E. Adikwu, O. Deo, Hepatoprotective effect of vitamin C (ascorbic acid), *Pharmacology & Pharmacy*, 4 (2013) 84.
- [12] D. Desai, J. Wang, H. Wen, X. Li, P. Timmins, Formulation design, challenges, and development considerations for fixed dose combination (FDC) of oral solid dosage forms, *Pharmaceutical development and technology*, 18 (2013) 1265-1276.
- [13] B. Blomberg, B. Fourie, Fixed-Dose Combination Drugs for Tuberculosis, *Drugs*, 63 (2003) 535-553.

- [14] S.A. Benetton, E.R.M. Kedor-Hackmann, M.I.R.M. Santoro, V.M. Borges, Visible spectrophotometric and first-derivative UV spectrophotometric determination of rifampicin and isoniazid in pharmaceutical preparations, *Talanta*, 47 (1998) 639-643.
- [15] M.R. Siddiqui, Z.A. AlOthman, N. Rahman, Analytical techniques in pharmaceutical analysis: A review, *Arabian Journal of Chemistry*, 10 (2017) S1409-S1421.
- [16] S. Rajaram, V.D. Vemuri, R. Natham, Ascorbic acid improves stability and pharmacokinetics of rifampicin in the presence of isoniazid, *J Pharm Biomed Anal*, 100 (2014) 103-108.
- [17] C. Vilcheze, T. Hartman, B. Weinrick, W.R. Jacobs, Jr., Mycobacterium tuberculosis is extraordinarily sensitive to killing by a vitamin C-induced Fenton reaction, *Nature communications*, 4 (2013) 1881.
- [18] B. Nadler, R.R. Coifman, Partial least squares, Beer's law and the net analyte signal: statistical modeling and analysis, *Journal of Chemometrics*, 19 (2005) 45-54.
- [19] M.A. Alam, J. Drennen, C. Anderson, Designing a calibration set in spectral space for efficient development of an NIR method for tablet analysis, *Journal of Pharmaceutical and Biomedical Analysis*, 145 (2017) 230-239.
- [20] M. Wang, G. Yan, Z. Fei, Kernel PLS based prediction model construction and simulation on theoretical cases, *Neurocomputing*, 165 (2015) 389-394.
- [21] D. Ronen, C.F.W. Sanders, H.S. Tan, P.R. Mort, F.J. Doyle, Predictive Dynamic Modeling of Key Process Variables in Granulation Processes Using Partial Least Squares Approach, *Industrial & Engineering Chemistry Research*, 50 (2011) 1419-1426.
- [22] K. Kim, J.-M. Lee, I.-B. Lee, A novel multivariate regression approach based on kernel partial least squares with orthogonal signal correction, *Chemometrics and Intelligent Laboratory Systems*, 79 (2005) 22-30.
- [23] R. Rosipal, L.J. Trejo, Kernel partial least squares regression in reproducing kernel hilbert space, *J. Mach. Learn. Res.*, 2 (2002) 97-123.
- [24] M.M. Sena, Z.F. Chaudhry, C.H. Collins, R.J. Poppi, Direct determination of diclofenac in pharmaceutical formulations containing B vitamins by using UV spectrophotometry and partial least squares regression, *Journal of Pharmaceutical and Biomedical Analysis*, 36 (2004) 743-749.
- [25] C. Bosch Ojeda, F. Sanchez Rojas, Recent developments in derivative ultraviolet/visible absorption spectrophotometry, *Analytica Chimica Acta*, 518 (2004) 1-24.
- [26] X. Yu, G. Jiang, H. Li, Y. Zhao, H. Zhang, L. Zhao, Y. Ma, C. Coulter, H. Huang, Rifampin Stability in 7H9 Broth and Löwenstein-Jensen Medium, *Journal of Clinical Microbiology*, 49 (2011) 784-789.

[27] J.C. Sung, D.J. Padilla, L. Garcia-Contreras, J.L. VerBerkmoes, D. Durbin, C.A. Peloquin, K.J. Elbert, A.J. Hickey, D.A. Edwards, Formulation and Pharmacokinetics of Self-Assembled Rifampicin Nanoparticle Systems for Pulmonary Delivery, *Pharmaceutical Research*, 26 (2009) 1847-1855.

[28] P. O'Hara, A.J. Hickey, Respirable PLGA Microspheres Containing Rifampicin for the Treatment of Tuberculosis: Manufacture and Characterization, *Pharmaceutical Research*, 17 (2000) 955-961.

[29] R. Bro, Multivariate calibration: What is in chemometrics for the analytical chemist?, *Analytica Chimica Acta*, 500 (2003) 185-194.

[30] J.C. Berridge, Chemometrics in pharmaceutical analysis, *Analytica Chimica Acta*, 223 (1989) 149-159.

CHAPTER 4 : SYNTHESIS AND CHARACTERIZATION OF HYDRAZONES FROM DIALDEHYDE FOR PH RESPONSIVE DRUG DELIVERY SYSTEM

4.1. Introduction

As briefly discussed in Chapter 2 section 2.7.1. Tuberculosis, for successful treatment/management of TB through nanomedicine is through targeted drug delivery. Targeting of macrophages would require a sugar-based moiety (Chapter 5) and pH linkers responsive to change in intracellular pH changes. Stimuli drug delivery system offers control on the drug release profiles of drug carriers. Stimuli drug release offers various benefits such as sustained drug release thus controls frequency of drug administration and reduction of side effects profile. This aids in improving patient compliance. The physicochemical changes can be utilized to control the drug release profile. Various diseases are known to change physicochemical features of various sites in the body. Apart from disease states, the various compartments of the body to cellular level have various physicochemical features. pH, ionic strength, proteins (enzyme) and other metabolites have been utilized in stimuli responsive drug delivery. pH responsive delivery is a widely used. In oral drug delivery, the pH varies in the gastric tract from acidic stomach lumen (pH 1-3) to the alkaline duodenum and ileum (pH 6.6-7.5). In tissue targeting, human tumours are known to exhibit pH that varies from 5.7 to 7.8. At a cellular level, the acid pH changes occur rapidly after endocytosis (2–3 min) due to vacuolar proton ATPase-mediated proton influx [1]. In the endosome pH of 5.5–6.0 occurs, followed by pH 4.5-5.0 in lysosomes [2]. Figure 4.1 illustrates the degradation of pH responsive carrier system as the intracellular pH changes.

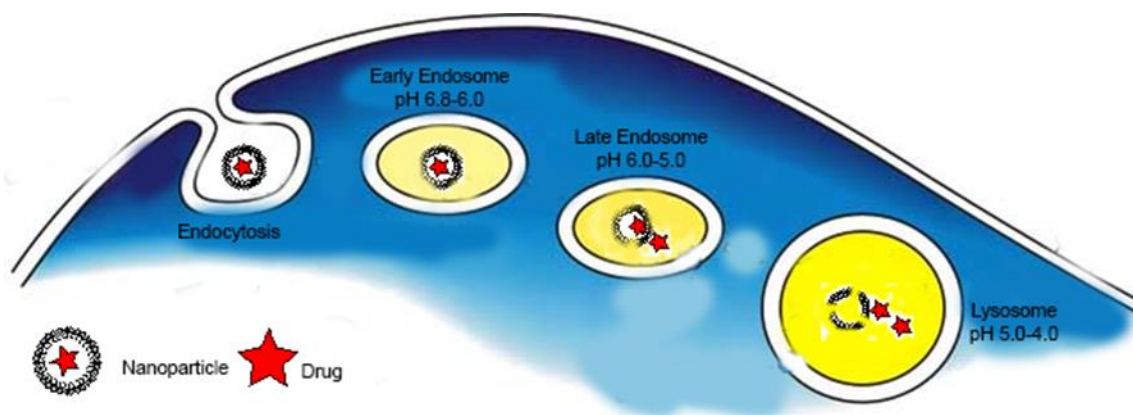


Figure 4.1: Overview of intracellular pH variations in various compartments.

The use of pH-labile cross-linkers can be utilized in controlling pH responsive drug delivery. Esters, hydrazones, cis-aconityl, oxime, acetal, silyl ether, imidazole, carbonyl dimethylmaleic anhydride, orthoester, imines, dialkyl/diaryl dialkoxysilane, β -thiopropionate, trityl, vinyl ether and polyketal and phosphoramidate have been utilized as pH responsive moieties [3, 4]. Hydrazones have been widely used pharmaceutical applications. They can be formed by means of condensation between hydrazine and ketone/aldehyde, Japp-Klingemann reaction whereby aryl diazonium salts couples with β -keto esters/acids or reaction between aryl halides and non-substituted hydrazones [5, 6]. Through these methods, the formed product precipitates from the reaction mixture. This allows easy purification steps with high yields. *In vitro* studies have shown that hydrazones are hydrolysed in the endo/lysosomal compartment at pH 5.

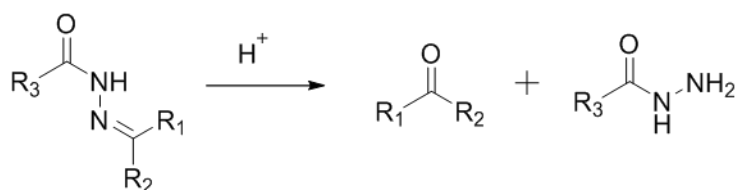


Figure 4.2: Structure of pH-labile hydrazone and hydrolysis products.

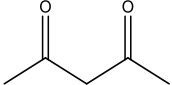
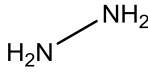
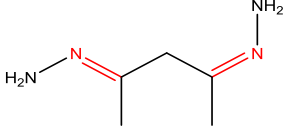
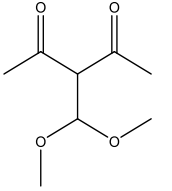
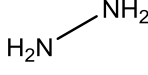
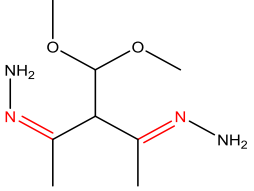
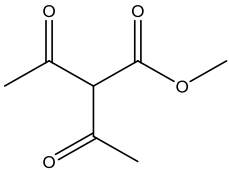
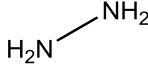
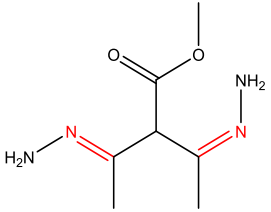
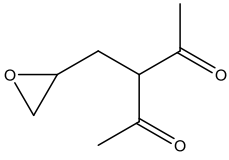
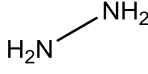
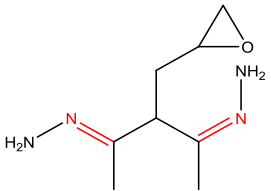
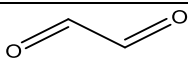
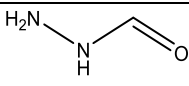
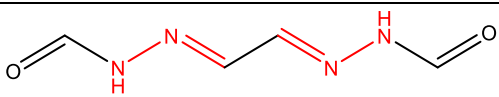
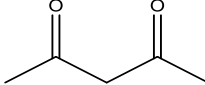
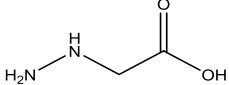
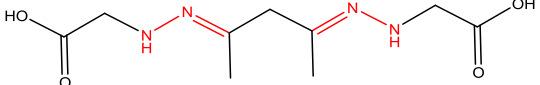
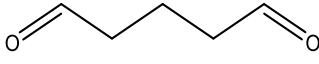
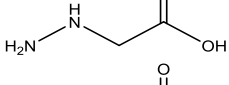
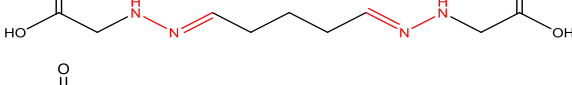
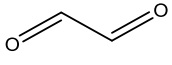
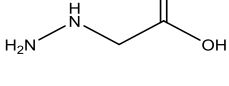
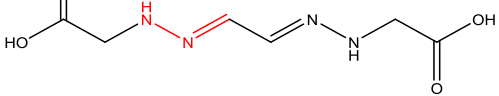
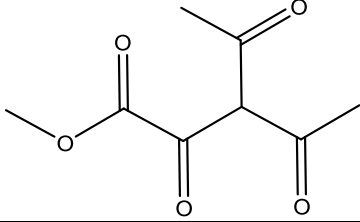
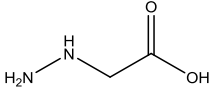
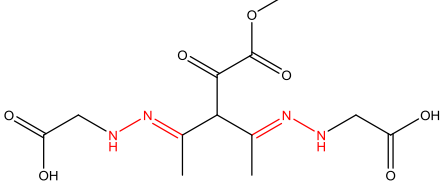
In this section, hydrazones were synthesized by condensation of respective hydrazine compound with dialdehyde/diketone. Electron donating groups are stated to be able to increase the rate of hydrolysis by facilitating protonation, where alkyl > H > phenyl. Furthermore, rate of hydrolysis through altering the pKa of the hydrazone with electron donating substituents facilitating protonation of the C=N nitrogen. The addition of electron withdrawing groups can also be used for increases the destabilizing effect. Based on this evaluation, it can be stated that aromatic aldehydes/ketones are too stable to be utilized in pH responsive linker without substituents for destabilizing effects hydrazone linker chemistry has been investigated in some detail, it is unlikely that the optimal linker has already been identified. It is expected that a thorough study of a wider range of linker structures may yet identify improved linkers that can find application as a module in a wide variety of drug-carrier conjugates.

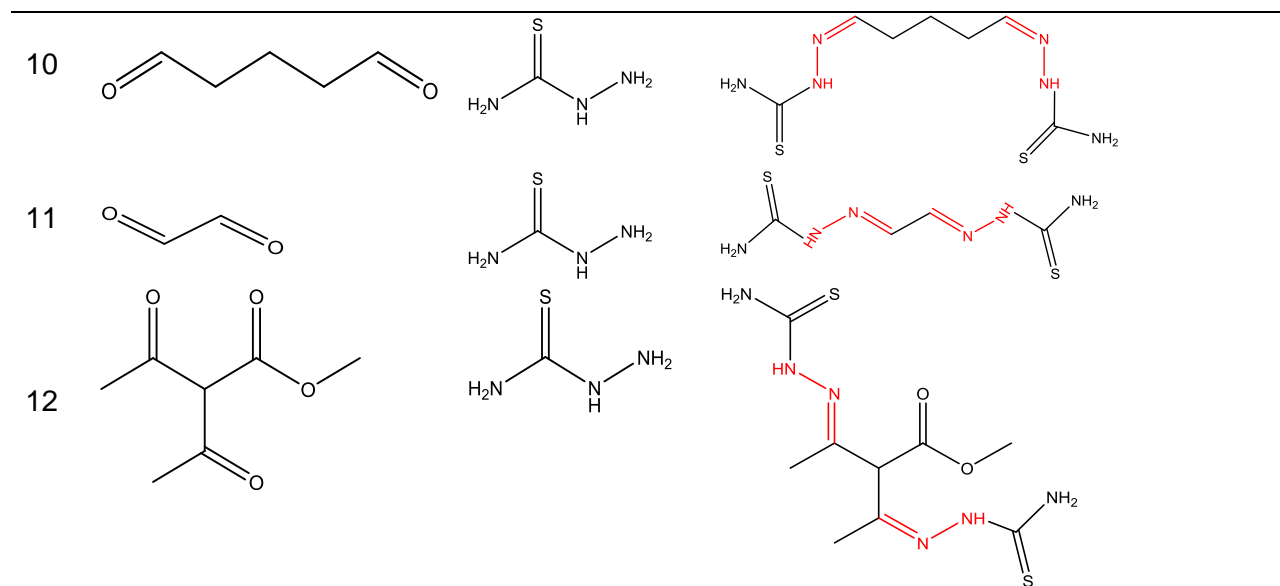
4.2. Materials and methods

4.2.1. General procedures and materials

The materials were obtained from commercial suppliers and used without further purification. Table 4.1 depicts the proposed hydrazones made from pure and modified hydrazines and aldehydes. Four groups of compounds were synthesized displaying carboxyl, aldehyde, amine and thioamide functional groups which can be used for coupling to drug delivery carriers.

Table 4.1: Illustration of aliphatic aldehydes derivatives and hydrazine derivatives used

#	Aliphatic Aldehydes	Hydrazine-Derivative	Hydrazone
1			
2			
3			
4			
5			
6			
7			
8			
9			



4.2.2. Synthesis of Hydrazone Derivatives

Aminoglycine: Following the method by Raj et al (2013), a solution of chloroacetic acid (1M) was made in 200mL ethanol. Hydrazine hydrate (1M) was then added dropwise to the solution [6]. The reaction mixture was refluxed for 3 hours with continuous stirring. Excess ethanol was evaporated on a rotary vapour. Thick oil resulted during the evaporation process. The compound was used without further purification. ^1H NMR: (300MHz, D_2O) δ 3.59, 2.39, 2.08. ^{13}C NMR (75MHz, D_2O) δ 170.93, 60.09.

Hydrazonecarboxaldehydyde: Following a method by Boland et al. (2006), ethyl formate (76.5mL, 1 equiv) was mixed carefully with hydrazine monohydrate (49mL, 1.2 equiv) in MeOH (200mL). The reaction mixture was then refluxed for 1 hour. The solvent was then removed using a rotavapor to give pale-yellow oil, which crystallized on standing. The white crystals were washed with PE and dried under high vacuum at 40°C. (78%). ^1H NMR (300MHz, D_2O) δ 7.86, 7.72, 4.79, 4.79. ^{13}C NMR (75MHz, D_2O) δ 162.18.

4.2.3. Synthesis of Aliphatic Aldehyde Derivatives

Acetylacetone Derivatives: Acetylacetone (4.5mL, 1 equiv) and K_2CO_3 (8.45g, 1.3 equiv) were mixed in MeCN (55mL). NaI (7.05g, 1 equiv) was then added, followed by addition of methyl chloroformate, (1.1 equiv). The mixture was refluxed for at 80°C for 2 hours. The colour changed from yellow to white after 1 hour. After the duration of the reaction time, the reaction was cooled

to room temperature. It was then washed with EtOAc (2 x 20mL), water (2 x 20mL), 1:1 water: brine (2 x 20mL) and brine (2 x 20mL) and dried over $MgSO_4$ overnight. It was then concentrated under reduced pressure forming orange-yellow solution.

4.2.4. Hydrazine Hydrazones (compound 1-4)

Briefly, a solution of hydrazine (0.01mol) in 50mL EtOH (5% acetic acid) was heated to 50°C. Respective di-aldehyde (0.005mol) was added dropwise. The mixture was then stirred to reflux until reactants have been used through monitoring with aluminium TLC. The reaction mixture was then cooled down in an ice bath. The precipitate was filter on HPLC filter paper, washed with 10mL water and 20mL EtOH. The compound was dried at 50°C overnight.

4.2.5. Formohydrazide Hydrazone (compound 5)

Briefly, a solution of formohydrazide hydrazine (0.01mol) in 50mL EtOH (5% acetic acid) was heated to 50°C. Glyoxal (0.005mol) was added dropwise. The mixture was then stirred to reflux until reactants have been used through monitoring with aluminium TLC. The reaction mixture was then cooled down in an ice bath. The precipitate was filter on HPLC filter paper, washed with 10mL water and 20mL EtOH. The compound was dried at 50°C overnight.

4.2.6. Thiosemicarbazide Hydrazones (compound 10-12)

Briefly, a solution of thiosemicarbazide (0.01mol) in 50mL EtOH (5% acetic acid) was heated to 50°C. Respective di-aldehyde (0.005mol) was added dropwise. The mixture was then stirred to reflux until reactants have been used through monitoring with aluminium TLC. The reaction mixture was then cooled down in an ice bath. The precipitate was filter on HPLC filter paper, washed with 10mL water and 20mL EtOH. The compound was dried at 50°C overnight.

4.2.7. Aminoglycine Hydrazones (compound 6-9)

Briefly, a solution of aminoglycine (0.01mol) in 50mL EtOH (5% acetic acid) was heated to 50°C. Respective di-aldehyde (0.005mol) was added dropwise. The mixture was then stirred to reflux until reactants have been used through monitoring with aluminium TLC. The reaction mixture was then cooled down in an ice bath. The precipitate was filter on HPLC filter paper, washed with 10mL water and 20mL EtOH. Some of the compounds were recrystallized in acetone. The compounds were then dried at 50°C overnight.

4.2.8. Hydrolysis Kinetics at acidic and neutral pH

Deuterated sodium acetate buffer was prepared by dissolving anhydrous sodium acetate (NaOAc) in D₂O to a concentration of 0.15M. Acidity was adjusted by adding acetic acid-d₄ to pDs 4.5. Hydrolysis was conducted following Kalia and Raines (2008) method with modification [7]. An excess of a deuterated aldehyde or ketone can be used to trap the liberated nitrogen base and thereby pushing the hydrolysis reaction to completion. However, in this study they deuterated aldehyde/ketone was unavailable for this study. The use of deuterated acetone did not push the hydrolysis reaction to completion. This was also reported by Kalia and Raines (2008), who indicated that deuterated formaldehyde is the ideal aldehyde. Thus, interference from the reverse (condensation) reaction due to limitation of allowing the forward (hydrolysis) reaction to be monitored was observed in some formulations. The hydrolysis was conducted by running proton NMR of each respective hydrazone in prepared buffer. For DMSO-d₆ soluble compounds, 0.2mL of the buffer was added into the dissolved samples in NMR tube, followed by vortexing the mixture to obtain homogeneity. For each test, 10 data points were collected within a 5-minute interval. The proton peak representing the N-H of the hydrazone was then integrated for reaction monitoring on Mestnerova v11.0 software (MestreLab Research, Minnesota, USA). Baseline and phase corrections were conducted on stacked spectra prior analysis. This was followed by reference peak labelling. The rate of hydrolysis/decay (k) was then determined.

$$Y = Y_0(1 - e^{-kt}) \quad (4.1)$$

Where Y is the final integral intensity at the time (t), k is the first-order rate constant, and Y_0 is initial integral intensity. The mono-exponential fit (First order kinetics, Exponential Decay) was extrapolated and fitted on OriginPro 2017 software for comparison of the obtained data curves (OriginLab Corporation, Massachusetts, USA). The outliers were removed from the curve. Half-life were calculated using equation 4.2.

$$t_{1/2} = 0.693/k \quad (4.2)$$

4.3. Results and discussion

Analytical data and physical properties of the synthesized Schiff bases are illustrated in table 4.2. A Gallenkamp melting point apparatus was used for determination of the melting points. It was observed that hydrazones made from glyoxal did not melt but underwent charring (decomposition process). This indicates these compounds are decomposing with charring. Aminoglycine also

showed charring characteristics. During charring, the oxygen and hydrogen are removed thus leaving the carbon.

Table 4.2: Analytical data and physical properties of synthesized compounds

Compound Number & Molecular Formula	Yield (%)	Melting Point (°C)	Colour
1: C ₅ H ₁₂ N ₄	96	115-119	Lemon Chiffon
2: C ₈ H ₁₈ N ₄ O ₂	26	99-111	Khaki 1
3: C ₇ H ₁₄ N ₄ O ₂	29	128-130	Light Goldenrod
4: C ₈ N ₁₆ N ₄ O	16	96-99	Light Goldenrod
5: C ₄ H ₆ N ₄ O ₂	93	238-240	Khaki 2
6: C ₉ H ₁₆ N ₄ O ₄	46	180-183	Yellow
7: C ₉ H ₁₆ N ₄ O ₄	88	196-198	White
8: C ₆ H ₁₀ N ₄ O ₄	57	218-220	Orange 3
9: C ₁₂ H ₁₈ N ₄ O ₇	84	176-180	Ivory
10: C ₇ H ₁₄ N ₆ S ₂	89	152-158	Yellow
11: C ₄ H ₄ N ₆ S ₂	95	218-223	Yellow
12: C ₉ H ₁₆ N ₆ O ₂ S ₂	49	196-200	Yellow

4.3.1. Structural chemistry analysis using infrared spectrometry

The hydrazone compounds are known to show a $\nu(\text{C}=\text{N})$ stretching frequency in the region of $1645\text{-}1557\text{cm}^{-1}$, whereby the position varies with the molecular structure[8]. For thiosemicarbazone, the stretch is expected to occur in region of $1655\text{-}1642\text{cm}^{-1}$, whilst carbonyl/phenyl groups have a stretch in the range of $1630\text{-}1610\text{cm}^{-1}$. The absence of the bands characteristic of $\nu(\text{C}=\text{O})$ aids in confirming the formation of the Schiff base. The spectra in figure 4.3 also show the $\text{CH}=\text{N}$ groups stretching vibrations appearance between 3000 and 2800cm^{-1} region. Furthermore, the $\text{C}-\text{N}$ stretching vibration of aliphatic amines can be observed in the region $1250\text{-}1020\text{cm}^{-1}$. Based on the evaluation of the hydrazine hydrazones, C01-C04, between $3400\text{-}3300$ and $3330\text{-}3250\text{cm}^{-1}$, the primary amine stretch can be observed. This is further supported by the $1650\text{-}1580\text{cm}^{-1}$ region due to the $\text{N}-\text{H}$ bending vibration of primary amines. The $\text{N}-\text{H}$ wag can also be seen from $910\text{-}665\text{cm}^{-1}$. These amine features were also observable in thiosemicarbazide hydrazones, although not as evident as those of the pure hydrazine. For the aminoglycine hydrazones, the $3000\text{-}2500\text{cm}^{-1}$ (broad, ν) representing the $\text{O}-\text{H}$ Stretch was conserved within this group. The $1780\text{-}1710\text{cm}^{-1}$ (s) region represented the $\text{C}=\text{O}$ stretch and $1440\text{-}1395\text{cm}^{-1}$ the OH stretch of the carboxylic acid. For the formohydrazone the strong $\text{C}=\text{O}$ stretch from the aldehyde can be seen $1740\text{-}1690\text{cm}^{-1}$ (s) region.

Due to some of the hydrazone designed to consisting of latent acids, the acetal group can be identified by the C-H stretching vibration bands within the 2830-2990 cm^{-1} , O-CH-O within the 1360-1396 cm^{-1} , O-CH₂-O between 1398-1400 cm^{-1} and O-CH₂-C within the 1383-1390 cm^{-1} [9]. C02 consists of dimethyl acetal group which is depicted by 1376 cm^{-1} . C03, C09 and C12 consist of esterified carboxylic acid. Other new peaks observed in C02 & C03 not present in C1 are 1217 and 1738 cm^{-1} . The 1738 indicates the presence of the aldehyde (C=O) stretch 1740-1720 cm^{-1} , whereas the 1217 cm^{-1} indicates the possibility of C-C, C-O and C=O stretching within the 212-1217 cm^{-1} range [10]. This shows that the latent acid did not react with the hydrazine during hydrazone synthesis. The thiosemicarbazide hydrazones all retained the 1288 cm^{-1} and 823 cm^{-1} which was due to the ν (C=S) and δ (C=S), thus retaining the thione form [11].

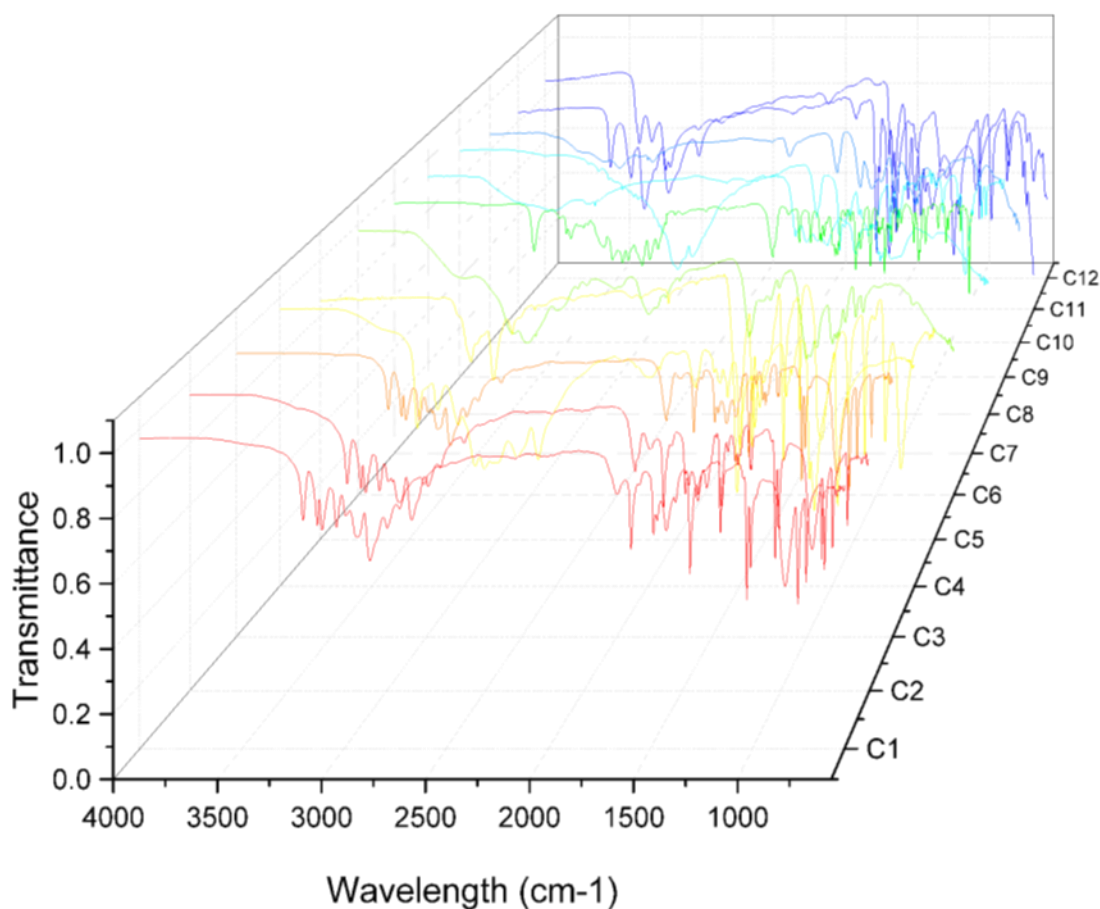


Figure 4.3: FTIR spectra of synthesized hydrazones.

4.3.2. Ultraviolet analysis of $\pi \rightarrow \pi^*$ transitions

The use of UV-visible spectroscopy allows the capability of studying tautomeric equilibrium in Schiff bases. UV analysis was conducted to confirm the presence of bands at the 300-350nm

range involve which are stated to involve the $\pi \rightarrow \pi^*$ transitions of the C=N group [12]. However, the band around 286nm was observed among all the compounds which is stated to be attributed to azomethine C=N bond (Figure 4.4). The bands within the observed region are distinctive to hydrazone synthesized from aliphatic aldehydes [13]. The synthesized hydrazone also show a shift due to $n \rightarrow \pi^*$ transitions and which can be caused by the formation of an intramolecular hydrogen bond. The electron donating groups donate a pair of electron to N-H proton. This therefore leads to decreased n orbital energy level and increased transition energy which resulted in the absorbed photon energy of shorter wavelength.

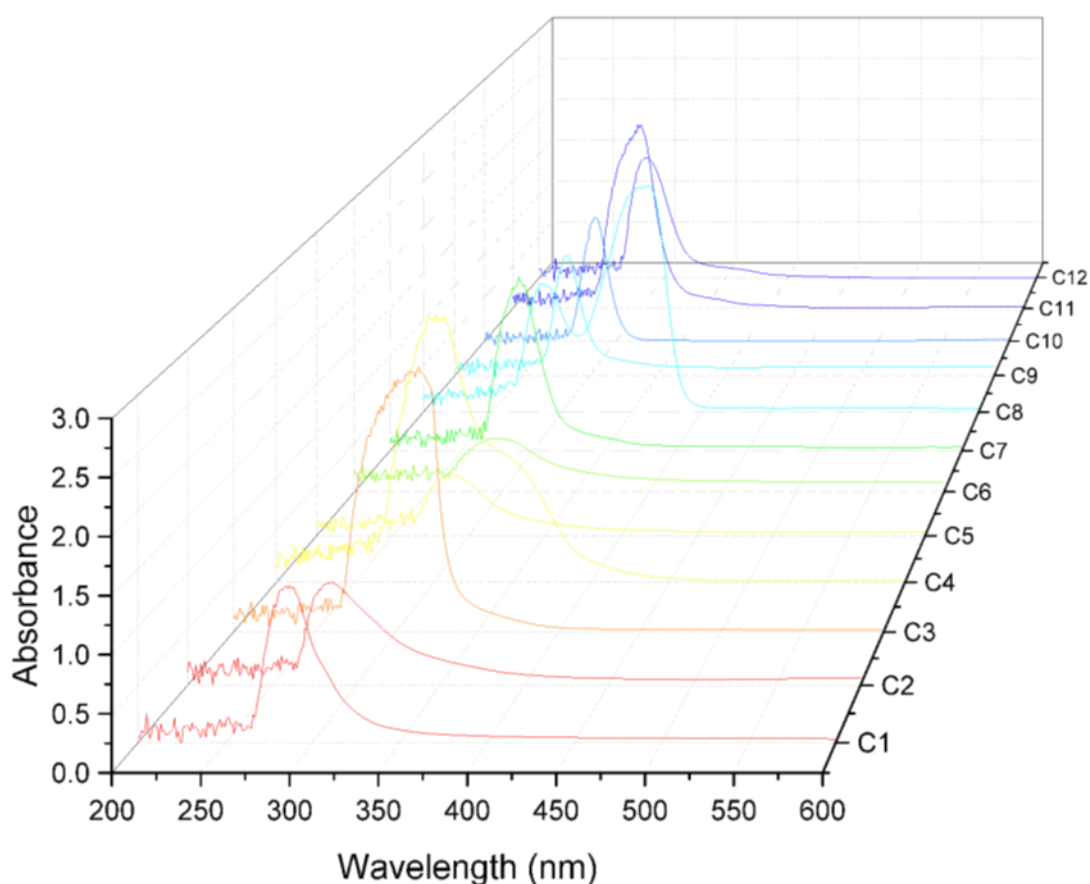


Figure 4.4: UV-Vis analysis of the hydrazones C1-C12 depicts compound 1-12, respectively.

4.3.3. Characterization of hydrazone molecular structure

The formation of hydrazone through the interaction of hydrazide and aldehyde shifts the aldehydic proton ($-\text{CHO}$) from 9.35-9.84 to 8-8.61ppm. In respect to carbon shifting, the aldehydic carbon ($-\text{CHO}$ to $-\text{N}=\text{CH}-$) changes from 191 to 144.14-148.58ppm Based on the review by Kitaev et

al., (1970) the variations in the molecular structures of the hydrazones, is stated to be due to the possibilities of intermolecular hydrogen bonding in the presence of C=N and N-H groups in monosubstituted and unsubstituted hydrazone [13]. This means that the stability of the resulting complexes will depend both on the structure of the hydrazone and on the nature of the solvent (formation of dimers). The formation of dimeric together with linear association complexes has been observed in solutions of semicarbazones, monoarylhydrazone, thiosemicarbazones, alkylhydrazones, and arylhydrazones of keto-acid. Furthermore, it has been shown that a hydrogen bond can be formed in hydrazones also when a hydroxy-group is present and appropriately located in the carbonyl or hydrazine portion. The synthesized hydrazones also variations based on UV, FTIR and NMR analysis. Some of the hydrazones did not indicate the proton shift from 9.35-9.84 to 8-8.61ppm.

4.3.4. Hydrazine monohydrate based hydrazones

Hydrazine monohydrate hydrazones were evaluated using DMSO-d₆ as a solvent. The product precipitated from the solution and attempts to further purify the compound via recrystallization continued to reduce the initial yields (figure 4.5). The samples were then evaluated as they were. They all showed an upfield presence of amine at 12.03. Compound 2 which was conjugated with acetal groups showed peak at 3.37 and 5.44ppm. The carboxylic acid ester of compound 3 was not seen. However, FTIR showed its presence. 1: ¹H NMR (300MHz, DMSO) δ 12.05, 5.73, 3.45, 2.50, 2.33, 2.12, 1.75. 2: ¹H NMR (300MHz, DMSO) δ 12.03, 5.73, 5.44, 3.37, 2.49, 2.32, 2.11, 1.90. 3: ¹H NMR (300MHz, DMSO) δ 12.03, 8.61, 7.68, 5.73, 5.45, 3.40, 2.50, 2.33, 2.12, 1.90. and 4: ¹H NMR (300MHz, DMSO) δ 8.34, 7.80, 3.48, 2.50, 2.11, 2.08.

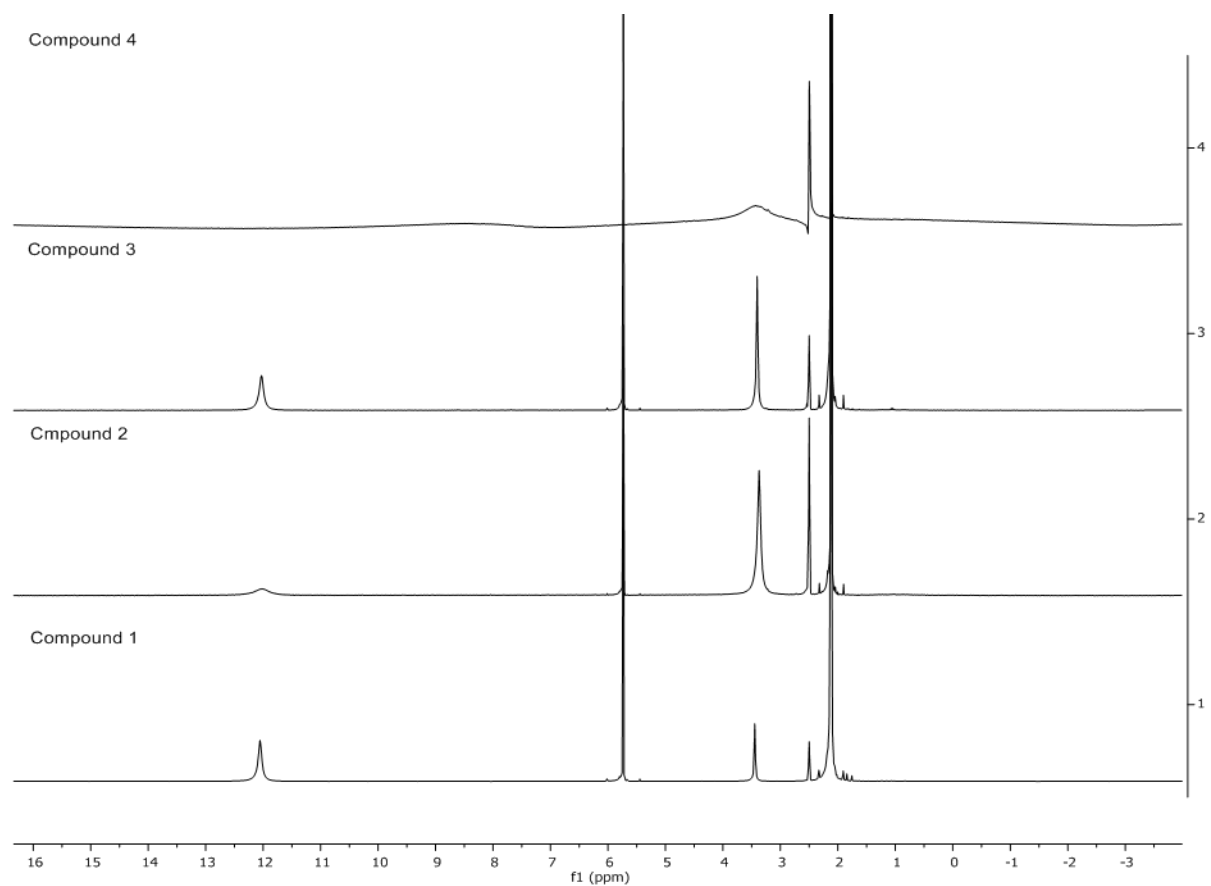


Figure 4.5: *Hydrazones synthesized from hydrazine monohydrate.*

4.3.5. Formylhydrazine

The presence of the hydrazone was more evident in compound 5 which had one of the highest yields (figure 4.6). Purification method did not rapidly decrease the quantity of the product. The upfield amine is also present in this compound at position 11.91ppm. ¹H NMR (300MHz, DMSO) δ 11.91, 11.67, 8.69, 8.60, 8.11, 7.86, 7.83, 7.73, 7.67, 3.36, 2.50, 2.50.

Compound 5

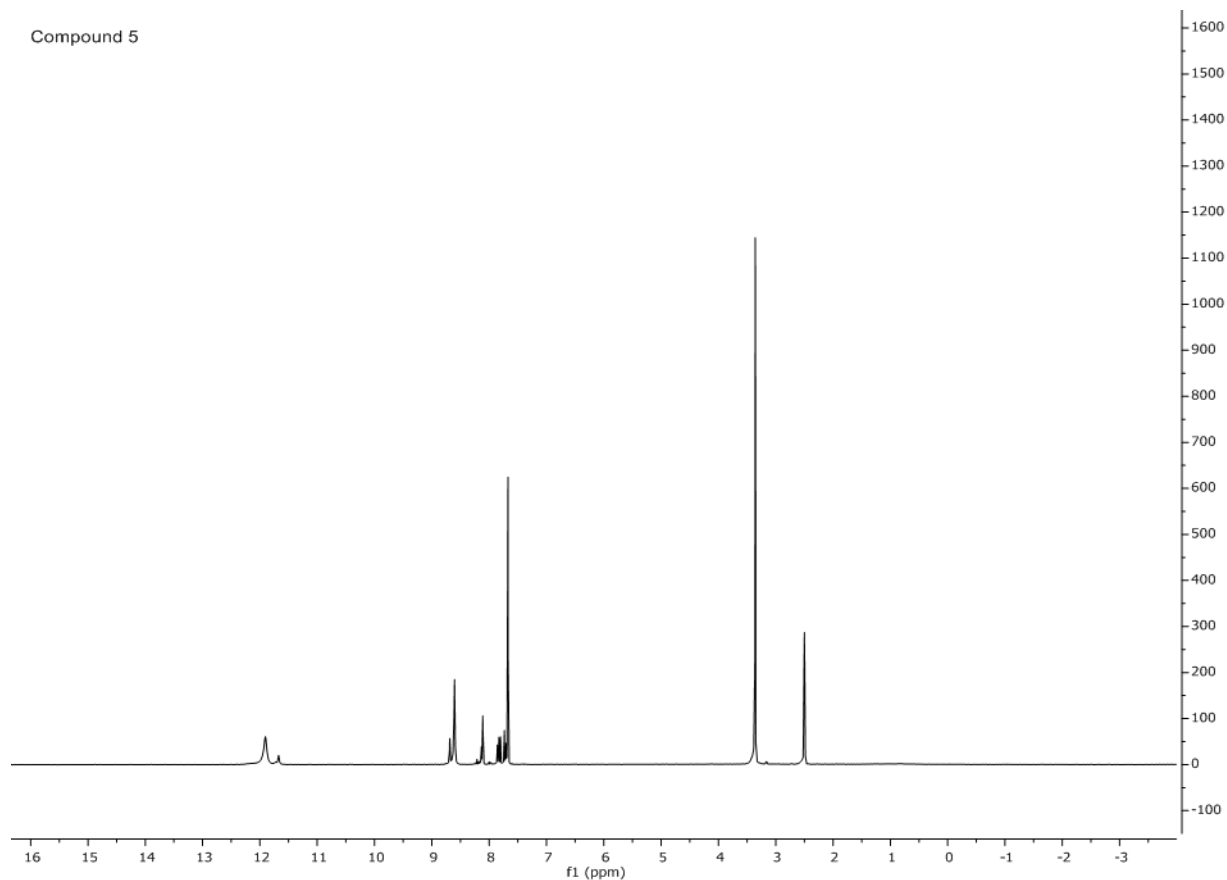


Figure 4.6: *Formylhydrazine hydrazone.*

4.3.6. Aminoglycine

Amino glycine compounds were hard to purify due to loss in quantity for further analysis (figure 4.7). Formulation 6 and 8 evidently showed the presence of the hydrazone proton with the expected range. 6: ^1H NMR (300MHz, DMSO) δ 7.25, 7.08, 6.90, 6.21, 4.79, 4.79, 4.14, 3.03, 2.27, 2.10, 1.96, 1.45. 7: ^1H NMR (300MHz, D_2O) δ 4.79, 4.79, 3.75, 3.59, 2.16, 1.96, 1.64. 8: ^1H NMR (300 MHz, D_2O) δ 8.95, 4.79, 4.79, 3.15, 2.71, 0.57. 9: ^1H NMR (300MHz, DMSO) δ 6.52, 4.79, 4.79, 3.94, 2.80, 2.54, 2.48, 2.15, 0.18.

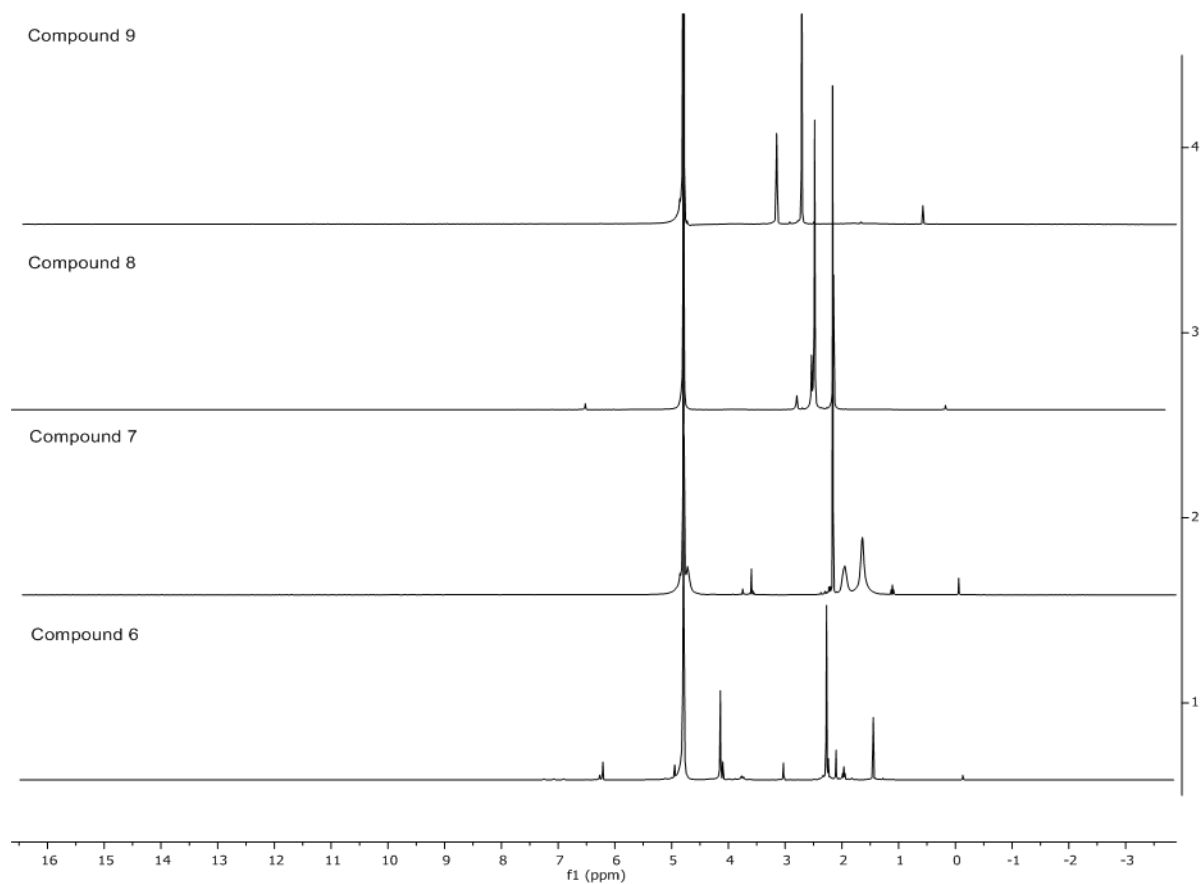


Figure 4.7: *Aminoglycine hydrazones.*

4.3.7. Thiosemicarbazide hydrazones

Hydrazones synthesized from thiosemicarbazide precipitated from the reaction mixture. After washing with ethanol and drying, they were then analysed using DMSO-d₆ (figure 4.8). 10: ¹H NMR (300MHz, DMSO) δ 11.08, 7.99, 7.50, 7.40, 7.39, 3.37, 2.50, 2.50, 2.19, 1.67, 1.02. 11: ¹H NMR (300MHz, DMSO) δ 11.69, 8.33, 7.90, 7.71, 3.35, 2.50, 2.50. and 12: ¹H NMR (300MHz, DMSO) δ 9.38, 8.08, 7.22, 3.42, 2.50, 2.50, 2.19, 1.89, 1.81, 1.05. The data shows high field displacement of the N-H proton due to the formation of the intramolecular hydrogen bond [14].

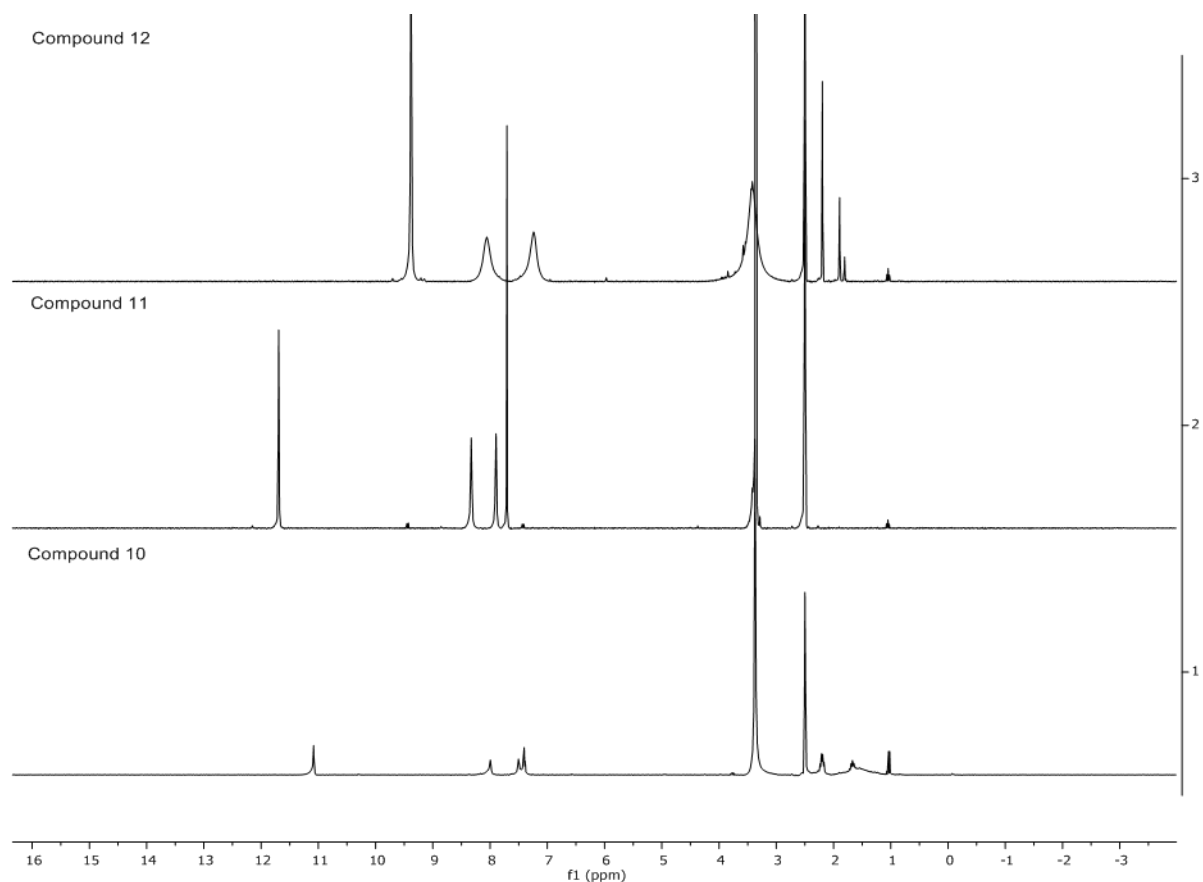


Figure 4.8: Proton NMR spectra of synthesized thiosemicarbazide hydrazones.

4.3.8. Hydrolysis kinetics

Exponential decay was evaluated for near neutral and acidic pH (figure 4.9). It can be observed on the data that C3 formulation showed better decay pattern than other hydrazone derivative. This supports the hypothesis about using latent acids in order to improve hydrolytic rate. Patel and colleagues evaluated the use of latent acids (lactones, anhydrides, lactams and esters) to generate a microenvironment for improving hydrolysis [15]. It was hypothesized that the latent acid member would hydrolyze into an organic acid in an aqueous environment thus leading to improved drug release. Figure 4.9 shows the decay of hydrazones in near neutral and acidic pH. Based on the evaluation C6 shows a slow response to hydrolysis. The reduced hydrolysis could be due to the presence of the carboxylic acid [15]. These could therefore be more prone to protonation than the azomethine region. The carboxylic group is not near the azomethine group to have promoted hydrolysis. Full proton transfer is also stated not possible to occur when organic acids (acetic acid) with like pKa of amino acids is used [15].

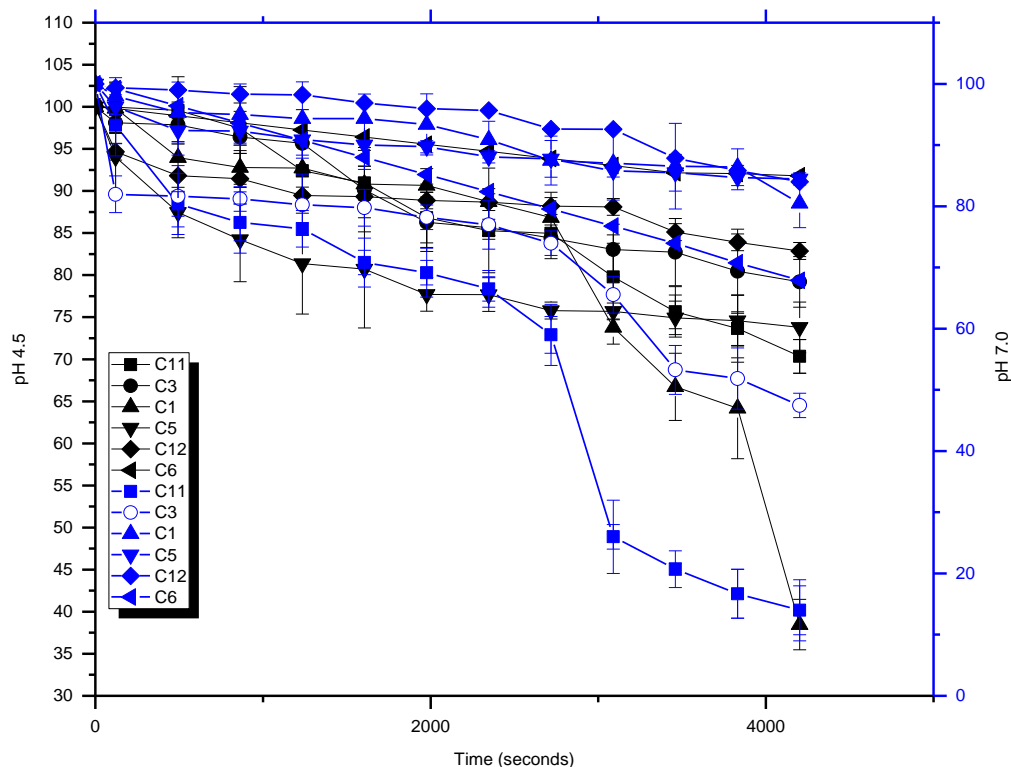


Figure 4.9: *Hydrolysis kinetics at neutral pH 7.4 and acid pH 4.5.*

The decay rate was evaluated to assess the variation between difference hydrazones (table 4.3). C1 showed the best results and had the most yield. However, this also showed that degradation also occur in near neutral pH. The introduction of the latent acid seems to have had an impact in the stabilization of the hydrazone in near neutral pH. The presence of the esterified carboxylic acid indicated to have slowed down the decay. During hydrolysis, water forms a tetrahedral intermediate with the carboxylic acid ester, which is a slow reaction [16]. This therefore can lead to slowing of the hydrolysis of the hydrazone bond due to the presence of the latent acid group. Upon decrease in pH to acidic conditions, the hydrolysis of the carboxylic acid is more rapid. This further leads to the hydrazone region becoming more acidic thus favoring rapid decay. The glyoxal based hydrazones C5 and C11 also showed good hydrolytic features. The intramolecular H-bonding with other reactive groups can have an impact on the rate of hydrolysis [5]. Future studies require the evaluation of the hydrolytic mechanism and intermediates formed during protonation.

Table 4.3: Predicted decay rate of the evaluated hydrazones in respective pH

Compound	pH 7.4		pH 4.5	
	k	$t_{1/2}$ (s)	k	$t_{1/2}$ (s)
C1	2.35e ⁻⁰⁵	43.76	9.34e ⁻⁰⁵	11.01
C3	0.00011	6300	7.03e ⁻⁰⁵	14.73
C5	1.59e ⁻⁰⁵	64.68	2.69e-05	38.23
C6	0.00014	4950	0.00020	3465
C11	0.00014	4950	2.39e ⁻⁰⁵	43.03

4.4. Concluding remarks

Various hydrazones were successfully synthesized. It was observed that addition of the latent acid does lead to improvement in rate of degradation. However, aminoglycine base hydrazone showed to have the lease rate of hydrolysis and low yields. Purity was also of poor quality in some formulations. This shows that purification of the initial synthesized hydrazine derivative is essential in improving yields. It is recommended that the synthesized hydrazone to undergo bioassay and screening for anti-bacterial activity. They can also be utilized in range of other applications such as herbicides, insecticides, nematocides, rodenticides, indicators, spot test reagents and plant-growth regulators [17]. Furthermore, Raman spectrometry is recommended for further analysis in combination to NMR data analysis. For further use in this study, formulation C1 was used in [Chapter 7](#) for crosslinking to gelatin and [Chapter 8](#) for optimized MSNs. This formulation had the highest yield for use in large formulation studies. However, future studies will require new synthetic strategies for improving yields of C3 and C11 as they show good half-life variations in acidic and near physiological pH.

4.5. Reference

- [1] W. Gao, J.M. Chan, O.C. Farokhzad, pH-Responsive Nanoparticles for Drug Delivery, *Molecular Pharmaceutics*, 7 (2010) 1913-1920.
- [2] E.R. Gillies, A.P. Goodwin, J.M.J. Fréchet, Acetals as pH-Sensitive Linkages for Drug Delivery, *Bioconjugate Chemistry*, 15 (2004) 1254-1263.
- [3] R. Tong, L. Tang, L. Ma, C. Tu, R. Baumgartner, J. Cheng, Smart chemistry in polymeric nanomedicine, *Chemical Society Reviews*, 43 (2014) 6982-7012.
- [4] G. Leriche, L. Chisholm, A. Wagner, Cleavable linkers in chemical biology, *Bioorg Med Chem*, 20 (2012) 571-582.
- [5] X. Su, I. Aprahamian, Hydrazone-based switches, metallo-assemblies and sensors, *Chemical Society Reviews*, 43 (2014) 1963-1981.

- [6] R.R. Phillips, The Japp-Klingemann Reaction, Organic Reactions, John Wiley & Sons, Inc.2004.
- [7] J. Kalia, R.T. Raines, Hydrolytic Stability of Hydrazones and Oximes, *Angewandte Chemie International Edition*, 47 (2008) 7523-7526.
- [8] R.M. Issa, A.M. Khedr, H. Rizk, ¹H NMR, IR and UV/VIS Spectroscopic Studies of Some Schiff Bases Derived from 2-Aminobenzothiazole and 2-Amino-3-Hydroxypyridine, *Journal of the Chinese Chemical Society*, 55 (2008) 875-884.
- [9] B. Wladislaw, A. Giora, G. Vicentini, The syntheses and infrared spectra of some acetals and ketals, *Journal of the Chemical Society B: Physical Organic*, (1966) 586-588.
- [10] E. Aracri, C. Diaz Blanco, T. Tzanov, An enzymatic approach to develop a lignin-based adhesive for wool floor coverings, *Green Chemistry*, 16 (2014) 2597-2603.
- [11] P. Bindu, M.R.P. Kurup, E.s.r. and electrochemical studies of four- and five-coordinate copper(II) complexes containing mixed ligands, *Transition Metal Chemistry*, 22 (1997) 578-582.
- [12] A. Çınarlı, D. Gürbüz, A. Tavman, A. Seher Birteksöz, Synthesis, spectra characterization and antimicrobial activity of some Schiff bases of 4-chloro-2-aminophenol, 2011.
- [13] P.K. Yu, I.B. Boris, T.V. Troepol'skaya, The Structure of Hydrazones, *Russian Chemical Reviews*, 39 (1970) 441.
- [14] E.L. Romero, R.F. D Vries, F. Zuluaga, M.N. Chaur, Multiple Dynamics of Hydrazone Based Compounds, *Journal of the Brazilian Chemical Society*, 26 (2015) 1265-1273.
- [15] P.J. Patel, R. Acharya, S.C. Dave, INCORPORATION OF LATENT ACID SOLUBILIZING AGENTS IN COATED PELLET FORMULATIONS TO OBTAIN pH INDEPENDENT RELEASE, Google Patents, 1999.
- [16] S. Rayne, K. Forest, Carboxylic acid ester hydrolysis rate constants for food and beverage aroma compounds, *Flavour and Fragrance Journal*, 31 (2016) 385-394.
- [17] R.B. Singh, P. Jain, R.P. Singh, Hydrazones as analytical reagents: a review, *Talanta*, 29 (1982) 77-84.

CHAPTER 5 : SYNTHESIS AND CHARACTERIZATION OF GLUCOSE BASED POLYMER FOR POSSIBLE USE AS HYGROSCOPIC LAYER AND MACROPHAGE RECRUITING SURFACE COAT

5.1. Introduction

As illustrated in [Chapter 2](#), for successful deposition of nanoparticles without the need of breath-holding maneuver, a hygroscopic growth can be utilized to promote a shift from Brownian deposition to gravitational sedimentation mechanism. Pulmonary drug delivery has been used for delivery of therapeutics for treatment and management of various respiratory diseases and hallucinogenics. Particles aerodynamic diameter (mass median aerodynamic diameter, MMAD) plays a major role in the region of deposition of the aerosols. The aerodynamic diameter, d_A , is defined as the diameter of a sphere of unit density, which reaches the same velocity in the air stream as a non-spherical particle of arbitrary density [1]. This diameter defines the mechanism of particle deposition in the respiratory system. Large particles ($>5\mu\text{m}$) have been shown to also be effective in aerosol deposition into the deep lung through change in particle density ($<0.4\text{ g/cm}^3$) by means of large pore structure [2]. This was designed based on the view that highly porous particles aggregate less and deaggregate more during dispersion (shear forces) than small particles [3]. The particles of aerosolized drugs can be hygroscopic to a greater or lesser extent.

Hygroscopicity of particles can change the aerodynamic diameter of the particles during inhalation, thus lead to change in deposition pattern in the respiratory tract [4]. Sugars are one of the well-known natural polymers that are hygroscopic. However, a major problem with the sugar alcohols used in pulmonary delivery study especially with the more hygroscopic substances sorbitol, maltitol and xylitol, was that they seem to be highly sensitive to humidity [5]. Sugars like mannitol can be used in pulmonary drug delivery for prevention of drug-to-carrier adhesion, hygroscopic growth and recognition by cell receptors. Macrophages contain a mannose receptor which can be a target for polysaccharides surface modified nano-carriers. Macrophages recognize, in addition to mannose and L-fucose, molecules and particles bearing galactose, glucose, and N-acetylneuraminic acid residue [6].

Table 5.1: Strategies to enhance or avoid particle uptake by alveolar macrophages (Adapted from [7]).

Particle characteristics to enhance uptake	Particle characteristics to avoid uptake
Particles of 100-200nm and 1-6 μ m size. Spherical particles. High positive or negative surface charge. Hard and non-porous particles. Insoluble and hydrophobic particles. Particles' surface modified with mannose.	Particle size of <1 μ m and >6 μ m. Elongated, rod and filament shape particles. Particles with relatively neutral surface charge. Soft and porous particles. Soluble and hydrophilic particles. Particles' surface modified with PEG, poloxamers and poloxamines.

There are various aerosol generation systems for pulmonary drug delivery; nebulizer, metered dose inhaler and dry powder inhaler. Dry powder inhalers have many advantages such as (i) they are propellant-free, portable, (ii) easy to operate (less inhalation maneuvers), (iii) low-cost devices and have (iv) improved stability of the formulation as they are stored and used in dry state [8]. However, DPI also has challenges like any inhalation delivery system when it comes to generation of particles with an adequate range of particle sizes. In terms of pulmonary drug delivery, it is stated that "pulmonary drug administration will only result in an effective and safe therapy when the inhaler is able to reproducibly deliver a high fine particle dose to the site of action (receptor, infection, absorption site) in the respiratory tract" [9]. Furthermore, for an effective therapy, correct inhaler techniques and adherence to the therapy is vital.

The correct use is mainly due to the demand for various maneuvers to assist in particle deposition in the lungs. The lack of adherence is linked to improper use of the device as therapeutic effect is not established or is minimal due to low doses reaching the site of action. In this section, hygroscopic polymers are designed for both. Thus, nanoparticles are known to have a uniform size distribution than large particles. Recent developments have shown the marketing of a multi-dose DPI delivering extra fine particles with MMAD < 1.5 μ m [10]. This means that ultrafine particles enable a better targeting of the central and small airways compared to conventional DPIs. Due to small particles (d_a < 1 μ m) being driven by diffusion, most of the particles can remain suspended and are exhaled. However, it has been shown that nanoparticles can be used for delivery of Insulin (255-400nm) and anti-tuberculosis drugs (186-400nm) to the lungs [11].

5.2. Materials and methods

5.2.1. Materials

All chemicals and solvents were purchased from Sigma-Aldrich. Millipore water was also used.

5.2.2. Synthesis of dibromopropane

To a 1-liter round-bottomed flask, fitted with a reflux condenser, 33.8mL of 48% hydrobromic acid are placed. 8.2mL of concentrated sulfuric acid are added in portions, with shaking. 10mL of propane-1, 3-diol slowly added dropwise, followed by 13mL (or 240g) of concentrated sulfuric acid. The reaction mixture is refluxed for 3 hours and when the reaction is complete 1, 3-dibromopropane is distilled (162-165°C). The crude 1,3-dibromopropane was washed with an equal volume of concentrated hydrochloric acid, then with water, a little 5% sodium bicarbonate solution, and finally with water. The 1, 3-dibromopropane is dried with anhydrous calcium chloride and purified by distillation. The fraction passing over 162-165°C was collected in a receiver cooled in ice (46%).

5.2.3. Synthesis of dibromobutane

A mixture of 170mL of 48% hydrobromic acid and 41mL of concentrated sulfuric acid were added to a 500mL flask. 20.5mL freshly distilled tetrahydrofuran are dropwise added. The flask is fitted with reflux condenser and the mixture is gently heated for 3 hours, forming two layers. The lower layer of 1,4-dibromobutane is separated and purified by distillation. The fraction passing over 83-84°C was collected (58%).

5.2.4. Synthesis of coat

5.2.4.1. Hydroxyl protection

The synthesis of the hygroscopic polymer was conducted following the modified method (Figure 5.1). Briefly, to a suspension of D-(+)-glucose (10g,) in 2,2 dimethoxypropene (30.5mL) was added p-TsOH monohydrate (277mg). The mixture was heated at 50°C under stirring for 1 hour to completely dissolve under inert atmosphere. This was then heated to 60°C for 4 hours at which a slightly yellowish solution formed. The solution was then cooled to room temperature and neutralized using a few drops of saturated K_2CO_3 solution. The neutralized solution was stirred a further during of 20 minutes. The solvent was then evaporated off on a rotary vapor leaving thick yellowish gel. This was then used immediately without further purification (89%).

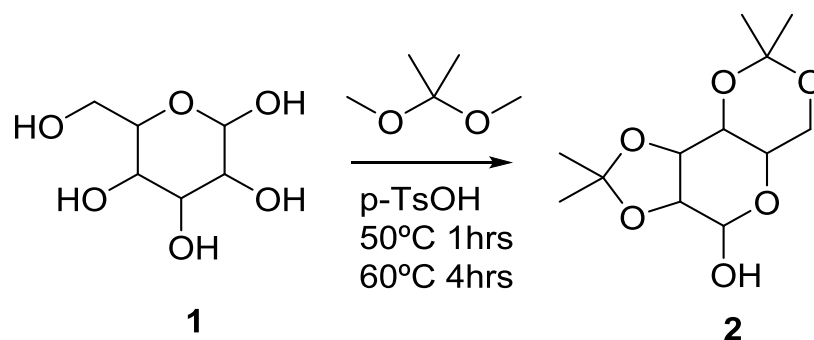


Figure 5.1: Protecting of glucose hydroxyl groups using acetal group.

5.2.4.2. Chain extension

Compound 2 (5g) was dissolved in THF (50mL), followed by cooling the solution to -75°C (dry ice/acetone mixture). NaH (915mg, 60% by weight in mineral oil) was added to the chilled solution. Under constant stirring, the temperature was allowed to slowly rise to 0°C (ice) and stirred at this temperature for 90minutes. The solution was then added into a chilled solution of respective dibromo alkyl derivatives in THF drop wise (Figure 5.2). The mixture was then allowed to be stirred at room temperature for 48 hours; the reaction was then quenched with water and extracted using EtOAc. The organic phase was then dried over anhydrous NaSO_4 ; the crude yellow product was concentrated into thick oil after evaporation of the solvent. The product was then attempted to be purified over silica to remove unreacted dibromo linkers.

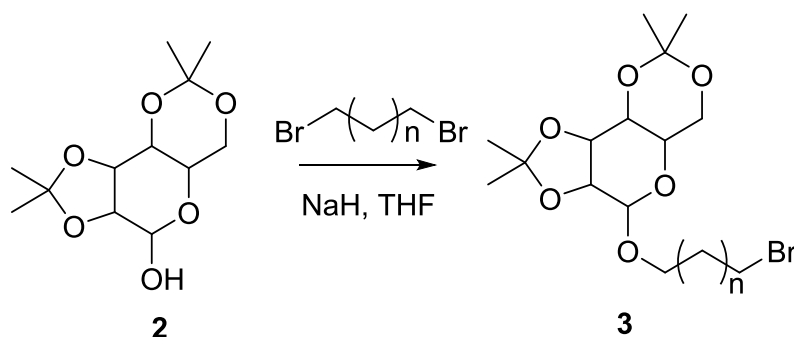


Figure 5.2: Chain length extension via dibromo alkyls.

5.2.4.3. Hydroxyl deprotection

Compound 3 (1g) was dissolved in MeOH (10mL), followed by addition of 4N HCL (2mL) dropwise (Figure 5.3). The reaction was allowed to stir at room temperature for 30 minutes through monitoring with TLC. The mixture was then neutralized to pH 7 using 4N NaOH. The solvent was then evaporated. The product (4) was analyzed and used without further purification.

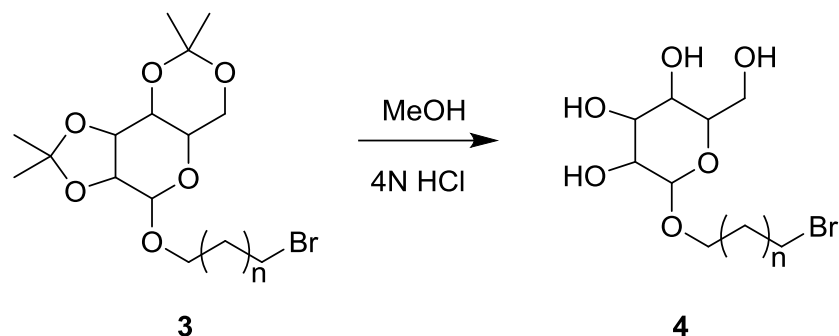


Figure 5.3: Hydroxyl group deprotection in acidic conditions.

5.3. Results and discussion

The study on synthesis of hygroscopic layer was abundant due to follow up online literature that shows the hypothesis of using hygroscopic growth can have negative features on the final dry powder. However, brief results are illustrated on the layer development as they are of great interest for future application of designing novel layers that can promote macrophage recognition for more rapid cellular uptake. It should however be used in caution as rapid immune response could result in inflammation thus creating a problem whilst trying to resolve another.

5.3.1. Pure glucose

Pure glucose was analysed on NMR to follow the changes that occur during hydroxyl group protection and chain length extension (Figure 5.4). The spectra shows the reported pattern [12]. The spectra show that there is no aldehyde pattern which can be characterized by 9-10ppm on 1H spectrum and no signal around 200ppm of ^{13}C . Figure 4 insert shows the structure of glucose. The hydroxyl at position 2, 3, 5 and 6 are the ones that can be targeted for cyclization during hydroxyl group protection. The data shows a doublet around 5.09ppm which relates to the existence of a proton that is bonded to the anomeric carbon, C1 (bonded to two oxygens). The shift in this region during chain extension can be utilized as a confirmation of successful chain addition. ^{13}C also shows the existence of this carbon at 91.99ppm. (1H NMR (400MHz, D_2O) δ 5.09, 5.08, 4.69, 4.50, 4.48, 3.76, 3.73, 3.70, 3.69, 3.68, 3.60, 3.59, 3.58, 3.56, 3.40, 3.37, 3.36, 3.34, 3.31, 3.26, 3.25, 3.23, 3.11, 3.09, 3.09, 3.07ppm. ^{13}C NMR (101MHz, D_2O) δ 95.80, 91.99, 75.83, 74.02, 72.66, 71.37, 69.53, 60.65ppm.

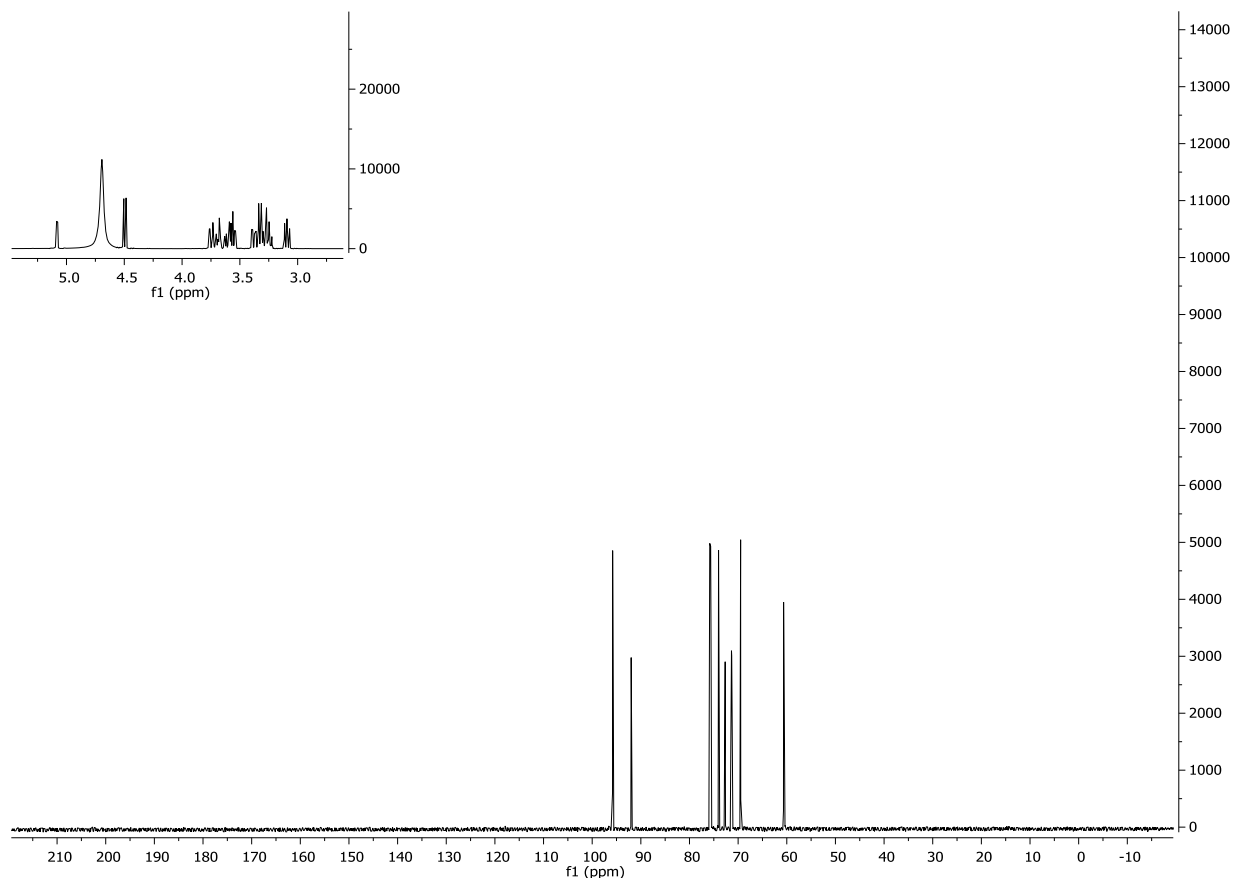


Figure 5.4: NMR spectra of pure glucose before protection and chain extension.

5.3.2. Acetal protected glucose

Evaluation of chain extension was conducted using NMR with the use of CDCl_3 as a solvent (Figure 5.5). Crude compounds were analysed after liquid-liquid extraction and solvent removal over the rotary vapour. The proton from the acetal methyl groups (CH_3) can be seen around 1.22-1.33ppm region. The region around 3.38-4.15ppm shows the presence of CH_2 groups near the oxygen of the acetal functional group. In terms of ^{13}C analysis, the CH_3 groups can be seen 25ppm region whilst the quaternary carbon of the acetal is located around 100-108ppm region. These features are a confirmation of successful protection of the hydroxyl groups in comparison to the unprotected glucose NMR analysis. There is also a disappearance of proton cluster from the OH (2,3,4 & 6) around 3-4.5ppm. The anomeric carbon (^1H 5.02ppm and ^{13}C 99.01ppm) features are however still evident in this spectrum. ^1H NMR (400MHz, CDCl_3) δ 7.72, 7.23, 5.85, 5.02, 4.76, 4.27, 3.99, 3.58, 3.41, 3.39, 3.34, 3.30, 2.83, 2.34, 2.10, 1.41, 1.36, 1.35, 1.29, 1.27ppm. ^{13}C NMR (101MHz, CDCl_3) δ 207.18, 129.29, 126.42, 111.25, 109.91, 104.27, 102.54, 99.01, 97.83, 85.13, 83.51, 82.01, 79.89, 77.38, 77.06, 76.74, 67.25, 58.58, 55.22, 50.57, 30.87, 26.73, 25.31ppm.

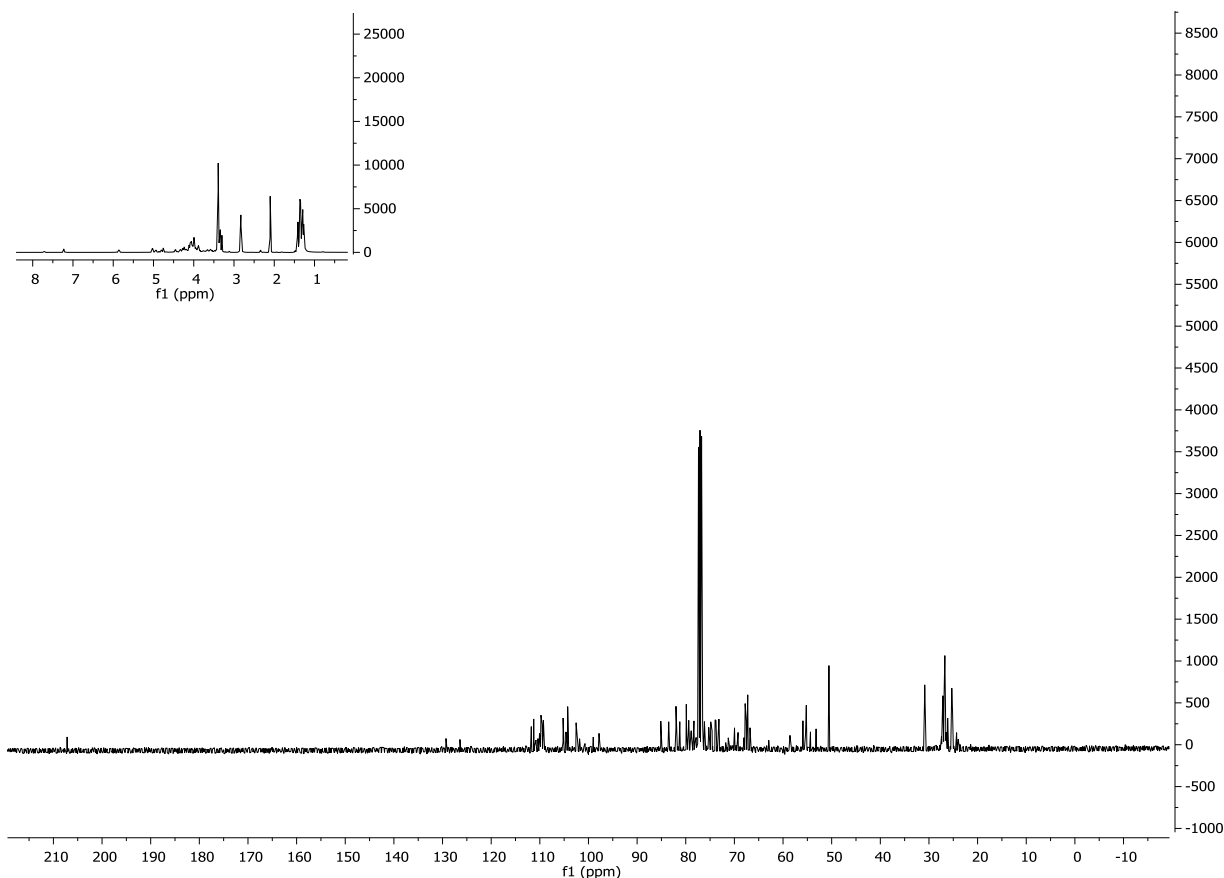


Figure 5.5: *Protection of hydroxyl groups into acetal functional groups.*

5.3.3. Chain length extension

Chain length extension was also evaluated using crude compounds after liquid-liquid extraction and removal of the solvent. The confirmation for successful chain length extension can be confirmed by the signal shift in the CH attached to the hydroxyl group into features of an ester. These can be seen by means of a minor shift from 4.76ppm to down field shift of 4.34ppm. On ^{13}C , this could result in a minor shift also. The occurrence of CH_2 near the nearly formed ester can be observed around near 63ppm. In terms of the anomeric C1, the ^{13}C pattern shows the complete disappearance. This further shows successful conjugation among all the chain extension experiments (Figure 5.6-5.11). Figure 5.6 is an illustration of some of the peaks observed in dibromo methane conjugate. ^1H NMR (400MHz, CDCl_3) δ 0.81, 1.19, 1.35, 1.83, 2.10, 3.34, 3.59, 4.00, 4.34, 4.81, 5.02, 5.86, 7.22ppm. ^{13}C NMR (101MHz, CDCl_3) δ 26.75, 29.67, 31.85, 33.19, 53.19, 55.23, 66.81, 67.81, 69.98, 75.28, 76.73, 77.05, 77.37, 79.91, 82.03, 85.11, 97.85, 104.28, 109.91ppm. The carbon near the bromine is seen by 29ppm region.

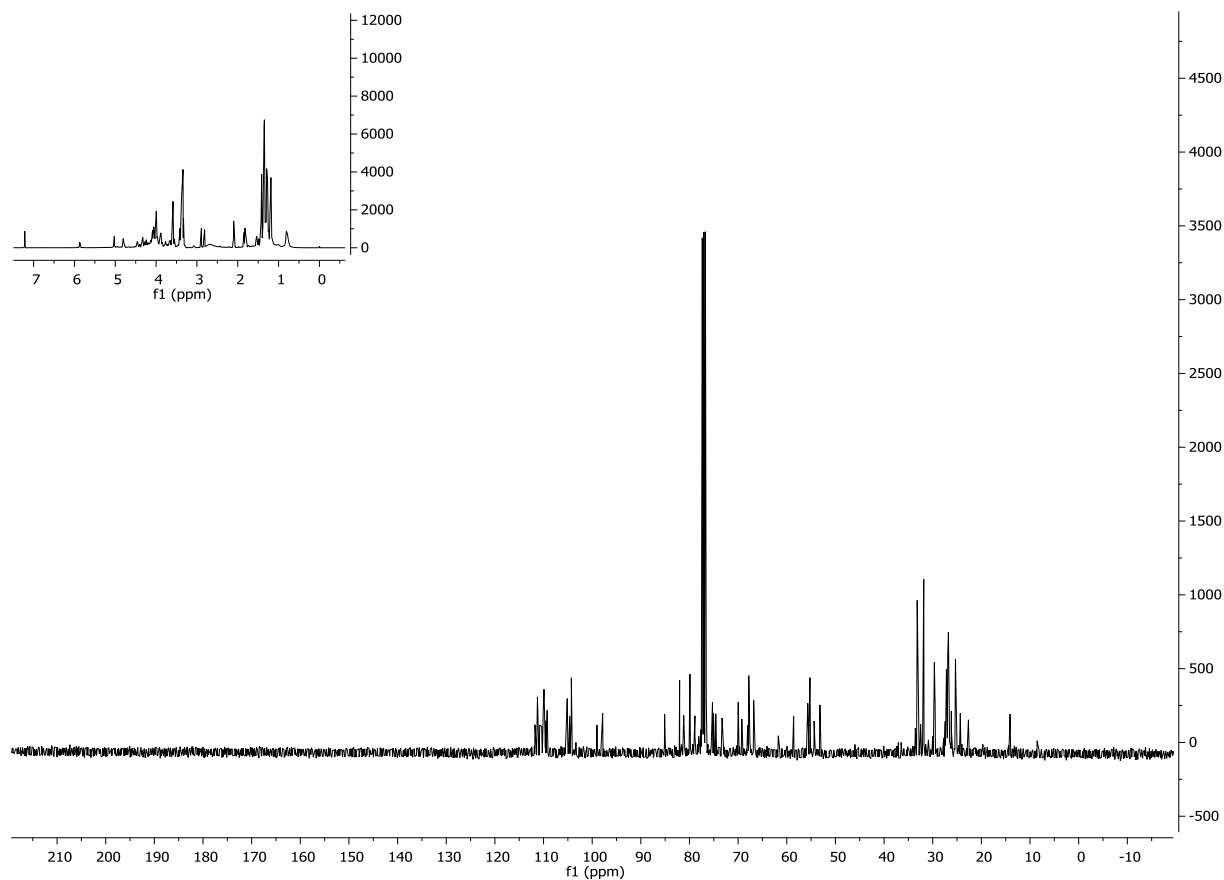


Figure 5.6: *Dibromomethane conjugation.*

Figure 5.7 illustrate the observed peak from dibromoethane conjugation. It can be seen that 63 ppm (^{13}C) is present showing the CH_2 near the ester bond. This also supported by the high intensity of the CH_2 near bromine around 29.68ppm. The compound also indicated some impurities which has smaller peak intensity that the analysed compound. ^1H NMR (400MHz, CDCl_3) δ 1.43, 2.18, 3.42, 3.66, 4.07, 4.18, 4.32, 4.41, 4.54, 4.88, 5.11, 5.95ppm. ^{13}C NMR (101MHz, CDCl_3) δ 26.76, 29.68, 55.25, 67.83, 76.71, 77.03, 77.35, 79.93, 81.16, 82.05, 85.10, 104.29, 109.93ppm.

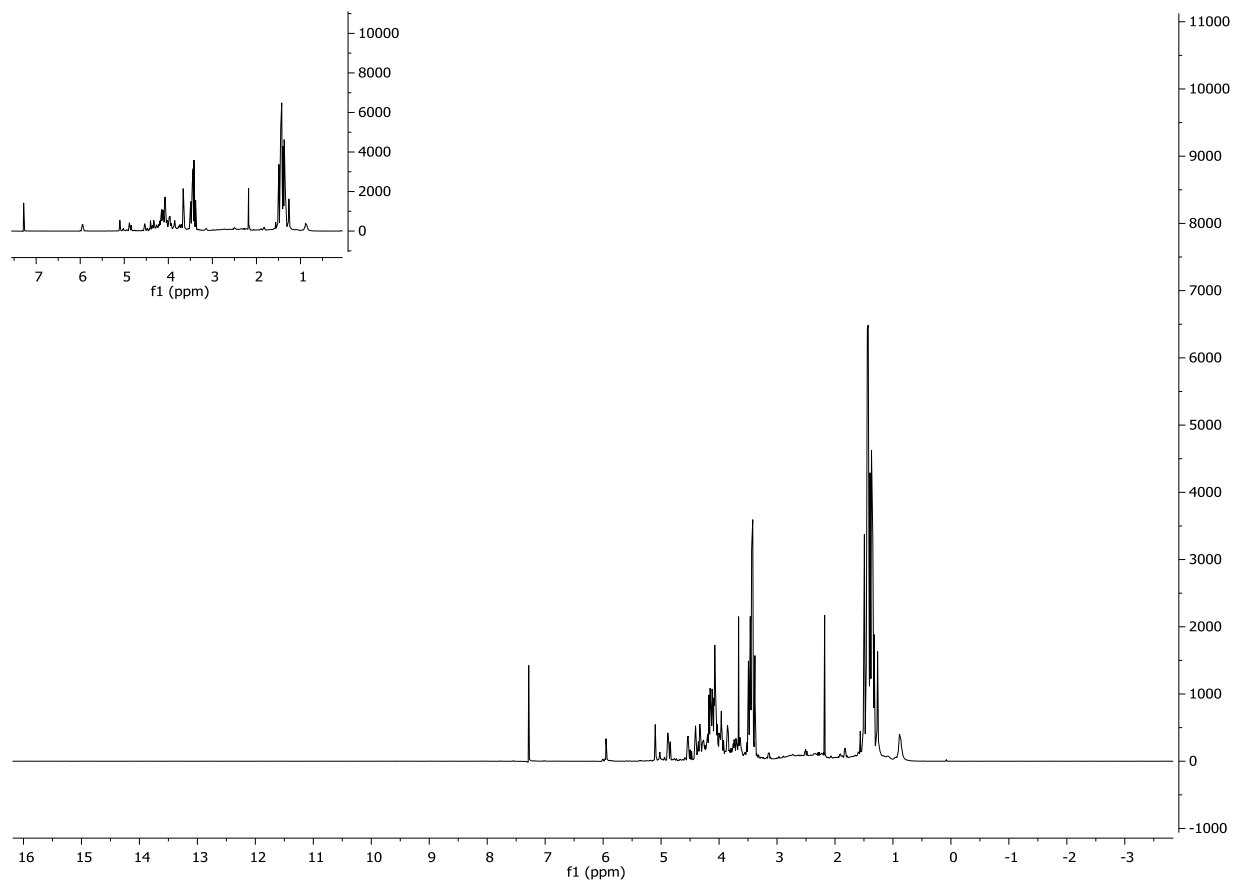


Figure 5.7: NMR spectra of dibromo-ethane modified glucose.

Figure 5.8 shows the conjugation of dibromopropane. However, unlike dibromoethane and dibromomethane, the intensity of the new CH₂ bond around 63ppm is lower. This could be attributed by the quality of the synthesized dibromopropane in comparison to other purchased dibromo alkenes. ¹H NMR (400MHz, CDCl₃) δ 1.36, 2.28, 3.34, 3.35, 3.47, 3.49, 3.50, 4.00, 4.06, 4.33, 4.34, 4.81, 5.02, 7.22ppm. ¹³C NMR (101MHz, CDCl₃) δ 25.39, 27.06, 31.05, 34.86, 53.18, 55.69, 58.60, 66.81, 67.81, 69.25, 69.99, 75.27, 77.37, 78.88, 79.91, 82.03, 97.85, 105.12, 109.26ppm.

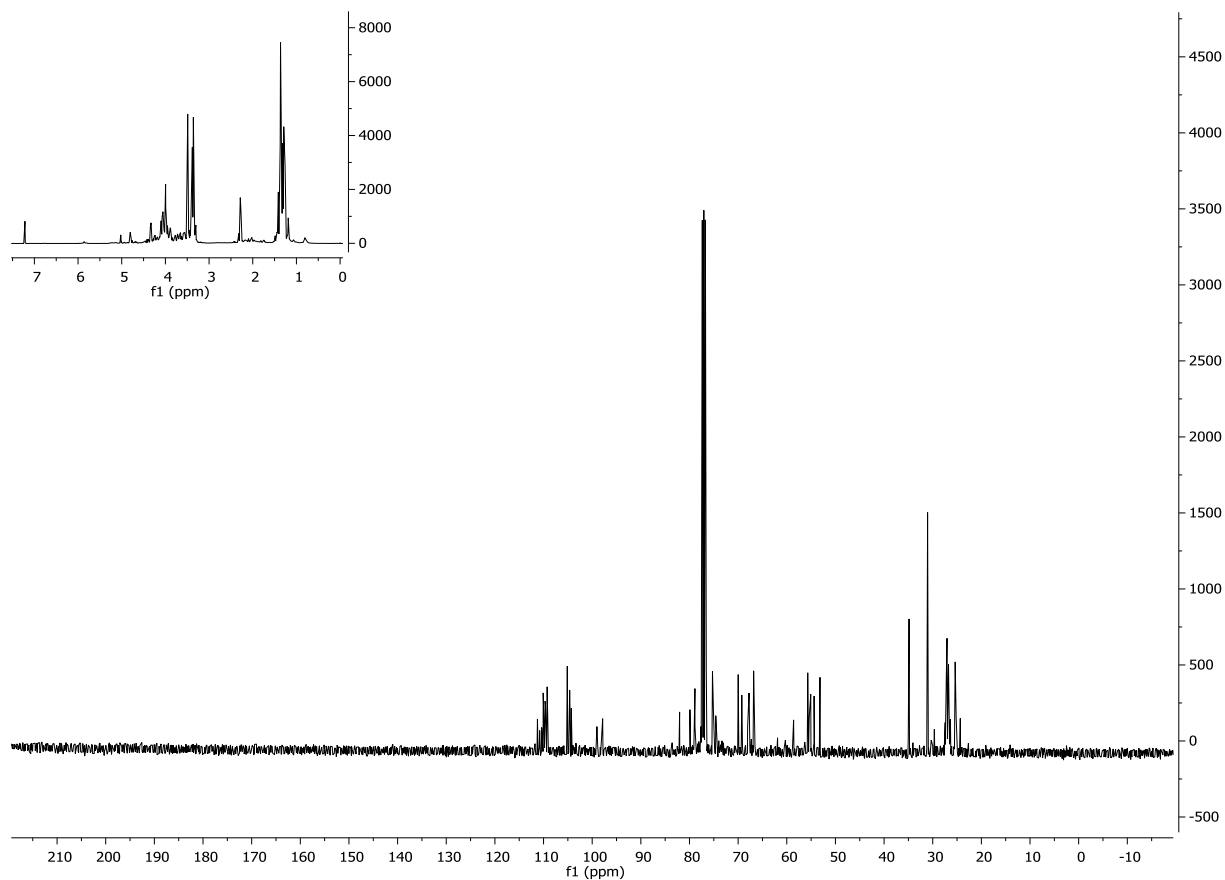


Figure 5.8: NMR spectra of dibromo-propane modified glucose.

Figure 5.9 shows the spectrum dibromobutane conjugate. This was also in lab synthesized dibromoalkene which lead to reduced yield of the conjugate product. ^1H NMR (400MHz, CDCl_3) δ 1.21, 1.31, 1.37, 1.39, 1.68, 1.99, 2.24, 2.27, 3.40, 4.01, 4.08, 4.35, 4.82, 5.05, 7.28ppm. ^{13}C NMR (101MHz, CDCl_3) δ 25.37, 26.78, 30.91, 53.16, 55.66, 58.56, 66.76, 67.70, 67.75, 69.19, 69.93, 75.25, 76.82, 77.14, 77.46, 78.88, 79.85, 81.96, 97.80, 105.12, 109.16ppm.

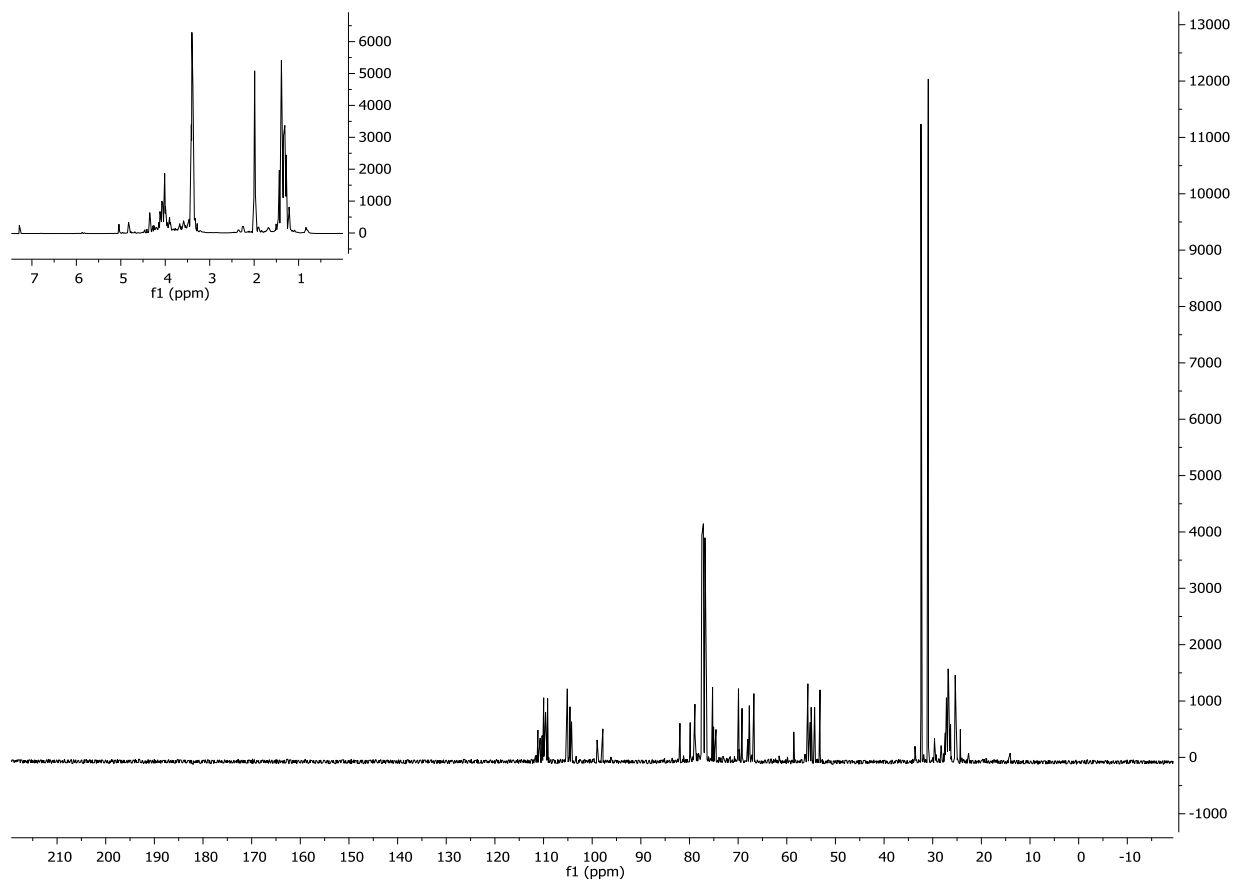


Figure 5.9: NMR spectra of dibromo-butane modified glucose.

Figure 5.10 illustrates the synthesis using dibromo-pentane. ^1H NMR (400MHz, CDCl_3) δ 0.80, 1.34, 1.51, 1.77, 1.79, 1.81, 1.83, 1.85, 2.08, 3.34, 3.54, 3.85, 3.96, 4.30, 4.77, 4.99, 5.82, 7.28ppm. ^{13}C NMR (101MHz, CDCl_3) δ 26.75, 27.24, 31.84, 32.49, 33.32, 33.66, 55.17, 67.68, 77.01, 77.32, 77.64, 79.76, 81.87, 97.75, 104.20, 109.07ppm.

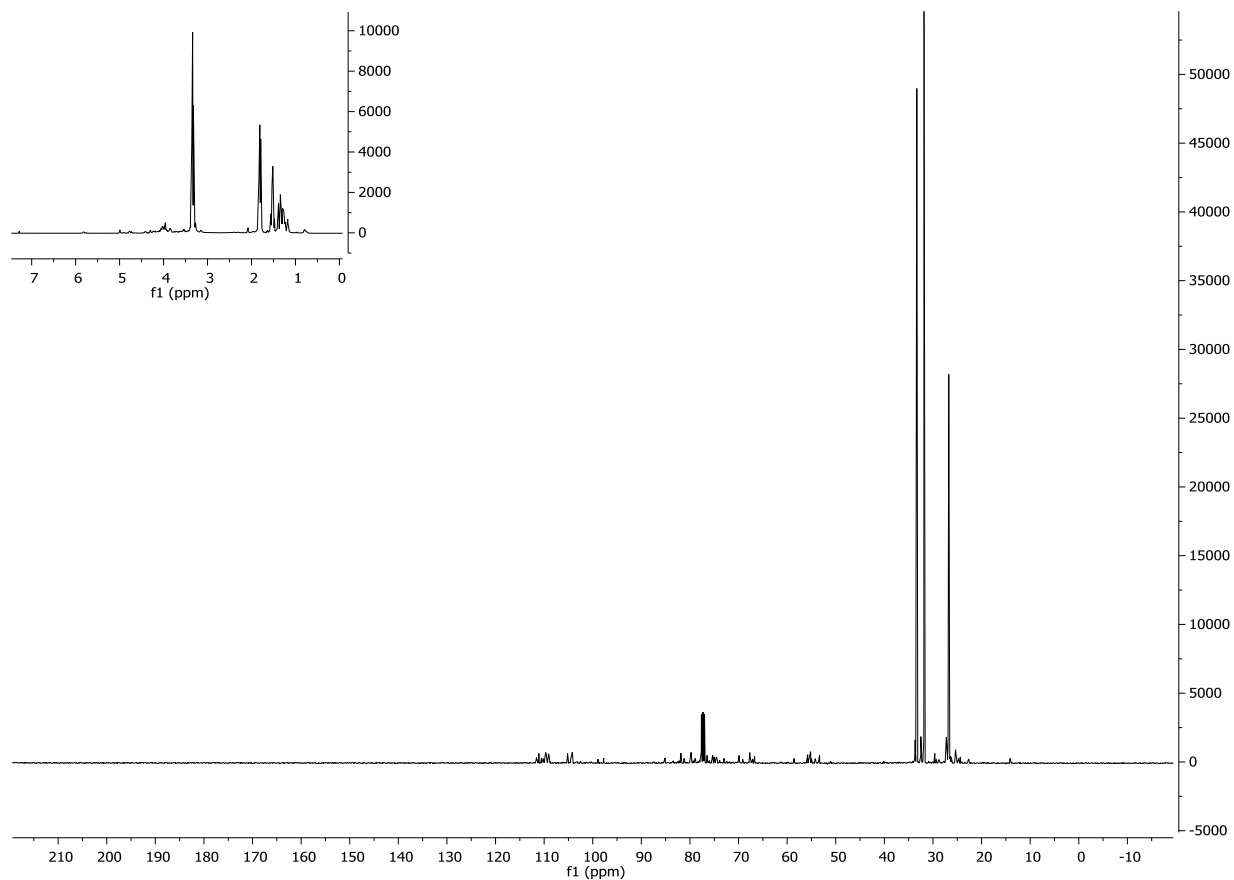


Figure 5.10: NMR spectra of dibromo-pentane modified glucose.

Figure 5.11 illustrate synthesis using dibromo-hexane. ^1H NMR (400MHz, CDCl_3) δ 0.71, 1.26, 1.33, 1.40, 1.79, 1.80, 1.82, 3.33, 3.34, 3.36, 3.53, 3.86, 3.97, 4.02, 4.31, 5.00, 5.84, 7.28ppm. ^{13}C NMR (101MHz, CDCl_3) δ 25.22, 26.77, 27.27, 32.73, 33.67, 55.18, 67.70, 77.01, 77.33, 77.65, 79.79, 81.90, 97.77, 105.17, 109.71ppm.

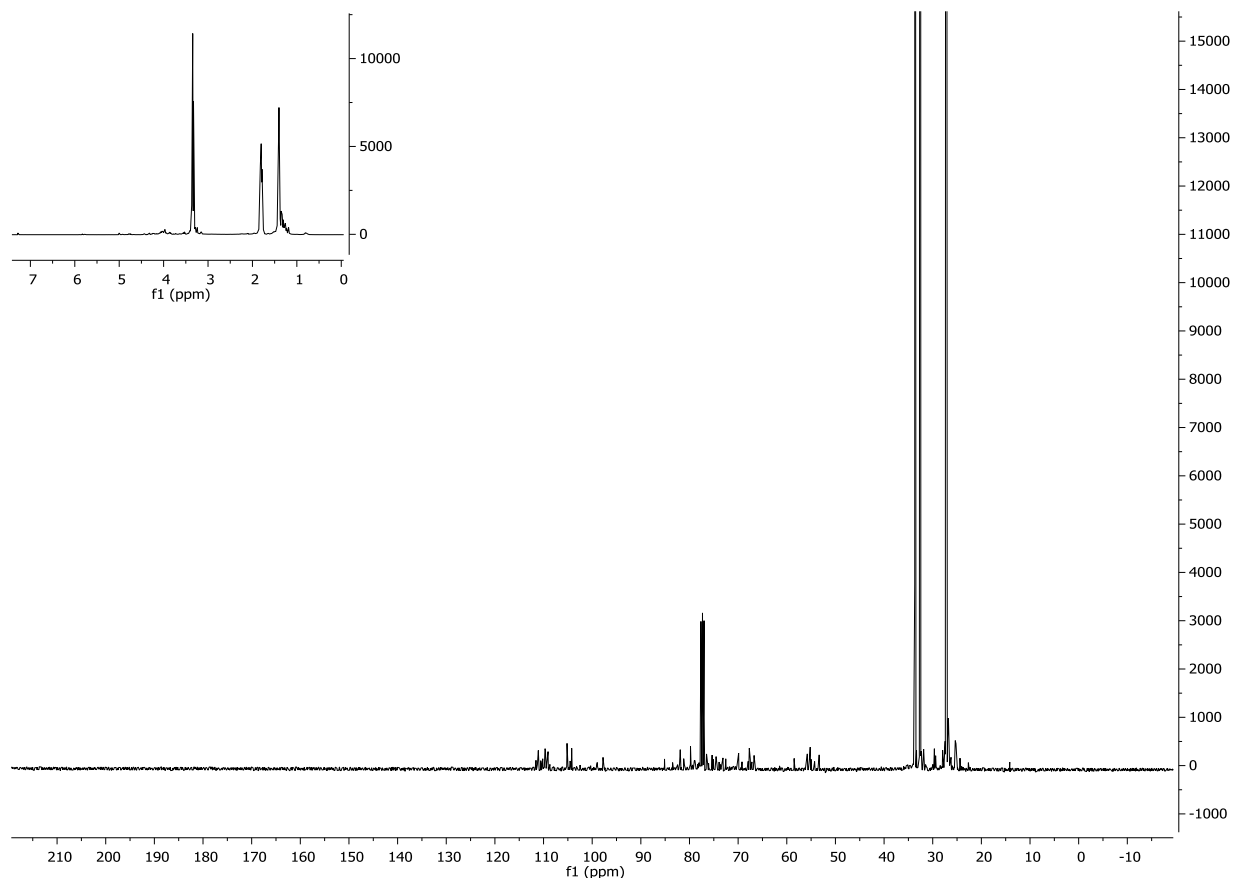


Figure 5.11: *NMR spectra of dibromo-hexane modified glucose.*

5.4. Concluding remarks

Glucose has been observed to undergo changes during equilibrium concentrations whereby different anomers can exist. Variations vary from 64% for the β anomer and 36% for the α anomer [12]. This means interpretation of NMR spectra must consider possible presence of these variations. However, this chapter is not focusing on these analytical features, but it is accepted that these features may be present. The polymer was removed from the study due to further online research on hygroscopic growth disadvantages. It was discovered that moisture may be a risk for the chemical stability of the product, and can also influence the dispersibility of the powder [9]. The concept of hygroscopic growth looks promising for improving gravitational sedimentation of nanoparticles; however this would require design on customized aerosol generator that would protect moisture uptake whilst powder is in storage. It has been proposed that re-usable DPIs should be kept air tight containers with a desiccant compartment to avoid interference from moisture [13]. However, the concept of excipient enhanced growth (EEG) principle remains a good whereby 90% delivery to the alveolar airways can be achievable [14]. The use of glucose moiety also can create a novel layer that can induce rapid macrophage uptake. Thus, this work

requires a balance between inducing macrophage uptake, inducing hygroscopic growth whilst not being affected by moisture during storage. Furthermore, the nanoparticles size dimension synthesized in Chapter 6-8 are also ideal for translocation into the systemic circulation. The preceding chapters focus on the development of the nanoparticles core made of silica or gelatin.

5.5. Reference

- [1] A.H.L. Chow, H.H.Y. Tong, P. Chattopadhyay, B.Y. Shekunov, Particle Engineering for Pulmonary Drug Delivery, *Pharmaceutical Research*, 24 (2007) 411-437.
- [2] D.A. Edwards, J. Hanes, G. Caponetti, J. Hrkach, A. Ben-Jebria, M.L. Eskew, J. Mintzes, D. Deaver, N. Lotan, R. Langer, Large Porous Particles for Pulmonary Drug Delivery, *Science*, 276 (1997) 1868-1872.
- [3] R. Vanbever, J.D. Mintzes, J. Wang, J. Nice, D. Chen, R. Batycky, R. Langer, D.A. Edwards, Formulation and Physical Characterization of Large Porous Particles for Inhalation, *Pharmaceutical Research*, 16 (1999) 1735-1742.
- [4] T. Reponen, K. Willeke, V. Ulevicius, A. Reponen, S.A. Grinshpun, Effect of relative humidity on the aerodynamic diameter and respiratory deposition of fungal spores, *Atmospheric Environment*, 30 (1996) 3967-3974.
- [5] H. Steckel, N. Bolzen, Alternative sugars as potential carriers for dry powder inhalations, *International Journal of Pharmaceutics*, 270 (2004) 297-306.
- [6] P.D. Stahl, The Macrophage Mannose Receptor: Current Status, *American Journal of Respiratory Cell and Molecular Biology*, 2 (1990) 317-318.
- [7] B. Patel, N. Gupta, F. Ahsan, Particle engineering to enhance or lessen particle uptake by alveolar macrophages and to influence the therapeutic outcome, *European Journal of Pharmaceutics and Biopharmaceutics*, 89 (2015) 163-174.
- [8] C. Bosquillon, C. Lombry, V. Pr at, R. Vanbever, Influence of formulation excipients and physical characteristics of inhalation dry powders on their aerosolization performance, *Journal of Controlled Release*, 70 (2001) 329-339.
- [9] M. Hoppentocht, P. Hagedoorn, H.W. Frijlink, A.H. de Boer, Technological and practical challenges of dry powder inhalers and formulations, *Advanced Drug Delivery Reviews*, 75 (2014) 18-31.
- [10] P.M. Young, J. Crapper, G. Philips, K. Sharma, H.K. Chan, D. Traini, Overcoming dose limitations using the orbital((R)) multi-breath dry powder inhaler, *J Aerosol Med Pulm Drug Deliv*, 27 (2014) 138-147.

- [11] J.C. Sung, B.L. Pulliam, D.A. Edwards, Nanoparticles for drug delivery to the lungs, *Trends in Biotechnology*, 25 (2007) 563-570.
- [12] J.E. Gurst, NMR and the Structure of D-glucose, *J. Chem. Educ*, 68 (1991) 1003.
- [13] L. Maggi, R. Bruni, U. Conte, Influence of the moisture on the performance of a new dry powder inhaler, *International Journal of Pharmaceutics*, 177 (1999) 83-91.
- [14] G. Tian, P.W. Longest, X. Li, M. Hindle, Targeting aerosol deposition to and within the lung airways using excipient enhanced growth, *J Aerosol Med Pulm Drug Deliv*, 26 (2013) 248-265.

CHAPTER 6 : EVALUATION OF SYNTHETIC PARAMETERS OF MESOPOROUS SILICA NANOPARTICLE THROUGH BOX-BEHNKEN DESIGN

6.1. Introduction

Tuneable properties of mesoporous silica nanoparticles make them ideal for pharmaceutical applications. The control of particle size, internal structure, composition, or physical properties is vital in targeted and controlled release. These nanoparticles can be formed by sol-gel technique. During the sol-gel technique, the silicon alkoxide undergoes hydrolysis and condensation reaction [1]. It is known that the nature of precursors, the molar ratios between the reactants, the nature of the solvent, the use of modifying agents, pH and the synthesis temperature can influence the chemo-physical properties of the nanoparticles [2]. During hydrolysis, the alkoxide groups (-OR) are replaced with hydroxyl groups (-OH) and the release of the corresponding ROH alcohol molecules. The quantity of water in the reaction vessel leads to variation in the hydrolysis rate. With small quantity of water, this leads to slow hydrolysis due to the reduced reactant concentration. Whereas, large quantities of water can also lead to slow hydrolysis due to the increased reactant dilution [3]. The use of reverse micelles plays a role in controlling the amount of water that leads to hydrolysis. The presence of partially hydrolysed monomers and those different types of oligomers can affect the composition and the homogeneity of the final material. During condensation reaction, the silanol groups (Si-OH) condense to produce siloxane bonds (Si-O-Si). Water and alcohol are produced as by-products.

To facilitate hydrolysis reaction completion, factors such as change in pH, water/silica molar ratio and amount of catalyst can be used before condensation reaction take place. The pH is known to affect the density of the particles [4]. Thus, in acidic conditions this leads to dense microporous networks, whereas in alkaline conditions mesoporous networks are produced. Due to Tetraethoxysilane (TEOS) being the mostly used precursor, the use of acidic/alkaline conditions can enhance the hydrolysis and condensation reactions. This is due to TEOS being less sensitive to hydrolysis. Due to incomplete hydrolysis and condensation in sol-gel reaction, calcination can be used to react the silanol groups to form stable bonds. It has been reported that the porosity of the xerogel film can reach 78% when the thermal temperature is 350°C [5]. In this study, alkaline conditions are used. This is due to TEOS silicate having a highly negatively-charged density which can only assemble with the cationic surfactants (CTAB) through strong electrostatic interaction [6]. Furthermore, at pH above 7.5 the stable surfactant-silicate composites can exist. Thus,

allowing control of the pore structure as the silicate condensation and dissolution are affected by the composite. Tuneable chemo-physical properties are ideal for drug delivery.

The study focuses on improving drug content of tuberculosis (TB) drug, rifampicin. TB is known as the second leading cause of death globally after HIV/AIDS [7]. Sub-Saharan Africa has high known prevalence of TB and combination of HIV/AIDS. Treatment of both diseases comes with complication as drug interaction can take place among the TB regiment themselves and with HIV regiment. The use of fixed dose (rifampicin, isoniazid, ethambutol and pyrazinamide) TB combination has allowed the ease of use and improved patient compliance. However, oral delivery remains to still have challenges in the bioavailability. The impaired bioavailability has been shown to arise from interaction of isoniazid with rifampicin in acid environment. For prolonging drug presence and pH response, mucoadhesive materials biodegradable polysaccharide chitosan was used. Due to the use of CTAB in this study, the use of temperatures about 350°C would be enough to degrade it from the nanoparticles. Based on the Material Safety Data Sheet (MSDS), CTAB is a known respiratory tract irritant that can cause damage to the liver, cardiovascular system, central nervous system (CNS).

6.2. Materials and methods

6.2.1. Materials

Tetraethoxysilane (TEOS 98%), hexadecyltrimethylammonium bromide (CTAB 95%), (3-Aminopropyl) triethoxysilane (APTES), 3-glycidoxypropyltrimethoxysilane (GPTMS), Chitosan, Lysozyme, Ninhydrin, Sodium Hydroxide, chloroform and ethanol were all purchased from Sigma Aldrich. Rifampicin was also purchased from Sigma-Aldrich and used without further purification.

6.2.2. Experimental design

A three-factor, three-level Box Behnken design was used for experimental design and optimization procedures. This design was selected for the study as it is suitable for exploration of quadratic response surfaces and constructs a second order polynomial model, thus helping in optimizing a process using a small number of experimental runs. The design consisted of replicated centre points and the set of points lying at the midpoints of each edge of the multidimensional cube that defines the region of interest [8].

6.2.3. Preparation of mesoporous silica nanoparticles

Tetraethyl orthosilicate (TEOS) was used as silica source, cetyltrimethyl ammonium bromide (CTAB) as surfactant. 1g of CTAB was dissolved in 12, 30 and 48mL NaOH buffer (pH 8 (0.001mM), 10 (0.1mM) and 12 (10mM)) respectively (Table 6.1). From the 10mM NaOH buffer, dilute HCl was used to drop the pH 8 and 10. The reaction was conducted in a two-necked round bottom flask with a condenser and rubber stopper attached. The surfactant solution was then heated for 30 minutes at 60°C until a clear solution formed. 5mL of TEOS mixed with 48, 30 and 12mL was injected over 5 minutes to each respective surfactant solution to make up 60mL emulsion mixture. The hydrolysis-condensation reaction was allowed to run for 2 hours. The solution was then allowed to cool to room temperature, 60mL of ethanol was added to precipitate the particles, followed by decanting supernatant. The recovered MSN were then dried for overnight at 100°C. The MSN were then calcinated for 2 hours at 350°C, 450°C and 550°C, respectively. The calcined MSN were then stored in vials prior further use.

Table 6.1: Experimental parameters for synthesis of mesoporous nanoparticles

Formulation	Temperature (°C)	pH	Molar ratio
F01	550	8	126
F02	350	12	126
F03	450	8	76
F04	450	12	176
F05	450	12	76
F06	550	10	176
F07	550	10	76
F08	450	10	126
F09	350	10	76
F10	450	8	176
F11	550	12	126
F12	350	8	126
F13	450	10	126
F14	350	10	176
F15	450	10	126

6.2.4. Determination of the grafting potential using ninhydrin test

Amino functionalization and quantification of MSNs with amino was conducted following modified Lu Hsu-Tung (2013) procedure [9]. Briefly, a round-bottom flask containing a mixture of 500µL (3-Aminopropyl) triethoxysilane (APTES), 0.5g MSNs and 50mL toluene were connected to a reflux condenser. The mixture was refluxed for 24 hours and allowed to cool to room temperature. Addition on ethanol allowed the particles to precipitate. The particles were washed with ethanol and collected using centrifugation. For the determination of the degree of amine grafting on the

surface of MSNs was determined by using the ninhydrin assay. 100mg of MSNs was added to the solution containing 1mL of sodium acetate/acetic acid buffer solution and 2mL of 3% ninhydrin agent. The mixture was heated at 100°C for 15 minutes and then cooled to room temperature in a water bath. The mixture was then diluted with 7mL of 50 vol % ethanol/water. After centrifugation, the supernatant volume was designated as V(L) and its absorbance at 570nm was measured against a blank reference by using a UV spectrophotometer. By using the calibration curve, the corresponding concentration of amine group (M, mol/L) was determined. The molar quantity of amine (AL, mol/g) grafting on the surface of MSNs based on the weight of MSNs is calculated by the following formula:

$$AL(mm\text{ol}/g) = MV/W_s \quad (6.1)$$

6.2.5. Functionalization of mesoporous silica nanoparticles with epoxy group

The grafting of 3-glycidoxypropyl trimethoxysilane on the surface of the synthesized MSNs. The determination the amount of coupling agent 3-glycidoxypropyltrimethoxysilane (GPTMS), which would be incorporated on the surface silica nanoparticles was done following literature [10]. Whereby the equation is defined as

$$W_1 = mW_2 \times A_{SiO_2}/A_{GPTMS} \quad (6.2)$$

Where W_1 is weight of GPTMS, m is the coefficient (multiple, usually equal 1), W_2 is the weight of MSNs, A_{SiO_2} is the specific surface area of silica (determined from BET) and A_{GPTMS} is the wetting area of GPTMS (330m²/g). Respective amount of MSNs was added to round bottom for each formulation, in 100mL toluene. The mixture was stirred at 1000rpm for 2 hours at 90°C under reflux. Respective amount of GPTMS was added to the round bottom flask and refluxed for 12 hours. The excess unreacted GPTMS was washed with water and methanol. Particles were then allowed to dry overnight in an 80°C oven.

6.2.6. Preparation of chitosan-capped mesoporous silica nanoparticles (CS-MSNs)

The capping of nanoparticles with chitosan was conducted by following Hu and colleague's procedure with modification. Briley, 2g of chitosan was place in 200mL of acetic acid (5% wt). The solution was stirred at room temperature for 24 hours. The formed transparent 1% chitosan solution was then used for coating the nanoparticles. 0.1g of MSNs dispersed via sonication in 10mL EtOH for 15 minutes. 20mL of chitosan solution was then added to the MSNs solution and

stirred for 24 hours. The particles were then collected using a centrifuge at 10000rpm and washed with and EtOH prior freeze-drying.

6.2.7. Drug loading and *in vitro* drug release

Rifampicin was selected for drug entrapment of anti-TB drug. Briefly, 150mg rifampicin was dissolved in water (pH 4.3) to give 1.82mM concentration. The pH was then reduced to pH 3 by means of 1M aqueous solution of HCl to allow drug entrapment. 100mg of CS-MSNs were dispersed in 10mL of drug solution. The solution was then shaking for 24 hours at room temperature. After 24 hours, 0.2M NaOH was used to increase the pH to 8.0, followed by allowing the mixture to stir for 2 hours. The particles were then collected via centrifugation and washed twice with the NaOH (pH 8.0, 0.2M) solution. The *in-vitro* drug release study was carried out using a dialysis bag (cellulose membrane, MW cut-off 12,400, Sigma-Aldrich. About 10mg of the drug-loaded nanoparticles were suspended in 2mL of respective 10mM buffer solution (pH 4.5 and 7.4) inside a dialysis bag. The dialysis bag was then placed in 20mL of the buffer solution (sink condition) at 37°C under magnetic stirring. At successive time intervals, aliquots (2.5mL) of the release medium was collected and replaced with a fresh buffer solution. The *in-vitro* drug release was carried out for 24 hours. Each experiment was conducted in triplicate. The drug release was evaluated using UV on PerkinElmer Lambda 25, utilizing PerkinElmer UV Winlab software (Version 6) (Waltham, Massachusetts, USA). Rifampicin was analysed at 337nm. Determination of drug content was directly measure by accurately weighing 10mg of drug in 1M methanolic solution. This was allowed to stand at 60°C for 30 minutes, followed by UV determination of drug mass per milligram of MSN particles.

6.2.8. Enzyme degradation drug release

10mg of lysozyme was dissolved in 2mL of each pH 6.8 10.0mM buffer solution. Subsequently, 10mg of CS-MSNs was dispersed in both lysozyme dissolved pH 6.8. Aliquots were taken from each suspension at different time intervals and the delivery of rifampicin from the pores of nanoparticles in the buffer solutions was observed. This experiment was also revised three times and the mean of these results was considered as the result. The drug released was evaluated using UV.

6.2.9. Morphological evaluation of mesoporous silica nanoparticles

The morphologies and dimensions of the samples were revealed with a JEOL transmission electron microscope operating at 120kV (Peabody, Massachusetts, USA). Samples were

dispersed in methanol by means of sonication and dried on holey carbon-coated Cu grids prior analysis overnight.

6.2.10. Surface chemistry of mesoporous silica nanoparticles

FTIR spectra were captured on PerkinElmer Spectrum 100, utilizing Spectrum software (Waltham, Massachusetts, USA). A total of 100 scans were averaged for each spectrum. The scans were evaluated at 650-4000 cm^{-1} range.

6.2.11. Evaluation particle surface area and pore size

The adsorption-desorption isotherms of nitrogen were measured at 77K using a Micrometrics ASAP 2020 Plus Physisorption (Atlanta, Georgia, USA). The pore size distributions were calculated from the adsorption branches of adsorption-desorption isotherms based on the BJH model.

6.2.12. Evaluation of particle size diameter and size distribution

Dynamic light scattering (DLS) studies were carried out on a Malvern NanoZS zetasizer (ZEN 3600, $\lambda = 633\text{nm}$, $\theta = 173^\circ$) (Worcestershire, UK). The calcinated particles were dissolved in deionized water and briefly sonicated for 15 minutes prior to size analysis. The sample was analysed in quartz cuvettes, the temperature was set to 25°C and the viscosity and refractive index (1.475) values used were that of silica. For each measurement data was acquired during 40 seconds in three runs.

6.2.13. Solid state analysis (^{29}Si NMR)

Solid state NMR was evaluated by following Mijatovic and colleague's procedure. Briefly, ^{29}Si CPMAS NMR spectroscopy was measured on a Bruker Avance III HD 400MHz spectrometer operating with a 4mm probehead at a frequency of 79.4905MHz (Billerica, Massachusetts, USA). The samples were filled into 4mm zirconia rotors, which were spun at 4000 Hertz. The spectra were acquired in the cross 3 polarization mode using contact times of 10 milliseconds and high-power dipolar decoupling to reduce line broadening. The pulse repetition time used was 5 seconds, with scan of between 10,000 and 30,000 used to achieve sufficient signal to noise ratio.

6.2.14. Dissolution profiling

This was also utilized in design of experiment and surface response plot. DDSolver an excel add-in was used for determination of mean dissolution time (MTD), dissolution efficiency (DE) and

modelling cumulative drug release percentage [11]. Sigmaplot v14.0 software was utilized for plotting the graphs (Systat Software Inc, California, USA). Using the Korsmeyer-Peppas model, the release exponent (n) was evaluated by fitting the first 60% drug release data.

$$M_t/M_\infty = kt^n \quad (6.3)$$

where M_t / M_∞ is a fraction of drug released at time t , k is the release rate constant and n is the release exponent. $0.45 \leq n$ corresponds to a Fickian diffusion mechanism, $0.45 < n < 0.89$ to non-Fickian transport, $n = 0.89$ to Case II (relaxation) transport, and $n > 0.89$ to super case II transport[12]. The non-Fickian indicates a combination of both diffusion and erosion-controlled release rate, whereas super-case II shows the erosion of the polymer chain. The mean dissolution time (MDT) was also calculated.

$$MDT = \sum J = \hat{t}_j \Delta Q_j \sum j = \ln \Delta Q_j \quad (6.4)$$

Where j is the sample number, n the number of time increments considered, \hat{t}_j the time at midpoint between t_j and t_{j-1} , and ΔQ_j the additional amount of drug dissolved in the period of time t_j and t_{j-1} [13]. For the determination of dissolution efficiency (DE), equation 6.5 was used.

$$DE = \left(\int_{t_1}^{t_2} y \cdot dt / y_{100} \times (t_2 - t_1) \right) \times 100 \quad (6.5)$$

Where, y is the percentage of dissolved product. DE. represents the area under the dissolution curve between time points t_1 and t_2 expressed as a percentage of the curve at maximum dissolution, y_{100} , over the same time period [14].

6.2.15. Statistical analysis

The data is presented as mean \pm standard deviation. Significant differences between group means were evaluated using one-way Anova, P value < 0.05 . The analysis was performed using OriginPro (OriginLab Corporation, MA, USA).

6.3. Results and discussion

6.3.1. Particle size and distribution evaluation

The zetasizer was used to assess the particle size and size distribution of each formulation prior to TEM analysis (Table 6.2). Based on the evaluation, only F01 and F06 had a polydispersity index (PDI) of above 0.5. Thus, this shows a very broad distribution of particle sizes. The post-synthesis grafting was also evaluated using ninhydrin test for determination of the quantity of amines on the surface of the MSNs. The data indicates that the size (physical properties) of the particles does not play a role in the grafting, but rather chemical features may play a role on the amount of amines on the surface. Thus, warranted the used of solid-state NMR for evaluation of the silanol groups density on each formulation. The pore size and particle size can be linked to the amount of drug each particle can carry. Based on the amount of drug (mg) entrapped per milligram of MSN, size and pore structure play a role quantity if drug entrapped. F01 has the highest size with every milligram of MSN retaining 2.38mg of drug. F11 evidently has a high pore structure based in the observation of the TEM images, thus lead to more drug filling up the cavity. F05 and F06 have a size of 209nm and 365nm, respectively. However, based on the porosity network, F05 has more pores allowing the more drug to be entrapped within the cavities. Apart from the nanoparticle size playing a role in the amount of drug that can be encapsulated. It is evident that the cavity size can also improve drug entrapment, despite small size. F02 indicates combination of both high porous nanoparticles and large particle size. Zeta potential was also evaluated were it was observed that the uncoated nanoparticles had zeta potential of -41.2 ± 2.2 mV, whilst the chitosan coated particles has a zeta potential of 28.3 ± 4.1 mV.

Table 6.2: Evaluation physicochemical features that can play a role in drug delivery systems

Formulation	Size (nm)	PDI	Amine (mmol g ⁻¹)	Pore size (cm ³ /g)	Drug ratio (mg/mg)
F01	609±44.44	0.869	0.034	0.039	2.38
F02	363.73±2.87	0.326	0.190	0.087	1.80
F03	151.00±1.40	0.224	0.160	0.066	1.08
F04	202.67±1.91	0.241	0.020	0.031	1.35
F05	209.13±1.71	0.195	0.015	0.112	2.74
F06	365±67.04	0.617	0.039	0.131	0.38
F07	141.40±3.01	0.313	0.020	0.101	1.09
F08	168.47±0.82	0.187	0.030	0.170	1.38
F09	152.33±3.82	0.276	0.100	0.004	1.29
F10	214.07±1.47	0.211	0.020	0.080	1.12
F11	115.37±4.17	0.328	0.120	0.329	2.02
F12	131.27±2.81	0.222	0.190	0.063	1.21
F13	176.93±4.01	0.198	0.029	0.036	1.38
F14	172.87±5.61	0.245	0.010	0.057	0.91
F15	177.13±3.01	0.175	0.030	0.046	0.35

6.3.2. Morphological analysis

The TEM images indicate the presence of a cavity network which is beneficial for improved encapsulation and controlled release (Figure 6.1). Due to the nature of TEOS hydrophobic characteristic, hydrolysed TEOS can only diffuse into the aqueous phase due to increased hydrophilicity [15]. This aids in controlling the hydrolysis and condensation rate of the silica source. The presence of chloroform may have acted as a pore expanding reagent. Due to the use alkali reaction conditions, the decrease in pH value indicates to have an impact on the morphology, size and porous structure is changed. This can relate to the rate of hydrolysis and condensation as the pH value changes. The amount of OH ions affects the rate of nucleation. Wang and colleagues (2016) indicated that the amount of the non-polar solvent can affect the size of the pores, whilst the concentration of the catalyst affect the morphology [16]. The dispersion correlates to reported data, whereby particles formed at $\text{pH} > 7.0$ are stable toward gelation due to repulsion effects [17]. It has been reported that CTAB micelles in water-chloroform system did not go through any type of phase transition or drastic modification when samples were heated from 20 to 70°C.

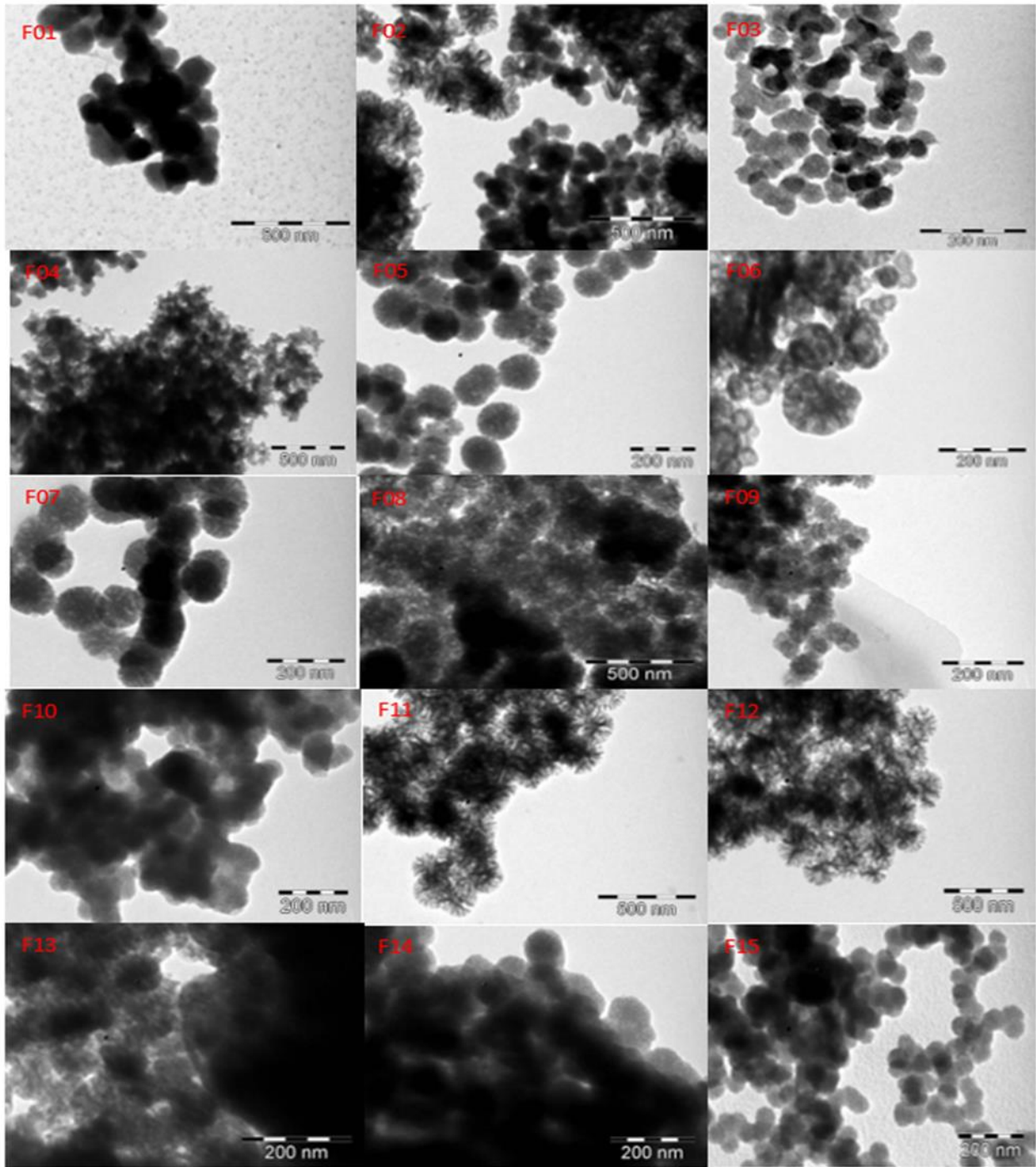


Figure 6.1: TEM images of F01-F15 MSNs.

Based on the DLS data correlation to TEM data, it was observed that from microscopic analysis that the silica nanoparticles appeared to be well separated, un-aggregated particles, whereas on DLS they revealed instability. Thus, warrant the observation of a larger particle size in DLS as compared to TEM. DLS functions by reporting the mean particle size along the dispersed particle

population size. Thus, aggregates size is also considered during analysis, thus leading to a broad size range. DLS is highly sensitive to dynamic aggregation, aggregation, agglomeration; however, which can be seen by the PDI value not below 0.1 which a major characteristic of highly monodisperse particles.

6.3.3. Evaluation of nanoparticle surface chemistry

The FTIR spectra (Figure 6.2) of the MSNs show absorption bands similar to literature where by asymmetric vibration of Si-O-Si (1050cm^{-1}), asymmetric vibration of Si-OH (966cm^{-1}), and symmetric vibration of Si-O (795cm^{-1}) are found in all spectra [18]. Scissor bending vibration of molecular water (1632 cm^{-1}) is also observed most formulations, whilst diminished peaks are observed in formulation of 550°C calcination. H-bonded silanol OH groups (3400cm^{-1}) are also observed in F-F. This region can also represent O-H stretching in H-bonded water. Under thermal treatment (calcination), this can remove the surface silanol groups (isolated and terminal hydroxyl groups). It has been shown that during a thermally induced dehydroxylation (water elimination) process, the silanols are condensed. This leads to a decrease of the hydrogen-bonded chains due to formation of siloxane bridges and an increase of the isolated species [19]. The absorption band 2980cm^{-1} and 2930cm^{-1} cannot be identified or is superimposed in the spectra by the 3400cm^{-1} region. The region is stated to represent the presence of unreacted TEOS in the silica particles. However, 2161cm^{-1} indicates the presence of Si-H.

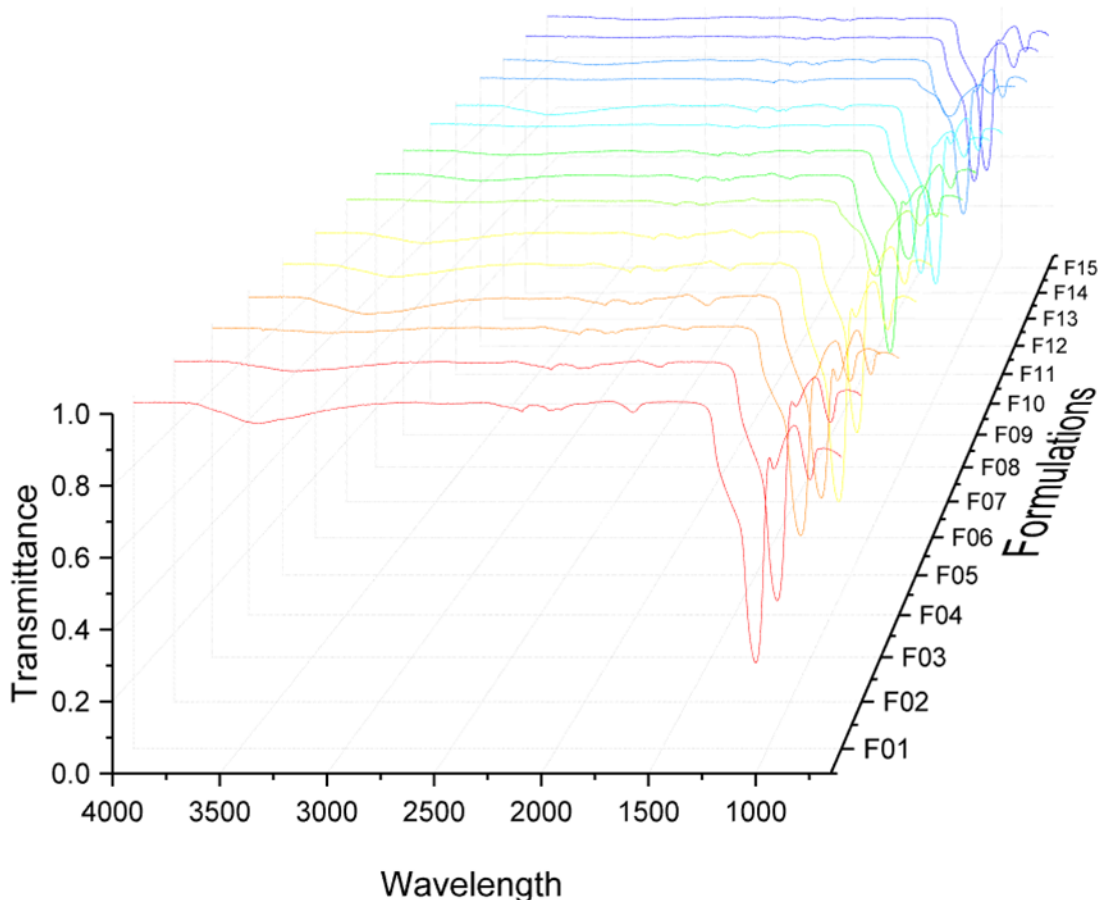


Figure 6.2: FTIR spectra of MSNs formulations after calcination.

Solid-state ^{29}Si NMR was used to characterize the chemistry of the silica surface (observation of connectivity and degree of condensation). ^{29}Si SS-NMR spectra (Figure 6.3) of the uncoated MSNs showed typical peaks assignable to a Si–O bond: signals at -94.04ppm , -102.14ppm (surface site) and -110.77ppm (core sites) that correspond to shifts [20]. The signal peak at -67.87ppm indicates a Si–C bond site. Silane functionalization leads to the formation of the site, during post synthesis crafting/co-condensation. It has been reported that during co-condensation, the silane's alkoxy groups could hydrolyse and self-condense to form the Si–O–Si. However, due to use of non-polar solvent during grafting, the self-condensation of organoalkoxysilane molecules has been shown to be unfavourable due to the absence of water. This leads to these molecules having to 'quest' for the surface hydroxyl groups by diffusing throughout the MSN surface [21]. Based on the observations, it has been reported that the bare silica surface is largely dominated by the mono-silanol groups, whereas the intensity of the region presence on the surface of another bonded moiety that is attached directly to the surface by a stable Si–C bond.

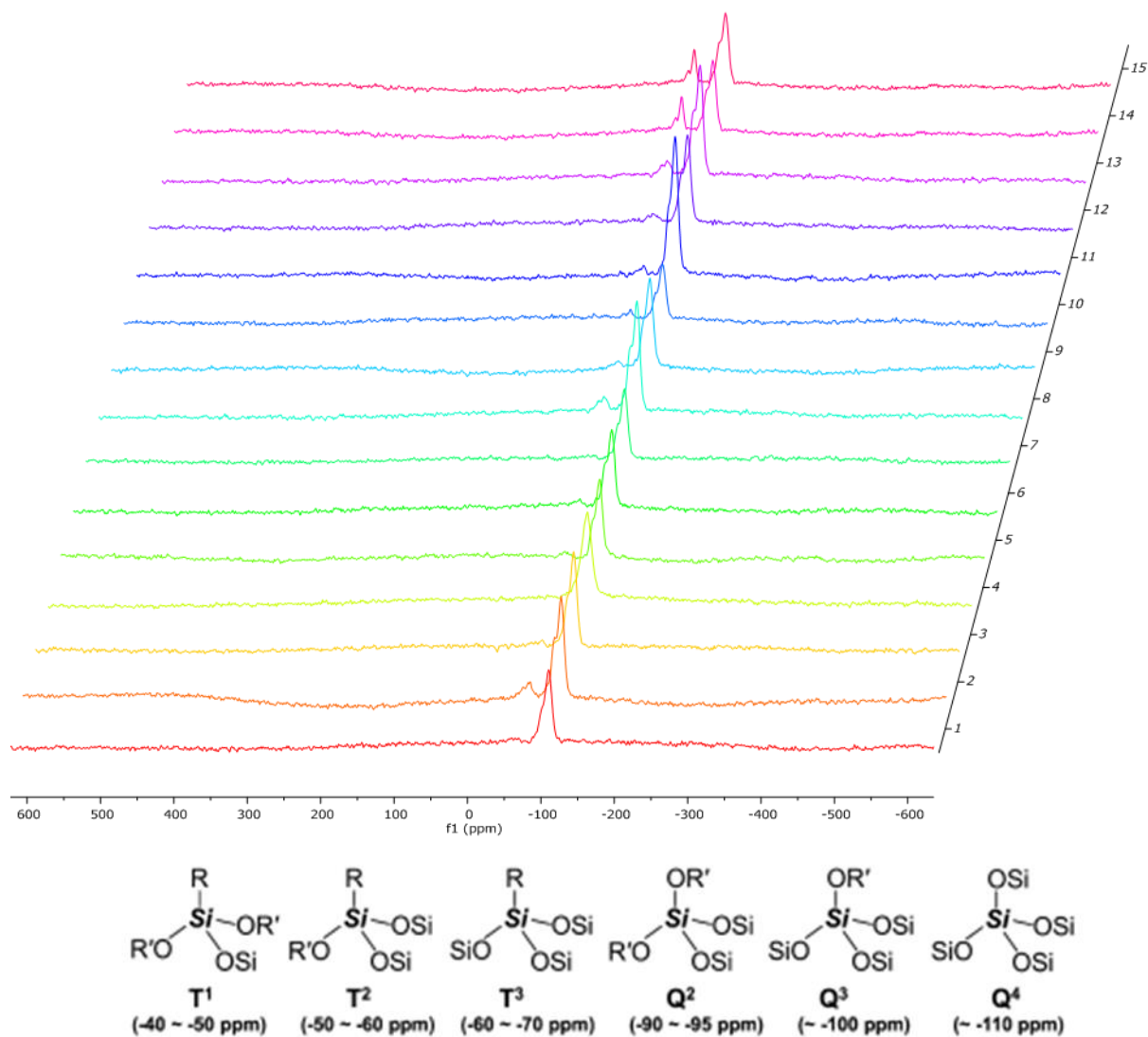


Figure 6.3: Solid state NMR of MSNs formulations evaluating the different silanol groups.

6.3.4. *In vitro* drug release profiles of rifampicin

In vitro drug release was evaluated to assess the impact of the synthetic parameters on the release kinetics of the rifampicin from the MSNs (Figure 6.4-6.6). The use of chitosan was used to serve as a pH responsive gate. Due to its biocompatibility and known pH responsiveness, this was used as a coating model for the nanoparticles to assess drug release prior use of novel pH responsive linkers. The degree of retaining the drug within the particles is linked to the degree of the interaction of the chitosan carboxylic group to the MSNs amine surface. It was observed that at an acidic pH of 4.5, some of the formulation indicated controlled release, whilst F03, F7, F10 and F15. Based on the DOE, F03 had the amine concentration of 0.160mmol/g, whilst F07, F10

and F15 had the lowest amine concentration of 0.020, 0.020 and 0.030mmol/g respectively (Table 6.2). Thus, this directly links to the amount of chitosan that can “gate” the drug within the particles. In relation to F03 which had the highest amine concentration respective to the mentioned formulations, this had the lowest density of Q⁴ based on Solid-state NMR evaluation. The release from lysozyme degradation of chitosan, the particles gave a burst release at the maximum time of 6 hours. However, F11 and F15 indicated a more sustained release. This can be attributed by the deep pore cavity/network structure reducing diffusion the enzyme from degradation of deep embedded chitosan. Analysis of drug release within the first hour, both pH 4.5 and 7.4 did not contain lysozyme. Using univariate ANOVA analysis, the F value was determined at 30.03 whilst the p value was 7.48E⁻⁰⁶. The data shows burst release from an acidic pH of 4.5 due to solubilization of chitosan as this pH. In relation of pH 6.8 to 4.5, it was observed that F value was 4.55 and the p value 0.042. Thus, enzymatic activity had more burst release than acidic release.

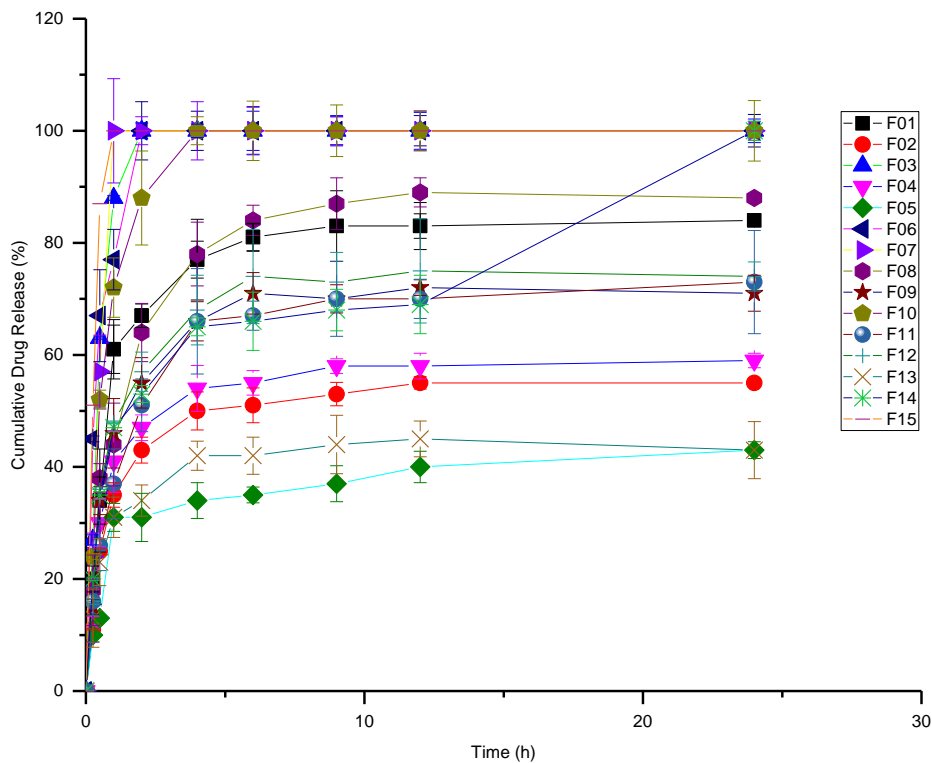


Figure 6.4: Cumulative drug release at acid pH 4.5 (Acetic Acid-Sodium Acetate).

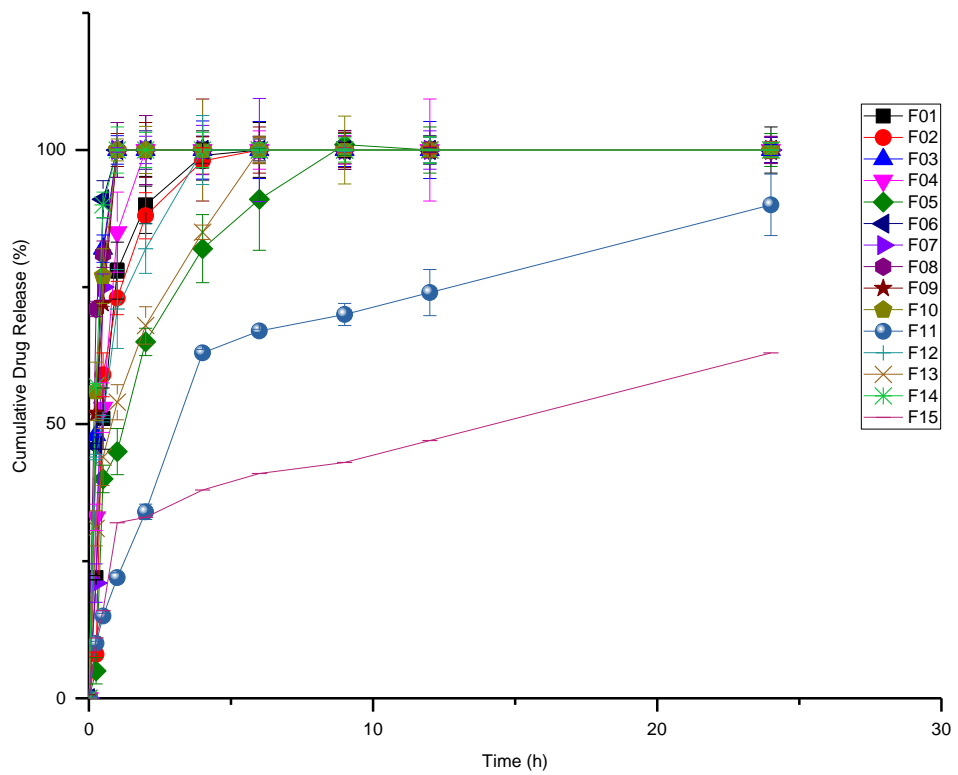


Figure 6.5: Cumulative drug release under enzymatic degradation by lysozyme (pH 6.8).

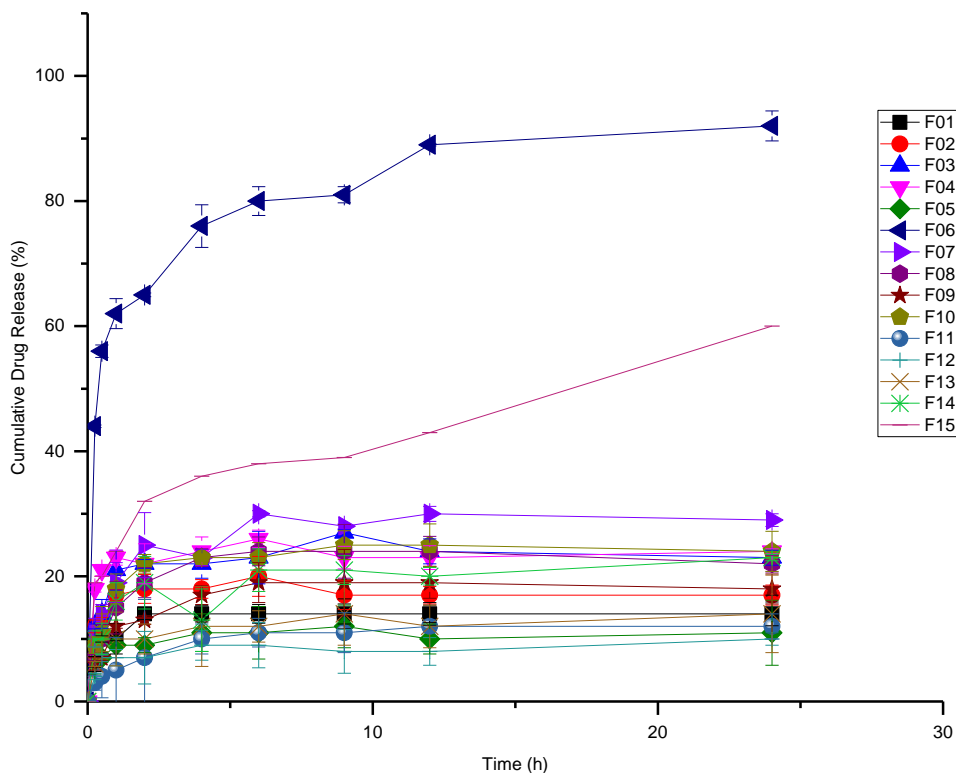


Figure 6.6: Cumulative drug release as near neutral pH 7.4 (PBS).

During development, *in vitro* dissolution results are used as a guide to formulation optimisation and to compare different formulations (Table 6.3). Dissolution efficiency (DE) is then the area under the dissolution curve between time points and expressed as a percentage of the curve at maximum dissolution, over the same time period [22]. DE is utilized in this study due to disintegration of the chitosan layer during hydrolysis and enzymatic degradation. Thus, the rate the rate of disintegration of chitosan will affect the dissolution and afterward the therapeutic efficacy of the therapeutic. In this study, the comparison between each formulation was conducted to assess the equivalence of each formulation. If the differences of the mean dissolution efficiencies as well as the 95% confidence intervals are within appropriate limits ($\pm 10\%$), one can conclude that the reference and test dissolution profiles are equivalent [14]. In pH 4.5 system, F05 (38%) and F13 (42%) had the lowest value below the 50-100%. Whilst in lysozyme system (pH 6.8), F15 had the lowest value of 47%. In pH 7.4, only F06 had the highest value of 78%.

Based on the DOE, these are the formulation had had low amine surface. F06 had the lowest drug content, which explains the high concentration in all systems.

Contrary to F15, which also had low drug content, in enzymatic media the dissolution efficiency was the lowest. However, this had high drug leaching at pH 7.4. This can correlate to the slow drug diffusion out of the particle. Evaluation of release exponent shows Fickian diffusion in pH 7.4 for all formulations due to drug leaking. In pH 6.8, F03, F06 and F07 had high values indicating super Case II. Whereas, in pH 4.5 formulations F07 showed super case transport, whilst F03 showed non-Fickian transport. For MDT, the large values indicate a higher drug retarding ability of the formulation, whereas high DE aids in comparison of the efficiency of the formulations. Furthermore, the closer the DE value is to 1, this can be theoretically related to *in vivo* data in delivery efficiency, if it is assumed that the degree of drug absorption *in vivo* is proportional to the concentration of the drug in solution and the time the solution is in contact with absorptive layers. [23].MD in pH 7.4 was not evaluated as 60% was not release within the *in vitro* release studies duration. However low DE values shown better retaining of the drug, whereby F15 and F06 had the worst profile in drug retaining properties, which can relate to low surface amine in correlation to the pore size, thus leading to instable chitosan gating effects. F02 and F12 showed best results in correlation to surface amine.

Table 6.3: Mean Dissolution Time (MDT), Dissolution Efficiency (DE) and Release Exponent (n)

Formulation	pH 4.5			pH 6.8			pH 7.4		
	n	MDT	DE	n	MDT	DE	n	MDT	DE
F01	0.202	0.459	0.790	0.306	0.434	0.965	0.127	-	0.136
F02	0.212	1.602	0.513	0.793	0.419	0.961	0.065	-	0.172
F03	0.716	0.268	0.978	0.871	0.228	0.986	0.123	-	0.232
F04	0.197	1.564	0.552	0.682	0.419	0.975	0.048	-	0.233
F05	0.221	3.032	0.375	0.627	0.730	0.913	0.130	-	0.104
F06	0.355	0.207	0.976	0.984	0.248	0.987	0.146	-	0.829
F07	0.931	0.476	0.476	1.837	0.305	0.982	0.181	-	0.276
F08	0.237	0.691	0.820	0.190	0.125	0.988	0.191	-	0.223
F09	0.208	0.977	0.674	0.469	0.194	0.985	0.208	-	0.175
F10	0.375	0.396	0.963	0.459	0.193	0.986	0.170	-	0.234
F11	0.242	1.212	0.662	0.698	1.739	0.687	0.269	-	0.107
F12	0.206	0.956	0.702	0.367	0.325	0.960	0.125	-	0.084
F13	0.181	0.683	0.417	0.354	0.547	0.931	0.122	-	0.124
F14	0.261	0.956	0.728	0.659	0.216	0.988	0.167	-	0.198
F15	0.424	0.228	0.987	0.290	6.218	0.466	0.258	-	0.435

6.3.5. Effect of synthetic parameters (Box-Behnken design)

In figure 6.7, there is a clear observation that molar ratio of TEOS to water plays a significant role in the size of the nanoparticles. Large amounts of water results in higher degree of polymerization. High alkali pH's were chosen in this study as it is known that high pH (more porous structures form) affects the dissolution of silica more than at low pH (fine pore networks and dense structure are obtained) [24]. Thus, at high pH values, nucleation and growth are the favoured mechanisms. Due to TEOS less sensitivity to hydrolysis due to Si being less electronegative, the rate of hydrolysis and condensation can be changed by changing the pH [3]. Apart from impact of pH, the selected emulsion solvent chloroform enabled reduction of particle-to-particle distance reduction due to solvent evaporation. F11 is an indicator of the impact of pH on the pore structure. It is known that the surfactant can be removed at calcination temperature of 350°C. The selection of 550°C as the maximum calcination temperature was based on literature, that indicates that an increase in hydrophilicity can occur up to temperature of 550°C where progressive loss of the hydrophobic effects of the alkyl chains occurs[25]. The 450°C was selected as it has been reported that many of the Si-O-Si bonds are not stable at temperature below 450°C [26].

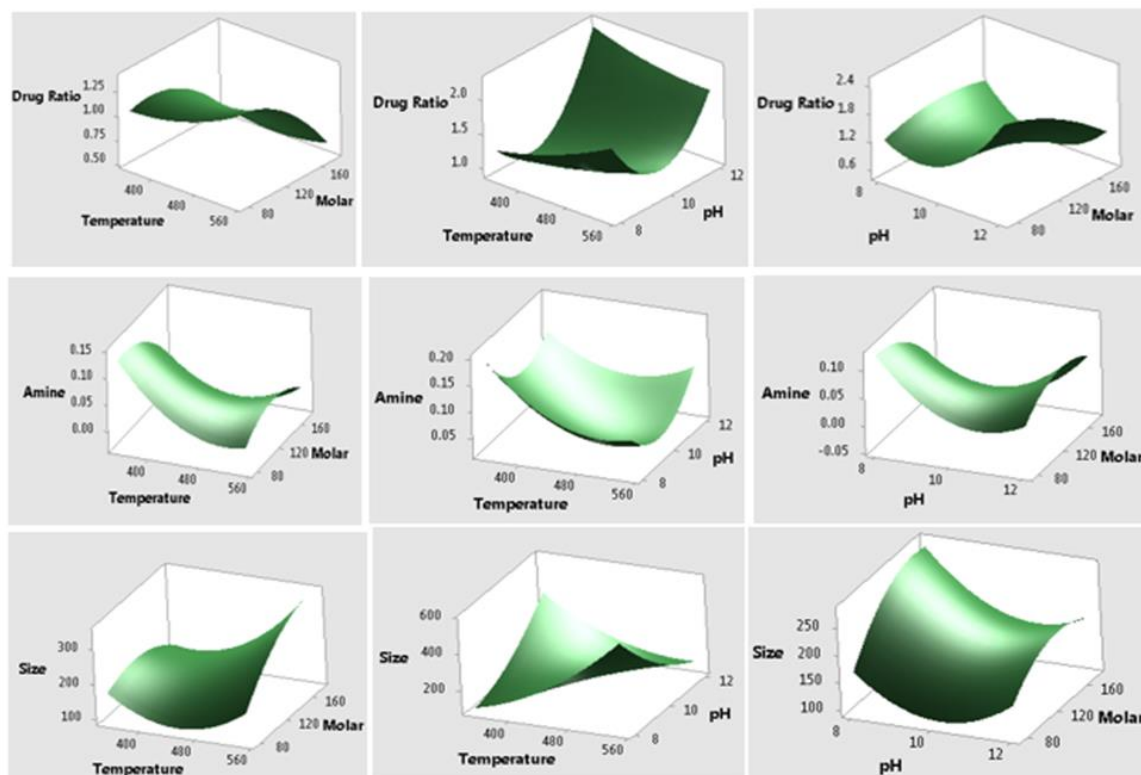


Figure 6.7: Surface plots showing the response of each parameter role on critical physiochemical properties of the MSNs.

6.4. Concluding remarks

The purpose of the experiment was to evaluate the synthetic parameter impact on MSNs application in drug delivery system. DOE evaluation indicates that post-synthesis grafting, and large drug ratio encapsulation and particle size can be controlled via the mentioned parameters. During synthesis of MSNs, the control of the rates of hydrolysis, condensation, re-esterification, and dissolution are essential in generating tuneable MSNs physiochemical properties is required. The calcination temperature does not only play a role in surfactant removal, but also removal of hydroxyl groups. This makes the silica surface more hydrophobic. Further evaluation of the surface chemistry is warranted for assessment of the post-grafting condensation reaction kinetics. With combination of computational model, the degree of post-grafting synthesis can aid in generating well capped MSNs (prevent drug leaching). The control of the synthetic parameters has allowed the evaluation of the impact of pH on pore structure that ultimately affects drug entrapment and release kinetics. Evaluation has also shown calcination temperature on the impact of surface hydrophilicity in post-synthesis grafting. And ultimately control of particle size due to the ratio of TEOS to water. Furthermore, the DOE has allowed showing the variations in MDT and DE between different formulation and pH levels. Thus, the bioavailability of rifampicin can be controlled through the change in nanoparticles pore size and volume. Conventional MSNs can load a dose of therapeutic drug with 200-300mg (maximally about 600mg) drug/1g silica [27]. In this study, the amount of drug loaded was drastically increase by 3 folds in highly porous formulations. Chapter 8 discusses the optimized MSNs based the observed synthetic parameters.

6.5. Reference

- [1] C. Brinker, Hydrolysis and condensation of silicates: effects on structure, *Journal of Non-Crystalline Solids*, 100 (1988) 31-50.
- [2] C. Barbé, J. Bartlett, L. Kong, K. Finnie, H.Q. Lin, M. Larkin, S. Calleja, A. Bush, G. Calleja, Silica Particles: A Novel Drug-Delivery System, *Advanced Materials*, 16 (2004) 1959-1966.
- [3] C.A. Milea, C. Bogatu, A. DuȚĂ, THE INFLUENCE OF PARAMETERS IN SILICA SOL-GEL PROCESS, *Bulletin of the Transilvania University of Brasov, Series I: Engineering Sciences*, 4 (2011) 59-66.
- [4] D. Balköse, Effect of preparation pH on properties of silica gel, 2007.
- [5] Z.W. He, C.M. Zhen, X.Q. Liu, W. Lan, D.Y. Xu, Y.Y. Wang, Microstructural characterization of low dielectric silica xerogel film, *Thin Solid Films*, 462-463 (2004) 168-171.
- [6] S.H. Wu, C.Y. Mou, H.P. Lin, Synthesis of mesoporous silica nanoparticles, *Chem Soc Rev*, 42 (2013) 3862-3875.

- [7] K.S.R. Raju, M. Gundeti, M.Y. Malik, N. Kadian, M. Rashid, I. Taneja, S.P. Singh, M. Wahajuddin, Bioanalysis of antitubercular drugs using liquid chromatography, *Journal of Pharmaceutical and Biomedical Analysis*, 134 (2017) 295-309.
- [8] A.A. Karnachi, M.A. Khan, Box-behnken design for the optimization of formulation variables of indomethacin coprecipitates with polymer mixtures, *International Journal of Pharmaceutics*, 131 (1996) 9-17.
- [9] H.-T. Lu, Synthesis and characterization of amino-functionalized silica nanoparticles, *Colloid Journal*, 75 (2013) 311-318.
- [10] M. Mohammad Alavi Nikje, Z. Mazaheri Tehrani, A. Bagheri Garmarudi, M. Haghshenas, Chemical Treatment of Silica Nanoparticles by Diethanolamine and γ -Glycidoxypropyltrimethoxysilane and Application of Modified Nanoparticles in Epoxy-Based Composites, *Polymer-Plastics Technology and Engineering*, 48 (2009) 891-896.
- [11] Y. Zhang, M. Huo, J. Zhou, A. Zou, W. Li, C. Yao, S. Xie, DDSolver: An Add-In Program for Modeling and Comparison of Drug Dissolution Profiles, *The AAPS Journal*, 12 (2010) 263-271.
- [12] S. Dash, P.N. Murthy, L. Nath, P. Chowdhury, Kinetic modeling on drug release from controlled drug delivery systems, *Acta poloniae pharmaceutica*, 67 (2010) 217-223.
- [13] M.L. Vueba, L.A.E. Batista de Carvalho, F. Veiga, J.J. Sousa, M.E. Pina, Influence of cellulose ether polymers on ketoprofen release from hydrophilic matrix tablets, *European Journal of Pharmaceutics and Biopharmaceutics*, 58 (2004) 51-59.
- [14] L. Kassaye, G. Genete, Evaluation and comparison of in-vitro dissolution profiles for different brands of amoxicillin capsules, *African Health Sciences*, 13 (2013) 369-375.
- [15] J. Wang, Z.H. Shah, S. Zhang, R. Lu, Silica-based nanocomposites via reverse microemulsions: classifications, preparations, and applications, *Nanoscale*, 6 (2014) 4418-4437.
- [16] X. Wang, Y. Zhang, W. Luo, A.A. Elzatahry, X. Cheng, A. Alghamdi, A.M. Abdullah, Y. Deng, D. Zhao, Synthesis of Ordered Mesoporous Silica with Tunable Morphologies and Pore Sizes via a Nonpolar Solvent-Assisted Stöber Method, *Chemistry of Materials*, 28 (2016) 2356-2362.
- [17] O. Malay, I. Yilgor, Y.Z. Menciloglu, Effects of solvent on TEOS hydrolysis kinetics and silica particle size under basic conditions, *Journal of Sol-Gel Science and Technology*, 67 (2013) 351-361.
- [18] A. Beganskienė, V. Sirutkaitis, M. Kurtinaitienė, R. Juškėnas, A. Kareiva, FTIR, TEM and NMR investigations of Stöber silica nanoparticles, *Mater Sci (Medžiagotyra)*, 10 (2004) 287-290.
- [19] P. Innocenzi, Infrared spectroscopy of sol-gel derived silica-based films: a spectro-microstructure overview, *Journal of Non-Crystalline Solids*, 316 (2003) 309-319.

- [20] L. Teresa Díaz-Faes, G. Alfonso Fernández, R. Ángel Del, M. María, E.D.-G. Marta, B.-L. Rosana, Engineered silica nanoparticles as additives in lubricant oils, *Science and Technology of Advanced Materials*, 16 (2015) 055005.
- [21] T. Kobayashi, D. Singappuli-Arachchige, Z. Wang, I.I. Slowing, M. Pruski, Spatial distribution of organic functional groups supported on mesoporous silica nanoparticles: a study by conventional and DNP-enhanced ²⁹Si solid-state NMR, *Physical Chemistry Chemical Physics*, 19 (2017) 1781-1789.
- [22] N.H. Anderson, M. Bauer, N. Boussac, R. Khan-Malek, P. Munden, M. Sardaro, An evaluation of fit factors and dissolution efficiency for the comparison of in vitro dissolution profiles, *Journal of Pharmaceutical and Biomedical Analysis*, 17 (1998) 811-822.
- [23] K.A. Khan, The concept of dissolution efficiency, *Journal of Pharmacy and Pharmacology*, 27 (1975) 48-49.
- [24] J. Estella, J.C. Echeverría, M. Laguna, J.J. Garrido, Effects of aging and drying conditions on the structural and textural properties of silica gels, *Microporous and Mesoporous Materials*, 102 (2007) 274-282.
- [25] M.T. Keene, R.D. Gougeon, R. Denoyel, R.K. Harris, J. Rouquerol, P.L. Llewellyn, Calcination of the MCM-41 mesophase: mechanism of surfactant thermal degradation and evolution of the porosity, *Journal of Materials Chemistry*, 9 (1999) 2843-2849.
- [26] C.J. Barbé, D.J. Cassidy, G. Triani, B.A. Latella, D.R.G. Mitchell, K.S. Finnie, K. Short, J.R. Bartlett, J.L. Woolfrey, G.A. Collins, Sol-gel bonding of silicon wafers, *Thin Solid Films*, 488 (2005) 153-159.
- [27] C. Bharti, U. Nagaich, A.K. Pal, N. Gulati, Mesoporous silica nanoparticles in target drug delivery system: A review, *Int J Pharm Investig*, 5 (2015) 124-133.

7. : EVALUATION OF SYNTHETIC PARAMETERS OF GELATIN SPHERES THROUGH BOX-BEHNKEN DESIGN

7.1. Introduction

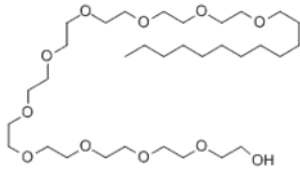
Gelatin remains one of the commonly used natural biopolymer in drug delivery[1]. Its use range from use in gelatin capsules to utilization of gelatin-based nanoparticles. The biopolymer is readily affordable and offers biocompatibility and biodegradability. The various active groups due to various amino acids, offers the possibility of conjugation of various molecules[2]. Due to its biodegradability and biocompatibility, gelatin occurs to be a good option for pulmonary drug delivery. In pulmonary drug delivery, the carrier must not bear any surface physiochemical properties that could induce inflammatory response. It is known that the pulmonary system bears various defense mechanisms against various foreign particulates[3, 4]. The activation of the defense system can lead to particles being removed before delivering the cargo. In drug delivery, the rapid pulmonary cleanse of the carriers can lead to sub-optimal dose reaching the delivery zone[5]. One of the main clearance mechanisms is rapid removal of particles of $5\mu\text{m}$ in size trapped in the upper respiratory tract. The particles of $1-5\mu\text{m}$ are known to be able to reach the deep lung where clearance is slower and involving innate immune response[6].

Innate immune response involves the removal of particles by means of macrophages. In drug delivery, the macrophages can be targeted for treatment of tuberculosis. Tuberculosis infects macrophages, which engulf inhaled bacteria bacilli. This leads to bacteria rapidly growing in the macrophages, which eventually lead to formation of granuloma. More macrophages will be recruited into this region in a defense mechanism to contain the biological threat. Various enzymes are also secreted during the defense process such as matrixmetallo proteinase, which breaks down the collagen for tissue remodeling. It is known that the enzyme is secreted in inflammatory disease. Due to collagen being the parent macromolecule of gelatin, the enzyme reach environment offers a region of degradation of the gelatin carriers in targeted delivery. Due to macrophages being the target for delivery anti-TB drugs, the intracellular drug release of the drugs is essential in ensuring that a high dose of drugs is release at targeted site. It has been shown that inflammatory site and intracellular environment have are more acidic environment.

In this study, a synthesized hydrazone is used as a crosslinker for pH stimuli response. Prior to crosslinking with a pH responsive linker, the particles are synthesized by emulsion and

coacervation technique. Briefly, due to hydrophilic nature of gelatin, this makes it able to interact with hydrophobic molecules. Thus, allowing the hydrophobic interaction leading to micelle-like spheres due to conformation changes. Two non-ionic surfactants are assessed on the degree of interaction with gelatin (Table 7.1). Brij® 52, (Polyethylene glycol hexadecyl ether) has a Hydrophile-Lipophile Balance (HLB) of 5, whereas C₁₂E₁₀ has an HLB of 12.8. Thus, the surfactants have different modes of formation of micelles. These are utilized to induce control of micelle formation during hydrophobic interaction with gelatin molecules. Gelatin, the biopolymer, is a polypeptide with representation, (Gly-X-Y)_n, where X is amino acid residue. It is made up of 18 amino acids with glycine (32-35%), proline (11-13%), alanine (10-11%), hydroxyproline (9-19%), glutamic acid (7-8%), aspartic acid (4–5%) and arginine (5%) predominant[7].

Table 7.1: Table illustrating the properties of the surfactants used for protein-surfactant interaction

Properties	Brij 52	C ₁₂ E ₁₀
Molecular weight	Mn~330	626.86 g/mol
HLB	5.3	12.8
density	0.978g/mL	0.99g/mL
Solubility	Oil soluble (Oil-in-Water)	Water soluble (Water-in-Oil)
State	Semi-solid	Wax
Structure	$C_{16}H_{33} \left[\text{O} \text{---} \text{CH}_2 \text{---} \text{CH}_2 \right]_n \text{OH}$	

7.2. Material and methods

7.2.1. Materials

Brij 52 (SP Brij® C2 MBAL-SO-(SG)), C₁₂E₁₀, fluorescein, chloroform and gelatin were purchased from Sigma-Aldrich. The samples were prepared using Millipore water. The samples containing gelatin and surfactants were prepared afresh using 10mM phosphate buffer.

7.2.2. Experimental design

A three-factor, three-level Box Behnken design was used for experimental design and optimization procedures. This design was selected for the study as it is suitable for exploration of quadratic response surfaces and constructs a second order polynomial model, thus helping in optimizing a process using a small number of experimental runs. The design consisted of replicated centre

points and the set of points lying at the midpoints of each edge of the multidimensional cube that defines the region of interest [8].

7.2.3. Critical micelle and critical association concentration

Ultra Violet (UV) spectrometry was used for the assessment of critical micelle concentration (CMC) and critical association concentration (CAC). The UV spectra were measured using high transparency quartz cuvettes of 1cm path length. Following Ledbetter & Bowen method (1969), fluorescein was used for spectrophotometric determination of the CMC of Brij 52 and C₁₂E₁₀[9]. Briefly; dye stock solutions of 5.00X10⁻⁶M and 1.00X10⁻⁵M were prepared using fluorescein disodium salt. Solutions of the surfactants were then prepared using each of the dye stock solutions (Table 7.2). These solutions were then allowed to stand for 2 hours and then analyzed using UV-analysis (PerkinElmer). The quant scan was used to change in absorption intensity and to also confirm absorption shift to due micellization. The wavelength at 515nm was identified and used as the maximum absorption peak of fluorescein.

Table 7.2: formulations for critical micelles concentration determination

Formulation	Brij 52 (mM)	C ₁₂ E ₁₀ (mM)
1	0.0000	0.0000
2	3.0300e ⁻⁷	1.7700e ⁻⁷
3	3.0300e ⁻⁶	1.7740e ⁻⁶
4	3.0300e ⁻⁵	1.7749e ⁻⁵
5	3.0300e ⁻⁴	1.7749e ⁻⁴
6	3.0300e ⁻³	1.7749e ⁻³
7	0.0303	0.0177
8	0.303	0.1775
9	3.03	1.7749
10	30.3	17.749
11	303.0	177.49

7.2.4. Dynamic light scattering study of gelatin-surfactant interaction

Dynamic light scattering analyses were conducted on Zetasizer Malvern instrument (Zetasizer Nano Series,). The gelatin solution (0.5%) was prepared by dissolving gelatin powder in 10mM PBS and heated at 55°C for 1 hour under stirring. The respective surfactant concentrations

ranging from 0-100mM (C₁₂E₁₀) and 0-50mM (Brij 52) were made using the gelatin solution. As illustrated by Chodankar and colleagues (2017), The signal generated by the light scattering from diffusing particles can be analyzed by its intensity autocorrelation function [10]

$$G^I(\tau) = \langle I(t)I(t + \tau) \rangle \quad (7.1)$$

Where I(t) is the scattered light intensity at time t and I(t+) is the scattered light intensity at some later time (t+τ). The normalized intensity autocorrelation function is

$$g^I(\tau) = G^I(\tau)/\langle I(t) \rangle^2 \quad (7.2)$$

The electric field autocorrelation function is related to the normalized intensity autocorrelation function by

$$g^I(\tau) = 1 + B[g^E(\tau)]^2 \quad (7.3)$$

For a mono-disperse system of particles follows a simple exponential decay with decay constant γ

$$g^E(\tau) = \exp[-\gamma\tau] \quad (7.4)$$

The average decay rate (γ) of has been estimated using the method of cumulants. The apparent diffusion coefficient (D_a), which represents an average diffusion coefficient of the protein macromolecules, is obtained from the relation $\gamma = D_a Q^2$ and the corresponding effective hydrodynamic size is calculated using Stoke-Einstein relationship. For the determination of the conformational changes of gelatin, the Perrin's factor can be used. For non-spherical particles, the Perrin or shape factor (F) can be used to estimate particle shape. The Perrin factor is defined as the ratio of the frictional coefficient for a sphere with the same volume as the particle being measured to the frictional coefficient for a sphere with the same mass as the particle being measured. The Perrin factor (F) is:

$$F = f_{vol}/f_{mass} = 6\pi D_{vol}/6\pi D_{mass} = D_{vol}/D_{mass} = D_H/D_{mass} \quad (7.5)$$

Where the hydrodynamic diameter is measured, is the diameter by mass calculated from the known molecular weight and the specific volume of the particle and is the particle frictional coefficient.

7.2.5. Gelatin conformational changes through circular dichroism

The evaluation of the gelatin conformational changes was evaluated using circular dichroism instrument. It is expected that the interaction of gelatin with surfactant will induce conformational changes as observed in figure 7.1. These changes are hypothesized to affect degree of crosslinking, swelling and drug release rate. A gelatin solution (0.5mg/mL) was created using 10mM PBS (pH 7.2). To each gelatin solution, respective amount of non-ionic surfactant was added to make a final solution of surfactant (0-0.8mg/mL). Each test was conducted in triplicate, with samples filtered using 0.22µm membrane filter prior analysis. Applied-Photophysics MCD was used in this experiment (Applied Photophysics, Leatherhead, UK). The machine was purged with nitrogen for an hour prior to analysis. Chira scan software was used for data acquisition, followed by use of deconvolution using CDNN for secondary structure analysis. Wavelength of between 185-300nm was used with 0.5nm step. The monochromator bandwidth was set to 1.5nm; with a sampling rate of 1 sec. smoothing of curves was done using 20 points. All CD spectra are represented as the mean residue ellipticity, in deg cm²/dmol. The α-helical content was determined from the mean residue ellipticities at 222nm, as illustrated in equation

$$\%Helix = ([\theta]_{obs} \times 100) / \{[\theta]_{helix} \times (1 - 2.57/l)\} \quad (7.6)$$

Where $[\theta]_{obs}$ is the mean-residue ellipticity observed experimentally at 222nm, $[\theta]_{helix}$ is the ellipticity of gelatin[11]

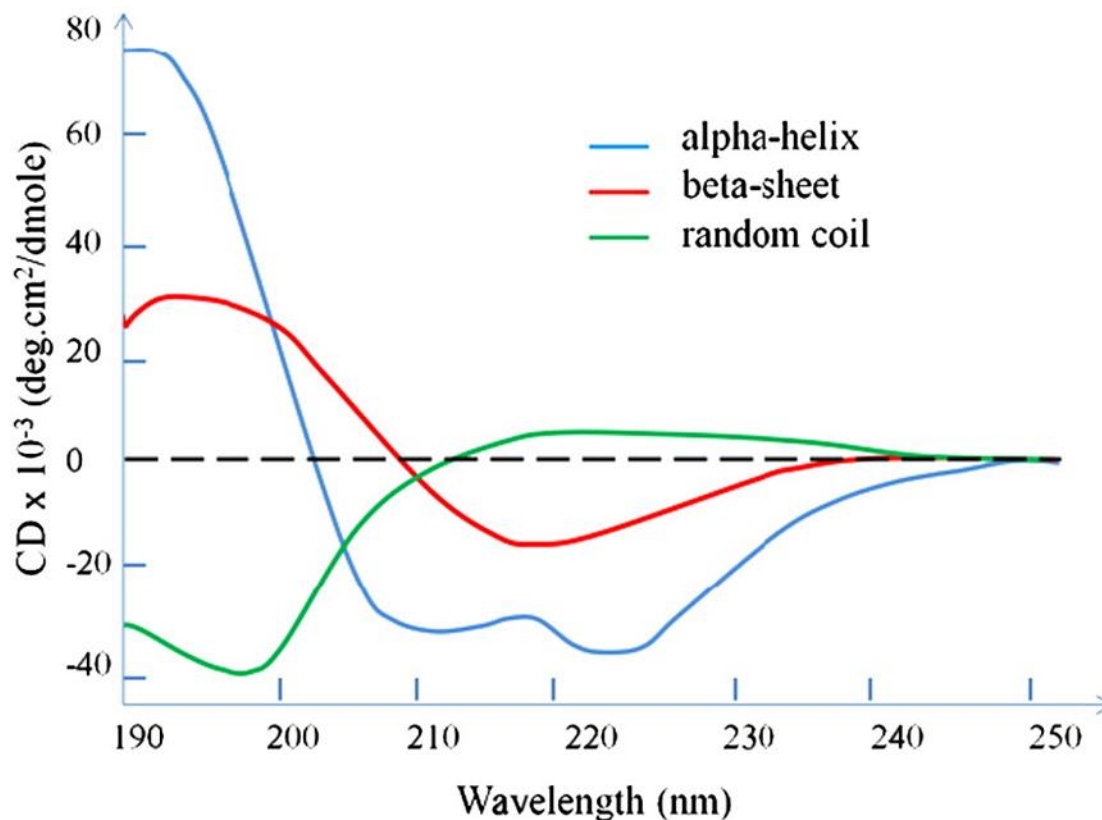


Figure 7.1: Standard CD spectra of the three basic secondary structures of a polypeptide chain (α -helix, β -sheet and random coil (Adapted from [12])

7.2.6. Synthesis of pH responsive hydrazone linker

A solution consisting of 50mL ethanol and 14.8mL 99% hydrazine hydrate (0.30mol) was placed in the flask reactor (Figure 7.2). 15mL 2,4-pentandione (0.15mol) dissolved in 20mL ethanol was added dropwise while stirring at the room temperature for one hour. Then the solution was heated to reflux for 5 hours. The solution was concentrated at reduced pressure, and then the residue solid was washed with petroleum ether, filtered and dried at 60°C to give white solid. NMR: ^1H NMR (300MHz, DMSO) δ 12.07, 5.73, 3.52, 2.13ppm.



Figure 7.2: Schematic for the synthesis of hydrazone.

7.2.7. Synthesis of gelatin nanoparticles

A solution (20mL) of 20% gelatin, respective amount of surfactant concentration could equilibrate at 60°C overnight (Table 7.3).

Table 7.3: Formulation strategies for the impact of non-ionic surfactant (Box–Behnken design)

Formulation	Surfactant (mM)	Sonication (min)	Crosslink (min)
G01	192	45	60
G02	32	45	60
G03	112	45	90
G04	112	30	120
G05	32	60	90
G06	192	45	120
G07	112	45	90
G08	112	30	60
G09	112	60	60
G10	32	45	120
G11	32	30	90
G12	192	60	90
G13	112	60	120
G14	192	30	90
G15	112	45	90

The solution was then mixed with 40mL chloroform and allowed for micellization at 60°C under the sonicator bath for respective time (Digital Ultrasonic Cleaner, PS-10A, Hilsonic, UK). The hot solution was then injected into the atomizer probe of the bench top ultrasonic atomizer nozzle generator at a constant rate (Ultrasonic Atomizer, Sonaer Inc., New York, USA). The generated atomized mist was at 30%, 60KHz frequency and power of 5-7 watts. The mist was dispersed into a flask of ice-chilled acetone under constant stirring for solidification of the dispersed gelatin spheres. The gelatin solidified spheres were then sonicated briefly to remove particles adhered to the glassware prior paper filtration (F1001 grade, 55mm Ø). Gelatin contains various amino acids whereby one-third are glycine residues, then proline and 4-hydroxyproline residues. A typical structure is -Ala-Gly-Pro-Arg-Gly-Glu-4Hyp-Gly-Pro-. This allows conjugation of the pH sensitive crosslinker as illustrated in Figure 7.3.

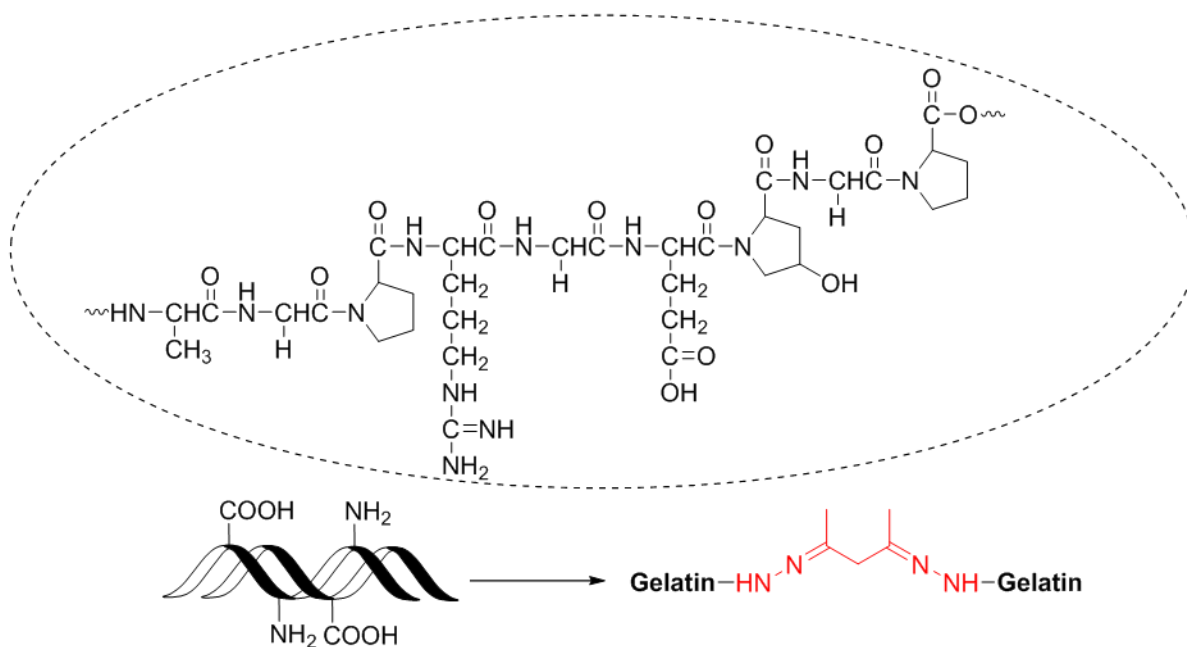


Figure 7.3: Synthesis of pH sensitive gelatin spheres via hydrazone linkage

7.2.8. X-ray powder diffraction (XRD)

Bruker D8 Discover (Billerica, Massachusetts, USA) was used for analysis of uncoated MSN and coated MSN crystallinity. Data were collected in the range of $2\theta = 10^\circ$ to 100° , scanning at $1.5^\circ \text{ min}^{-1}$ with a filter time-constant of 0.38 s per step and a slit width of 6.0mm. The MSN samples were placed on a silicon wafer slide. The X-ray diffraction data patterns were treated using the Eva (evaluation curve fitting) software. Baseline correction was performed by subtracting a spline function fitted to the curved background on each diffraction pattern [13].

7.2.9. Swelling studies

The swelling behavior of drug loaded gelatin nanoparticles was evaluated using two different pH buffer systems (pH 4.5 and 7.4) for over a 1-hour period. As illustrated by Sarmah and colleagues (2016) dry nanoparticles were weighed and were placed onto watch glasses and immersed with two buffer solutions of either pH 4.5 or 7.4 [14]. At predetermined time interval, the buffer medium was removed followed by blotting the particles with filter paper to eliminate the excess swelling medium from the surface. The weight of the swollen nanoparticles after definite time was taken. The swelling experiment was performed in duplicate and presented as mean value. The swelling percentages were calculated as:

$$\text{Swelling (\%)} = [(W_1 - W_2)/W_2] \times 100 \quad (7.7)$$

Where W_1 is the weight of the particle after swelling and W_2 is the weight of the dry particles before swelling.

7.2.10. Structural molecular analysis using infrared

FTIR was used to confirm the conjugation of the hydrazone onto the gelatin spheres. The analysis was conducted on a PerkinElmer AT-IR within 100 scans over a range of 550-4000 cm^{-1} .

7.2.11. Drug loading and drug content (rifampicin)

For drug loading of rifampicin, 100mg of nanoparticles were immersed in a solution of rifampicin to allow swelling in the solution until equilibrium (3 hours) was reached. The particles were then washed and lyophilized prior further use. Drug content was assessed through weighing 10mg of drug loaded nanoparticles and hydrolyzed for 30 minutes. The drug content was analyzed using UV and the entrapped amount obtained from equation following Chen and Hu (2011) method [15].

$$M_{measured} = M_{UV\ measured} / V_{supernatant\ volume} \quad (7.8)$$

$$EE(\%) = (M_{measured} / M_{initial\ load}) \times 100 \quad (7.9)$$

7.2.12. In vitro drug release

For in vitro drug release studies, phosphate buffer pH 7.4 and acetate buffer pH 4.5 were used. 20mL volume of dissolution media was used for studying diffusion through a dialysis tubing. To each dialysis tube 10mg drug loaded nanoparticles were added, followed by addition of 1mL of the respective buffer. The study was evaluated in duplicate, at 37°C \pm 0.5 on a Carousel Reaction Station™. The study was evaluated over 24 hours, with 2mL buffer sampling volume with replacement with fresh buffer. The supernatant fluid was collected for UV/Vis spectrophotometer. For analysis of drug release mechanism, literature method was used [16]

$$W_t / W_\infty = kt^n \quad (7.10)$$

Where W_t / W_∞ the fractional release at the time t and k is is rate constant. The exponent n, called as diffusional exponent is used as an indicator of the mechanism of drug transport. The value is between 0.5 and 1.0. When n=0.5, the release is Fickian, when=1 is considered zero order (Case

II transport). Within the range of $0.5 < n < 1$, the release is described as anomalous. When, t is the half-life. For the calculation of the diffusion coefficient, where the diffusion of the drug across the nanoparticle surface is assumed as one-dimensional, the early time equation can be used ($0 \leq W_t/W_\infty \leq 0.6$), where L is the diameter of the dry nanoparticle.

$$W_t/W_\infty = 4(D_t/\pi L^2)^{0.5} \quad (7.11)$$

The mean dissolution time (MDT) was also evaluated in this study for comparison between different formulations. This can be estimated from equation 7.12.

$$MDT = \int_0^{W_\infty} t \cdot dW(t) / \int_0^{W_\infty} dW(t) \quad (7.12)$$

Where $W(t)$ is the cumulative amount of drug dissolved at time, t . This equation is however application for in vitro and in vivo MDT correlation[17]. In terms of analysis of dissolution data, equation 7.13 was used

$$MDT = ABC/a_{tmax} \quad (7.13)$$

Where a_{tmax} the maximum amount of the dissolved drug and ABC is the area between the cumulative dissolution curve.

DE, dissolution efficiency was also evaluated, whereby the area under the dissolution curve up to a specific time, t , is expressed as a percentage of the area of the rectangle described by 100% dissolution in the same time [18].

$$DE = \left(\int_0^t y \cdot dt / y_{100} \cdot t \right) \times 100 \quad (7.14)$$

Where y is the percentage of drug dissolved at time t and y_{100} maximum percentage of drug dissolved over the time $0 - t$.

7.2.13. Statistical analysis

The data is presented as mean \pm standard deviation. Significant differences between group means were evaluated using one-way Anova, P value < 0.05. The analysis was performed using OriginPro (OriginLab Corporation, MA, USA).

7.3. Results and discussions

A nonionic surfactant can influence the physicochemical properties of a protein-stabilized emulsion by means of specific protein-surfactant interactions depletion flocculation. For a nonionic surfactant, specific interactions usually occur between the nonpolar tail of the surfactant molecule and any exposed hydrophobic patches on the protein molecule. Whereas, depletion flocculation occurs when the concentration of excess surfactant micelles in the aqueous phase exceeds a critical level and is the result of the osmotic pressure that arises because of the exclusion of micelles from a narrow region surrounding the droplet.

7.3.1. Determination of critical micelle concentration

In the spectral dye method when the dye-micelle complex is formed, the spectral characteristics of the dye are changed. This may result visually in a pronounced change in the colour or fluorescence of the solution. In the case of fluorescein above the solution exhibits a green fluorescence and a very slight pink coloration. However, below the CMC the fluorescence is quenched, and the solution is a light greenish-yellow. The absorption spectra in the visible region of the dye and the dye-micelle complex were determined. When the complex is formed the overall spectrum shifts bathochromically and a new maximum occurs. This represents a maximum difference in absorbance between the dye and the dye-micelle complex [9]. Figure 7.4 and 7.5 represents the CMC of Brij 52 and C₁₂E₁₀, respectively.

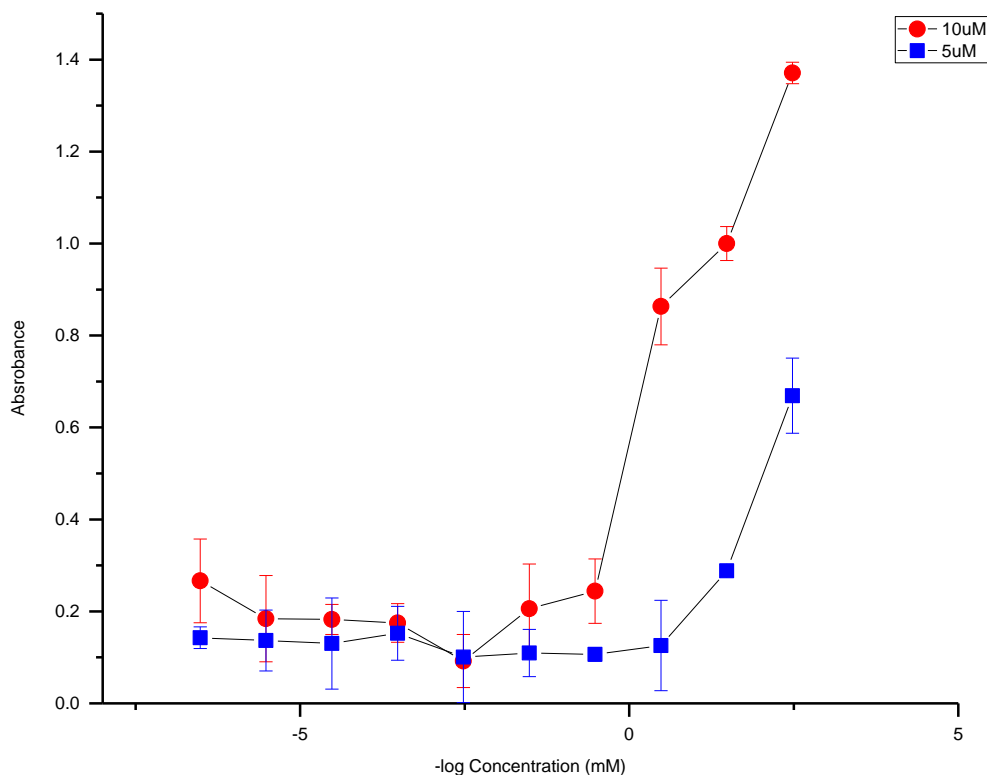


Figure 7.4: Determination of CMC of Brij 52 in water (3.2×10^{-4} mM).

Due to the difference in the HLB values of the surfactants, the micelles show a variation in CMC formation. Literature indicates that the HLB values for water-in-oil (W/O) emulsifiers lie within a range of 3.5-6, whilst those belonging to oil-in-water (O/W) are in the range 8-18 [19]. These characterized as wetting agents have HLB values in the range 7-9. Based on Brij 52 which is lipophilic, (HLB = 5.3), it shows that it is a W/O emulsifier, whilst $C_{12}E_{10}$ is hydrophilic (HLB=12.8) is an O/W emulsifier. To form kinetically stable emulsions, the surfactant type and shear forces for droplet formation play a major role in emulsions stability. Surfactants are required to for stabilization of emulsion against flocculation (cause by attractive versus repulsive forces), coalescence (caused by instability of the liquid film between the droplets), Ostwald ripening (caused by the solubility of the disperse droplets and the particle size distribution) and phase inversion (O/W emulsion inverts to W/O). Other issues are sedimentation and creaming, whereby gravitational or centrifugal forces exceed the thermal motion of the droplets (Brownian motion)

leading to aggregation [20]. Therefore, selection of appropriate surfactant concentration is vital in evading emulsion breakdown processes mentioned.

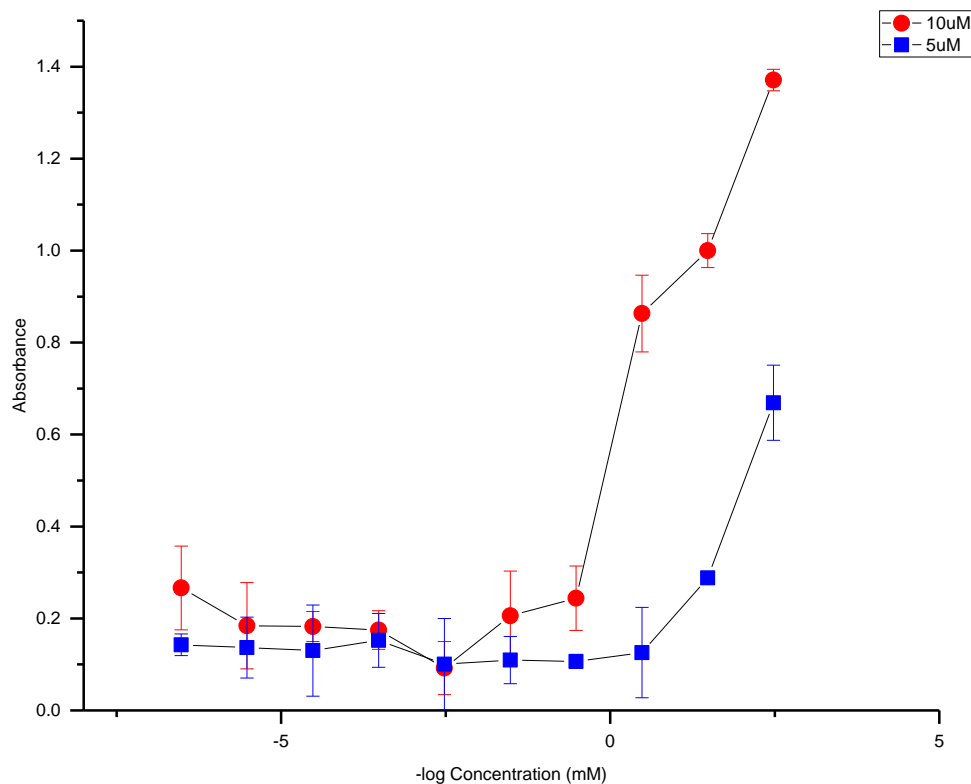


Figure 7.5: Determination of $C_{12}E_{10}$ CMC in water (1.58×10^{-6} mM).

7.3.2. Dynamic light scattering for critical micelle concentration

The change in aggregation number as well as hydrodynamic radius indicates that gelatin affects the micellar growth of the surfactants[21]. The axial ratio and Perrin's factor were also obtained from the light scattering analysis (Table 7.4). Due to gelatin being known to have a typical helix length ≈ 200 nm, the existence of gelatin molecules in mixed conformation state (random coil or helix) can be assessed by the Perrin factor[22]. Gelatin starts off as random coils. But when the concentration of the surfactant increases, the hydrophobic interaction with surfactants promotes relaxation of the coils into strands/rod-like conformation. This is supported by the CD data analysis.

Table 7.4: Evaluation of C₁₂E₁₀ and Brij 52

Concentration (mM)	Size (nm)	Aggregation Index	Perrin's factor
C₁₂E₁₀			
0.0	68.93	4.94	29.298
0.05	66.36	5.24	28.206
0.1	64.65	5.57	27.479
0.2	62.74	5.71	26.667
0.4	61.76	5.91	26.251
0.8	61.6	6.35	26.183
5.0	38.88	14.8	16.526
10.0	31.67	18.1	13.461
50.0	12.08	48.2	5.135
100.0	8.48	74.4	3.604
Brij 52			
0.0	56.47	9.90	24.002
0.05	59.83	8.79	25.430
0.1	59.58	7.05	25.328
0.2	65.43	5.17	27.811
0.4	88.67	4.29	37.689
0.8	147.7	1.24	62.779
1	466.1	1.45	198.112
8	56.47	9.90	24.002

Most biological polymers, such as proteins and nucleic acids and some synthetic polymers, have relatively inflexible chains. For rigid particles, the size is no longer of predominant importance, because the polymer chain is no longer in the form of a flexible random coil; instead, shape becomes an important parameter. Following are some theoretical proposals for the estimation of the shape factor p from the viscosity measurement. The term f/f_0 is sometimes denoted as p , Perrin constant. Gelatin is a low charge density polyampholyte, in the presence of a strong polyelectrolyte the charge distribution on gelatin can get polarized which enables it to assume an extended rod-like shape. However, in this study, non-ionic surfactants were used. The change in Perrin's factor indicate reduction in the molecular shape asymmetry due to inter and

intramolecular interactions. This information strongly correlates with circular dichroism data that shows that the surfactants can generate conformational changes. Thus, the determined critical association concentrations were determined by both DLS and UV to be 1.26×10^{-4} mM for Brij 52 and 3.16×10^{-5} mM for C₁₂E₁₀.

7.3.3. Fourier-transform spectroscopy analysis

Based on FTIR, it is also possible to attribute various conformation states, whereby $1645\text{-}1657\text{cm}^{-1}$ is stated to related to random coils and the 1660cm^{-1} band to triple helix, with contribution from α -helix and β -turns (Figure 7.6). Thus, the amide I component, at 1690 cm^{-1} , can be attributed to helices of aggregated gelatin. Peptides can be characterized by distinguishing feature of amide A, B, I, II, III, VII. The amide A band (about 3500cm^{-1}) and amide B (about 3100cm^{-1}) originate from a Fermi resonance between the first overtone of amide II and the N-H stretching vibration. Amide I and amide II bands are known as the two major bands of the protein infrared spectrum. The amide I band ($1600\text{-}1700\text{cm}^{-1}$) is mainly associated with the C=O stretching vibration and is directly related to the backbone conformation. Amide II results from the N-H bending vibration and from the C-N stretching vibration. This band is conformational sensitive. Whereas, Amide III and IV are stated as very complex bands resulting from a mixture of several coordinate displacements[23].

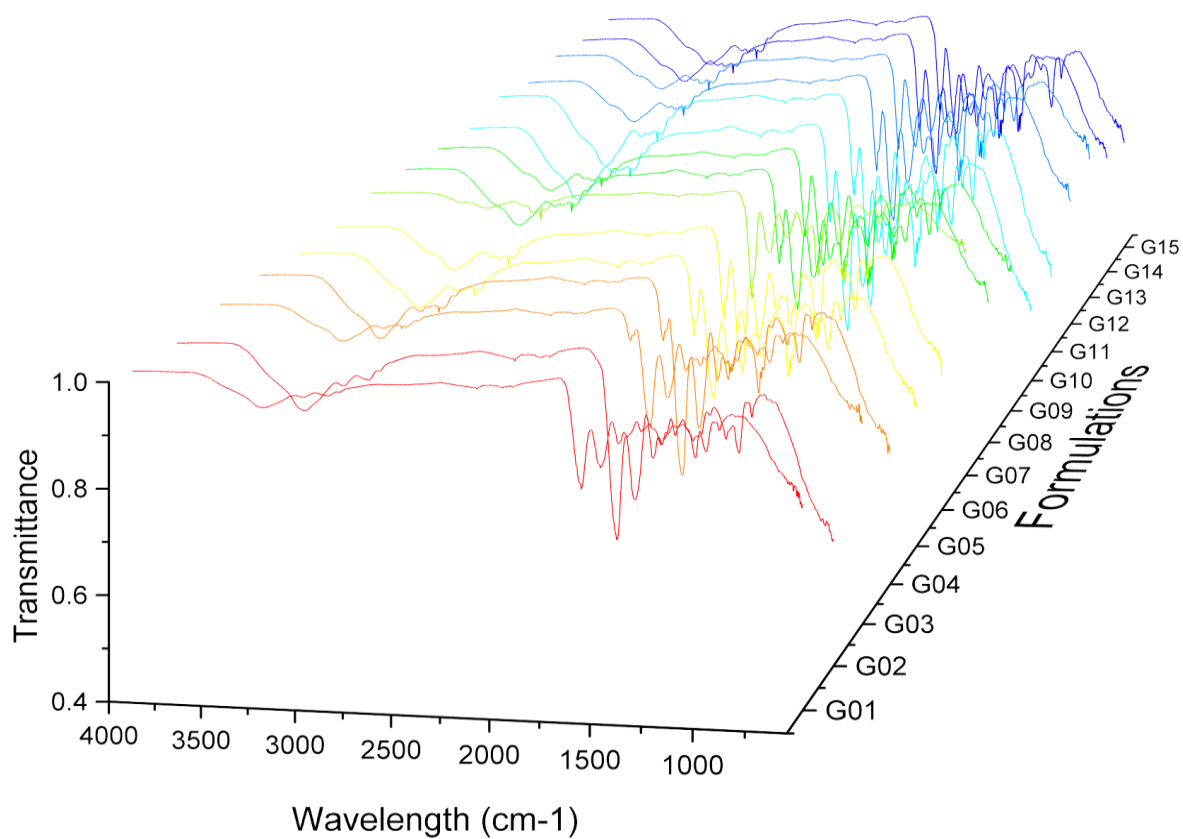


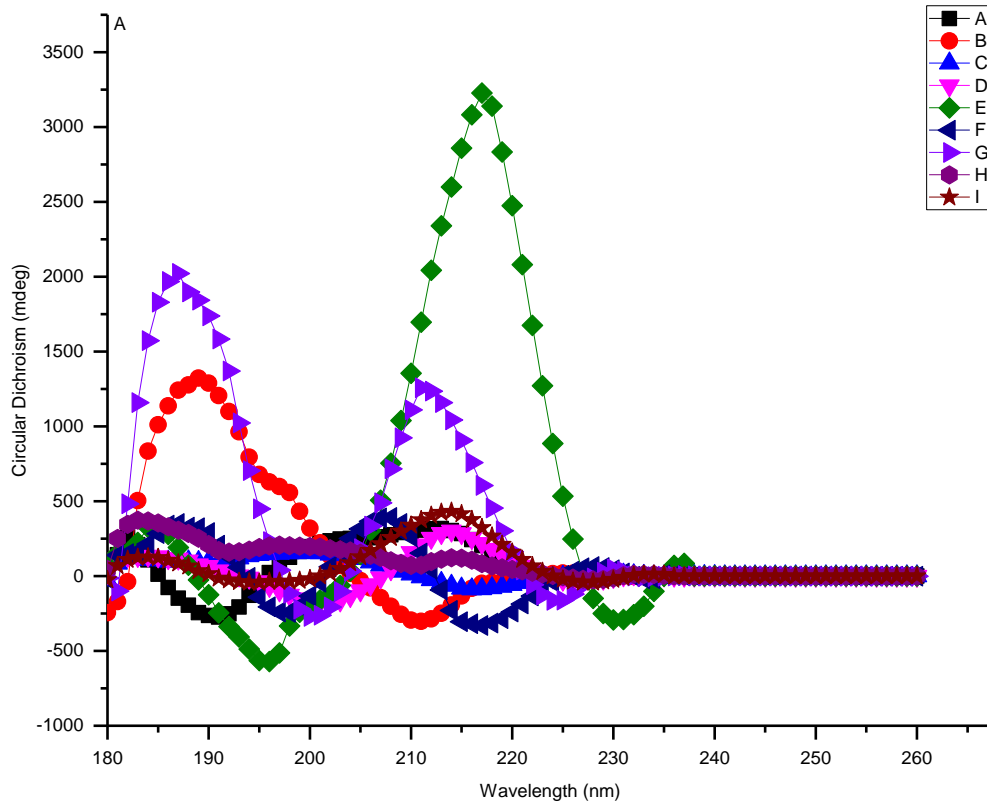
Figure 7.6: FTIR spectra of crosslinked gelatin spheres.

7.3.4. Conformational changes of gelatin in different surfactant concentrations

Circular dichroism is a tool used for assessing conformational (unfolding) changes (Figure 7.7). Protein–surfactant interactions can occur by means of hydrophobic and electrostatic interactions. It has been shown that there is significant dependence on polymer/surfactant type, its structure, molecular weight or other common variables such as pH and ionic strength on the degree on protein-surfactant [7]. Recent studies have shown that non-ionic surfactants do not have a significant impact on the protein structure [24]. The study shown that's there is accelerated coil-helix transition, due to hydrophobic interaction. It has been reported that gelatin has a relatively high content of apolar amino acids such as leucine and proline. When the CMC is reached and the viscosity of the solution increases, there is a non-cooperative hydrophobic binding of a small content of the nonionic surfactants to the polymer. Thus, the surfactants can cause a shielding of the apolar regions against the polar environment and promote the unfolding of the polymer. Through this interaction can also lead to renaturation[25].

Table 7.5: Depiction of surfactant concentration in figure 7.7

Formulation	Brij 52 (mM)	C ₁₂ E ₁₀ (mM)
A	0.0000	0.0000
B	3.0300e ⁻⁷	1.7700e ⁻⁷
C	3.0300e ⁻⁶	1.7740e ⁻⁶
D	3.0300e ⁻⁵	1.7749e ⁻⁵
E	3.0300e ⁻⁴	1.7749e ⁻⁴
F	3.0300e ⁻³	1.7749e ⁻³
G	0.0303	0.0177
H	0.303	0.1775
I	3.03	1.7749



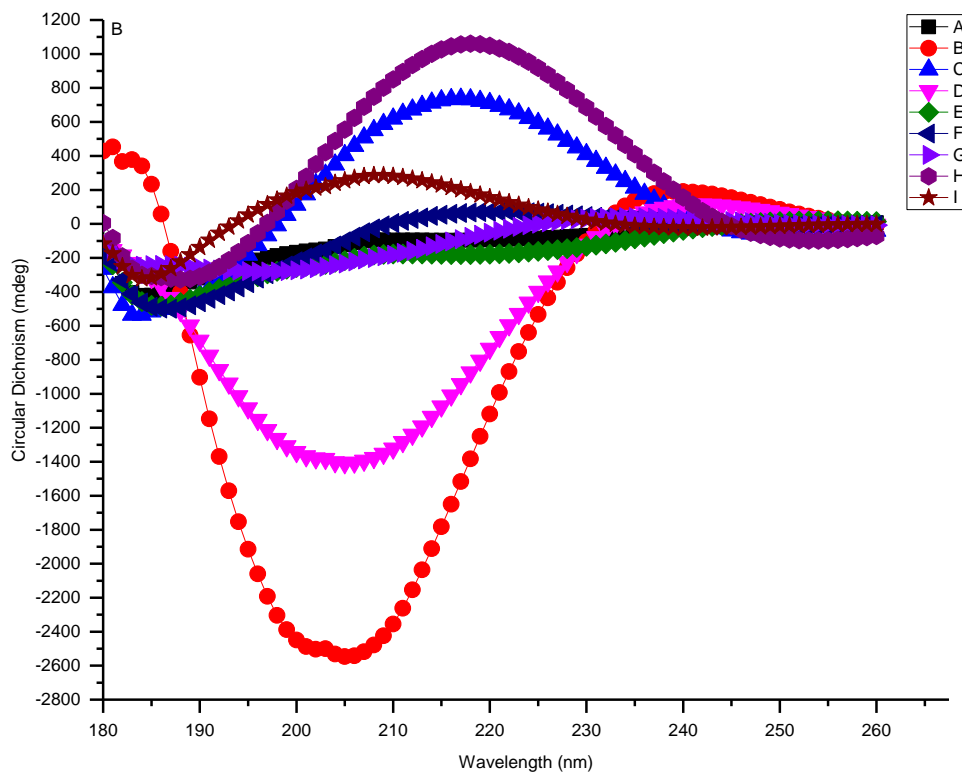


Figure 7.7: Circular dichroism data illustrating the folding of gelatin with various surfactant concentrations (A)-Brij 52 and (B)- $C_{12}E_{10}$

7.3.5. Degree of crystallinity analysis

XRD analysis was conducted to evaluate changes of gelatin crystallinity after crosslinking. A sharp peak that may represent the crystalline structure was observed at around 20° (Figure 7.8). This is a reported diffraction pattern of gelatin, which verifies the random coiled conformation of the macromolecules [26]. The intensity of the peak dropped after crosslinking with the hydrazine. The introduction of hydrazone bonds into the gelatin structure could have caused modification on the un-crosslinked gelatin texture (distortion of the coiled conformation and possibly the formation of the triple helix structure) thus leading to reduction in peak intensity. Although not all formulations were evaluated, it is expected that the crosslinking time can cause a variation in crystalline structure which will ultimately have an impact on the rate of gelatin swelling due to change in dissolution/solubility rate.

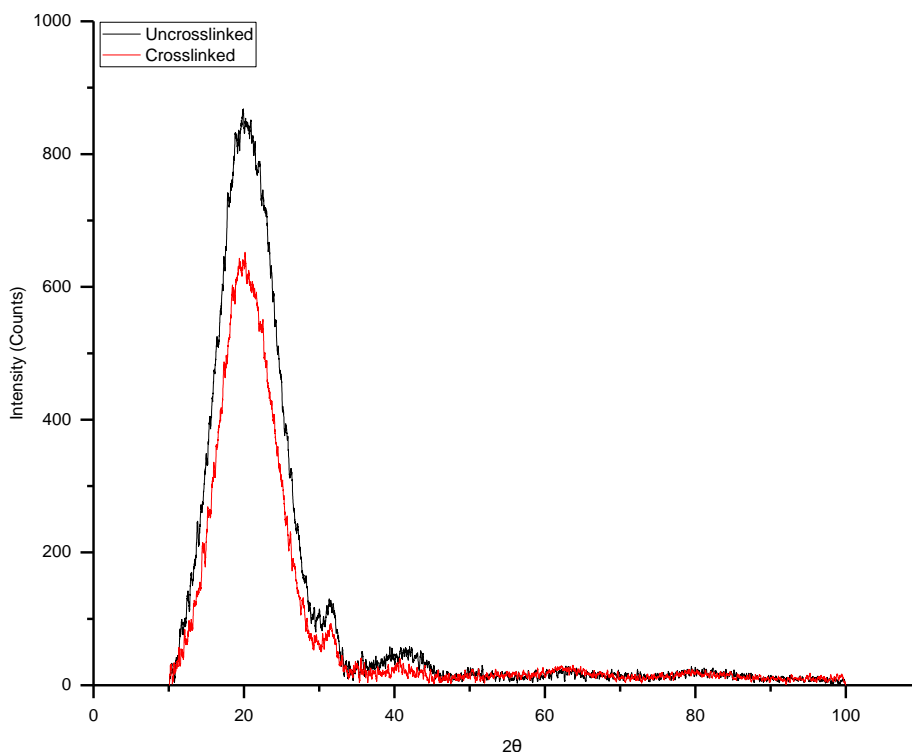
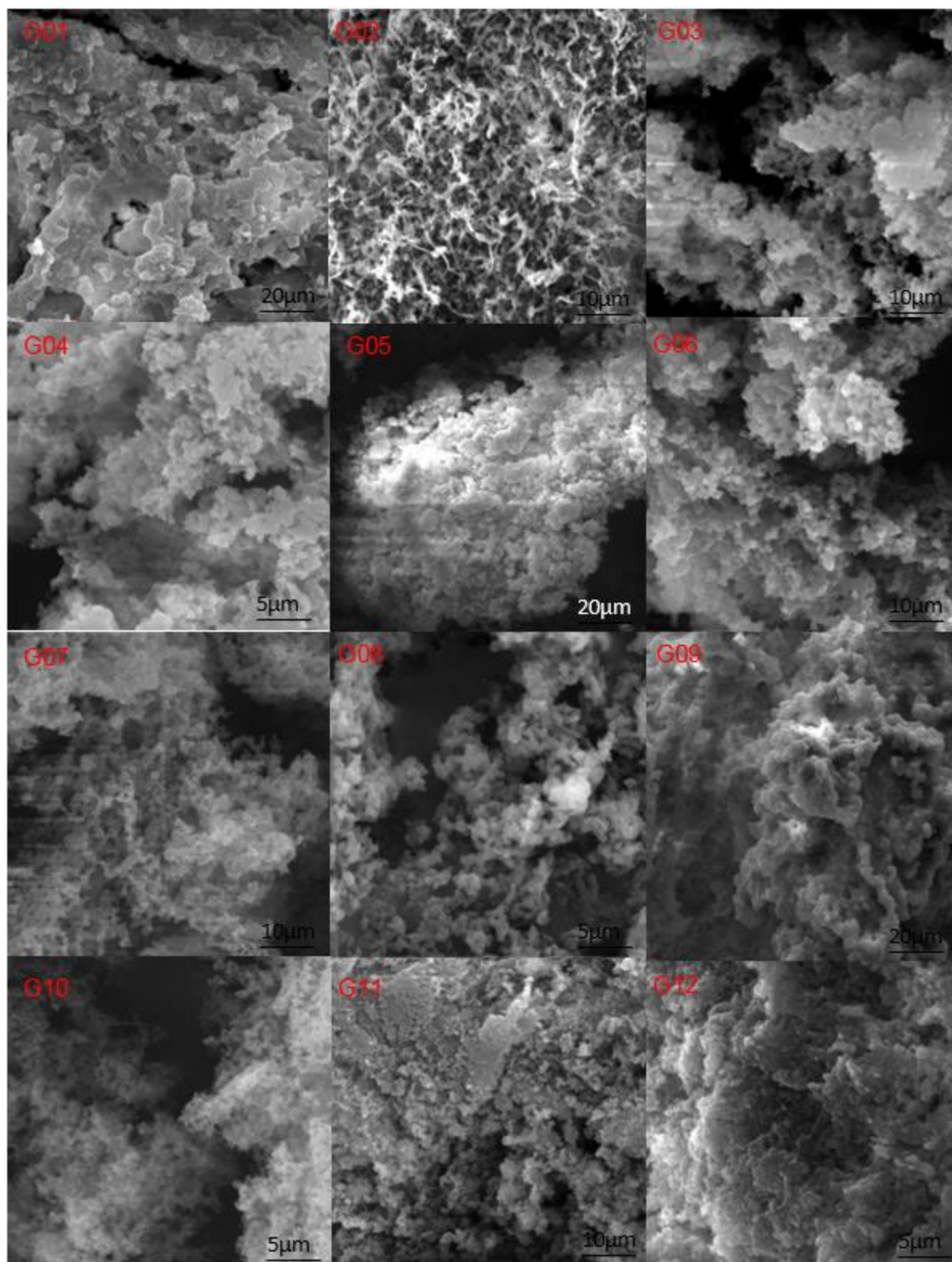


Figure 7.8: X-Ray Diffraction of crosslinked and un-crosslinked gelatin nanoparticles.

7.3.6. Morphological analysis of gelatin nanoparticles

SEM was used to characterize the size and morphology of the nanoparticles (Figure 7.9). The figure in that some of the formulations had high aggregation, whilst others showed some stable nanoparticles. G02 indicated the presence of fibers., whilst others show strong aggregation. Some of the formulation show breakdown processes. The coacervation process could have led to observed high aggregation due to use of magnetic stirring as a mode of dispersion during nanoparticle solidification process. This therefore shows that stirring speed during coacervation process could aid in improving gelatin nanoparticles dispersity and reduce aggregation.



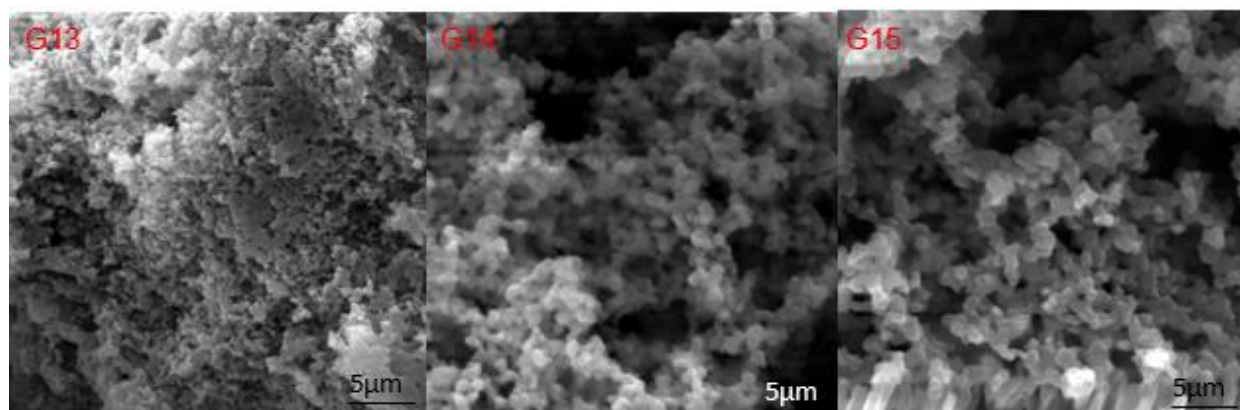


Figure 7.9: SEM images of gelatin nanoparticles.

7.3.7. Particle size, distribution characterization and entrapment efficacy

The particle size was characterized by DLS (Table 7.6). This was utilized to assess the stability and dispersion of the particles in relation for the SEM images. Based on SEM, the particles have a size range of 209-90.22nm particle size, whereby formulation G04 had the biggest size and formalization G12 had the smallest size. In comparison to TEM and SEM, the DLS data shows that those particles had a broad range of hydrodynamic size due to issues of aggregation. Due to re-suspending of particles in water, this induced intermolecular electrostatic interactions between the gelatin molecules which can result in formation of aggregates that can impact the DLS hydrodynamic size. The drug content was determined thorough direct drug content analysis. The analysis of the zeta potential was conducted using deionized water to re-suspend the gelatin spheres. The results indicate that there is variation in the amount of free amino acids that can affect the zeta potential. This can be influenced by both the crosslinker and the conformational changes of the protein during synthesis. Formulation G11, G12 and G13 showed the lowest zeta potential. In terms of G12 and G13, the formulation difference was due to crosslinking time, whilst other factors were constant. In relation to G11, surfactant concentration can be correlated to CD studies which showed that low concentration can lead to refolding of the gelatin structure, whilst an increase leads to renaturation. The stability of the particle seems to relate to the sonication time, whereby long sonication time led to high particle size which could be attributed to aggregation. Based on EE (%) G06 had the highest entrapment, whilst G11 has the lowest. Based on the zeta potential drift, these formulations could have folding variations. These variations could attribute to the low entrapment content.

Table 7.6: Evaluation of gelatin spheres size, dispersity, and stability.

Formulation	Size (d. nm)	PDI	Zeta Potential (mV)	TEM	EE (%)
G01	626.5	0.958	16.1	145.81±10.33	41.62
G02	72.95	0.822	4.24	99.54±15.72	94.04
G03	535.1	0.736	9.31	164.21±59.83	52.05
G04	410.2	0.502	6.76	209.92±32.57	50.72
G05	602.1	0.712	12.5	134.87±42.72	45.89
G06	564.1	0.802	10.4	115.36±40.23	97.92
G07	1763	0.594	2.36	107.82±33.02	73.22
G08	1313	0.802	14.4	152.45±44.19	64.18
G09	1204	0.728	5.96	159.38±54.3	54.38
G10	3024	0.647	10.8	110.54±10.36	54.49
G11	2046	0.760	-0.06	140.57±33.86	11.16
G12	929.2	0.760	1.07	90.22±21.89	51.26
G13	1683	0.967	-0.07	113.90±18.39	23.53
G14	7185	0.421	18.2	101.33±23.37	43.60
G15	2651	0.910	8.55	156.38±46.94	33.39

7.3.8. Swelling studies

Swelling studies on gelatin were studied to evaluate the impact of the crosslinker on the swelling ratio (Figure 7.10). Formulation G01 occurred to have the smallest swelling which was crosslinked for 60 minutes and had the highest surfactant amount. G10 had the highest swelling which had the longest crosslinking time of 120 min but lowest surfactant concentration. This can relate to the impact of gelatin structural folding thus leading to change in accessible functional groups that play a role in crosslinking i.e. carboxylic groups interaction with hydrazine.

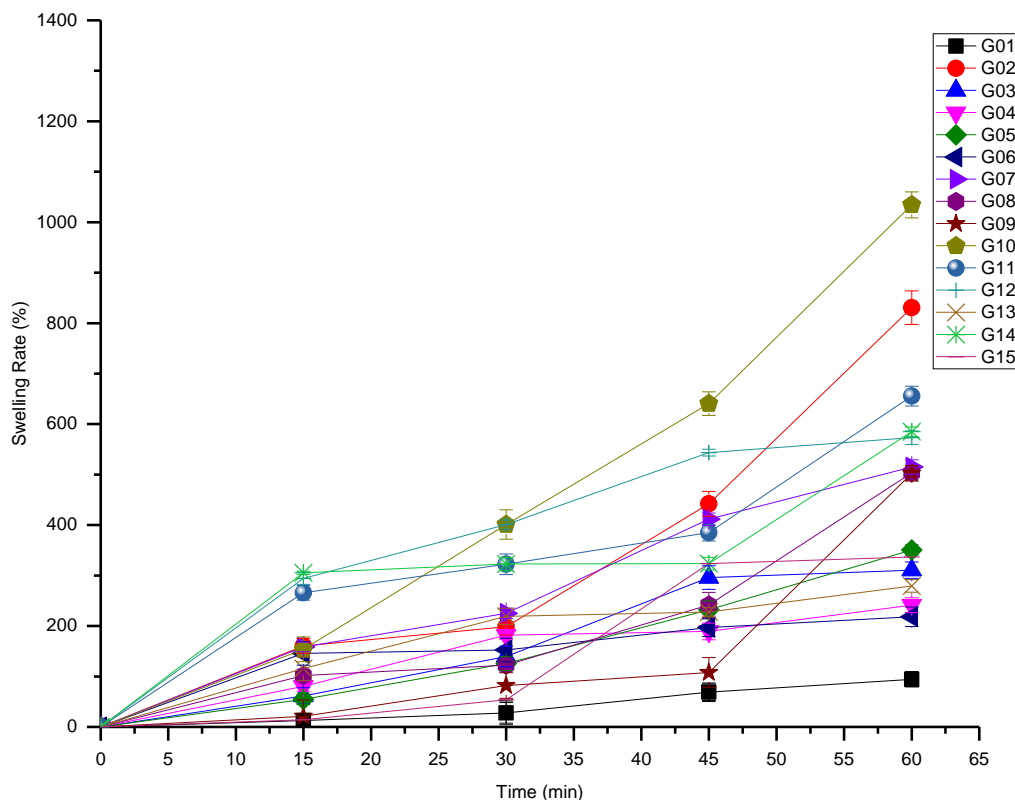


Figure 7.10: Swelling ratio of gelatin nanoparticles in water at room temperature.

7.3.9. Drug release profile

Drug release studies were used to assess the drug leaking effect and the pH responsiveness of the hydrazone linker. Based on recent gelatin studies it is stated that there are several mechanisms by which the release of therapeutic agents from the delivery systems to the surrounding can be controlled: i) diffusion; ii) swelling followed by diffusion (mostly in hydrogels); iii) diffusion and degradation (erodible systems); iv) hydrolysis of the covalent bond in case the drug is covalently bound to the biodegradable polymer (pendant chain systems); v) osmotic pressure; and vi) externally or self-regulated systems[27]. Based on figure 7.11, formulations G02, G06 and G11 indicate the least drug leaking. However, in figure 7.12, F06 still indicates drug the same release profile. Due to incorporation of hydrazone bond, is expected for release mechanism to follow hydrolysis mechanism. However, there is evidence of swelling and diffusion as both pH 7.4 and 4.5 release therapeutic agents at slightly similar levels. This can relate to the impact of

crosslinking density and the packaging of the gelatin in formation of the nanoparticles influenced by the surfactant concentration.

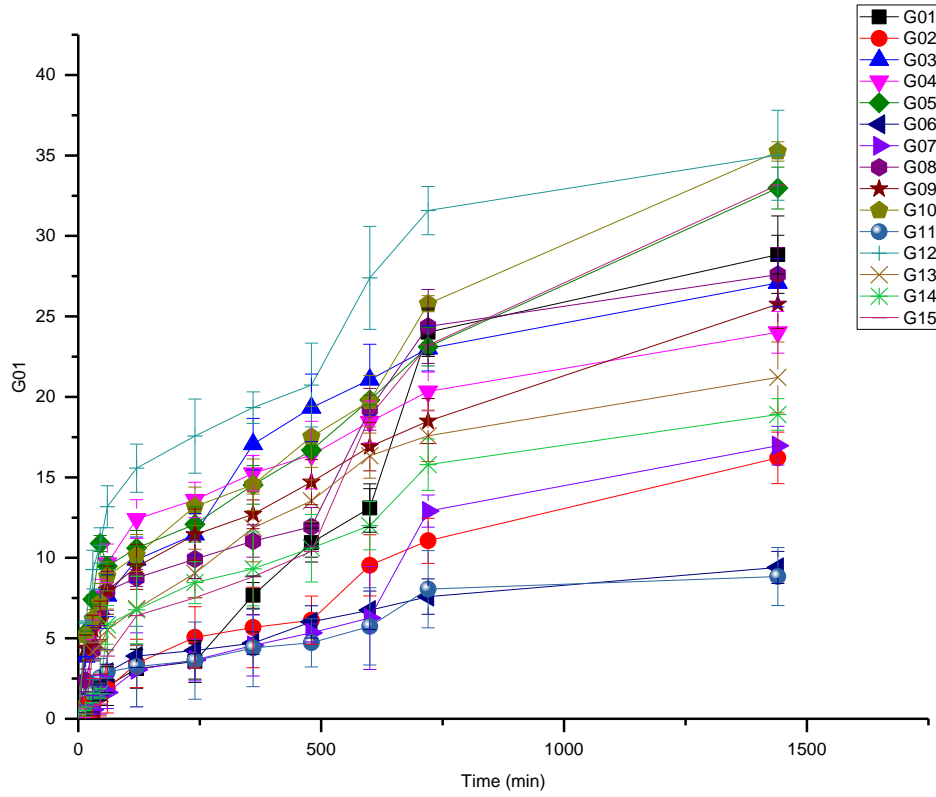


Figure 7.11: Cumulative drug release profile of rifampicin at pH 7.4.

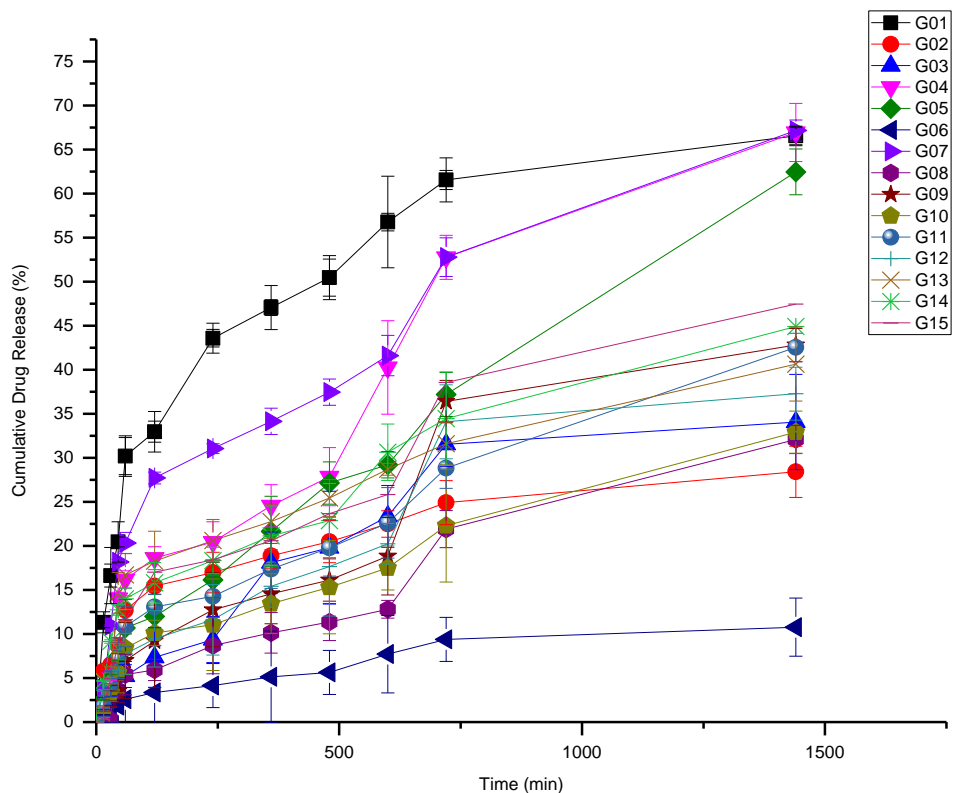


Figure 7.12: Cumulative drug release profile rifampicin at pH 4.5.

In pH 4.5, the hydrazone is expected to rapidly undergo hydrolysis which can lead to burst responsive release of rifampicin. There are three main forces that drive solute transport in hydrogel systems which include a penetrant concentration gradient, a polymer stress gradient and osmotic forces. Fickian diffusion plays a role in systems where polymer relaxation rate is slow, thus non-swelling controlled delivery systems. Due to the variation in the degree of crosslinking and that gelatin is swellable in water. The MDT and DE values were also determined (Table 7.7). The MDT was evaluated as it can characterize the drug release rate from the dosage form and the retarding efficacy of the polymer[28]. The large values indicate that there is high retarding ability. G01 had the best release rate whilst G08 had the lowest. In terms of DE, it shows that G06 had the lowest release rate in both pH values. This correlates well with swelling studies which shows it was the second lowest degree of swelling.

Table 7.7: Evaluation of the mode of drug release, mean dissolution time and dissolution efficiency.

Formulation	n value		MDT (minutes)		DE	
	pH 4.5	pH 7.4	pH 4.5	pH 7.4	pH 4.5	pH 7.4
G01	0.324	0.874	262.23	570.00	0.544	0.174
G02	0.317	0.688	302.18	571.22	0.224	0.0978
G03	0.599	0.420	414.44	366.01	0.242	0.202
G04	0.592	0.358	507.71	336.10	0.433	0.184
G05	0.707	0.418	621.86	505.42	0.354	0.214
G06	0.516	0.432	419.73	408.39	0.0763	0.0673
G07	0.427	0.853	436.32	598.63	0.468	0.0991
G08	0.774	0.503	607.51	435.97	0.185	0.192
G09	0.701	0.407	519.81	464.68	0.273	0.174
G10	0.555	0.495	544.54	508.22	0.204	0.228
G11	0.555	0.448	544.54	393.68	0.264	0.0642
G12	0.563	0.358	449.55	344.57	0.256	0.266
G13	0.380	0.466	401.92	399.35	0.293	0.153
G14	0.430	0.509	457.20	426.28	0.306	0.133
G15	0.519	0.809	468.75	598.36	0.320	0.194

7.3.10. Analysis of response surface design

Surface plots can aid in assessment of the how the parameter changes can affect the evaluated response. Based on the particle size, the increase in surfactant led to a decrease in particle size (Figure 7.13). Whereas increase in sonication time, led to increase in particle size. The evaluation of the drug release was conducted using the n value as the response at pH 4.5. This release mechanism serves as the indication of how well particles can respond to the change in pH (Figure 7.14). Increase in crosslinking time leads decrease in drug release rate.

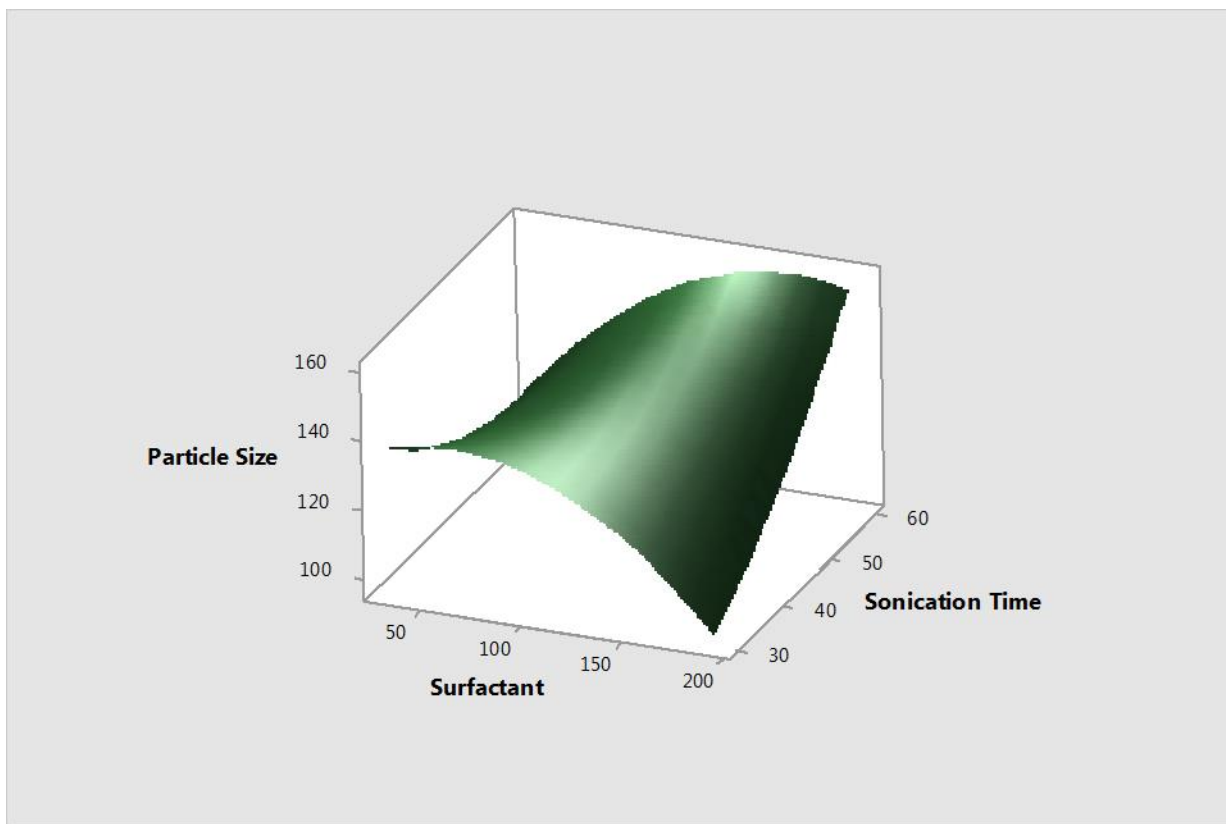


Figure 7.13: *Evaluation of particle size in relation to surfactant concentration and sonication time.*

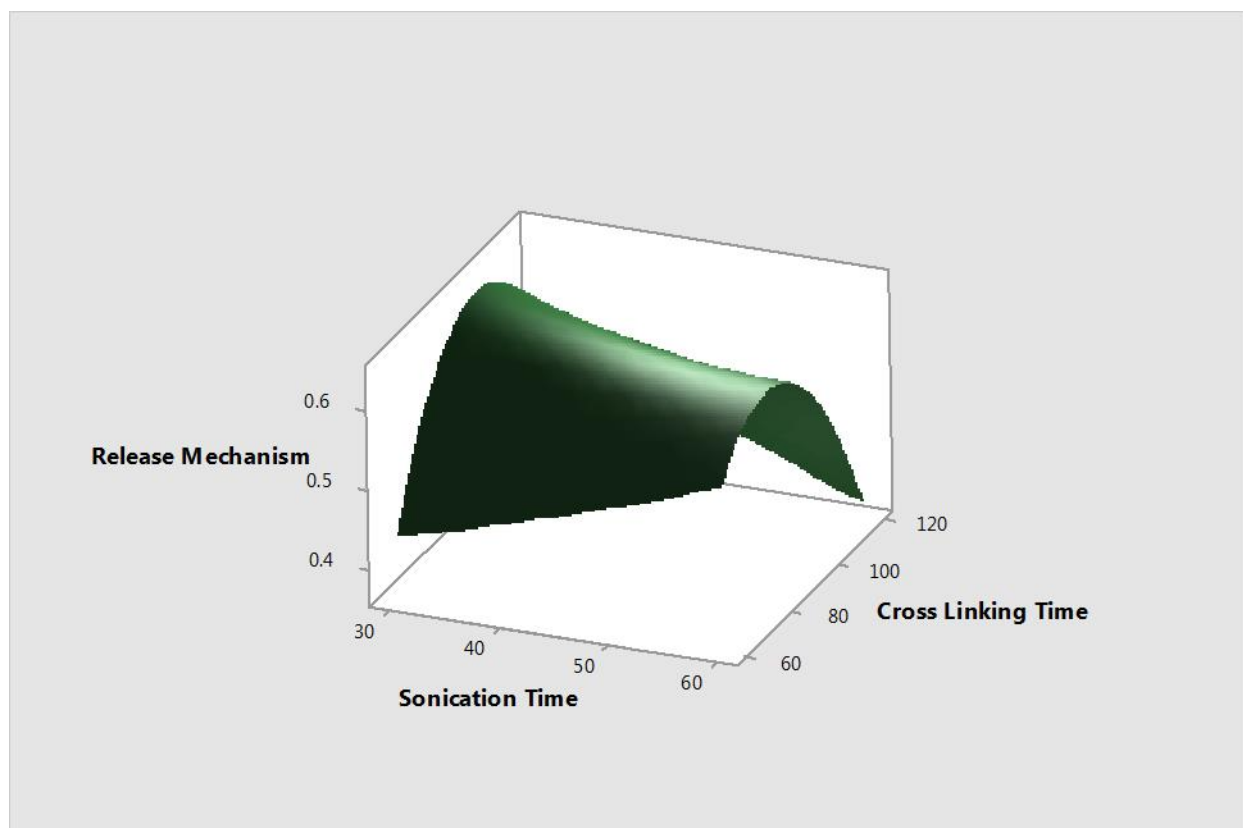


Figure 7.14: Evaluation of drug release mechanism in relation to crosslinking time and sonication time.

7.4. Concluding remarks

The comparison between Brij 52 and C₁₂E₁₀ clearly indicates that have different behaviour in suspension. Brij 52. Based on FTIR, it has been shown on literature that Beta sheet structures can be characterized by the amide I absorption which is primarily determined by the backbone conformation and is independent of the amino acid sequence[29]. For antiparallel, the average frequency of the main component is about 1629cm⁻¹ with a minimum of 1615cm⁻¹ and a maximum of 1637cm⁻¹. Whilst The average value for the second frequency is 1696 cm⁻¹ (lowest value 1685cm⁻¹). For beta strands, amide I absorption near 1640cm⁻¹. For alpha-helical structures the mean frequency was found to be 1652cm⁻¹ for the amide I and 1548cm⁻¹ for the amid II absorptions. For beta turns, However, an absorption near 1680cm⁻¹ is now clearly assigned to beta turns. These observations correlate well with the CD data and DLS data. Based on CDNN evaluation (180-260nm), gelatin without surfactant showed abundance of random coils and antiparallel sheets. With initial addition of Brij 52, helix structure became prevalent then shifted

back to random coils with more surfactant. For C₁₂E₁₀, similar initial changes of helix conformation were observed.

Unlike Brij 52, the beta turn and helix were slightly sustained through the increase in surfactant concentration. This then reversed back into antiparallel but with a sustained beta turn than random coil, the finally random coils and antiparallel at maximum surfactant levels. This shows that non-ionic surfactant has reversible effect on the gelatin structure as the increase in surfactant level (above CMC), the interference of the surfactant gets diminished. In terms of drug delivery application, C₁₂E₁₀ seem to be have better impact in structure refolding of peptide, which can be useful and peptide drug delivery systems. The surfactant can play a role in drug release profile as the interaction with the gelatin as it may create a folding that can retard drug release. The retardation in the structure correlates well with CD, FTIR and zeta potential values variations. Based on these studies G02,06,08,10,14 and F15 had the best dispersion in terms of TEM. These formulations indicate that the force of dispersion and surfactant concentration during formulation is vital in generation of more disperse formulation. Future studies warrant the use of homogenizer to improve particle formation. Due to gelatin been shown to be susceptible to degradation by gelatinase (Matrix Metalloproteinase) in diseases regions, gelatin was utilized in the optimized MSNs as gatekeeping layer for control of drug release ([Chapter 8](#)). The pH responsive linker was also used for formation of a pH responsive gate.

7.5. Reference

- [1] J.F. Coelho, P.C. Ferreira, P. Alves, R. Cordeiro, A.C. Fonseca, J.R. Góis, M.H. Gil, Drug delivery systems: Advanced technologies potentially applicable in personalized treatments, *The EPMA Journal*, 1 (2010) 164-209.
- [2] S. Podaralla, O. Perumal, R. Kaushik, Design and Formulation of Protein-Based NPDDS, *Drug Delivery Nanoparticles Formulation and Characterization*, CRC Press2009, pp. 69-91.
- [3] L. Nicod, Pulmonary defence mechanisms, *Respiration*, 66 (1999) 2-11.
- [4] T. S Wilkinson, J.-M. Sallenave, J. Simpson, Pulmonary Defence Mechanisms, *Current Respiratory Medicine Reviews*, 8 (2012) 149-162.
- [5] A.H.L. Chow, H.H.Y. Tong, P. Chattopadhyay, B.Y. Shekunov, Particle Engineering for Pulmonary Drug Delivery, *Pharmaceutical Research*, 24 (2007) 411-437.
- [6] N.R. Labiris, M.B. Dolovich, Pulmonary drug delivery. Part I: Physiological factors affecting therapeutic effectiveness of aerosolized medications, *British Journal of Clinical Pharmacology*, 56 (2003) 588-599.

- [7] J. George, P. Sudheesh, S.M. Nair, L. Sreejith, Circular dichroism and viscosity studies of gelatin with anionic surfactant, SDBS, *Composite Interfaces*, 15 (2008) 653-659.
- [8] A.A. Karnachi, M.A. Khan, Box-behnken design for the optimization of formulation variables of indomethacin coprecipitates with polymer mixtures, *International Journal of Pharmaceutics*, 131 (1996) 9-17.
- [9] J.W. Ledbetter, J.R. Bowen, Spectrophotometric determination of the critical micelle concentration of some alkyldimethylbenzylammonium chlorides using fluorescein, *Analytical chemistry*, 41 (1969) 1345-1347.
- [10] S. Chodankar, V.K. Aswal, P.A. Hassan, A.G. Wagh, Structure of protein–surfactant complexes as studied by small-angle neutron scattering and dynamic light scattering, *Physica B: Condensed Matter*, 398 (2007) 112-117.
- [11] K. Kawai, S. Suzuki, Y. Tabata, Y. Ikada, Y. Nishimura, Accelerated tissue regeneration through incorporation of basic fibroblast growth factor-impregnated gelatin microspheres into artificial dermis, *Biomaterials*, 21 (2000) 489-499.
- [12] N.J. Greenfield, Using circular dichroism spectra to estimate protein secondary structure, *Nature protocols*, 1 (2006) 2876-2890.
- [13] P. Kempgens, J. Britton, Powder-XRD and ¹⁴N magic angle-spinning solid-state NMR spectroscopy of some metal nitrides, *Magnetic Resonance in Chemistry*, 54 (2016) 371-376.
- [14] M. SARMAH, A. HUSSAIN, A. RAMTEKE, T.K. MAJI, Isoniazid loaded gelatin-cellulose whiskers nanoparticles for controlled drug delivery applications, *Journal of Chemical Sciences*, 128 (2016) 1291-1301.
- [15] W. Chen, S. Hu, Suitable carriers for encapsulation and distribution of endostar: comparison of endostar-loaded particulate carriers, *Int J Nanomedicine*, 6 (2011) 1535-1541.
- [16] A.K. Bajpai, J. Choubey, Design of gelatin nanoparticles as swelling controlled delivery system for chloroquine phosphate, *Journal of Materials Science: Materials in Medicine*, 17 (2006) 345-358.
- [17] E. Rinaki, A. Dokoumetzidis, P. Macheras, The Mean Dissolution Time Depends on the Dose/Solubility Ratio, *Pharmaceutical Research*, 20 (2003) 406-408.
- [18] K.A. Khan, The concept of dissolution efficiency, *Journal of Pharmacy and Pharmacology*, 27 (1975) 48-49.
- [19] A.I.A. Mohamed, A.S. Sultan, I.A. Hussein, G.A. Al-Muntasher, Influence of Surfactant Structure on the Stability of Water-in-Oil Emulsions under High-Temperature High-Salinity Conditions, *Journal of Chemistry*, 2017 (2017) 11.
- [20] T.F. Tadros, *Emulsion formation and stability*, John Wiley & Sons 2013.

- [21] P.K. Misra, J. Meher, S. Maharana, Investigation on the gelatin-surfactant interaction and physiochemical characteristics of the mixture, *Journal of Molecular Liquids*, 224 (2016) 900-908.
- [22] S.S. Singh, H.B. Bohidar, S. Bandyopadhyay, Study of gelatin–agar intermolecular aggregates in the supernatant of its coacervate, *Colloids and Surfaces B: Biointerfaces*, 57 (2007) 29-36.
- [23] J.H. Muyonga, C.G.B. Cole, K.G. Duodu, Fourier transform infrared (FTIR) spectroscopic study of acid soluble collagen and gelatin from skins and bones of young and adult Nile perch (*Lates niloticus*), *Food Chemistry*, 86 (2004) 325-332.
- [24] A. Jelińska, A. Zagożdżon, M. Górecki, A. Wisniewska, J. Frelek, R. Holyst, Denaturation of proteins by surfactants studied by the Taylor dispersion analysis, *PLOS ONE*, 12 (2017) e0175838.
- [25] W. Schütze, C.C. Müller-Goymann, Interactions between nonionic surfactant aggregates and gelatin-rheological measurements, *Colloid and Polymer Science*, 271 (1993) 992-996.
- [26] C. Qiao, X. Ma, J. Zhang, J. Yao, Molecular interactions in gelatin/chitosan composite films, *Food Chemistry*, 235 (2017) 45-50.
- [27] M. Foox, M. Zilberman, Drug delivery from gelatin-based systems, *Expert Opin Drug Deliv*, 12 (2015) 1547-1563.
- [28] A. Afroz, M. Asaduzzaman, M. Rahman, A. Islam, Development and Evaluation of Muco-Adhesive Ciprofloxacin Bi-Layer Tablet for Extended Drug Release, 2011.
- [29] A. Barth, Infrared spectroscopy of proteins, *Biochimica et Biophysica Acta (BBA) - Bioenergetics*, 1767 (2007) 1073-1101.

8. : OPTIMIZED MESOPOROUS SILICA NANOPARTICLES: USE OF NATURAL POLYMERS GATE-KEEPERS: CYCLODEXTRIN AND GELATIN CONJUGATED TO SYNTHESIZED HYDRAZONE LINKER

8.1. Introduction

The employment of pH responsive drug delivery has allowed control of localized drug delivery. Tumors and inflammatory tissues (pH ~ 6.8 versus normal pH of 7.4), endosomes (pH ~ 5.5-6), and lysosomes (pH ~ 4.5-5.0) are known to have variations in pH[1]. Literature indicates that pH-sensitive linkers, such as acetal bond, imine bond, hydrazone bond, and ester bond can be cleaved under acidic condition[2]. Mesoporous silica nanoparticles have been well studied for application in drug delivery. The particles over control of physicochemical properties through the control of the Stöber process. Through this process, the silica matrix produced is non-crystalline and also contains surface silanol groups in abundance, thus allowing further post-synthetic transformation of the silica surface[3]. Due to the ability for tunable physicochemical properties, MSNs allow ability to load diverse cargoes such as small molecule drugs, short peptides, and large proteins. Due to these physiochemical properties, Yu and colleagues (2012) showed that the MSNs can be cleared within 24 hours post-injection [4]. The biodistribution was linked to the surface chemistry and porosity of the nanoparticles appears than the particles geometry (sphere/rod). In terms of excretion, MSNs hydrolyze under physiological conditions. This can lead to the body to either absorb dissolved silica or excrete it through the urine in the form of silicic acid or oligomeric silica species [5].

In pulmonary drug delivery (alveolar surface area - 160m^2), the airway epithelium leads to various barriers whereby nanoparticles have to cross overcome the pulmonary epithelia, ciliated epithelial cells, type I and type II pneumocytes[6]. A recent review has shown that mesoporous silica nanoparticles can be functionalized with stimuli responsive groups and polymers that function as caps and gatekeepers in controlling drug release [7]. It is known that tuberculosis bacilli reside inside macrophages. Therefore, the uptake of antituberculous nanoparticles by macrophages can aid in target specific and stimuli release drug delivery. By releasing therapeutics only in the cytoplasm of macrophages allows reaching pharmacologically effective dosing where it is required whilst avoiding/reducing side effects. It has been shown that cellular uptake by macrophages for particles less than 200-300nm can be taken up via endocytosis. Various mechanisms such as clathrin dependent, caveolin-dependent, receptor-mediated and clathrin

and caveolin-independent endocytosis play a role in endocytosis [8]. In this section, cyclodextrin is one of gatekeeper used as it has been shown that it can enhance drug delivery through biological barriers without affecting their barrier function. Thus it will not interfere with mucociliary functions, will not show ciliostatic effect, and will be non-irritating and non-allergenic [9].

Cyclodextrins (CD) are widely used natural cyclic oligosaccharides derived from starch and used as excipients in marketed pharmaceutical products. As stated CD can utilized as penetration enhancers by increasing drug availability at the surface of the biological barrier [10]. Furthermore, CD are said to have a direct disruption effect on alveolar epithelial membrane. Dimethyl- β -cyclodextrin > α -cyclodextrin > β -cyclodextrin > γ -cyclodextrin > hydroxypropyl- β -cyclodextrin are ranked in enhanced trans-mucosal protein transport of calcitonin via pulmonary absorption [11]. Gelatin can also be used in drug delivery as it is highly biocompatible and biodegradable in a physiological environment [12]. It has been reported that gelatin nanoparticles have higher intracellular uptake and are more suited for intravenous delivery or for targeted drug delivery to the brain [13]. Furthermore, they have exhibit a high ability to absorb water. Recent study has shown that overexpression of matrix metalloproteinase-2 (MMP-2) can digest gelatin. This would allow dual response of drug release [14]. Both MMP-2 (gelatinase A) and MMP-9 (gelatinase B) are released by Lymphocytes, macrophages and neutrophils [15].

8.2. Materials and methods

8.2.1. Materials

Tetraethyl orthosilicate (TEOS), glycidyoxypropyl trimethoxysilane, cetyltrimethylammonium bromide (CTAB), gelatin, α -cyclodextrin, monochloroacetic acid, sodium hydroxide, acetylacetone and hydrazine were purchased from Sigma-Aldrich (Sigma-Aldrich, Sigma-Aldrich). All solvents were used without further purification.

8.2.2. Preparation of carboxymethyl- α -CD (CM- β -CD)

CM- β -CD was prepared following online literature [16]. Briefly a mixture of β -CD (10g, 8.8mmol) and NaOH (9.3g, 232.5mmol) in water (37mL) was treated with a 16.3% monochloroacetic acid solution (27mL) at 50 °C for 5 hours. Then the reaction mixture was cooled to room temperature, and pH was adjusted (6.5) using hydrochloric acid. The obtained neutral solution was then poured to superfluous methanol solvent which produced white precipitation. The solid precipitation was filtered and dried under vacuum to give carboxymethylated β -CD (89.3%). NMR: ^1H NMR (400MHz, D_2O) δ 5.17, 4.97, 4.97, 4.69, 4.09, 4.03, 4.01, 3.99, 3.91, 3.89, 3.86, 3.84, 3.82, 3.78,

3.77, 3.75, 3.56, 3.53, 3.51, 3.50, 3.27ppm. ^{13}C NMR (101MHz, D_2O) δ 177.41, 101.37, 81.20, 73.27, 71.96, 60.39, 49.01ppm.

8.2.3. Synthesis of pentane-2,4-diylidenebis(hydrazine)

Acetylacetone (2mL, 1 equiv.) was mixed with EtOH (50mL), followed by addition of hydrazine (2 equiv.) in EtOH (20mL) dropwise (Figure 8.1). The mixture was stirred for an hour at room temperature and then refluxed for 5 hours and cooled to room temperature. The solution was then concentrated under reduced pressure. NMR: ^1H NMR (300MHz, DMSO) δ 12.05, 9.01, 5.73, 3.45, 2.50, 2.50, 2.12ppm. ^{13}C NMR (75MHz, DMSO) δ 139.01, 103.62, 39.89, 13.30ppm.

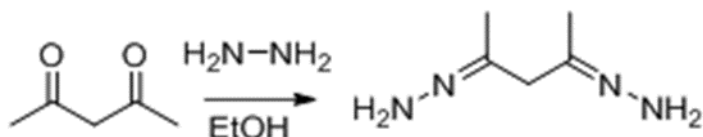


Figure 8.1: Synthesis of pentane-2, 4-diylidenebis (hydrazine).

8.2.4. Synthesis of epoxy functionalized mesoporous silica nanoparticle

0.1M solution of NaOH was freshly prepared. Following the predicted optimum conditions in Chapter 6, the solution (82.5mL) was added into a round bottom flask, followed by addition of CTAB (3.0g). This was allowed to dissolve followed by addition of chloroform (97.5mL). The emulsion was allowed to reflux for 30 minutes, followed by addition of TEOS (15mL) dropwise. The solution was refluxed for 3 hours. It was then cooled to room temperature followed by evaporation of the solvent under high air current (fume-hood). This was then stored overnight in an oven. The particles were then calcined for 3 hours at 550°C. Approximately 1g of MSNs were then added into 100mL toluene solution. Glycidyloxypropyl trimethoxysilane (15mL) was then added. The reaction was allowed to reflux for 24 hours. The particles were then washed 3 times with ethanol.

8.2.5. Natural polymer gate keeping

8.2.5.1. Cyclodextrin gate-keeping

Cyclodextrin was used as gate keeper (Figure 8.2). A solution of pentane-2,4-diylidenebis(hydrazine) was added to a dispersed solution of epoxy functionalized MSNs. The reaction was allowed to stir at 50°C for 5 hours. The conjugated particles were then centrifuge and washed with ethanol-DMSO mixture to remove excess pentane-2,4-diylidenebis(hydrazine).

The particles were then allowed to coat with a suspension of carboxymethyl- α -CD overnight. The particles were then centrifuged and washed to remove excess carboxymethyl- α -CD. The particles were then washed with water and lyophilized prior to further use.

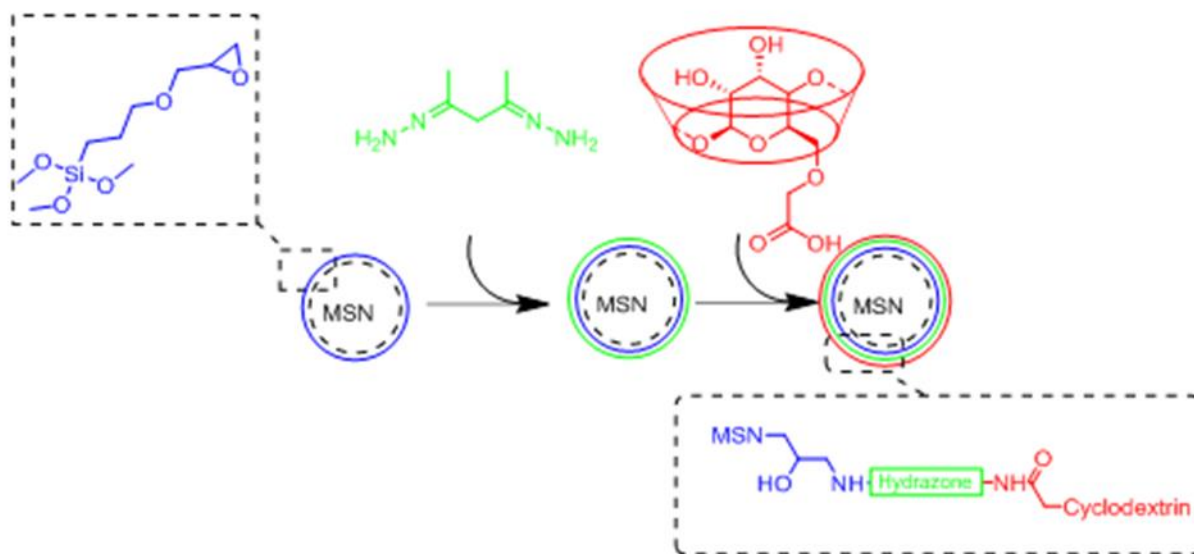


Figure 8.2: Conjugation of hydrazones to MSNs and CD.

8.2.5.2. Gelatin gate-keeping

MSNs were gently shaken with an aqueous gelatin solution (1%) at 50 °C for 6 hours to achieve pore saturation (Figure 8.3). This was followed by addition of a 1% pentane-2,4-diylidenebis(hydrazine) solution was added to cross-link the gelatin. The reaction was allowed to stir overnight. Then, the samples were centrifuged, rinsed by water three times. The particles were then lyophilized prior to further use.

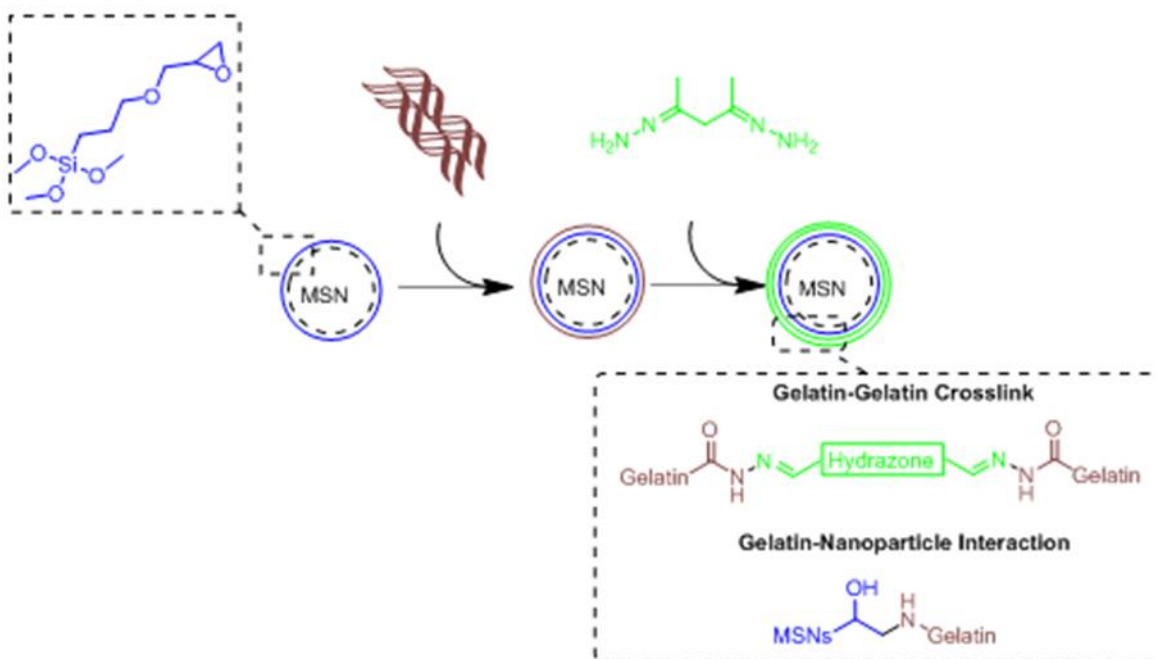


Figure 8.3: Conjugation of gelatin pH responsive gate.

8.2.6. Analysis of molecular binding using NMR

Synthesized linker and functionalized cyclodextrin were analyzed with Bruker AMX 400 NMR spectrometer (Bruker Corporation, Massachusetts, United States) using DMSO-d₆.

8.2.7. Analysis of molecular structural groups using infrared

The lyophilized mesoporous silica nanoparticles were analyzed on a Perkin Elmer 2000 FTIR spectrometer (PerkinElmer, Massachusetts, United States) using 100 scans over a range of 550-4000cm⁻¹ at resolution 4cm⁻¹.

8.2.8. Morphological analysis using transmission microscopy

Particles were suspended in methanol followed by sonication for 10 minutes for dispersion. The particle suspension was then coated on a copper grid. These were allowed to dry overnight. The particles were then analyzed on a Zeiss Libra 120 TEM operating at operating voltage of 100kV (Carl Zeiss, Oberkochen, Germany).

8.2.9. X-ray diffraction patterns analysis

Bruker D8 Discover (Billerica, Massachusetts, USA) was used for analysis of uncoated MSN and coated MSN crystallinity. Data were collected in the range of 2θ = 10° to 100°, scanning at

1.5° min⁻¹ with a filter time-constant of 0.38 s per step and a slit width of 6.0mm. The MSN samples were placed on a silicon wafer slide. The X-ray diffraction data patterns were treated using the Eva (evaluation curve fitting) software. Baseline correction was performed by subtracting a spline function fitted to the curved background on each diffraction pattern [17].

8.2.10. Thermostability studies

TGA analysis was performed using a PerkinElmer TGA 4000 (PerkinElmer, Massachusetts, United States) at a heating rate of 10°C/min under a nitrogen purge of 20mL/min in a 25-600°C range. Pure MSNs, Drug loaded gelatin coated and cyclodextrin coated nanoparticles were analyzed.

8.2.11. Mean size, particle distribution and stability

Particles mean particle size, polydispersity and zeta potential were determined by dynamic light scattering (DLS) using a Zetasizer Nano Instrument (Malvern Instruments, Worcestershire, UK). A suitable amount of nanoparticles was dispersed in ddH₂O to create a total concentration of 1%. All measurements were then performed in triplicates at a scattering angle of 173° and the results were reported in terms of mean diameter ± SD.

8.2.12. Direct drug content analysis

The lyophilized 1g of respective coated nanoparticles was dispersed in drug solutions (MeOH) containing 150mg rifampicin, 100mg isoniazid and 1g ascorbic acid as the stabilizer [18, 19]. The immersed particles were allowed to stir for 48 hours to allow drug to diffuse into the pore cavities. The particles were then centrifuged and briefly washed and lyophilized. 10mg of drug loaded nanoparticles were then suspended in 1M HCl solution and sonicated for 2 hours to break the hydrazone bond and allow drug to diffuse. The supernatant was then analyzed on a PerkinElmer Lamda 25 UV-VIS (PerkinElmer, Massachusetts, United States). The scan range of 200-450nm was used for simultaneous analysis of the drugs.

$$M_{measured} = M_{UV\ measured} / V_{supernatant\ volume} \quad (8.1)$$

$$EE(\%) = (M_{measured} / M_{initial\ load}) \times 100 \quad (8.2)$$

8.2.13. *In vitro* drug release models

Drug release was evaluated in duplicate. 0.1M sodium acetate buffer of pH 4.5 and 5.5 were made from acetic acid and anhydrous sodium acetate in ddH₂O. 0.1M of pH 7.4 phosphate buffer was made from monobasic sodium phosphate and dibasic sodium phosphate. NaOH and HCl were used to adjust the pH to required levels using a pH meter. 10mg of each formulation was then added into a dialysis tube (cut-off 20kDa) and filled with 1mL of respective buffer before sealing the tube. The tubes were then suspended into 20mL of media at 37±0.5°C. 2mL of the media was taken out for analysis at respective time intervals and replaced with 2mL fresh medium to maintained sink conditions. The study was conducted over a period of 24 hours. The withdraw medium was analyzed over on a PerkinElmer Lamda 25 UV-VIS (PerkinElmer, Massachusetts, United States) using a scan range of 200-400nm, followed by chemometric extraction of the release drug concentration. Cumulative drug release for each drug was then plotted against time after analysis with DDSolver excel add-in with volume replacement. The software was also used for modeling different mathematical functions (model dependent functions), which describe the dissolution profile. The model dependent approaches included zero order, first order, Higuchi, Hixson-Crowell and Korsmeyer-Peppas regression models [20].

Zero-order

This model evaluates drug dissolution from dosage forms which do not disaggregate and have a slow drug release profile. This is the ideal model for drug delivery whereby the system releases the drug at a constant rate. This can be represented by the equation:

$$Q_t = Q_0 + K_0 t \quad (8.3)$$

Where Q_t is the amount of drug dissolved in time t , Q_0 is the initial amount of drug in the solution and K_0 represents the zero-order release constant expressed in units of concentration/time. This is plotted as cumulative % drug released vs. time

First order

This model focuses on the water-soluble drug release that is proportional to the amount of drug that still remains inside the a porous matrix, whereby the amount of drug released by unit of time diminishes [21]. The drug release profile which follows the first order kinetics can be expressed by the equation:

$$\log C = \log C_0 - Kt/2.303 \quad (8.4)$$

Where C_0 is the initial concentration of drug, k is the first order rate constant, and t is the time. This is plotted as log cumulative of % drug remaining vs. time.

Higuchi

The Higuchi model is used to describe the release of a drug from an insoluble matrix as the square root of a time-dependent process based on Fickian diffusion. Thus, during drug release there are simultaneous processes such as penetration of the surrounding liquid into the matrix, dissolution of the drug, and leaching out of the drug through interstitial channels or pores from the matrix.

$$Q_t = K_H(t)^{0.5} \quad (8.5)$$

Where K_H is the release rate constant for the Higuchi model. This is plotted as cumulative % drug released vs. square root of time.

Hixson-Crowell

This model describes drug release from a where there is a change in surface area and diameter of the release matrix.

$$\sqrt[3]{Q_0} - \sqrt[3]{Q_t} = K_{HC}t \quad (8.6)$$

Where, Q_t is the amount of drug released in time t , Q_0 is the initial amount of the drug in the matrix and K_{HC} is the rate constant for Hixson-Crowell rate equation. This is plotted as cube root of drug % remaining in matrix vs. time.

Korsmeyer-Peppas

This model drug release from a polymeric system whereby various several simultaneous processes considered to be occurring in the model: diffusion of water into the matrix, swelling of the matrix as water enters, gelation, drug diffusion and then dissolution of the polymer matrix.

$$M_t/M_\infty = Kt^n \quad (8.7)$$

where M_t/M_∞ is a fraction of drug released at time t , K is the release rate constant and n is the release exponent. This is plotted as log cumulative % drug released vs. log time. In order to find out the mechanism of drug release, the first 60% drug release data were fitted in Korsmeyer-Peppas model. The n value as illustrated in table 8.1 can then be used for understanding of the release mechanism.

Table 8.1: Interpretation of diffusional release mechanisms

Release exponent (n)	Drug transport mechanism
0.5	Fickian diffusion
$0.5 < n < 1$	Non-Fickian diffusion
1	Case II Transport
>1	Super Case II Transport

8.2.14. Statistical analysis

The data is presented as mean \pm standard deviation. Significant differences between group means were evaluated using one-way Anova, P value < 0.05 . The analysis was performed using OriginPro (OriginLab Corporation, MA, USA).

8.3. Results and discussion

8.3.1. Microscopic analysis of coated mesoporous silica nanoparticles

The TEM micrographs of the prepared mesoporous silica nanoparticles revealed that the particles have spherical shape (Figure 8.4). The particle core transparency indicates the mesoporous structure. Literature on TEM images indicates that the colorization can indicate the degree of crystallinity of the particles. Dark regions on the particles are stated to be indication of the presence of a crystalline region. Whilst on the contrary, a bright region should correspond to an amorphous phase. This can be seen with both uncoated and coated nanoparticles which depict an amorphous phase [22]. The abundant dark region in the cluster can be attributed to the shadow/lack of light diffusion through the particles due to particles aggregation during analysis within the chamber. The particles were shown to have variation in size. For uncoated MSN, the particles had a size of 83.09 ± 14.06 nm. For epoxy functionalized nanoparticles, the observed size was 73.62 ± 11.14 nm. Cyclodextrin coated nanoparticles had a size of 74.43 ± 1.57 nm. Gelatin coated had a size of 111.55 ± 14.46 nm.

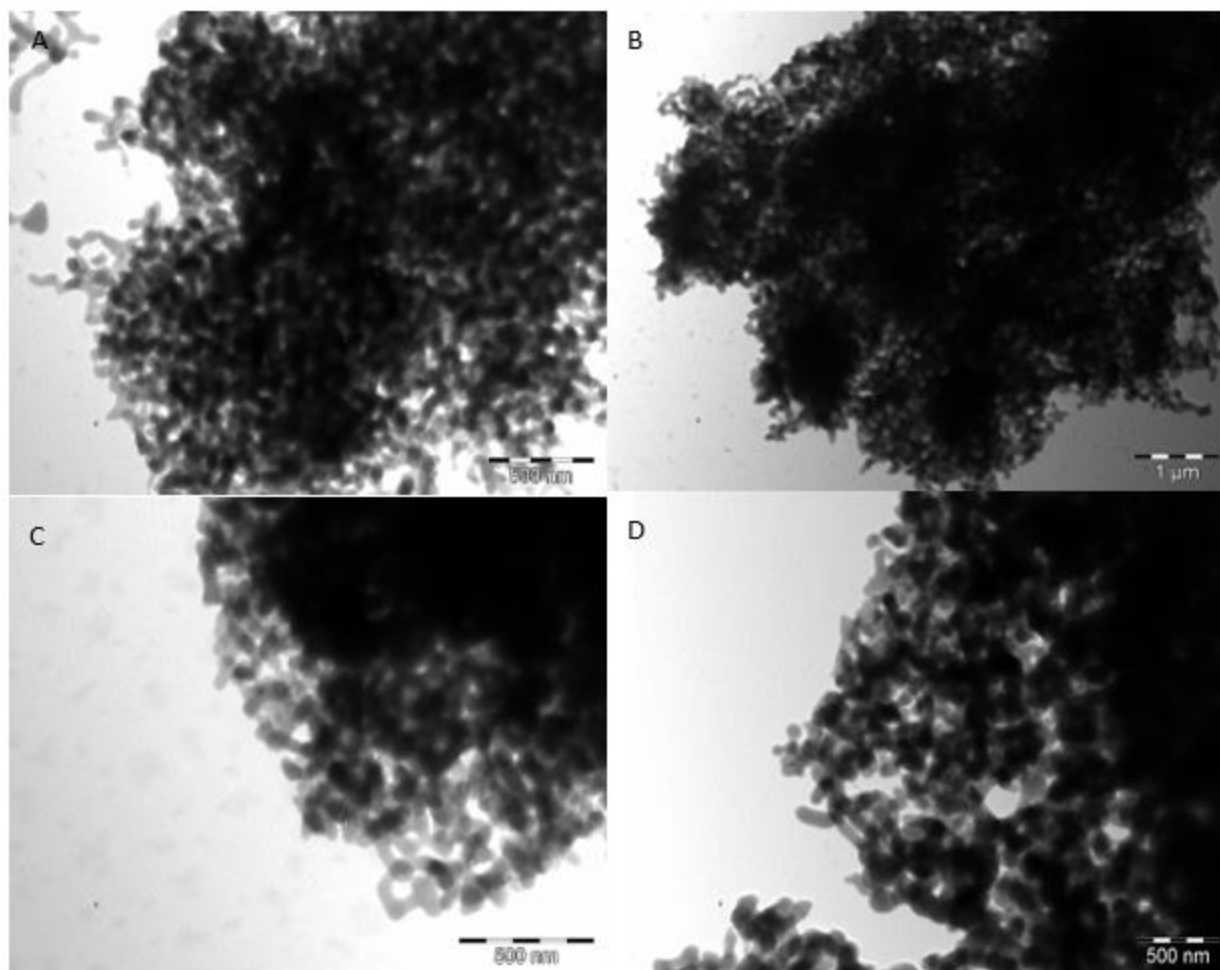


Figure 8.4: TEM images of mesoporous silica nanoparticles a) MSNs b) epoxy-MSNs c) Gelatin-MSNs d) CD-MSNs

8.3.2. Dynamic light scattering analysis

Dynamic light scattering technique was used to assess the hydrodynamic radius and polydispersity index (PDI) which will enable the determination of the presence of agglomeration. The comparison between DLS and TEM particle radiuses show different particle size distribution. DLS allows the evaluation of particle size and distribution within suspension. This also accounts also to agglomerating particles which shows deviation in size to TEM data. Zeta potential was also evaluated as it is an important parameter for explaining the stability of colloid against the agglomeration. The study showed that the uncoated MSN were highly stable as they have a zeta potential of -41.5mV (Figure 8.5 and table 8.2). The size seemed to occur within a similar range of between $0.5\text{-}1\mu\text{m}$. This size also accounts agglomerating particles. Gelatin indicates to have even high particle size which could be due to gelation of the MSN coat and rapid agglomeration

(Figure 8.6). The shifts in zeta potential amongst the formulations indicate that the particles have different surface charge which could be attributed to the surface functional groups. The particles started with a negative charge which then shifted to positive region (Figure 8.5). Gelatin and cyclodextrin shielding of the inert silica negative charge. SiO₂ is stated to be inherently an acidic oxide, whereby the pH of an aqueous suspension of silica will be slightly acidic due to the water pH being above silica isoelectric point (IEP) [23]. This can be deduced as a confirmation of successful coating.

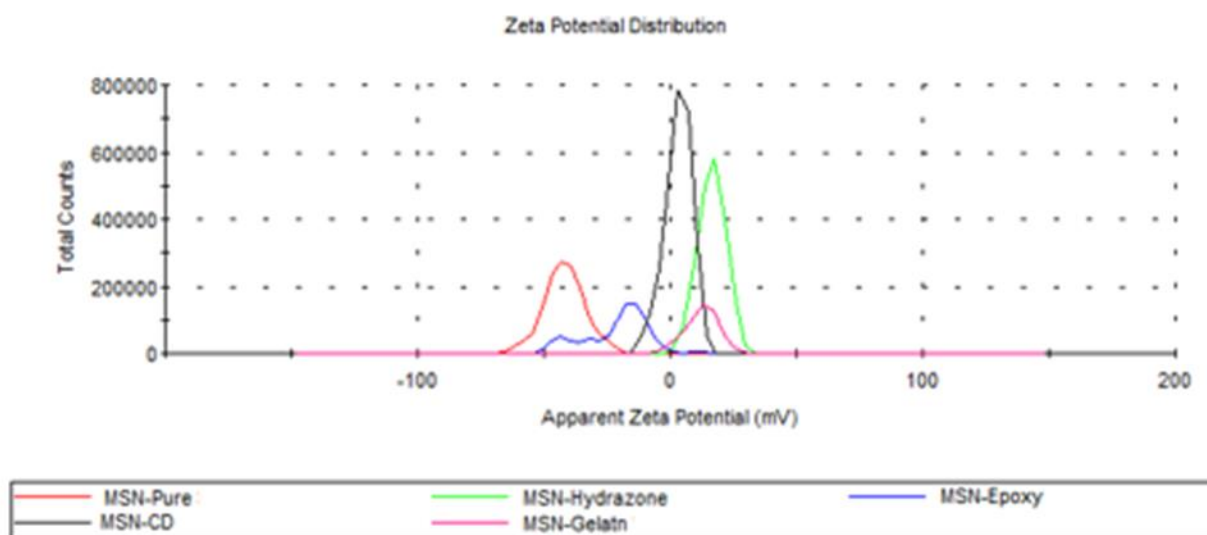


Figure 8.5: Zeta potential drifts of mesoporous silica nanoparticles

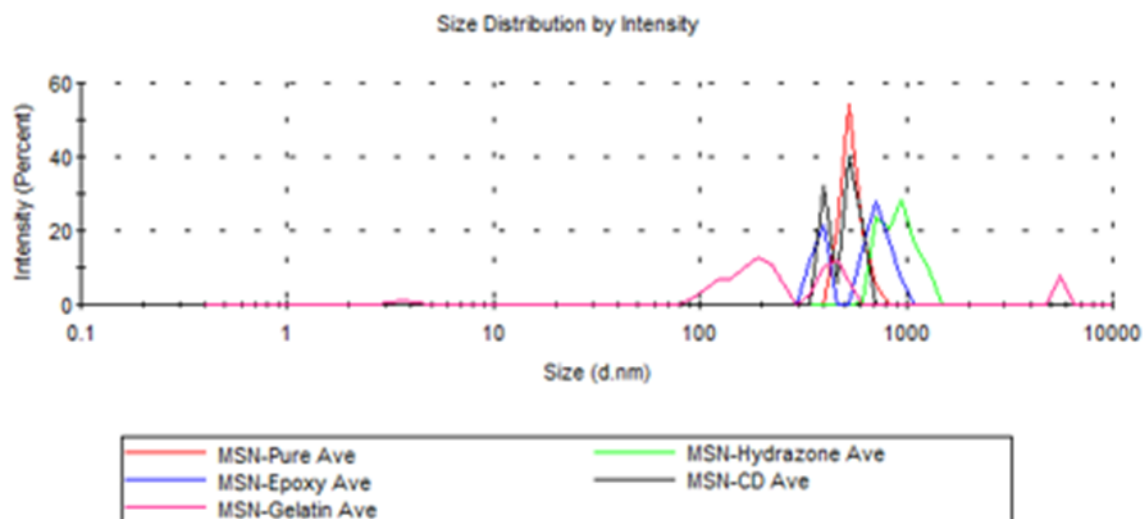


Figure 8.6: Size drifts of mesoporous silica nanoparticles

Table 8.2: Summary of observed DLS data

Formulation	Size (nm)	PDI	ζ -potential (mV)
MSN-Pure	542.7 \pm 22	0.923	-41.5
MSN-Epoxy	667.4 \pm 12	0.742	-21.3
MSN-Hydrazone	996.1 \pm 45	0.644	14.5
MSN-Cyclodextrin	581.6 \pm 33	0.371	2.81
MSN-Gelatin	444.4 \pm 22	0.497	10.7

8.3.3. Analysis of functional groups

FTIR was used for evaluation of various vibration modes of different groups of the MSN before and after coating with cyclodextrin or gelatin (Figure 8.7). Peaks around 1096.5 and 807.3 cm^{-1} were observed on all the spectra, which are the characteristic peak of the antisymmetric and symmetric stretching vibrational mode of the Si–O–Si siloxane bridges [24]. Inspection of the calcined nanoparticles indicates the presence of O–H vibrational mode free silanol as well as adsorbed water at 3300–3700 cm^{-1} region. The presence of water is also supported by peak at \sim 1634 cm^{-1} . For the epoxy functionalized nanoparticle, C–H stretching vibration bands around 2927–2944 cm^{-1} are characteristic of epoxides [25]. For the cyclodextrin coated MSN, under normally circumstances the characteristic absorption bands of cyclodextrin are stated to appear at \sim 1030, 1080 and 1155 cm^{-1} for C–C and C–O stretching vibrations and the asymmetric stretching of C–O–C glycosidic bonds [26]. In our study, the bands between 1050 and 1200 cm^{-1} which relate to the various C–O stretching vibrations of the cyclodextrins were also overlapped with a strong and broad Si–O–Si asymmetric stretching vibration of the MSNs appeared at \sim 1100 cm^{-1} . Both ζ -potential and XRD support successful adsorption. For gelatin coated MSN, this indicated the presence of amide I (1650 cm^{-1}) and amide II (1545 cm^{-1}) indication of gelatin adsorption [27].

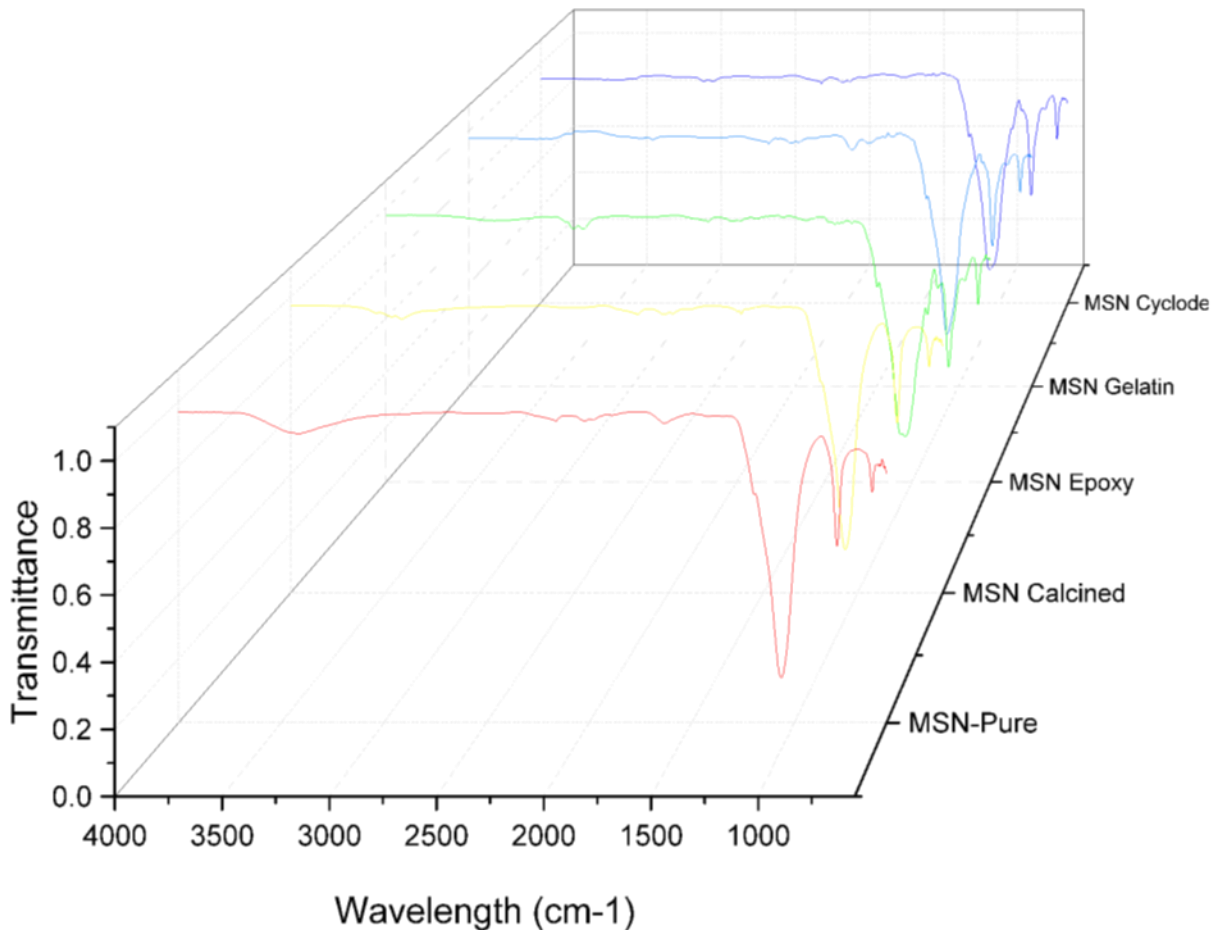


Figure 8.7: FTIR spectra overlay of MSN coated with gelatin and cyclodextrin gates

8.3.4. Crystallinity of modified mesoporous silica nanoparticle

XRD confirmed the surface modification of the mesoporous silica nanoparticles (Figure 8.8). All the diffractograms indicated a conserved pattern of the mesoporous silica nanoparticles [28]. Surface modification of the particles led to some degree of variation in the conserved pattern. For cyclodextrin functionalized MSN, the observed shift to lower diffraction angles and the decrease in reflection intensity was observed. This is stated to be attributed by the incorporation of cyclodextrin molecule into the mesostructured silica pore channels indicating successful gate-keeping [29]. The addition of epoxy and gelatin shows the presence of amorphous state.

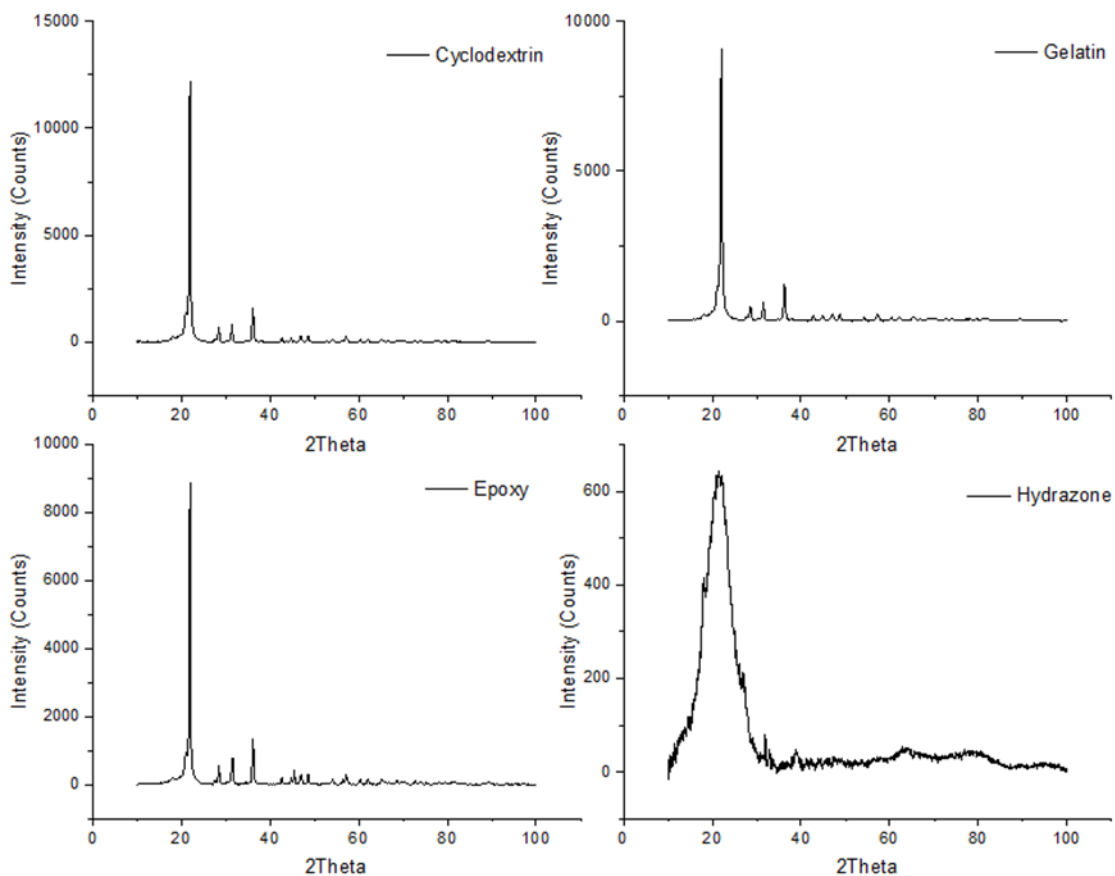


Figure 8.8: XRD diffraction patterns of MSN before and after coating

8.3.5. Analysis of particles thermostability and degradation temperature

It is stated that TGA can also aid in quantification of the overall amount of loaded drug [30]. This is however not possible with these systems as some of the degradation points of the drugs are near each other or those of the coat. Due to the MSN being un-degradable within the used range, the degradation of the coating layer and drug can be able to estimate the amount of drug within the carrier system. The multiple degradation patterns illustrated in figure 8.9 shows the degradation of coating layers in comparison to the uncoated MSNs. The patterns show adsorbed and bound water loss up to 200°C. The uneven observed big drop in temperature could be to equipment error or due to adsorbed water affecting the protein-protein interaction by decreasing the thermal stability (degradation associated with hydrolysis) of the gelatin system [31]. For gelatin it is reported range of around 250-291°C shows a transition that is associated with protein thermal degradation or decomposition. For cyclodextrin major pyrolysis of cyclodextrins was observed above 300 °C with primary loss of adsorbed water similar to gelatin [26].

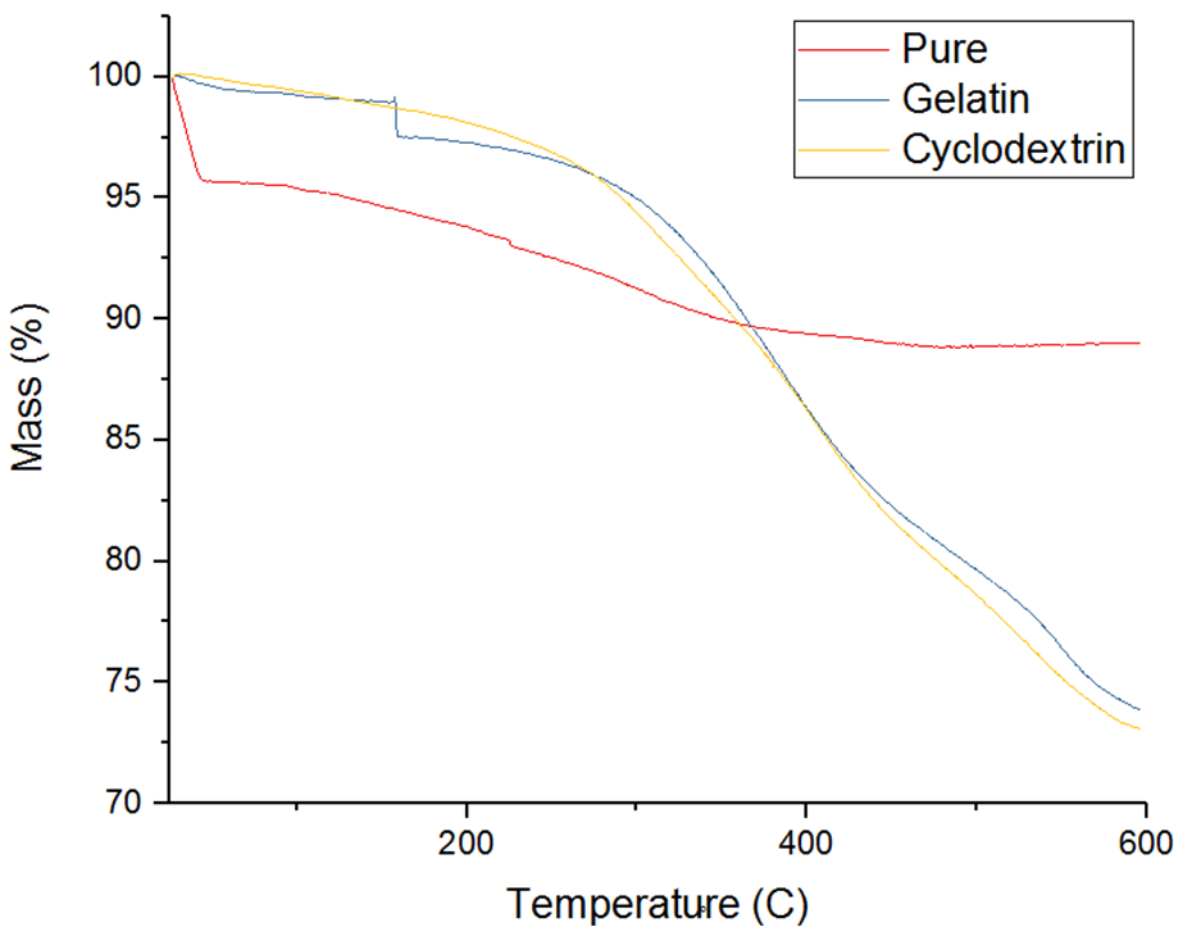


Figure 8.9: TGA graphs of MSN before and after coating

8.3.6. Evaluation of drug content

The chemometric tool designed in Chapter 3 was utilized for simultaneous drug analysis. Table 8.3 shows the drug entrapment efficiency. The data indicates that gelatin-based carriers were able to encapsulate more drug than cyclodextrin coated MSN. The increased load in gelatin is due to swelling of gelatin allowing more drug to diffuse into the pore cavities. In terms of cyclodextrin, this was hampered due to slow diffusion of the drug into the pores. The low loading is also attributed by the drug-drug interaction and drug interaction with the coat thus leading to reduce diffusion of drug into the core. This phenomenon is well reported in MSN drug uptake whereby the MSN pore size has been shown to affect drug loading. The determination of ascorbic acid was inaccurate due to interference from the gelatin leaching from the surface. This affected the accuracy of the drug.

Table 8.3: Drug entrapment efficiency

Formulation	Isoniazid	Rifampicin	Ascorbic Acid
	Entrapment Efficiency (%)		
Gelatin-MSN	35.45%	57.38%	-
α -CD-MSN	25.47%	24.04%	44.52%

8.3.7. Drug release profiles

Various model dependent methods were utilized to assess the drug release kinetics from each media and drug, respectively. Cumulative drug release was initially evaluated for each drug, followed by fitting the release profile to fit the models. Drug release was evaluated under varying pHs. Figure 8.10 depicts drug release of RIF and figure 8.11 depicts release of INH. However, the evaluation of ascorbic acid release was not plotted as the analysis showed inaccurate values from the analysis overtime. This is hypothesized to be caused by strong inclusion complex of ascorbic acid with cyclodextrin which could have had a stronger association constant than the other used drugs [32]. This is also observable with RIF as release does not reach 100%. Based on the drug release, the standard deviation occurs to increase as the media becomes acidic. This could be associated with drug-drug interaction previous discussed between isoniazid and rifampicin. This increase is only overserved as the duration of the study increases. This shows the hypothesis that ascorbic acid does have some protective function on prevent rifampicin decomposition in acidic conditions. Overall, the drug release occurred to be more profound as the acidity increases. Thus, showing the hydrazone linker is hydrolyzed as the pH drops. The release in pH 7.4 could be attributed by drug leaching or unstable hydrazone at this near neutral pH.

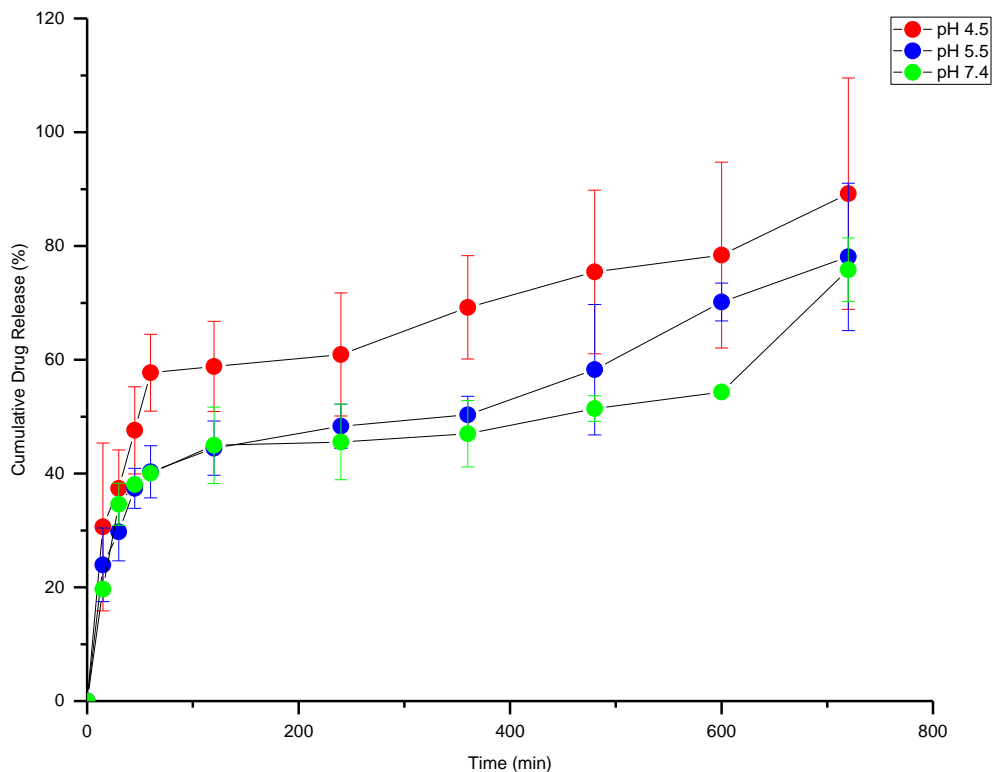


Figure 8.10: Cumulative drug release of RIF from cyclodextrin coated nanoparticles

Figure 8.10 indicates the drug release using various profile release models. Table 8.4 illustrates the observed adjusted R^2 values, the release rate constants, and the release mechanism (n value). Based on the model it shows that the n value lies within the range for non-Fickian release mechanism. This was obtained by the first 60% drug release data into Korsmeyer-Peppas model. The non-Fickian release mechanism indicates that multiple processes play a role in drug release. Surface erosion, swelling and dissolution are possible processes that could be occurring [33]. This shows that the carrier system follows Hixson-Crowell in pH 4.5 based on the adjusted R^2 value. This supports the Hixson-Crowell model well, due to the correlation of drug release from system due to polymer erosion and/or dissolution which resulted in a change in surface area and diameter of particles. The surface area can be changed by swelling or removal of the coat due to breakage of the hydrazone bonds. This model was then followed by first order and then Korsmeyer-Peppas models. Due to various in rate of gelatin swelling and water diffusion into the matrix, the rate of gelatin relaxation affected the drug release that supported first order and

Korsmeyer-Peppas [34]. Evaluation of the mean dissolution time (MDT) had values of 218.47 for pH 4.5, 282.78 for pH 5.5 and 381.33 for pH 7.4.

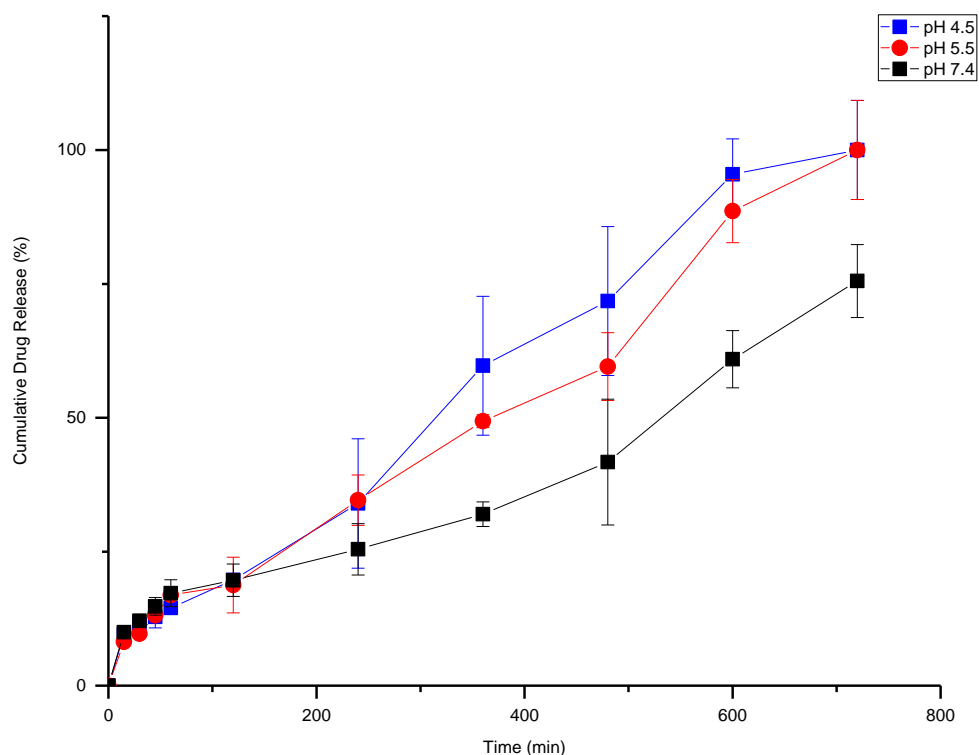


Figure 8.11: Cumulative drug release of INH from cyclodextrin coated nanoparticles

Table 8.4: Drug release kinetic models

	pH 4.5	pH 5.5	pH 7.4
Zero Order			
Adjusted R ²	0.4637	0.4689	0.7704
k	0.110	0.101	0.094
First Order			
Adjusted R ²	0.9656	0.9512	0.9401
K1	0.004	0.003	0.002
Higuchi			
AdjustedR ²	0.8708	0.9299	0.8984
kH	3.443	3.160	2.788
Hixson-Crowell			
Adjusted R ²	0.9666	0.9571	0.9333
kHC	0.001	0.001	0.001

	Korsmeyer-Peppas		
Adjusted R ²	0.9371	0.9032	0.9262
KkP	0.809	0.780	2.677
n	0.774	0.671	0.548

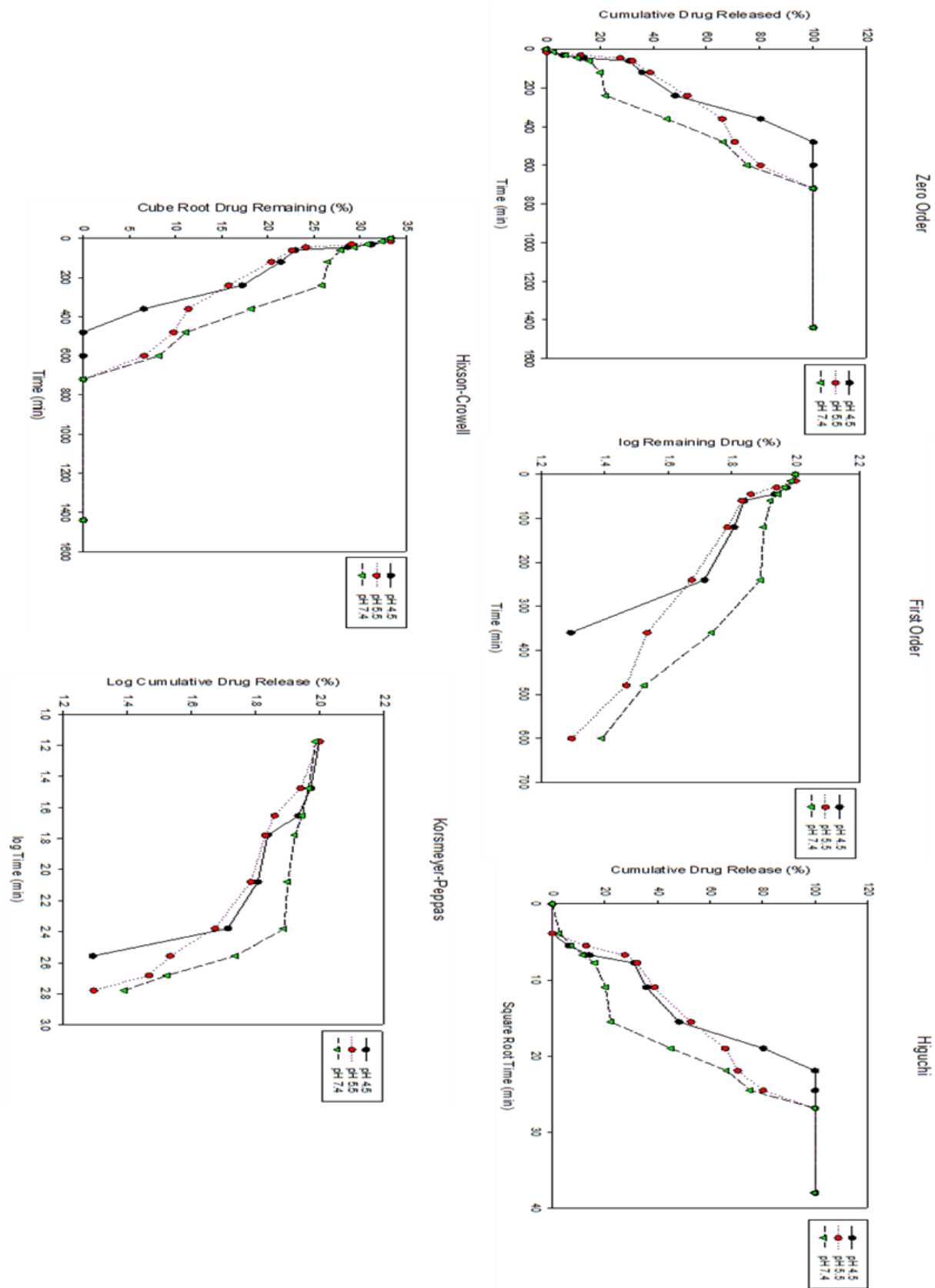


Figure 8.12: Drug release kinetics of rifampicin release from gelatin coated MSNs

8.4. Concluding remarks

Based on the study, gelatin occurs to be the ideal gate-keeper for mesoporous silica nanoparticles as it was able to entrap most of the drug and it is susceptible to degradation by proteinase in the inflamed lungs. However, the amount entrapment is not of satisfactory amount in comparisons to formulation studies whereby drug loading was increased 3-fold. This can however be hypothesized that drug loading prior coating is the ideal is warranted to increase drug capacity. This would allow the drug to diffuse easier into the pores without major strain caused by the gate. The pH response was found to agree with hydrolysis studies whereby hydrolysis is more rapid in acidic media than near neutral. However due to gelatin layer swelling inside the drug release medium, this led to increasing drug diffusion overtime. This therefore wants a requirement to improve control of drug diffusion through increase in crosslinker concentration or crosslinking time. The rate of hydrazine hydrolysis correlates well with Chapter 4, which shows that rate of hydrolysis at the observed pH's 7.4 and 4.5 are nearly similar. This linker was chosen as it had highest yield for application in dissolution studies. The study however shows possible application of MSNs are pH responsive carriers for pulmonary drug delivery through coating with gelatin. Gelatin is more favorable than cyclodextrin in pulmonary drug delivery in delivery therapeutics in diseased lungs due to expression of gelatinases (matrix metalloproteinases) overexpression [33, 34]. Gelatin coated nanoparticles have also been shown to be taken up by macrophages with reduced inflammation responses compared to bare MSNs [35]. Future will require improving the yield of latent acid hydrazine for dissolution studies.

8.5. References

- [1] R. Sun, W. Wang, Y. Wen, X. Zhang, Recent Advance on Mesoporous Silica Nanoparticles-Based Controlled Release System: Intelligent Switches Open up New Horizon, *Nanomaterials*, 5 (2015) 2019-2053.
- [2] Y. Song, Y. Li, Q. Xu, Z. Liu, Mesoporous silica nanoparticles for stimuli-responsive controlled drug delivery: advances, challenges, and outlook, *International Journal of Nanomedicine*, 12 (2017) 87-110.
- [3] R. Roggers, S. Kanvinde, S. Boonsith, D. Oupický, The Practicality of Mesoporous Silica Nanoparticles as Drug Delivery Devices and Progress Toward This Goal, *AAPS PharmSciTech*, 15 (2014) 1163-1171.

- [4] T. Yu, D. Hubbard, A. Ray, H. Ghandehari, In vivo biodistribution and pharmacokinetics of silica nanoparticles as a function of geometry, porosity and surface characteristics, *Journal of controlled release : official journal of the Controlled Release Society*, 163 (2012) 46-54.
- [5] J.M. Rosenholm, V. Mamaeva, C. Sahlgren, M. Linden, Nanoparticles in targeted cancer therapy: mesoporous silica nanoparticles entering preclinical development stage, *Nanomedicine (London, England)*, 7 (2012) 111-120.
- [6] M.A. Deli, Potential use of tight junction modulators to reversibly open membranous barriers and improve drug delivery, *Biochimica et Biophysica Acta (BBA) - Biomembranes*, 1788 (2009) 892-910.
- [7] J.L. Vivero-Escoto, I.I. Slowing, B.G. Trewyn, V.S.Y. Lin, Mesoporous Silica Nanoparticles for Intracellular Controlled Drug Delivery, *Small*, 6 (2010) 1952-1967.
- [8] G.J. Doherty, H.T. McMahon, Mechanisms of endocytosis, *Annual review of biochemistry*, 78 (2009) 857-902.
- [9] G. Tiwari, R. Tiwari, A. Rai, Cyclodextrins in delivery systems: Applications, *Journal of Pharmacy And Bioallied Sciences*, 2 (2010) 72-79.
- [10] M. Másson, T. Loftsson, G.s. Másson, E. Stefánsson, Cyclodextrins as permeation enhancers: some theoretical evaluations and in vitro testing, *Journal of Controlled Release*, 59 (1999) 107-118.
- [11] A. Hussain, J.J. Arnold, M.A. Khan, F. Ahsan, Absorption enhancers in pulmonary protein delivery, *Journal of Controlled Release*, 94 (2004) 15-24.
- [12] M. Santoro, A.M. Tatara, A.G. Mikos, Gelatin carriers for drug and cell delivery in tissue engineering, *Journal of Controlled Release*, 190 (2014) 210-218.
- [13] M. Foox, M. Zilberman, Drug delivery from gelatin-based systems, *Expert Opin Drug Deliv*, 12 (2015) 1547-1563.
- [14] Y.-T. Liao, C.-H. Lee, S.-T. Chen, J.-Y. Lai, K.C.W. Wu, Gelatin-functionalized mesoporous silica nanoparticles with sustained release properties for intracameral pharmacotherapy of glaucoma, *Journal of Materials Chemistry B*, 5 (2017) 7008-7013.
- [15] K.-i. Shimokawa, M. Katayama, Y. Matsuda, H. Takahashi, I. Hara, H. Sato, S. Kaneko, Matrix metalloproteinase (MMP)-2 and MMP-9 activities in human seminal plasma, *MHR: Basic science of reproductive medicine*, 8 (2002) 32-36.
- [16] A.Z.M. Badruddoza, G.S.S. Hazel, K. Hidajat, M.S. Uddin, Synthesis of carboxymethyl- β -cyclodextrin conjugated magnetic nano-adsorbent for removal of methylene blue, *Colloids and Surfaces A: Physicochemical and Engineering Aspects*, 367 (2010) 85-95.

- [17] P. Kempgens, J. Britton, Powder-XRD and ^{14}N magic angle-spinning solid-state NMR spectroscopy of some metal nitrides, *Magnetic Resonance in Chemistry*, 54 (2016) 371-376.
- [18] B. Abdous, S.M. Sajjadi, L. Ma'mani, β -Cyclodextrin modified mesoporous silica nanoparticles as a nano-carrier: Response surface methodology to investigate and optimize loading and release processes for curcumin delivery, *Journal of Applied Biomedicine*, 15 (2017) 210-218.
- [19] Z. Zou, D. He, X. He, K. Wang, X. Yang, Z. Qing, Q. Zhou, Natural Gelatin Capped Mesoporous Silica Nanoparticles for Intracellular Acid-Triggered Drug Delivery, *Langmuir*, 29 (2013) 12804-12810.
- [20] G. Singhvi, M. Singh, Review: In vitro Drug Release Characterization Models, *International Journal of Pharmaceutical Studies and Research*, 2 (2011) 77-84.
- [21] P. Costa, J.M. Sousa Lobo, Modeling and comparison of dissolution profiles, *European Journal of Pharmaceutical Sciences*, 13 (2001) 123-133.
- [22] S. Papadimitriou, D. Bikiaris, Novel self-assembled core-shell nanoparticles based on crystalline amorphous moieties of aliphatic copolyesters for efficient controlled drug release, *Journal of Controlled Release*, 138 (2009) 177-184.
- [23] J.A.A. Júnior, J.o.B. Baldo, The Behavior of Zeta Potential of Silica Suspensions, *New Journal of Glass and Ceramics*, Vol.04No.02 (2014) 9.
- [24] M. Zhao, L. Zheng, X. Bai, N. Li, L. Yu, Fabrication of silica nanoparticles and hollow spheres using ionic liquid microemulsion droplets as templates, *Colloids and Surfaces A: Physicochemical and Engineering Aspects*, 346 (2009) 229-236.
- [25] I. Ojea-Jiménez, P. Urbán, F. Barahona, M. Pedroni, R. Capomaccio, G. Ceccone, A. Kinsner-Ovaskainen, F. Rossi, D. Gilliland, Highly Flexible Platform for Tuning Surface Properties of Silica Nanoparticles and Monitoring Their Biological Interaction, *ACS Applied Materials & Interfaces*, 8 (2016) 4838-4850.
- [26] F. Topuz, T. Uyar, Cyclodextrin-functionalized mesostructured silica nanoparticles for removal of polycyclic aromatic hydrocarbons, *Journal of Colloid and Interface Science*, 497 (2017) 233-241.
- [27] R. Cortesi, C. Nastruzzi, S.S. Davis, Sugar cross-linked gelatin for controlled release: microspheres and disks, *Biomaterials*, 19 (1998) 1641-1649.
- [28] L.A. Solovyov, O.V. Belousov, R.E. Dinnebier, A.N. Shmakov, S.D. Kirik, X-ray Diffraction Structure Analysis of MCM-48 Mesoporous Silica, *The Journal of Physical Chemistry B*, 109 (2005) 3233-3237.

- [29] X. Xu, Z. Liu, X. Zhang, S. Duan, S. Xu, C. Zhou, β -Cyclodextrin functionalized mesoporous silica for electrochemical selective sensor: Simultaneous determination of nitrophenol isomers, *Electrochimica Acta*, 58 (2011) 142-149.
- [30] Y. Zhang, Z. Zhi, T. Jiang, J. Zhang, Z. Wang, S. Wang, Spherical mesoporous silica nanoparticles for loading and release of the poorly water-soluble drug telmisartan, *Journal of Controlled Release*, 145 (2010) 257-263.
- [31] K.P. Chuaynukul, T; Benjakul, S, Preparation, thermal properties and characteristics of gelatin molding compound resin *Research Journal of Chemical and Environmental Sciences*, 2 (2014) 1-9.
- [32] S. Saha, A. Roy, K. Roy, M.N. Roy, Study to explore the mechanism to form inclusion complexes of β -cyclodextrin with vitamin molecules, *Scientific Reports*, 6 (2016) 35764.
- [33] J.-H. Xu, F.-P. Gao, L.-L. Li, H.L. Ma, Y.-S. Fan, W. Liu, S.-S. Guo, X.-Z. Zhao, H. Wang, Gelatin–mesoporous silica nanoparticles as matrix metalloproteinases-degradable drug delivery systems in vivo, *Microporous and Mesoporous Materials*, 182 (2013) 165-172.
- [34] Z. Zou, X. He, D. He, K. Wang, Z. Qing, X. Yang, L. Wen, J. Xiong, L. Li, L. Cai, Programmed packaging of mesoporous silica nanocarriers for matrix metalloprotease 2-triggered tumor targeting and release, *Biomaterials*, 58 (2015) 35-45.
- [35] Z. Luo, Y. Hu, R. Xin, B. Zhang, J. Li, X. Ding, Y. Hou, L. Yang, K. Cai, Surface functionalized mesoporous silica nanoparticles with natural proteins for reduced immunotoxicity, *Journal of Biomedical Materials Research Part A*, 102 (2014) 3781-3794.

9. : DEVELOPMENT OF COMPUTATIONAL FLUID DYNAMICS MODEL OF TUBERCULOSIS INFECTED LUNGS

9.1. Introduction

For successful pulmonary drug delivery it has been shown that various factors can affect aerosol particle deposition in the airways, such as the physical and hydrodynamic characteristics of the particles, the inhalation flowrate, the health state of the individual and the geometrical and morphological details of the airways [1]. The profound changes in the airways are caused by the disease state of the lungs. Lung disease states such as bronchoconstriction, inflammation and airway narrowing can alter lung deposition. Due to changes the architecture of the lung through alterations in bifurcation angles and obstruction of the airways caused mostly by mucus accumulation, this affects aerodynamics thus modifying the deposition and distribution patterns of aerosols [2]. Tuberculosis is an infectious disease cause by bacillus *Mycobacterium tuberculosis* (M. tuberculosis) which affects the lungs. This is ranked the second leading cause of death after the human immunodeficiency virus (HIV) [3]. During pulmonary TB infection lung remodelling occurs such as cavitation, fibrosis (facilitate latency and selection of drug resistance), and distorted architecture thus leading to volume loss (airway restriction), and tuberculous bronchiectasis and bronchostenosis [4]. matrix metalloproteinases (MMPs) such as MMP-9 is one of the enzymes that has been shown to cause lung remodelling during granuloma formation and macrophage recruitment [5].

In terms of particles physical and hydrodynamic characteristics, Literature reviews indicate that 1-5 μm size is essential in pulmonary drug delivery [6]. However, other literature show that inhalable nanoparticles have a more profound advantage to microparticles as they can achieve a high drug loading and have a better mucosal cell adherence (can enhance net drug delivery to the lungs) [7]. it also shows that nanoparticles are also efficiently taken up by alveolar macrophages [8]. In order to facilitate nanoparticle deposition and uptake with an aerodynamic diameter of < 0.5 μm , which are known to be susceptible to be exhaled, if they are not aggregated and/or if insufficient time is available for their deposition [9]. Their deposition can therefore be promoted by slow deep breathing and breath holding[10]. A large number of studies have developed various formulations for pulmonary drug delivery via dry powder inhalers. These powder formulations carrying antitubercular drugs (anti-TB drugs) such as isoniazid, rifampicin, ethambutol and pyrazinamide can be delivered directly to the lung. Upon inhalation, they are

taken up by alveolar macrophages where the bacteria develop. Thus, this form of local delivery can lead to high drug concentration localized in the lung which can lead to reducing of the duration of treatment (conventional treatment-6–9 months) and preventing multi-drug resistance (MDR).

There are limitations in studying aerosol deposition *in vivo* using animals or humans due to ethical and safety concerns with studying aerosol deposition. The use *in silico* models based on Computational Fluid Dynamics (CFD) can help in filling this gap by providing an unprecedented level of information that would allow rapid evaluation of formulations strategies. Within the airways unsteady turbulent flows are observed due to airways bifurcation. The use of whole-lung models can be used to estimate particle deposition efficiencies in various respiratory tract regions (Figure 9.1) utilizing specific flow conditions for deposition mechanisms (diffusion, impaction, interception, and gravitation). CFD has widely been used for analysis of fluid flows, which focused on solving of dynamic equations governing fluid motion numerically over a physical region of interest. Currently, there are there are three techniques for solving turbulent flow equations using a computer: direct numerical simulations (DNS), Reynolds averaged Navier–Stokes (RANS) and large eddy simulations (LES).

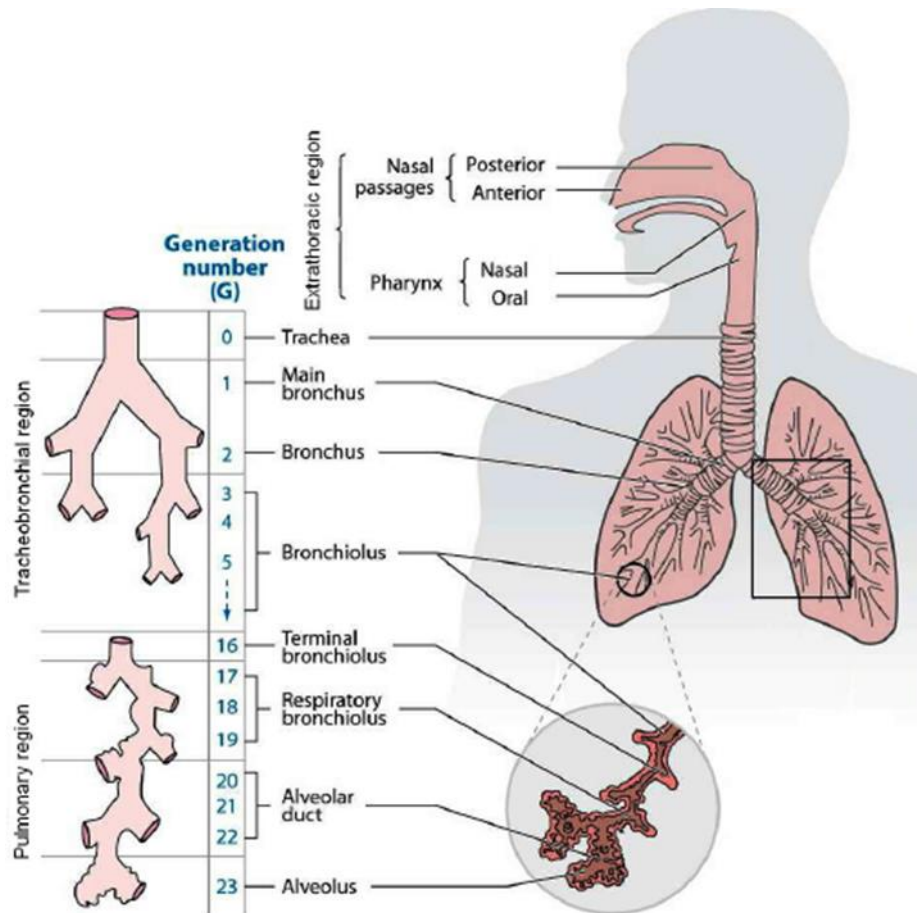


Figure 9.1: Diagram depicting various airway generations used in CFD modelling (Adapted from [11])

For tracking of particle trajectories and prediction of regions of particle interception with the airway wall surface, Lagrangian methods have proven useful. For particles that intercept with these surfaces can be considered to have deposited, allowing for a quantification of deposition efficiency for a given airway geometry [12]. Due to the disease state affecting the geometry of the airways, recent study has been conducted on *in silico* modelling of asthma whereby MRI and SPECT images were used for building the model [13]. The results indicated that the *in silico* model was able to provide a crucial information for addressing effects of disease on the administration of aerosolized drugs. This suggested that modelling should be used in a complementary manner with future inhalation therapy protocols. In this section, MRI data is used to model the TB diseased lung and evaluate the deposition of nanoparticles within the diseased lung.

9.2. Methods

9.2.1. Design of the airway geometry

The use of MRI has allowed detailed visualization of various anatomical features in profound details (Figure 9.2). The MRI scans were obtained from the Lung Image Database Consortium (LIDC) of a patient with tuberculosis. The MRI scans in DICM format (125 images) were then imported into 3D slicer v4.3. Volume rendering was then utilized. The lung pre-sets were selected during volume rendering to assist in cropping region of interest. The ROI was generated, followed by creation of label map by selecting the region of interest. This was then followed by building of the lung model and saving it in an STL format for mesh design.

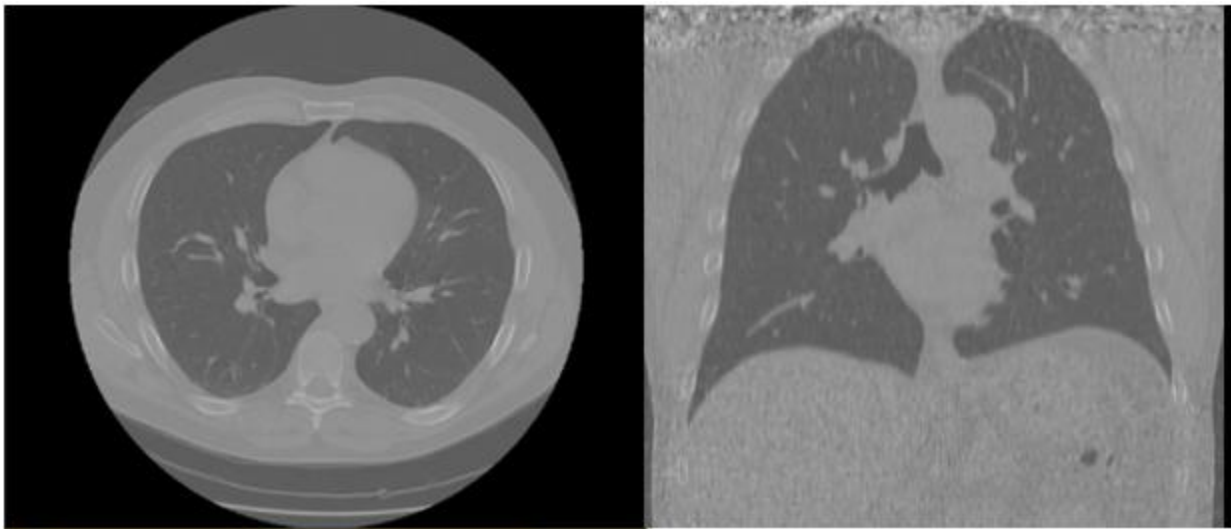


Figure 9.2: *MRI scans of tuberculosis infected lung (A) axial view) and (B) coronal view*

The developed segmented lung region was then imported into 3D metrics medical in an STL format. This was then used to remove layers of skin that were segmented with the lung. Figure 9.3 illustrate the obtained lung model after refining out some of the unwanted layers. The model indicates that the pulmonary region is present within the model.

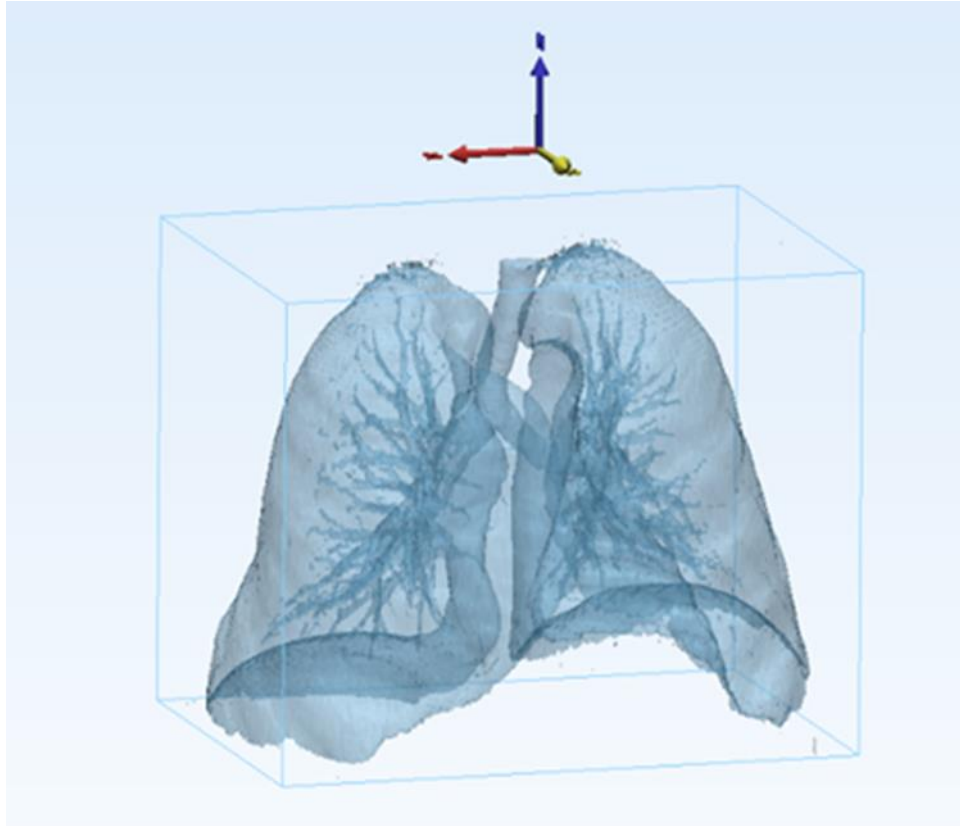


Figure 9.3: *Images of the segmented lungs*

9.2.2. Drug deposition prediction using OpenFoam

For the assessment of nanoparticles deposition, table 9.1 indicates the parameters that can be used for CFD prediction. Nanoparticles are known to deposit via Brownian motion, thus wants the use of gravity and drag force as the forces driving deposition. pimpleDyM is a transient solver that can be used on a moving mesh for solving incompressible, turbulent flow of Newtonian fluids. For particles tracking, icoUncoupledKinematicParcel is also an OpenFoam transient solver used for the analysis of passive transport of a single kinematic particle cloud.

Table 9.1: Proposed OpenFoam parameters (Adapted from [14])

OpenFOAM	V1661
Mesh	snappyHexMesh
Solver	pimpleDyM & icoUncoupledKinematicParcel
Spatial Discretisation	Linear/Upwind
Temporal Discretisation	Fully Implicit

Mesh Motion	Kinetic, self-similar & sinusoidal
Fluid-Particle Coupling	One way coupled
Particle Forces	Standard gravity & Drag

9.3. Results and discussion

A CFD model was developed to aid in studying the deposition of synthesized nanoparticles in the airway remodelled by TB (Figure 9.4). A mesh file was designed to be imported into OpenFoam software and analysed with the aforementioned parameters in table 9.1. The mesh was designed using snappyHexMesh utility. The mesh retained the morphology and dimensions of the segmented lung from the MRI scans. It was found the synthesized particles had some degree of polydispersity. Further analysis using cascade impaction and particle aerosol particle mass analyser (APM) could aid in accurately characterization of the particles aerodynamic features prior CFD analysis. Due to aforementioned polydisperse/aggregation features, aerosol modelling will require to discretize the PSD into sections followed by solving transport equation for each particle size [15]. This would therefore become computationally expensive for the numerical techniques to follow.

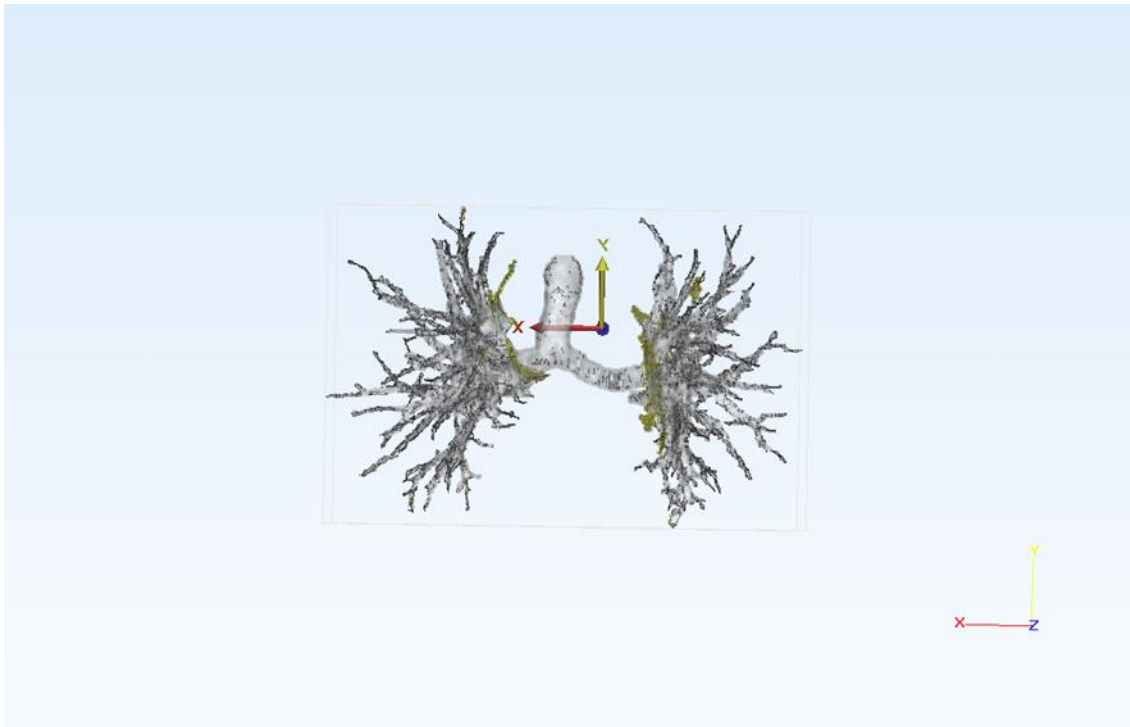


Figure 9.4: *Generated mesh of the whole lung model.*

9.4. Concluding remarks

A realistic lung model was successfully developed for the deposition of particles in a disease remodelled lungs. CFD studies were not conducted as accuracy of the prediction depends on a number of aerodynamic properties which were not evaluated in the whole study. Various instruments were required to accurately assess the prediction of the synthesized particles. The differential mobility analyser (DMA) was required for the assessment of the particle electrical mobility which is crucial for DPI as particles are known to accumulate a charge after dispersion. This charge can affect final deposition as illustrated in literature review section. For accurate assessment various parameters such as effective density, mass–mobility exponent, aerodynamic diameter, and dynamic shape factors are required for CFD modelling. These can be measured with tandem systems of a DMA and a mass classifier (aerosol particle mass analyser (APM) or centrifugal particle mass analyser (CPMA), and a DMA and an impactor. Tandem evaluation of the particles was limited in this study to be complete, resource availability [16]. Despite these limitations, a good model depicting to alveolar ducts has been successfully developed for future implementation of CFD works for study in TB drug delivery carrier systems. The emitted particle dose from a DPI can also be evaluated for this model in the future once the dispersed particle aerodynamic features have been characterized.

9.5. Reference

- [1] P.G. Koullapis, S.C. Kassinos, M.P. Bivolarova, A.K. Melikov, Particle deposition in a realistic geometry of the human conducting airways: Effects of inlet velocity profile, inhalation flowrate and electrostatic charge, *Journal of Biomechanics*, 49 (2016) 2201-2212.
- [2] N.R. Labiris, M.B. Dolovich, Pulmonary drug delivery. Part I: Physiological factors affecting therapeutic effectiveness of aerosolized medications, *British Journal of Clinical Pharmacology*, 56 (2003) 588-599.
- [3] D.-D. Pham, E. Fattal, N. Tsapis, Pulmonary drug delivery systems for tuberculosis treatment, *International Journal of Pharmaceutics*, 478 (2015) 517-529.
- [4] K. Dheda, H. Booth, J.F. Huggett, M.A. Johnson, A. Zumla, G.A.W. Rook, Lung Remodeling in Pulmonary Tuberculosis, *The Journal of Infectious Diseases*, 192 (2005) 1201-1210.
- [5] J.L. Taylor, J.M. Hattle, S.A. Dreitz, J.M. Troudt, L.S. Izzo, R.J. Basaraba, I.M. Orme, L.M. Matrisian, A.A. Izzo, Role for Matrix Metalloproteinase 9 in Granuloma Formation during Pulmonary Mycobacterium tuberculosis Infection, *Infection and Immunity*, 74 (2006) 6135-6144.
- [6] J. Shaji, M. Shaikh, Current Development in the Evaluation Methods of Pulmonary Drug Delivery System, *Indian Journal of Pharmaceutical Sciences*, 78 (2016) 294-306.

- [7] R. Pandey, G.K. Khuller, Antitubercular inhaled therapy: opportunities, progress and challenges, *The Journal of antimicrobial chemotherapy*, 55 (2005) 430-435.
- [8] L. Zhang, D. Pornpattananangku, C.M. Hu, C.M. Huang, Development of nanoparticles for antimicrobial drug delivery, *Current medicinal chemistry*, 17 (2010) 585-594.
- [9] A.H.L. Chow, H.H.Y. Tong, P. Chattopadhyay, B.Y. Shekunov, Particle Engineering for Pulmonary Drug Delivery, *Pharmaceutical Research*, 24 (2007) 411-437.
- [10] M. Paranjpe, C. Müller-Goymann, Nanoparticle-Mediated Pulmonary Drug Delivery: A Review, *International Journal of Molecular Sciences*, 15 (2014) 5852.
- [11] H. Majid, P. Madl, Lung deposition predictions of airborne particles and the emergence of contemporary diseases Part-I, 2011.
- [12] N.B. Carrigy, C.A. Ruzycski, L. Golshahi, W.H. Finlay, Pediatric in vitro and in silico models of deposition via oral and nasal inhalation, *J Aerosol Med Pulm Drug Deliv*, 27 (2014) 149-169.
- [13] T. Martonen, J. Fleming, J. Schroeter, J. Conway, D. Hwang, In silico modeling of asthma, *Advanced Drug Delivery Reviews*, 55 (2003) 829-849.
- [14] P. Hofemeier, Computational simulation of inhaled ultrafine aerosol in the distal regions of the lung, Israel OpenFoam user group meeting, OpenFoam, 2012.
- [15] R. Guichard, E. Belut, Simulation of airborne nanoparticles transport, deposition and aggregation: Experimental validation of a CFD-QMOM approach, *Journal of Aerosol Science*, 104 (2017) 16-31.
- [16] F. Tavakoli, J.S. Olfert, Determination of particle mass, effective density, mass–mobility exponent, and dynamic shape factor using an aerodynamic aerosol classifier and a differential mobility analyzer in tandem, *Journal of Aerosol Science*, 75 (2014) 35-42.

10. : CONCLUDING REMARKS, RECOMMENDATIONS AND OUTLOOK

10.1. Concluding remarks

Pulmonary Tuberculosis remains one of the second leading cause of death after HIV AIDS. One in five people who have HIV infection can be found in South Africa [1]. These numbers also constitute TB-HIV co-infection. Current method for TB treatment depends of the use of rifampicin, isoniazid, ethambutol and pyrazinamide (six months regimen). In 2001–2002, a surveillance on TB drug resistance found that 1.8% of new TB patients and 6.7% of previously treated TB patients had developed multidrug resistant (MDR)-TB [2]. These showed resistances to isoniazid, rifampicin, ethambutol, and streptomycin. Resistance has been linked to low rates of treatment completion, irregular and inadequate treatment plan (non-compliance) [3, 4]. The introduction of the directly observed therapy (DOT) was designed to improve inadequate treatment plan due to patient non-compliance. The DOT program centers around a surrogate/nurse to aid observe that the patient takes their medication when required to do so. The used of fixed dose combination has also been able to improve compliance. However, in South Africa where patients may have both TB and HIV, this leads to some patients failing to absorb the antituberculosic drugs and occurrence of drug-drug interaction [5]. Rifampicin and ethambutol are the drugs that have the most pronounced reduction in intestinal absorption [6]. This increases the risk of treatment failure, relapse and acquisition, toxicity of drug-resistant strains. Thus, warrants an alternative mode of delivery that would not be affected by gastrointestinal malabsorption.

Drug delivery can be used as a tool to improve drug solubility, stability and bioavailability issues, enhance compliance and adherence and enable targeted delivery to alveolar macrophages which are a reservoirs for TB infection [7]. Thus, local administration of antituberculosic drugs can aid in improving TB treatment plan. Two types of carrier systems were synthesized in this project. This started by evaluation of features that could improve drug loading capacity in mesoporous silica nanoparticles. The study was a success as drug loading was improved by more than threefold in comparison to recent literature studies. The gelatin nanoparticles were also synthesized as an alternative carrier to inorganic MSNs. The surfactant concentration occurred to play a major role in the folding of gelatin during synthesis which ultimately affected drug release rate and degree of swelling ratio. They also indicated high drug encapsulation. Due to these nanoparticles possible applicability in targeting of macrophages and releasing drug within the cells, pH responsive linkers were also synthesized. It was observed that through the addition of latent acids into the

hydrazones, degree of hydrolysis and stability in neutral and acidic pH could be controlled. The attempt to incorporate a hygroscopic layer was removed from this study as further research in dry powder delivery showed that stability was a concern when carriers were hygroscopic. The evaluation of deposition mechanism *in silico* was also halted due to concern of data accuracy as several aerodynamic properties still had to be evaluated. However, a model for studying drug delivery into TB infected lungs has been designed for future applications.

10.2. Recommendations

The thesis has shown that physicochemical properties of MSNs can be attenuated to support loading of drug combination. The drug release from using chitosan was successful as it is a natural pH responsive polymer. The use of our novel linker showed promise and a good linker for using with various gate keepers. It is therefore recommended that for future studies, the latent acid carrying hydrazone be used for drug release studies after yields of the compound have been improved. It further shows that online literatures that encourage drug loading via diffusion after polymer coating can hamper the attenuated properties of improving drug loading. It is therefore proposed that drugs be loading first then followed by coating with the gate keeping polymers. In terms of gelatin-based nanoparticles, the use of a homogenizer instead of the use still magnetic stirrer during coacervation process. It further showed that protein nanoparticles can also be synthesized using our newly developed novel method with the use of nonionic surfactants not used before. Due to the use of nanoparticles in this study, long term exposure may have unforeseen potential toxicity. For evaluation of possible toxicity, the Calu-3 which is one of the commonly used for tracheobronchial epithelial cell studies can be utilized. An MTT assay can be utilized for this study [8]. To study the uptake of nanoparticles, internalization of nanoparticles by macrophage cells can be assessed using confocal microscopy and flow cytometry studies. Any morphological changes would be able to confirm macrophage activation [9]. Apart from long term exposure to the body, the stability the drug loaded nanoparticles can also be evaluated. TGA decomposition kinetics can be utilized to determine lifetime stability.

Overall, the thesis represented several novel techniques for developing nanocarrier systems that are capable of encapsulating various drugs. This shows that the carrier systems can be utilized for drug delivery treatment of more than TB. Systemic drug delivery via pulmonary drug delivery is of great interest and requires animal studies to assess the distribution of the nanoparticles after inhalation. This would then provide more realistic information on the possible long-term effect of the carrier system. Under dosing of antituberculous drugs is of great concern. Pulmonary drug

delivery technologies have focused initially on the device features. Current studies have considered particles characteristics for aerosolization. This work has designed particles with the expected range to reach the deep lung and cellular uptake by macrophages. The use of equipment like cascade impactor is vital in determination of the emitted dose to assess the amount of drug that the DPI can release. This is of great importance to avoid under-dosing. The infected lung also can affect lung deposition as seen in literature review section. Our CFD model has been designed for TB infected drugs for future studies.

10.3. Outlook

The current work has shown that current MSN can be greatly improved for incorporation of multiple drugs in comparison to conventional synthetic method. The work shows great promise after the development of novel pH linkers which can be conjugated to various carrier systems. Novel method for the design of gelatin nanoparticles was also developed which showed that the drug release kinetics can be improved by affecting the folding states of the protein. This information is vital development of protein based nanocarrier systems. The application of our carrier systems in South African TB treatment plan can help reduce TB treatment related issues during simultaneous TB and AIDS treatment. The malabsorption of some of the antituberculous drug can be evaded by delivering them directly to the lungs. The technology also helps reduce side effects profile thus help with improving patient compliance. The long treatment plan occurs to of major concern to adherence to TB as incomplete treatment is one of the risk factors of drug resistance. Recent studies in nanoparticle carrier systems for TB have that nebulization of nanoparticles to guinea pigs infected TB with at every 10th day resulted with no tubercle bacilli being detected in the lung after only five doses of treatment. This was of great improvement in comparison to 46 daily doses of orally administration in order to obtain an equivalent therapeutic benefit [10].

10.4. Reference

- [1] B.G. Williams, S. Gupta, M. Wollmers, R. Granich, Progress and prospects for the control of HIV and tuberculosis in South Africa: a dynamical modelling study, *The Lancet Public Health*, 2 (2017) e223-e230.
- [2] R. McNerney, The emergence and spread of incurable tuberculosis in South Africa, *International Journal of Mycobacteriology*, 5 (2016) S68.

- [3] N.R. Gandhi, A. Moll, A.W. Sturm, R. Pawinski, T. Govender, U. Lalloo, K. Zeller, J. Andrews, G. Friedland, Extensively drug-resistant tuberculosis as a cause of death in patients co-infected with tuberculosis and HIV in a rural area of South Africa, *The Lancet*, 368 (2006) 1575-1580.
- [4] R.F. Jacobs, Multidrug-resistant tuberculosis, *Seminars in Pediatric Infectious Diseases*, Elsevier, 1996, pp. 170-181.
- [5] E.D. Chan, M.D. Iseman, Current medical treatment for tuberculosis, *BMJ : British Medical Journal*, 325 (2002) 1282-1286.
- [6] I. Smith, Mycobacterium tuberculosis pathogenesis and molecular determinants of virulence, *Clin Microbiol Rev*, 16 (2003) 463-496.
- [7] A. Sosnik, Á.M. Carcaboso, R.J. Glisoni, M.A. Moretton, D.A. Chiappetta, New old challenges in tuberculosis: Potentially effective nanotechnologies in drug delivery, *Advanced Drug Delivery Reviews*, 62 (2010) 547-559.
- [8] L. Sun, X. Zhang, Z. Wu, C. Zheng, C. Li, Oral glucose- and pH-sensitive nanocarriers for simulating insulin release in vivo, *Polymer Chemistry*, 5 (2014) 1999-2009.
- [9] W. Xia, H.-M. Song, Q. Wei, A. Wei, Differential Response of Macrophages to Core–Shell Fe(3)O(4)@Au Nanoparticles and Nanostars, *Nanoscale*, 4 (2012) 10.1039/c1032nr32070c.
- [10] S. Gelperina, K. Kisich, M.D. Iseman, L. Heifets, The Potential Advantages of Nanoparticle Drug Delivery Systems in Chemotherapy of Tuberculosis, *American Journal of Respiratory and Critical Care Medicine*, 172 (2005) 1487-1490.

11. Appendix

10.1. 11.1 Research Presentations

22nd International Conference and Expo on

NANOSCIENCE AND MOLECULAR NANOTECHNOLOGY

November 06-08, 2017 | Frankfurt, Germany

Control of mesoporous silica nanoparticles physicochemical properties through control of synthetic parameter using box-behnken design

Mpho P Ngoepe and Rui MW Krause
Chemistry Department, Rhodes University, SA

Statement of the Problem: Mesoporous silica nanoparticles (MSN) have been utilized in drug delivery due to their controllable release kinetics. The control of the physicochemical properties of nanoparticles for applications is stated to be complex despite the use of computational model. The pH, molar ratio of silica source and water and calcination temperature impact in drug delivery have not been studied before. Understanding of these critical synthetic parameters can aid in controlling the particle size, pore structure and size, surface chemistry and drug loading capacity. Methodology & Theoretical Orientation: Box-Behnken design was utilized for evaluation of these parameters. Whereby, post-grafting of amine, surface chemistry post calcination, drug loading particle size and pore structure were studied. For application in drug delivery, rifampicin was loaded into the particles followed by capping with pH responsive chitosan. Findings: Based on the surface response plot from the experimental design, the size of the particle indicates to be dependent on the amount of water available for hydrolysis and dissolution to occur at a near neutral pH. The highest size obtained was 609 ± 44.44 (n=3), whereby pH 8 and molar ratio of 126 was used. The smallest size was observed was observed at pH 12. The calcination temperature played a role in condensation of the free silanols which lead to changes in the grafting potential of the silica surface to (3-Aminopropyl) triethoxysilane. The amount of drug entrapped indicates can be improve though increase in particle size and increase in the porous particle structure. Conclusion & Significance: This works adds to previous work that indicate that TEOS: water ratio plays a role in particle size, pH plays a role in the control of the network structure, whilst calcination temperature affects the degree of post synthesis silanol condensation.



Figure 1: Synthetic procedures for MSNs for control of particle size, porosity and surface chemistry.

Biography

Mpho Phehelo Ngoepe has experience in pharmaceutical formulation and design for drug delivery system. Obtained an MSc(Med) in Pharmaceuticals at the University of the Witwatersrand (South Africa). Currently doing a PhD in Chemistry at Rhodes University (South Africa), to better understand and gain experience in nanomaterial chemistry. Using experimental design, various synthetic parameters can be used to improve the performance of currently utilized drug delivery carriers. The understanding of material chemistry and physics can aid in improving drug delivery systems.

mphongoepe@hotmail.com

Notes:

INTERNATIONAL MEETING ON
ADVANCED NANOMATERIALS AND NANOTECHNOLOGY
NOVEMBER 07-08, 2017 SINGAPORE**Control of mesoporous silica nanoparticles physicochemical properties through control of synthetic parameter using Box-Behnken design**Mphe Phshello Ngoepe and Rui MW Krause
Rhodes University, South Africa

Statement of the Problem: Mesoporous silica nanoparticles (MSN) have been utilized in drug delivery due to their controllable release kinetics. The control of the physicochemical properties of nanoparticles for applications is stated to be complex despite the use of computational model. The pH, molar ratio of silica source and water and calcination temperature impact in drug delivery has not been studied before. Understanding of these critical synthetic parameters can aid in controlling the particle size, pore structure and size, surface chemistry and drug loading capacity.

Methodology & Theoretical Orientation: Box-Behnken design was utilized for evaluation of these parameters. Whereby, post-grafting of amine, surface chemistry post calcination, drug loading particle size and pore's structure was studied. For application in drug delivery, rifampicin was loaded into the particles followed by capping with pH responsive chitosan.

Findings: Based on the surface response plot from the experimental design, the size of the particle indicates to be dependent on the amount of water available for hydrolysis and dissolution to occur at a near neutral pH. The highest size obtained was 609 ± 44.44 (n=3), whereby pH 8 and molar ratio of 126 was used. The smallest size was observed was observed at pH 12. The calcination temperature played a role in condensation of the free silanols which lead to changes in the grafting potential of the silica surface to (3-Aminopropyl) triethoxysilane. The amount of drug entrapped indicates can be improves though increase in particle size and increase in the porous particle structure.

Conclusion & Significance: This works adds to previous work that indicates that TEOS: water ratio plays a role in particle size, pH plays a role in the control of the network structure, whilst calcination temperature affects the degree of post synthesis silanol condensation.

mphongope@hotmail.com